



NATIONAL TECHNICAL UNIVERSITY OF ATHENS

SCHOOL OF NAVAL ARCHITECTURE AND MARINE ENGINEERING

**Modelling and numerical/experimental investigation
of granular cargo shift in maritime transportation**

by

Christos C. Spandonidis

Doctoral Thesis

Athens, August 2016



NATIONAL TECHNICAL UNIVERSITY OF ATHENS

SCHOOL OF NAVAL ARCHITECTURE AND MARINE ENGINEERING

**Modelling and numerical/experimental investigation
of granular cargo shift in maritime transportation**

by

Christos C. Spandonidis

*A dissertation submitted in partial fulfilment
of the requirements for the degree of
Doctor of Philosophy*

Advisory Committee:

Konstantinos J. Spyrou, *Professor* (Supervisor)

Gerassimos A. Athanassoulis, *Professor*

Apostolos D. Papanikolaou, *Professor*

Athens, August 2016

This thesis is dedicated to the three precious women in my life:

my wife, my daughter and my mother.

Also to my father.

Abstract

The study of granular materials (powders, sands, grains, metal ore etc.) should be a topic of great interest in naval architecture, since cargo shift represents a major hazard for ship safety and probably the most common cause of capsizing of large ships. Despite its great importance, the behaviour of granular cargoes transported by sea has not been sufficiently investigated yet from a theoretical perspective. As a result, international regulations governing the procedures of loading and stowage of bulky cargoes, while continuously updated and improved, remain mainly empirical.

In the current Thesis, a micro-scale modelling approach is presented, aimed to develop capability for simulating the dynamic behaviour of granular materials having physical properties conforming to those of bulky cargoes commonly transported through the sea, inside ship holds. The well-established method of “*Molecular Dynamics*” is employed for modelling particles’ interactions and for predicting macroscopic features of the excited granular material behaviour. The algorithm is further combined with standard models of ship motion, in order to understand the interplay of granular material flow with vessel motion.

At the first stage, “dry” granular materials comprised of spherical particles and affected by non-linear frictional forces are employed. Later, a number of improvements are incorporated, to bring the model closer to reality, by introducing the effect of environmental humidity and also the irregularity in particles’ shape. To discern qualitatively different patterns of behaviour, a variety of materials and filling ratios have been examined. Moreover, to improve performance, the computational algorithm was parallelized for Graphical Processing Unit (GPU) implementation and the merit of it was properly evaluated.

Characteristic simulation results of a 2D rectangular scaled barge, partly filled with bulky cargo and vibrated in roll, sway and heave are included in the Thesis. The barge is, either, forced to oscillate in a prescribed motion; or is free to move under the effect of wave loads and her cargo’s occasional fluid-like movement. Critical parameter values where cargo shift is initiated are identified. The intention has been to maintain the excitation amplitudes and frequencies close to realistic open sea conditions although the scaling problem is in itself a major scientific challenge.

Judging from the qualitative character of the obtained results and also from comparisons of some key findings with experimental results, it appears that the described simulation model has good potential to evolve into a useful and practical computational tool for the investigation of stability of ships carrying solid cargoes in bulky form.

Keywords: *granular material, molecular dynamics, cargo shift, ship stability, capsizing*

Table of Contents

Abstract	v
Table of Contents	vii
List of Figures	xi
List of Tables	xvi
Chapter 1: Introduction	17
1.1 General framework and aim of research.....	17
1.2 Focal points of interest	19
1.3 Need for further research.....	20
1.4 Methodology	21
1.5 Contributions of the thesis.....	21
1.6 Thesis outline	22
Chapter 2: Critical literature review	25
2.1 Granular nature	25
2.2 IMO bulk cargo regulation review	27
2.3 Granular materials behaviour	27
2.4 Research approaches for investigating granular materials.....	28
2.4.1 Granular material modelling approaches	30
2.5 Angle of repose	33
2.6 Behaviour of granular material under prescribed vibration	36
2.6.1 Vertical (heave) vibration.....	36
2.6.2 Lateral (sway) vibration	39
2.7 Coupled ship-cargo motion	39
2.8 “Weakly wet” granular materials	39
2.9 Granular material behaviour computing in Graphical Processing Unit	42
2.10 Non-spherical particle research	43
2.10.1 Non-spherical DEM approaches.....	45
2.10.2 Realistic shape descriptors	48
Chapter 3: Objectives	51
Chapter 4: Basic Mathematical Model.....	53
4.1 Molecular Dynamics simulation	53
4.1.1 Coupled ship-cargo motion implementation.....	54

4.2	Interaction forces.....	56
4.2.1	Dry granular solids and aggregates	56
4.2.2	Implementation of humidity	59
4.3	Systems of coordinates.....	60
4.4	Model verification.....	61
4.5	Validation.....	62
Chapter 5: Granular Flow under Prescribed Tank Motion		65
5.1	System Definition	65
5.2	Dependence of granular flow on particle's properties	66
5.2.1	Slow tilting of tank – identification of angle of repose.....	67
5.2.2	Motion under horizontal (sway) and vertical (heave) excitation.....	69
5.3	Dependence of granular flow on system's configuration	74
5.3.1	Dependence of angle of repose on initial free surface configuration	75
5.3.2	Dependence of angle of repose on side wall height.....	78
5.3.3	Slow tilting of tanks with different filling	79
5.3.4	Investigation of material's hysteretic behaviour.....	82
5.3.5	Granular material flow depending on the position of the roll centre.....	83
5.4	Scaling effects.....	86
5.4.1	Horizontal motion under sway excitation.....	87
5.4.2	Slow tilting of the tank – identification of angle of repose.....	89
5.5	Concluding remarks	90
Chapter 6: Code Parallelization in CUDA Environment.....		93
6.1	Implementation	93
6.2	Numerical verification/validation of the algorithm	95
6.3	Performance results.....	98
6.4	Discussion.....	100
6.5	Concluding remarks	101
Chapter 7: Coupled ship - cargo motion in regular beam seas		103
7.1	System definition	103
7.2	Single Degree of Freedom - Roll.....	104
7.2.1	Equation of motion.....	104
7.2.2	Case study	107
7.3	Three degrees of Freedom (Roll - Sway - Heave)	113
7.3.1	Equations of motion	113

7.3.2	Dry cargo	115
7.3.3	Implementation of humidity	120
7.4	Concluding remarks	123
Chapter 8: Cargo with Irregularly-Shaped Particles.....		125
8.1	Methodology description	125
8.1.1	Object generation	125
8.1.2	Contact detection.....	129
8.1.3	Physics and visualisation.....	131
8.2	Validation results and discussion	132
8.2.1	Investigation of semi-static behaviour: angle of repose.....	132
8.2.2	Dynamic behaviour – sway oscillation.....	133
8.2.3	Coupled fluid-ship-material motion in 3 DOF.....	135
8.2.4	Discussion	136
8.3	Numerical experiments with irregularly - shaped particles	136
8.3.1	Dependence of the angle of repose upon the Fourier Descriptors.....	137
8.3.2	Dependence of angle of repose on phase angle distribution	139
8.3.3	Shipboard test method	141
8.4	Concluding remarks	142
Chapter 9: Experimental reproduction of key results		143
9.1	Experimental Setup	143
9.2	Evaluation of qualitative efficiency of simulations	144
9.2.1	Response of granular material under slow tilting	145
9.2.2	Scaling effects	146
9.2.3	Different filling ratios and tilting rates	147
9.3	Evaluation of simulation results’ accuracy.....	149
9.4	Experimental investigation of cargo liquefaction.....	152
9.4.1	Results for sand.....	153
9.4.2	Results for olive pomace	154
9.5	Concluding remarks	155
Chapter 10: Conclusions		157
10.1	General overview	157
10.2	Outcome of investigation	158
10.3	Discussion.....	161
10.4	Future work.....	162

References.....	165
Appendix A: General Purpose Graphical Processing Unit Architecture	181
A.1 CUDA and the NVIDIA GeForce GTX Architecture	181
A.2 THRUST library	183
Appendix B: Trajectory Generation for the 2D case.....	185
Appendix C: Scaling technique.....	189
Appendix D: Investigation of angle of repose using the shipboard test method.....	193
D.1 System description	193
D.2 Comparison with tilting box test	197
D.3 Concluding remarks	198
Appendix E: Coupled ship-cargo 3 DOF equations of motion	199
Appendix F: Initialisation of wave propagation	205

List of Figures

FIGURE 1.1 ABOUT 15% OF SHIP LOSSES (LEFT) AND 40.0% OF THE TOTAL LOSS OF LIFE (RIGHT), ASSOCIATED WITH BULK-CARRIER SHIPS, OVER THE PERIOD 2005 – 2015, HAVE BEEN ATTRIBUTED TO A CARGO RELATED CAUSE AND MAINLY TO LIQUEFACTION (INTECARGO 2016).	18
FIGURE 2.1 GRANULAR MATTER ON MICROSCOPE. LEFT: SAND, RIGHT: OLIVE POMACE. DIFFERENT GRAIN SIZES, SHAPES AND EVEN MATERIAL ARE FORMING THE ACTUAL MATERIAL.	25
FIGURE 2.2 SCHEMATIC AND PHYSICAL DESCRIPTION OF MATERIAL STATE BASED ON ITS LIQUID CONTENT (SOURCE: MITARAI & NORI 2006).	40
FIGURE 2.3 GRAPHICAL REPRESENTATION OF THE MAJOR NON-SPHERICAL DEM APPROACHES: A) ELLIPTICAL, B) SUPER QUADRIC C) POLYGON, D) DISCRETE FUNCTION REPRESENTATION AND E) MULTI-ELEMENT METHOD.....	44
FIGURE 2.4 M-R PLOTS FOR SINGLE <i>Fractal</i> ELEMENT (LEFT) AND SEDIMENTARY PARTICLE USING MULTIPLE <i>Fractal</i> ELEMENTS (RIGHT). (SOURCES: A) ORFORD & WHALLEY 1983, B) KENNEDY & LIN, 1992).....	50
FIGURE 4.1 MOLECULAR DYNAMICS SIMULATION	53
FIGURE 4.2 MOLECULAR DYNAMICS'S PROCESSING STEP FOR THE CASE OF COUPLED SHIP-CARGO SIMULATION.	55
FIGURE 4.3 GRAINS PENETRATION.	56
FIGURE 4.4 PARTICLE CONDITION AFTER COLLISION (SOURCE; RICHEFEU ET AL 2006).	59
FIGURE 4.5 THE THREE DIFFERENT COORDINATE SYSTEMS (SOLID LINES) AND THEIR IRROTATIONAL EQUIVALENTS (DASHED LINES) ARE BEING DEPICTED.....	61
FIGURE 4.6 COMPARISON OF SIMULATION RESULTS TO EXPERIMENTAL DATA WHEN A TWO DIMENSIONAL STACK IS IN GUIDED FALL. 62	
FIGURE 4.7 COMPARISON OF SIMULATION RESULTS TO EXPERIMENTAL DATA. TESTING OF GRANULAR MATTER INVOLVING HORIZONTAL SHAKING, FOR VARIOUS FILLING HEIGHTS IN TANK.	63
FIGURE 5.1 DIFFERENT TIME INSTANTS OF THE SLOWLY TILTED TANK, FOR MATERIAL A (LEFT), B (MIDDLE) AND C (RIGHT) IN THE CASE OF THE 1 ST TANK CONFIGURATION. UP: TANKS AT THE BEGINNING OF THE TEST (0 s). DOWN: TANKS' STATE WHEN THE FREE SURFACE GRANULES BEGIN TO FLOW (AT 6 s, 5.5 s AND 3.9 s, FROM LEFT TO RIGHT).....	67
FIGURE 5.2 SNAPSHOTS OF THE STATE OF THE TANKS AS THE TILTING PROGRESSES. DIFFERENT TIME INSTANTS OF TANK TILTING, FOR MATERIAL A, B AND C IN THE CASE OF THE 2 ND TANK CONFIGURATION.	68
FIGURE 5.3 STEADY OSCILLATION AMPLITUDE OF MASS CENTRE UNDER HORIZONTAL OSCILLATION.....	69
FIGURE 5.4 HORIZONTAL (LEFT) AND VERTICAL (RIGHT) MOVEMENT OF CENTRE OF MASS OF MATERIAL A (RED), B (GREEN) AND C (BLUE), UNDER SWAY OSCILLATION WITH TWO DIFFERENT EXCITATION FREQUENCIES: i) 0.2 Hz (DASHED LINE), ii) 1.5 Hz (SOLID LINE). TANK WIDTH IS 19.2CM.....	70
FIGURE 5.5 TIME INSTANTS OF MOTION OF MATERIAL B, FOR EXCITATION FREQUENCY 1.5 Hz (HORIZONTAL). LEFT: BEGINNING OF THE MOTION. MIDDLE: TIME INSTANT BETWEEN THE BEGINNING AND THE INSTANT OF MAXIMUM AMPLITUDE. RIGHT: INSTANT RIGHT AFTER THE MAXIMUM AMPLITUDE IS REACHED AND THE TANK MOVES TO THE LEFT FOR THE FIRST TIME.	70
FIGURE 5.6 HORIZONTAL (LEFT) AND VERTICAL (RIGHT) MOVEMENT OF CENTRE OF MASS OF MATERIAL A (RED), B (GREEN) AND C (BLUE), UNDER VERTICAL OSCILLATION IN TWO DIFFERENT EXCITATION FREQUENCIES: i) 0.2 Hz (DASHED LINE), ii) 1.5 Hz (SOLID LINE). THE TANK WIDTH IS FIXED.....	71
FIGURE 5.7 HORIZONTAL (LEFT) AND VERTICAL (RIGHT) MOVEMENT OF CENTRE OF MASS OF MATERIAL A (RED), B (GREEN) AND C (BLUE) UNDER SWAY OSCILLATION IN TWO DIFFERENT EXCITATION FREQUENCIES: i) 0.2 Hz (DASHED LINE), ii) 1.5 Hz (SOLID LINE). TANK'S HEIGHT TO WIDTH RATIO VALUE IS FIXED.	72
FIGURE 5.8 STEADY OSCILLATION AMPLITUDE OF CENTRE OF MASS UNDER HORIZONTAL HARMONIC EXCITATION.....	72
FIGURE 5.9 STATUS OF PARTICLES OF MATERIAL B UNDER HORIZONTAL HARMONIC EXCITATION WITH FREQUENCY 1.5 Hz. LEFT: BEGINNING OF THE MOTION. MIDDLE: TIME INSTANT BETWEEN THE BEGINNING AND THE INSTANT OF MAXIMUM AMPLITUDE. RIGHT: INSTANT WHEN THE MAXIMUM AMPLITUDE IS REACHED FOR THE FIRST TIME.	72
FIGURE 5.10 BEHAVIOUR OF B MATERIAL'S CENTRE OF MASS, FOR THE TWO TANK CONFIGURATIONS (HORIZONTAL VIBRATION, $F = 1.5$ Hz). THE PHASE BETWEEN RESPONSE AND EXCITATION APPEARS TO BE ALMOST 180°	73
FIGURE 5.11 HORIZONTAL (LEFT) AND VERTICAL (RIGHT) MOVEMENT OF MASS CENTRE FOR MATERIAL A (RED), B (GREEN) AND C (BLUE) UNDER VERTICAL (HEAVE) HARMONIC EXCITATION WITH FREQUENCY: 0.2 Hz (DASHED LINE); 1.5 Hz (SOLID LINE). THE NUMBER OF PARTICLES IS THE SAME WHILE TANKS ARE SCALED TO PARTICLE SIZE.	73

FIGURE 5.12 THREE DIFFERENT INITIAL FREE SURFACE CONFIGURATIONS: A) UNDISTURBED FREE SURFACE (LEFT), B) SLIGHTLY DISTURBED FREE SURFACE (MIDDLE) AND C) DISTURBED FREE SURFACE (RIGHT).....	75
FIGURE 5.13 DISPLACEMENT OF B MATERIAL'S CENTRE OF MASS, FOR TILTING RATE $0.3^\circ/\text{s}$. COMPARATIVE STUDY FOR THREE DIFFERENT INITIALIZATIONS. SUFFICIENTLY HIGH TANK WALLS ARE ASSUMED.	75
FIGURE 5.14 DISPLACEMENT OF B MATERIAL'S CENTRE OF MASS, FOR DIFFERENT TILTING RATES WHEN THE FREE SURFACE IS A) SLIGHTLY DISTURBED (UPPER), B) ABSOLUTELY UNDISTURBED (LOWER).	76
FIGURE 5.15 SNAPSHOTS OF B MATERIAL PARTICLES DURING TILTING, WITH RATE OF ROTATION $3^\circ/\text{s}$, FOR TWO DIFFERENT CASES: A) TANK WITH SUFFICIENTLY HIGH-SIDED WALLS (LEFT), B) TANK WITH SIDE WALL HEIGHT EQUAL TO MATERIAL'S HEIGHT (RIGHT).	77
FIGURE 5.16 BEHAVIOUR OF THE PARTICLES DURING TILTING WITH RATE $0.3^\circ/\text{s}$ IN THE LOW-SIDED TANK, MONITORED BY TWO DIFFERENT MACROSCOPIC INDICES: A) DISPLACEMENT OF CENTRE OF MASS (LEFT) B) RATIO OF PARTICLES LEAVING THE TANK TO TOTAL NUMBER OF FREE - TO - MOVE PARTICLES (RIGHT).	78
FIGURE 5.17 THREE SIMILAR TANKS WERE USED FOR THE NUMERICAL EXPERIMENTS. WHILE THE TANK LENGTH IS THE SAME, MATERIAL'S HEIGHT INSIDE THE TANK IS VARIED, LEADING THUS TO DIFFERENT FILLING RATIOS.	79
FIGURE 5.18 MASS CENTRE DISPLACEMENT FOR THE THREE TANKS, UNDER DIFFERENT TILTING RATES: A) $1 \text{ DEG}/\text{s}$, B) $0.5 \text{ DEG}/\text{s}$, C) $0.3 \text{ DEG}/\text{s}$	80
FIGURE 5.19 HYSTERETIC BEHAVIOUR OF MATERIAL INSIDE TANK A (LEFT) AND B (RIGHT).....	82
FIGURE 5.20 TIME SHOTS FROM FINAL MATERIAL POSITION AFTER REVERSE MOTION WITH TILTING RATE $-1 \text{ DEG}/\text{s}$	82
FIGURE 5.21 MASS CENTRE'S DISPLACEMENT IN TANK A FOR $1 \text{ DEG}/\text{s}$ TILTING RATE. THE TANK ALTERS ITS TILTING RATE FROM ANTICLOCKWISE TO CLOCKWISE RIGHT AFTER MATERIAL COLLAPSE OCCURS. IT IS SHOWN THAT DESPITE THE OPPOSITE ROTATIONAL MOTION, MATERIAL INSIDE THE TANK SETTLED TO ITS FINAL POSITION AFTER THE COLLAPSE.....	83
FIGURE 5.22 INITIAL SEPERATED MATERIAL PART.	83
FIGURE 5.23 DISPLACEMENT OF MATERIAL'S CENTRE OF MASS, FOR VARIOUS ROLL CENTRES. THE EXCITATION FREQUENCY IS 1.3 Hz AND THE AMPLITUDE IS 20 DEG	84
FIGURE 5.24 MATERIAL'S BEHAVIOUR FOR DIFFERENT ROLL CENTRES. THE EXCITATION FREQUENCY IS 0.3 (LEFT) AND 1.3 (DOWN) Hz WHILE THE AMPLITUDE IS 30 DEG	85
FIGURE 5.25 TANK'S DISPLACEMENT (30 DEG AND 0.1 Hz) WHEN ROLLPOINT 0 (WHITE) AND 3 (BLACK) ARE CONSIDERED.	86
FIGURE 5.26 THE HEIGHT-TO-WIDTH-RATIO h_i/l_i , ($1 \leq i \leq 3$) IS FIXED TO A CONSTANT VALUE.....	87
FIGURE 5.27 MOTION OF MATERIAL INSIDE TANK C (EXCITATION FREQUENCY 1.5 Hz). LEFT: TIME INSTANT LITTLE AFTER THE BEGINNING OF THE MOTION; MIDDLE: TIME INSTANT WHEN THE MAXIMUM AMPLITUDE IS REACHED FOR THE FIRST TIME; RIGHT: TIME INSTANT AFTER TANK CROSSES THE INITIAL POINT FOR THE FIRST TIME.....	87
FIGURE 5.28 HORIZONTAL (LEFT) AND VERTICAL (RIGHT) MOVEMENT OF MATERIAL'S MASS-CENTRE INSIDE TANK C UNDER SWAY OSCILLATION FOR THREE DIFFERENT EXCITATION FREQUENCIES (EXCITATION AMPLITUDE IS 4 CM).	88
FIGURE 5.29 MASS CENTRE RESPONSE FOR VARIOUS EXCITATION FREQUENCIES.	88
FIGURE 5.30 DISPLACEMENT OF CENTRE OF MASS FOR A TILTING RATE $0.3^\circ/\text{s}$. COMPARATIVE STUDY FOR THREE TANK CONFIGURATIONS. HIGH TANK WALLS ARE ASSUMED.	89
FIGURE 5.31 THE ANGLE OF REPOSE AGAINST THE WIDTH OF THE TANK FOR CONSTANT HEIGHT-TO-WIDTH RATIO.	90
FIGURE 6.1 COMPARISON OF CUDA_C SIMULATION RESULTS AGAINST SIMILAR CPU CODE, BOTH FOR SINGLE AND DOUBLE PRECISION FLOATING POINT HANDLING.	97
FIGURE 6.2 MASS CENTRE DISPLACEMENT ALONG Y-AXIS FOR THE GPU AND SINGLE PRECISION CPU CODES ARE COMPARED AGAINST THAT OF DOUBLE PRECISION CPU CODE CALCULATING THE CORRESPONDING DEVIATION.	97
FIGURE 6.3 SPEEDUP OF TOTAL RUNTIME, INCLUDING ANY STARTUP/SHUTDOWN USING THRUST LIBRARY COMPARED TO CUDA RUNTIME API. AS SHOWN A 13x SPEEDUP OCCURS FOR 50000 PARTICLE SIMULATION.	98
FIGURE 6.4 TIME SPEEDUP FOR THE CASE OF DOUBLE PRECISION - $15,560$ PARTICLES SIMULATION, BOTH FOR KERNEL AND ALGORITHM EXECUTION.	99
FIGURE 6.5 SPEEDUP OF TOTAL RUNTIME, INCLUDING ANY STARTUP/SHUTDOWN (DASHED LINE) AND MD LOOP (SOLID LINE) RUN USING THRUST LIBRARY AND SINGLE PRECISION FLOATING POINTS.....	99
FIGURE 6.6 SPEEDUP OF TOTAL RUNTIME, INCLUDING ANY STARTUP/SHUTDOWN (DASHED LINE) AND MD LOOP (SOLID LINE) RUN USING THRUST LIBRARY AND DOUBLE PRECISION FLOATING POINTS.	100

FIGURE 7.1 THE THREE DIFFERENT COORDINATE SYSTEMS (SOLID LINES) AND THEIR IRROTATIONAL VERSIONS (DASHED LINES).....	104
FIGURE 7.2 THE GZ CURVE IN CALM WATER AS CALCULATED NUMERICALLY FROM THE ALGORITHM.	106
FIGURE 7.3 ROLL RESPONSE OF THE BARGE FOR FREE OSCILLATING MOTION (RIGHT) AND THE SINGLE-SIDED AMPLITUDE SPECTRUM OF THIS RESPONSE AFTER FAST FOURIER TRANSFORMATION (RIGHT).	107
FIGURE 7.4 COMPARISON OF RESPONSE OF FROZEN AND GRANULAR CARGO. THE EXCITATION AMPLITUDE S IS FIXED AT 1 CM AND THE FREQUENCY VARIES AS FOLLOWS: A) 3.5 RAD/S ($\sigma = 0.71$), B) 4.4 RAD/S ($\sigma = 0.9$), C) 4.7 RAD/S ($\sigma = 0.96$) AND D) 6.5 RAD/S ($\sigma = 1.33$).	108
FIGURE 7.5 PHASE PLOTS OF VESSEL RESPONSE (MODEL SCALE) WHEN CARRYING SOLID (DASHED LINE) AND GRANULAR (CONTINUOUS LINE) CARGO, FOR WAVE AMPLITUDE 1CM AND FREQUENCY 4.4 RAD/S ($\zeta=0.9$).	109
FIGURE 7.6 MEAN ROLL AMPLITUDE (UP) AND ABSOLUTE MAXIMUM ROLL ANGLE (DOWN), FOR 1 CM ROLL EXCITATION AMPLITUDE.	110
FIGURE 7.7 COMPARISON OF RESPONSE OF SOLID AND GRANULAR CARGO: (LEFT) EXCITATION AMPLITUDE 0.005M AND FREQUENCY 4.5 RAD/S ($\zeta=0.92$); (RIGHT) EXCITATION 0.015M AND FREQUENCY 4.3 RAD/S ($\zeta=0.88$).	110
FIGURE 7.8 MEAN ROLL AMPLITUDE FOR WAVE AMPLITUDE 1.7 CM.	111
FIGURE 7.9 COMPARISON OF RESPONSE FOR THE SOLID AND GRANULAR CARGO CASES, WHEN THE WAVE AMPLITUDE IS 1.7 CM AND THE FREQUENCY IS 4.5 RAD/S ($\zeta=0.92$). VESSEL CAPSIZE IS REALISED IN THE CASE OF THE GRANULAR CARGO.	111
FIGURE 7.10 STATE OF THE CARGO INSIDE THE HOLD DURING THE THREE LAST ROLL CYCLES BEFORE CAPSIZE: 6 TH , 7 TH AND 8 TH (UPPER TO LOWER, RESPECTIVELY). THE CREATION OF A SUBSTANTIAL ROLL BIAS DUE TO CARGO'S SHIFT TO PORT IS NOTICED.	112
FIGURE 7.11 PHASE PLOTS OF VESSEL RESPONSE (MODEL SCALE) WHEN CARRYING SOLID (DASHED LINE) AND GRANULAR (CONTINUOUS LINE) CARGO, FOR WAVE AMPLITUDE 1.9 CM AND FREQUENCY 4.3 RAD/S ($\zeta=0.88$).	113
FIGURE 7.12 MEAN ROLL AMPLITUDE FOR WAVE AMPLITUDE 1.9 CM.	113
FIGURE 7.13 ROLL RESPONSE OF THE BARGE FOR FREE OSCILLATING MOTION (RIGHT) AND THE SINGLE-SIDED AMPLITUDE SPECTRUM OF THIS RESPONSE AFTER FAST FOURIER TRANSFORMATION (RIGHT).	115
FIGURE 7.14 MEAN (SOLID) AND ABSOLUTE (DOTTED), ROLL AMPLITUDE FOR 1 CM EXCITATION. BOTH SYSTEMS (SOLID AND GRANULAR CARGO) HAVE THE SAME DYNAMIC BEHAVIOUR.	116
FIGURE 7.15 ROLL RESPONSE OF SHIP FOR EXCITATION AMPLITUDE OF 2 CM AND EXCITATION FREQUENCY 4.2 (LEFT) AND 4.5 (RIGHT) RAD/S ($\zeta=0.92$ AND 0.97, RESPECTIVELY).	117
FIGURE 7.16 MEAN ROLL AMPLITUDE (UP) AND ABSOLUTE MAXIMUM ROLL ANGLE (DOWN), FOR 2.5 CM ROLL EXCITATION AMPLITUDE.	118
FIGURE 7.17 MEAN (UP) AND ABSOLUTE (DOWN), ROLL AMPLITUDE FOR 2.7 CM EXCITATION.	119
FIGURE 7.18 MASS CENTRE DISPLACEMENT OF GRANULAR MEDIA (SOLID) AND SCALED (1:2000) ROLL AMPLITUDE (DOTTED) FOR 2.5 CM EXCITATION.	119
FIGURE 7.19 MEAN (SOLID) AND ABSOLUTE (DOTTED), ROLL AMPLITUDE FOR 3 CM EXCITATION. SOLID MARKER CORRESPONDS TO BULK WHILE OPEN TO SOLID CARGO.	120
FIGURE 7.20 ROLL RESPONSE OF SHIP WITH WET AND DRY BULK CARGO FOR EXCITATION AMPLITUDE 2 CM.	121
FIGURE 7.21 MEAN AMPLITUDE AND ABSOLUTE MAXIMUM ROLL RESPONSE OF SHIP WITH WET AND DRY BULK CARGO, FOR EXCITATION AMPLITUDE 2.5 CM.	121
FIGURE 7.22 ROLL RESPONSE OF SHIP WITH WET (SOLID) AND DRY (DOTTED) BULK CARGO FOR EXCITATION AMPLITUDE 2.7 CM AND FREQUENCY 4.7 RAD/S.	122
FIGURE 7.23 MOVEMENT OF CENTRE OF MASS WHEN CARGO IS DRY (DOTTED) AND WET (SOLID) FOR WAVE FREQUENCY 4.7 RAD/S (ζ CLOSE TO 1). WAVE AMPLITUDE HAS A FIXED VALUE OF 2.7 CM.	122
FIGURE 8.1 DISCRETE ELEMENT METHOD (DEM) ANALYSIS PIPELINE.	125
FIGURE 8.2 TWO DIFFERENT ARBITRARILY-SHAPED PARTICLES CREATED AS PERTURBATIONS OF THE SAME SPHERICAL (CIRCULAR) PARTICLE. THE SAME FOURIER DESCRIPTORS (UP-LEFT) BUT RANDOMLY CHOSEN HARMONIC PHASES (UP-RIGHT) HAVE BEEN USED. LEFT PARTICLE CORRESPONDS TO GREY WHILE RIGHT TO BLACK DISTRIBUTION.	127
FIGURE 8.3 REPRESENTATION BY THE "FOURIER DESCRIPTORS METHOD" OF CONVENTIONAL CARGOS TRANSPORTED IN BULKY FORM: A) WHEAT (SIMILAR TO BARLEY), B) RICE, C) CORN, D) BEANS (COMMON WHITE), E) SOYBEANS, F) SUNFLOWER SEEDS, G) SAND. (SOURCES: A) DEMYANCHUK ET AL (2013), B) HTTP://EYEOFSCIENCE.DE , C) HTTP://BLUETRACK.COM , D-F) HTTP://AGROPOL.GR , G) HTTP://SANDATLAS.ORG)	128

FIGURE 8.4 CONTACT DETECTION AND RESOLUTION BETWEEN TWO DISCRETIZED IRREGULARLY-SHAPED PARTICLES.....	129
FIGURE 8.5 PREDICTED ANGLE OF REPOSE ACCORDING TO CFR AND DFR (WITH VARIOUS NODE NUMBERS) METHODS. THE TILTING BOX METHOD IS PERFORMED FOR TWO DIFFERENT TILTING RATES (0.3 AND 10 DEG/s).....	133
FIGURE 8.6 MASS-CENTRE DISPLACEMENT (Y-AXIS) WHEN DFR WITH 120-NODE-PARTICLES (SOLID) AND CFR (DOTTED) SIMULATION IS USED. EXCITATION AMPLITUDE 5 CM AND FREQUENCY 1.8 HZ ARE CONSIDERED.	134
FIGURE 8.7 MEAN AMPLITUDE RESPONSE OF MASS-CENTRE (ALONG THE Y-AXIS) FOR DIFFERENT VALUES OF EXCITATION FREQUENCY. THE TANK IS FORCED TO OSCILLATE WITH A PRESCRIBED MOTION.	134
FIGURE 8.8 MEAN ROLL RESPONSE AMPLITUDE OF THE SCALED BARGE MODEL WHEN WAVE AMPLITUDE OF 2 CM AND FREQUENCY RANGE BETWEEN 3 AND 6 RAD/S IS CONSIDERING. CFR (DOTTED LINE) AND DFR (SOLID LINE) WITH 120 NODES ARE CONSIDERING.	136
FIGURE 8.9 PARTICLE SHAPES DESCRIBED BY FOURIER REPRESENTATION OF A PERTURBED SPHERICAL PARTICLE WHEN ONLY ONE DESCRIPTOR (D_n) IS NONZERO. FROM LEFT TO RIGHT: D_2, D_3, D_4, D_8	137
FIGURE 8.10 PREDICTED ANGLE OF REPOSE WHEN ONLY ONE DESCRIPTOR (D_n) IS NONZERO.	138
FIGURE 8.11 DISTRIBUTION OF FOURIER DESCRIPTORS FOR THE TWO CATEGORIES OF PARTICLES: A) SLIGHTLY DISTURBED SPHERES (BLACK) AND B) FULLY IRREGULAR (GREY).	139
FIGURE 8.12 EXAMPLES OF SLIGHTLY DISTURBED (LEFT) AND IRREGULAR SHAPED (RIGHT) PARTICLE, COMPARED WITH A SPHERICAL PARTICLE (DOTTED LINE).	139
FIGURE 8.13 PREDICTED ANGLE OF REPOSE FOR FIXED FOURIER DESCRIPTORS (D_n) AND VARIOUS RANDOMLY CHOSEN HARMONIC PHASE ANGLES. THE SOLID LINE CORRESPONDS TO THE MEAN ANGLE OF REPOSE FOR SPHERICAL PARTICLES, COMPUTED BY CFR; AND THE DOTTED LINE TO THE MEAN ANGLE OF REPOSE FOR PARTICLES HAVING D_2 AS THE ONLY NON-ZERO VALUE DESCRIPTOR ($D_2/D_0 = 0.16$). THE VALUE OF THE ANGLE OF REPOSE FOR THE CASE OF SLIGHTLY DISTURBED PARTICLE IS DEPICTED WITH A DOT WHILE FOR THE CASE OF IRREGULAR SHAPED PARTICLE WITH A STAR.	140
FIGURE 8.14 PREDICTED ANGLE OF REPOSE FOR SPHERICAL AND IRREGULARLY SHAPED PARTICLES BY THE ALTERNATIVE “SHIPBOARD” TEST METHOD.	141
FIGURE 9.1 EXPERIMENTAL SETUP: A) THE 6 DOF SHAKING TABLE AND B) TANK MONITORING CONFIGURATION.	144
FIGURE 9.2 A GREEK VARIETY OF CHICKPEAS (<i>CICER ARIETINUM</i>) WITH PARTICLES’ DIAMETER VARYING IN THE RANGE OF 4 - 12 MM WERE SELECTED AS GRANULAR MATERIAL CARGO.	144
FIGURE 9.3 SLIGHTLY DISTURBED (UP) AND DISTURBED (DOWN)	145
FIGURE 9.4 TIME SHOTS OF THE TANK WITH FILLING RATIO 0.3 AFTER A) THE SECOND CRITICAL ANGLE OF 48.5° AND B) INITIAL POSITION FOR THE SECOND TIME, HAS BEEN REACHED.....	146
FIGURE 9.5 MEAN VALUE OF THE ANGLE OF REPOSE AS THE TANK WIDTH IS INCREASED.....	147
FIGURE 9.6 THREE OF THE FIVE DIFFERENT FILLING RATIOS UNDER INVESTIGATION: 0.2, 0.3 AND 0.467 FROM LEFT TO RIGHT RESPECTIVELY.....	148
FIGURE 9.7 DEPENDENCE OF CRITICAL ANGLES UPON HEIGHT-TO-WIDTH RATIO FOR THREE DIFFERENT TILTING RATES. THE 1 ST ANGLE CORRESPONDS TO ANGLE OF REPOSE WHILE 2 ND TO NEXT CRITICAL ANGLE.	148
FIGURE 9.8 DISPLACEMENT OF THE MATERIAL RIGHT AFTER THE FIRST MATERIAL FLOW HAS BEEN STOPPED FOR TWO DIFFERENT FILLING RATIOS (0.2 AND 0.467, LEFT AND RIGHT RESPECTIVELY) AND TILTING RATE 0.5 DEG/s.	149
FIGURE 9.9 PARTICLE SIZE DISTRIBUTION USED IN EXPERIMENTS.	150
FIGURE 9.10 DISTRIBUTION OF FOURIER DESCRIPTORS (LEFT) AND GENERAL FORM (RIGHT) OF THE TWO KINDS OF IRREGULAR SHAPED PARTICLES USED FOR THE SIMULATIONS. DOTTED LINE CORRESPONDS TO THE SPHERICAL PARTICLE.	150
FIGURE 9.11 MASS-CENTRE DISPLACEMENT FOR SPHERICAL AND IRREGULAR SHAPED PARTICLES UNDER SLOW TILTING (0.5°/s) OF THE TANK.....	151
FIGURE 9.12 COMPARISON OF EXPERIMENTAL AND NUMERICAL VALUES OF ANGLE OF REPOSE.	152
FIGURE 9.13 SAND WITH MC 27.5% AFTER BEING EXCITED IN ROLL. LEFT) $F=0.15\text{Hz}$, $\phi_{\text{MAX}}=4.2\text{DEG}$; RIGHT) $F=0.5\text{Hz}$, $\phi_{\text{MAX}}=13.2\text{DEG}$	154
FIGURE 9.14 SAND WITH MC 40% EXCITED IN ROLL: LEFT) $F=0.1\text{Hz}$, $\phi_{\text{MAX}}=22.2\text{DEG}$. THE UPPER WATER LAYER IS THE ONLY PART THAT MOVES; RIGHT) $F=0.8\text{Hz}$, $\phi_{\text{MAX}}=9.05\text{DEG}$	154
FIGURE 9.15 SAND WITH MC 40% EXCITED IN HIGH FREQUENCY - SMALL AMPLITUDE SWAY. LEFT) $F=2.5\text{Hz}$, $A=2.37\text{CM}$; RIGHT) $F=1.4\text{Hz}$, $A=4.3\text{CM}$	154

FIGURE 9.16 WET OLIVE POMACE (LEFT) BEFORE; AND (RIGHT) AFTER THE APPLICATION OF SWAY EXCITATION ($F=2.2\text{Hz}$, $A=4.3\text{cm}$).	155
FIGURE A.1 DIFFERENCES BETWEEN CPU (LEFT) AND GPU (RIGHT) ARCHITECTURE.	181
FIGURE A.2 GPU MEMORY HIERARCHY	182
FIGURE A.3 COMPILING (LEFT) AND EXECUTION (RIGHT) PROCESS FOR A CUDA CODE WRITTEN IN CUDA_C.	183
FIGURE C.1 WAVE ENERGY SPECTRA WITH INDICATION OF GENERATION MECHANISMS (SOURCE: TECHET 2005).	190
FIGURE C.2 RELATIVE IMPORTANCE OF POTENTIAL (RADIATION AND DIFFRACTION) OR VISCOUS (DRAG) FLOW EFFECTS ON A FIXED PILE [SOURCE: VASSALOS 2005 (BODY), FALTINSEN 1993 (DETAIL)].	191
FIGURE D.1 TIME INSTANTS FOR THE INITIALIZATION OF THE SYSTEM : (0 s, 3.5 s, 10 s, 0.5 s AFTER THE TIP OPENS, FROM TOP LEFT TO BOTTOM RIGHT,, RESPECTIVELY).	194
FIGURE D.2 TIME INSTANTS (7.8 s) INDICATE THE DIFFERENCE ON PILE FORMATION BETWEEN FUNNELS WITH LARGE (LEFT) AND SMALL (RIGHT) FUNNEL OPENING.	195
FIGURE D.3 TIME INSTANTS OF PARTICLE FLOW WHEN THE FUNNEL IS FREE TO MOVE WITH VELOCITY 2.5 CM/S (TOP) AND 5 CM/S (MIDDLE) OR HAS A FIXED HEIGHT ABOVE THE BASE (BOTTOM).	196
FIGURE D.4 DEPENDENCE OF ANGLE OF REPOSE ON THE FUNNEL'S DISTANCE FROM THE BASE (LEFT) AND VERTICAL VELOCITY (RIGHT).	197
FIGURE D.5 COMPARISON BETWEEN PREDICTED ANGLES FOR THE SHIPBOARD TEST WITH LARGE (DOTTED LINE) AND SMALL (DASHED LINE) BASE AND THAT PREDICTED BY THE TILTING BOX METHOD.	197
FIGURE D.6 TIME INSTANTS RIGHT AFTER PILE FORMATION FOR LARGE (LEFT) AND SMALL (RIGHT) BASE WIDTH.	198
FIGURE F.1 ROLL RESPONSE OF SHIP WITH (SOLID) AND WITHOUT (DOTTED) THE USE OF TRANSITION FUNCTION, FOR TWO CHARACTERISTIC VALUES OF EXCITATION AMPLITUDE-FREQUENCY: LEFT) 2.5 CM - 4.7 RAD/S, RIGHT) 2.7 CM - 4.5 RAD/S.	205
FIGURE F.2 ROLL RESPONSE OF SHIP WITH (SOLID) AND WITHOUT (DOTTED) USE OF THE TRANSITION FUNCTION, FOR TWO CHARACTERISTIC VALUES OF EXCITATION AMPLITUDE-FREQUENCY : LEFT) 2.5 CM - 4.7 RAD/S, RIGHT) 2.7 CM - 4.5 RAD/S.	206
FIGURE F.3 MASS CENTRE DISPLACEMENT OF MATERIAL INSIDE THE TANK FOR EQUATION OF MOTION WITH (SOLID) AND WITHOUT (DOTTED) USE OF THE TRANSITION FUNCTION, FOR FOUR CHARACTERISTIC VALUES OF EXCITATION AMPLITUDE-FREQUENCY : A) 2CM - 4.5 RAD/S, B) 2.5 CM - 4.5 RAD/S, C) 2.5 CM - 4.7 RAD/S, D) 2.7 CM - 4.5 RAD/S.	206

List of Tables

TABLE 2.1 ADVANTAGES AND LIMITATIONS OF GRANULAR MATERIAL SIMULATION METHODS	33
TABLE 2.2 RECOMMENDED TEST METHODS ACCORDING TO THE IMSB CODE (IMO, 2012A)	36
TABLE 2.3 MOLECULAR DYNAMICS SOFTWARE PACKAGES INVOLVING GPGPU PROGRAMMING	43
TABLE 4.1 POPULAR NORMAL FORCE (F_N) SCHEMES APPLIED IN SIMULATIONS OF GRANULAR MATERIALS.	57
TABLE 4.2 POPULAR TRANSVERSE FORCE (F_T) SCHEMES APPLIED IN SIMULATIONS OF GRANULAR MATERIALS.....	58
TABLE 4.3 PERFORMED TESTS FOR RELIABILITY OF THE CODE.....	61
TABLE 5.1 PARTICLES' PROPERTIES	66
TABLE 5.2 NUMERICAL VALUES FOR PARTICLE COEFFICIENTS.	86
TABLE 6.1 PSEUDO-CODE FOR MD SIMULATION WITHOUT THRUST LIBRARY.....	94
TABLE 6.2 TABLE 4.PSEUDO-CODE FOR MD SIMULATION USING THRUST LIBRARY	95
TABLE 6.3 PERFORMED CODE VERIFICATION TESTS	95
TABLE 8.1 PSEUDO-CODE FOR DFR MD SIMULATION	130
TABLE B.1 PSEUDO-CODE FOR MD SIMULATION.	185
TABLE B.2 PSEUDO-CODE FOR MD SIMULATION FOR COUPLED MOTION.	187

Chapter 1: Introduction

1.1 General framework and aim of research

Whilst in terms of physical appearance materials in nature come in various forms, they can be classified under the four well - known states of matter: solid, liquid, gas and plasma. Yet experience suggests that some materials cannot be put strictly under one category because, under different circumstances, they can exhibit substantial differences in their behaviour. A profound example are granular materials, which despite their seeming simplicity, depending on how they are vibrated, they can demonstrate the physical properties of two, or even more, states of matter. Adopting Brown & Richards' definition, in what follows, by "granular material" will be meant a conglomeration of macroscopic, discrete solid particles (Brown & Richard 1970).

Investigation of granular material behaviour has been of high academic interest, especially during the last two decades (Zhu et al 2007). But it is not only curiosity that drives granular dynamics research. Every day, a person uses almost twenty dry bulk products (INTERCARGO 2012). Also, almost 10% of the energy produced on earth is spent for granular materials processing. As realised, several practical issues are closely tied to granular materials behaviour and as Duran (2000) pointed out, even a whole book would not be enough to adequately cover them all. In addition, granular material dynamics plays a vital role in many "catastrophic" natural phenomena such as avalanches (snow or soil) and earthquakes. Whether occurring naturally or after processing, granular materials present high interest for the industry and their transportation through the oceans is a vital activity for world's economies (Richard, 2005).

For naval architecture, the study of the behaviour of granular materials should be a topic of great interest, due to the serious hazard of cargo shift which can lead to a vessel's capsize. Bulk carrier vessels carry the equivalent of over 8 billion ton-miles of commodities a year, from all over the world (INTERCARGO 2012). Aggregates from Norway; alumina, iron ore, bauxite and coal from Australia; cement and nickel ore from India; copper from Chile; salt from USA and sugar from Brazil are only some kinds of granular materials crossing every day the oceans to come into our lives. Unfortunately, however, accidents having cargo shift as the core event are not rare. The rapid capsize of the cement carrier "Dystos" in the Aegean Sea in 1996 was stipulated as possibly owed to cement cargo's shift (e.g. Argyriadis 2005). It

led to the loss of 20 crew members, attracting naturally a lot of publicity in Greece. Recent statistics reveal a bleak picture of ship safety with respect to cargo shift phenomena: within the decade 2005 – 2015, there have been 71 bulk carrier losses, costing an annual average number of 23.2 lost lives (INTERCARGO 2016). Of those, cargo failure has been identified as the perceived reason for 15.5% of ship losses and 40.0% of total loss of life (Figure 1.1). While the safety record of bulk carriers has been improved in the last years (following the general trend of maritime industry), incidents of cargo failure resulting in total loss greatly increased after 2010 (2 before; 9 after). Accidents like that of Bulk Jupiter, which sank in early 2015 while carrying a non-dangerous, according to the International Maritime Organization, cargo (bauxite – characterized as C-Class), highlight the need for continued vigilance and awareness of potential solid bulk cargo risks. The most common reasons for these accidents are: the phenomenon known as “liquefaction”; and the “cargo shift” effect.

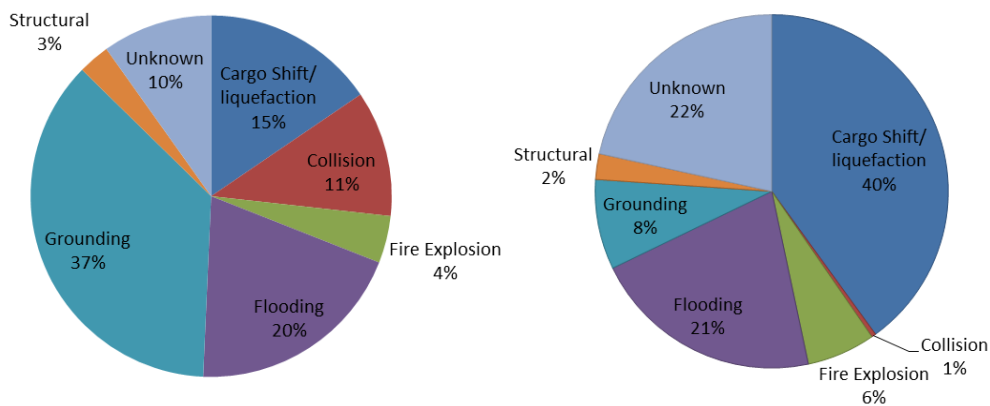


Figure 1.1 About 15% of ship losses (left) and 40.0% of the total loss of life (right), associated with bulk-carrier ships, over the period 2005 – 2015, have been attributed to a cargo related cause and mainly to liquefaction (INTECARGO 2016).

Liquefaction is particularly dangerous, since, it turns what appears to be an apparently safe cargo into an easily movable cargo with a very detrimental effect on the carrying vessel’s stability. According to Munro & Mohajerani (2016), between 1988 and 2015 there have been 24 accidents where liquefaction was the suspected cause, leading to loss of 18 vessels and 164 people. The physical basis of the phenomenon can be understood as follows: The oscillatory movement of the material, which comes as a result of the material – tank (and hence vessel) interaction, leads to compaction of the intra - particle spaces in the cargo. If combined with the presence of moisture exceeding the limits prescribed in IMO’s International Maritime Solid Bulk Cargoes Code, specifically the Transportable Moisture Limit (TML) and the Flow Moisture Limit (FML), favorable conditions are sometimes setup for the cargo to behave like a liquid (IMO, 2012a).

Dry cargo shift is one of the most important macroscopic characteristics of granular matter and it is related to many important phenomena, including avalanching (Frette et al, 1996), stratification (Tuzun et al, 1998) and segregation (Buchholtz & Poschel, 1994). As type of problem, cargo shift could be classified along with sloshing; with clear methodological analogies prevalent in particular when, for the latter, a smooth particles hydrodynamics (SPH) modelling approach is applied.

Taking a step in the direction of modelling and systematic investigation of bulky cargo shift phenomena pertinent to maritime transportation, in the current work we set in focus granular materials behaviour for ranges of excitation associated with sea wave effects upon the carrier vessel. The practical problem of interest is the understanding of the mechanics of cargo shift, from initiation to the subsequent stage of a progressing cargo shift, incurring back on the ship a dynamic effect, and so forth. We are thus keen to understand the interplay of granular material flow with the containing ship hold structure, observed to occur sometimes during operations in heavy seas, for a ship carrying granular cargo in which no sufficient securing provisions for restricting cargo's movement have been enforced. The longer term objective is to understand better, and develop capability for predicting, phenomena of cargo movement inside ships performing realistic motions due to wave loads.

1.2 Focal points of interest

The main queries that have motivated the current research are:

1. *What are the critical parameters that influence the behaviour of a bulky cargo inside a tank forced to move in prescribed motion?*
2. *How does bulky cargo's shift influence a vessel's stability?*

As the current research progressed, additional queries have emerged:

3. *What are the effects of tank scaling upon granular material behaviour?*
4. *How could we gain computational efficiency? What are the restrictions?*
5. *How does environmental humidity affect cargo shift and ship stability?*
6. *How does particle shape affect cargo shift and ship stability?*

Lastly, a big question that evolved from the very beginning of our research was:

7. *How feasible is it to combine micro-scale modelling with ship motions in a practical framework of study, with due account of all above factors?*

1.3 Need for further research

Despite the intense interest accruing from the vast industrial applications of granular materials, an overall interdisciplinary framework for their study has not been fully set up yet. Furthermore, the link between fundamental and applied studies is still quite weak (Lumay et al 2012). To devise a research approach on granular materials behaviour that is relevant to ship cargos is, for a number of reasons, daunting. Environmental excitations are random and they affect the cargo under the filtered form of ship responses; which in turn are affected by cargo's movement. Stick - slip phenomena observed at low frequency and moderate-to-high-amplitude are rarely examined in granular materials research where fully dynamic states are mostly considered. There is variety of transported materials that differ substantially in their properties and sizes, the presence of humidity etc. As a result, approaches with potential to establish a solid scientific basis for this problem, using micro-scale modelling of cargo particles' motion and their interaction with the moving ship under wind/wave excitations, are still lacking. Such modelling is very demanding and it calls for an interdisciplinary approach overcoming the often fragmented nature of scientific efforts.

On the other hand, in the real world, the transportation of granular materials by sea is regulated by several national and international codes. They contain mostly empirical instructions for the safe handling (loading, unloading) and stowage of bulk cargos. Commonly applied are IMO's codes referring to the transportation of grains; solid bulk cargos (except grains); and dangerous goods (IMO 1991, 2012a & 2012b respectively). IMO's Solid Bulk Cargoes Code became mandatory under the provision of the SOLAS Convention from the 1st of January 2013. It describes a prescriptive and empirical method and it is an updated version of the earlier Code of Safe Practice for Solid Bulk Cargoes (IMO, 1998). Despite that the hazards of transporting specific cargo types have been recognized and regulatory actions undertaken, cargo shift incidents keep on appearing, making the effectiveness of these regulations questionable. It seems that there is necessity for a fundamental rethinking of appropriate safety measures, vessel design and risk identification. Cargo shift appears missing from the research topics usually considered in the framework of risk-based ship design and operation. This thesis aims to contribute towards establishing a first-principles-approach for the study of cargo shift phenomena, by setting up a mathematical model that could be used effectively for the systematic identification of the critical system (cargo-ship) parameters of behaviour which can incite such dangerous behaviour.

1.4 Methodology

Numerical simulations of interacting discrete media drive in the last twenty years explorations in the granular microstructure and its link with macroscopic behaviour. Even by personal computers, sophisticated 2D or 3D systems can be simulated within reasonable time, offering the possibility to explore the effect of many parameters that would hardly be possible to monitor by direct experimentation. Such an approach of microscopic simulation has been developed in our research, employing the so called “Soft Sphere Molecular Dynamics” method (to be called “Molecular Dynamics” from now on). Thus a mathematical model was developed, and it was used in order to target the research questions posed.

Our main effort was given on 2D numerical simulations of cargo consisting of spherical¹ particles inside a hold of a barge that can either oscillate in prescribed motion or is free to move under the effects of wave loads. Special attention was given in the investigation of the angle of repose following the titling box method proposed by IMO (IMO 2012a). The focus of our approach was on the basic modelling of cargo shift phenomena, in a way that is not constrained by the presence of moisture, but environmental effects are also considering. An optimized algorithm capable for execution on Graphical Processing Unit that reduces the time efficiency was critically presented in order to evaluate its necessity in fields such as ship stability. Finally, the “Fourier descriptor” method and a new contact detection algorithm were implemented for dealing with the irregular shapes of the particles, based on the “Discrete Function Representation” (DFR) method (Hogue 1998).

Experimental reproduction of numerical findings was performed when this was feasible, by use of the NTUA “shaking table” facility enabling forced motions in up to six degrees of freedom.

1.5 Contributions of the thesis

The main novelty of the present thesis accrues from the introduction of the combination of micro-scale modelling with ship motions in a practical framework. This work can lead to the development of a first-principles numerical tool for assessing potential risks that may be involved when carrying solid bulk cargoes.

Main contributions accruing from specific research tasks defined in this thesis are:

¹ We refer spherical and not circular (2D case) particles following the common practice in the literature.

- The understanding of the dependence of granular “fluid-like” behaviour upon particles’ properties and system’s configuration, with focus on the low frequency range (usually encountered in ship motions).
- The evaluation of the empirical methods proposed by IMO in the light of the proposed numerical approach.
- The shedding of light on various facets of the scaling problem, with reference to a series of rectangular tanks partly filled with granular material.
- The systematic development of mathematical models of increasing complexity for the coupled ship - granular cargo motion and the evaluation of their different predictions.
- The development of better understanding for the mechanism controlling the formation of the angle of repose during the avalanching associated with cargo shift.
- The capturing of hysteretic phenomena and the demonstration of their critical role in triggering vessel capsize.
- The development of a method for investigating the behaviour of particles with irregular shape, that is capable of reproducing the shapes of particles of standard granular cargos transported by sea, by combining methods for the construction of arbitrarily-shaped particles and for contact detection. Then, the investigation of differences in the dynamic behaviour between spherical and irregular particle materials.
- The experimental investigation of liquefaction of sand and olive pomace cargos in a rectangular container, focusing on low frequency ranges and influence of simulation time upon material dynamic behaviour.

1.6 Thesis outline

The first introductory chapter, where are presented the motivation, the general scientific and legislative framework and the focal points of interest, is followed by a critical literature review and the definition of the specific objectives of the current thesis. This is followed by an in-depth analysis of the adopted methodology deriving from a molecular dynamics approach, followed by the description of the developed mathematical model of coupled ship and granular cargo motions and then by selected simulation results for prescribed tank motions. In the next stage, algorithm’s optimization on the basis of a well-known method of parallel processing (GPGPU porting) is described. Moreover, the code is expanded so that it can deal with non-spherical particle shapes. Further simulation results for coupled tank-cargo motion and investigation of the effect of particle’s shape on the dynamics of the cargo are presented. Lastly, the experimental reproduction of the key numerical

findings is followed by a brief outlook of the achieved progress and by the concluding remarks that include some suggestions for further research. More specifically:

In *Chapter 2* a review of the most profound scientific efforts is presented. The chapter is divided into different sections addressing in a critical manner, the research background of the current work. Research progress in granular matter is followed by review in other aspects that include, scaling effects, GPGPU porting and irregular-shaped simulation of granular matter.

The specific objectives of our work are described in *Chapter 3*. In *Chapter 4*, the adopted Discrete Element Method (DEM) is described, based, as already said, on the “Molecular Dynamics” method. Moreover, decisions made for achieving a modelling that would be suitable for our specific problem are discussed. The way to take environmental humidity under considering is also described. The chapter concludes with results about validation and verification of the algorithm.

Chapter 5 is dedicated to the numerical investigation of the behaviour of granular matter under the specific excitations of interest. Two categories of tests were performed, for investigating the influence of particle (density, radius etc.) and system parameters (filling ratio, side tank height, tilting rate etc.) upon cargo’s behaviour. The stick - slip phenomena associated with cargo shift were on focus and critical values of the forcing parameters were identified. Comparisons between the dynamic behaviour patterns exhibited by these materials are presented and useful results about the importance of some particle parameters are extracted. Furthermore, we investigate, by direct simulation, the problem of scaling for a rectangular tank partly filled with granular material. Simulation results for geometrically similar containers are presented, assuming horizontal harmonic vibration and slow tilting, of the container and conclusions are drawn about the influence of scaling on these motions.

In *Chapter 6*, two different General Purpose Graphical Processing Unit (GPGPU) implementations, using either only CUDA runtime Application Program Interface (API) or a combination of CUDA runtime and the Thrust API, were tested. Comparison between Central Processing Unit (CPU) and Graphical Processing Unit (GPU) simulations results prove that, up to 150x speedup could be reached, while the accuracy of the results remains under acceptable limits. Discussion about barriers and borders of GPGPU implementation as well as suggestions about future research work are included.

In *Chapter 7* we investigate the interplay of granular material flow with a vessel’s motion. The method of “Molecular Dynamics”, is combined initially with a rudimentary (1 DOF - roll) and later with an improved (3DOF – sway, heave, roll) ship motion model. This study is expanded by considering the effect of one type of humidity on the coupled motions.

Characteristic simulation results, including comparisons against cases of rigid cargo behaviour, are presented.

An attempt to investigate the effect of particle's shape on the dynamics of the cargo (and eventually of the hold) is presented in *Chapter 8*. The adopted, "Fourier descriptor" method, is described, and then irregularly-shaped particles are constructed by this method. Moreover, a new contact detection algorithm is implemented for dealing with the irregular shapes of the particles, based on the "Discrete Function Representation" (DFR) method (Hogue 1998). It is shown that that adopted approach is workable when a sufficient number of nodes are considered. Further discussion about the effectiveness and limitations of the approach has been included.

Chapter 9 contains the results of the experimental reproduction of key numerical findings. These results are used for evaluating both, algorithm's efficiency on providing the qualitative dynamic behaviour of granular material, as well as, its quantitative accuracy.

In the last chapter (*Chapter 10*), the major conclusions of the current work are presented. Effort has been directed towards providing a direct answer to each one of the research queries shown earlier. A general discussion, and some suggestions for further analysis and research, is also part of this final chapter.

Chapter 2: Critical literature review

In the current chapter a critical literature review of the most profound scientific efforts related with aspects of importance to this thesis is provided. Initially review of relevant IMO regulations for handling bulk cargo and the research progress of granular matter investigation are presented. After that, research conducted addressing the following issues is assessed: a) scaling effects, b) General Purpose Graphical Processing Unit parallel programming; and c) wet granular media and irregularly-shaped simulation of granular matter.

2.1 Granular nature

In Figure 2.1 pictures of two popular granular materials taken with use of an optical microscope are presented. It is obvious that a great variety of particle sizes, shapes and even material types, may comprise a considered granular material, although, macroscopically, it might had created the impression of being consisted of very similar particles.



Figure 2.1 Granular matter on microscope. Left: sand, Right: olive pomace. Different grain sizes, shapes and even material are forming the actual material.

In contrast to their solid nature, granular materials conform to the shape of the containing tank and they flow when tilted sufficiently. On the other hand, unlike liquids, they remain stable when the tilt remains less than a critical angle corresponding to the maximum stability of the specific granular assembly (Albert et al 1997). Between these two states, a quasi-static state is experienced. The limiting angle may depend also on whether the tilting is slow or fast. When the container is vibrated at a relatively high frequency, the grains rearrange themselves in the packing (decrease of volume). On the other hand, if the container is very strongly vibrated, the grains display free motion and the granular assembly behaves like a dissipative gas (Lumay et al, 2012).

“Steric repulsions” (these are intermolecular interaction due to overlapping electron clouds related to the geometry of grains), friction forces (influenced by surface properties), cohesive forces (liquid bridges, electric charges, van der Waals and magnetic interactions) and interactions with a surrounding fluid influence the behaviour of granular material inside a tank (Lumay et al 2012). The two former mainly concern interaction between grains in non-cohesive condition while the third in cohesive (mainly for smaller grains). Interactions with the surrounding fluid are dominant whenever these occur. Thus, investigation of wet granular media is a different area, and it can be performed for cohesive or non-cohesive material (Koromila et al 2013). In the case of non-cohesive dry granular material composed of nearly spherical grains, the surface properties (inter-particulate friction) are the main contributors to their macroscopic dynamical response (characterized by materials resistance to differential movement between particles when subjected to external excitation, according to Train 1958). Subsequently, their handling often needs special attention.

Two important aspects that contribute to the unique properties of granular materials are discussed by Jaeger et al (1996): the ordinary temperature plays no role (thus thermodynamic arguments are useless and the phase transition is consequence of external vibration only, although authors like Radhika & Leslie (2004) try to establish a quasi-thermo dynamical frame for powders and granular matter), due to the great gravitational potential energy (10^{12} times bigger than $K_B T$ at room temperature) and the interactions between particles are dissipative due to friction.

Before leaving this section it is beneficial to clarify the range of granular materials that concern us in the current work. It was considered as general enough, and it was relied upon, the Brown & Richards (1970) definition of granular matter, according to whom, three different categories can be established based on the diameter of particles: a) Powders, that have diameter less than $100\ \mu m$, b) Granular solids with diameter in the range between $100\ \mu m$ and $3\ mm$ and c) Broken solids (aggregates and rocks) when particle diameter is larger than $3\ mm$. Furthermore, according to Mitarai & Nori (2006), depending on the type and magnitude of the surrounding fluid, granular materials may be distinguished in five more states: a) Dry, when the surrounding fluid is air, b) Pendular when particles are held together by liquid bridges, c) Funicular, when some pores are fully saturated, d) Capillary, when all voids between particles are fully covered with water; and lastly, e) Slurry, when particles are fully surrounded by water.

2.2 IMO bulk cargo regulation review

The main legislation governing safe carriage of solid bulk cargoes (other than grains) is the International Maritime Solid Bulk Cargoes (IMSBC) Code, which became mandatory on January 1, 2011, under the SOLAS Convention. Since then, the Code has been amended by resolutions MSC.318(89), MSC.354(92) and resolution MSC.393(95). The primary aim of the IMSBC Code, which replaces the Code of Safe Practice for Solid Bulk Cargoes (BC Code), is to facilitate the safe stowage and shipment of solid bulk cargoes by providing information on the dangers associated with the shipment of certain types of solid bulk cargoes and instructions on the procedures to be adopted when the shipment of solid bulk cargoes is contemplated.

Specific requirements for the transport of grain (wheat, maize (corn), oats, rye, barley, rice, pulses, seeds and similar) are covered by the International Code for the Safe Carriage of Grain in Bulk (IMO 1991), which was adopted by resolution MSC.23 (59) and has been mandatory under SOLAS chapter VI since 1 January 1994. The purpose of the Code is to provide an international standard for the safe carriage of grain in bulk, by focusing on the necessity of the grain surfaces to be reasonably trimmed, compartment hatch covers to be secured in the approved manner and ship's compliance with intact stability criteria at all stages of the voyage.

Furthermore the International Code for the Construction and Equipment of Ships carrying Dangerous Chemicals in Bulk (IBC Code) provides an international standard for the safe carriage in bulk by sea of dangerous chemicals and noxious liquid substances listed in chapter 17 of the Code.

Lastly, the Code of Practice for the Safe Loading and Unloading of Bulk Carriers (BLU Code) provides guidance to ship masters of bulk carriers, terminal operators and other parties concerned for the safe handling, loading and unloading of solid bulk cargoes and is linked to regulation VI/7 (Loading, unloading and stowage of bulk cargoes) of the 1974 SOLAS Convention, as amended by resolution MSC.47(66). IMO suggests that provisions of the Code should be applied with due regard to the provisions of the International Maritime Solid Bulk Cargoes Code (IMSBC Code), where applicable.

2.3 Granular materials behaviour

Very notable scientists have dealt with granular materials' behaviour: Coulomb's law of friction was originally proposed for granular materials. Faraday discovered the convective

instability by experimenting with a vibrated container filled with powder. Reynolds investigated how compacted granular matter can dilate under shear. These were a few among the outstanding scientists who have greatly contributed to the field over the years (Duran 2000).

Granular materials are responsible for fascinating natural pattern formations, such as “desert dunes”. See, for example Bagnold’s famous book on desert dunes which remains an important reference to this day (Bagnold 1941). During the last three decades the issue of granular material behaviour has attracted the attention of several scholars, trying to explain the dynamics and/or the physics of these materials. Exotic phenomena like the “Brazil nut effect” (e.g. Williams 1976, Metcalfe et al 1997), “silo music” (eg Teichman & Gudehus 1993), “granular dendrites” (eg Liu et al 1991, Coppersmith et al 1996), “parametric wave patterns” (eg Moon et al 2001), sudden transitions from flowing to sticking (eg Savage & Sayed 1984), granular jets (Johnson & Grey 2011) and pile avalanches (eg Holsapple 2013) have been extensively investigated. In the work of Jaeger et al (1996) useful information about important issues of the granular state can be found. Authors deal with some of the distinctive properties of granular materials and show that these materials act as highly unusual solids, liquids, and gases, depending on how we prepare and excite them. They further discuss about a multitude of scientific challenges like the relevance of packing history with packing, boundaries treatment, Efficiency of Newtonian hydrodynamics, etc. A comprehensive review on the physics of granular matter is provided in Duran (2000). Issues like angle of repose, cohesion, compaction, dendrites, Faraday waves and granular dynamics are critically discussed by the author. An attempt to describe the most commonly used experimental and numerical methodologies is also attempted.

2.4 Research approaches for investigating granular materials

Experimental methods

To systematically observe granular material dynamics, several experimental works have been performed, sometimes with very sophisticated equipment. As an example, Wong et al (2005) used Positron Emission Particle Tracking to investigate behaviour in vertically vibrated beds, focusing on heap formation, surface waves and arching. Kawaguchi (2010) applied Magnetic Resonance Imaging to some dense granular flows or fluid - particle flows, such as the rotating drum, vibrated granular bed, hopper flow and spouted bed. Sellerio et al (2011) studied experimentally the mechanical behaviour of granular materials submitted to

forced vibrations, using mechanical spectroscopy. Optical methods, using digital cameras have been used extensively. For example, Krenzel et al (2013) presented interesting pattern formation in a horizontally shaken granular sub-monolayer.

Continuum methods

The idea of using a micro - scale method for understanding macroscopic behaviour is not new for maritime research. Smooth particles hydrodynamics (SPH) methods share a common basis with methods of granular materials modelling (e.g. see Delmore et al 2009). In contrast to SPH where the continuum system itself is approximated by a discrete set of fluid particles, in the case of granular materials, continuum fields are constructed from discrete particle data; i.e. properties such as density, velocity field and stress tensor are obtained by averaging positions, velocities, and forces associated with (true) particles. In these methods, an important issue is to satisfy conservation laws. Amongst other techniques directly addressing continuum fields, the coarse - graining approach (Goldhirsch 2010) and the method of planes (Todd et al, 1995) are quite popular. A general drawback for all “continuum” methods however, is that they are not universal (for every kind of granule). In addition, Weinhart et al (2012) notes that they may lead to contradictory results when applied near boundaries.

Numerical methods

As in all disciplines of quantitative research, the growth of computational capacity has resulted in an expanded number of numerical efforts on granular materials too. As a matter of fact, various modelling methods have been developed over the years in order to investigate the dynamic behaviour of particles inside some granular medium. In particular, numerical simulations of interacting discrete media drive in the last twenty years explorations in the granular microstructure and its link with macroscopic behaviour. Several methods, like the “molecular dynamics” method, involve solution of Newton’s equation of motion for all particles. Competing with molecular dynamics are several other simulation methods applied for granular flows such as (Poschel & Schwager 2005; Duran et al 1999): a) the “event-driven method” a variant of molecular dynamics, b) “Direct simulation Monte Carlo” that is approximately valid for dilute granular systems, c) the method of “Rigid-body dynamics”, that allows for realistic simulation of sharp-edged particles, d) “cellular automata”, e) “bottom-to-top reconstruction”; and f) “Langevin dynamics”.

2.4.1 Granular material modelling approaches

Below is given a brief description of the most important simulation methods that are currently applied internationally in order to investigate the behaviour of particles in granular media, summarizing also their advantages and limitations:

“Event-Driven Molecular Dynamics”

Molecular dynamics algorithms can be divided into two broad classes: those for “soft” and those for “hard” bodies. The hard sphere modelling (*event-driven molecular dynamics*) is based on the absence of interpenetration or deformation during impact. It implies that, velocities change according to the collision rule but the positions of the particles are the same before and after such an event. During the time intervals between collisions, the particles move along known ballistic trajectories. Therefore, the positions of the particles at the time of the next collision can be computed in one step. The calculation is purely algebraic because collisions are taken as perfectly elastic: during a collision no energy is transferred either to deform or to change its internal state. The loss of linear momentum is characterized solely by means of the coefficient of elastic restitution, at least when rotations are neglected. In spite of its algebraic determinism, the algorithm produces phase-space trajectories that are chaotic. The simulation of granular gases is the main application of event-driven methods.

“Soft-Sphere Molecular Dynamics”

“Molecular dynamics” (MD) is the most acceptable among the simulation methods for granular flows. It involves solution of Newton’s equation of motion for all particles. The method allows, in principle, to simulate systems of complicatedly - shaped particles in static and in dynamic conditions, including cases of multi-particle contacts. MD requires knowing the forces and torques acting between contacting particles as functions of these particles’ position, velocity, angular orientation and angular velocity. Here, friction and elastic restitution come into play when spheres penetrate into each other, and the magnitude of the interaction depends on the penetration depth. Such simulations have been proven to be very useful and predictive in many applications, in particular when the dynamical behaviour of the grains dominates the system properties. Pioneering work in the modelling of granular materials by the molecular dynamics method has been performed by Cundall (1979).

Direct Simulation Monte - Carlo

The method of Direct Simulation Monte - Carlo (DSMC) is used for very specific systems and is not for general use. Unlike other Monte - Carlo schemes, a palette of distributions is available, e.g. for the velocity as function of the spatial position \mathbf{r} and time t . This integration is performed by subjecting pseudo probability units $\Delta f(r, t)$ to the action of the collision operator. Since the velocity distribution function represents the probability to find a particle in a certain phase - space interval, in a sense, these probability units can be understood as “quasi – particles”.

Direct Simulation Monte Carlo, is more efficient than the event-driven method, although, further simplifying assumptions are required. The necessary precondition of uncorrelated motion of particles (molecular chaos assumption) is approximately valid for dilute granular systems, also called granular gases. As granular gases have been studied intensively by means of kinetic theory, Direct Simulation Monte Carlo is suited for direct comparison with the results of kinetic theory.

In addition, although the physical and mathematical basis of Monte Carlo may be less transparent to a novice than that for molecular dynamics, Monte Carlo is usually easier than molecular dynamics to code in a high-level language such as C++. Monte Carlo is also easier than Molecular Dynamics to implement for systems in which it is difficult to extract the intermolecular force law from the potential function. Systems having this difficulty include those composed of molecules that interact through discontinuous forces. Similar difficulties arise in systems for which the potential function is a complicated multidimensional surface.

For determination of simple equilibrium properties such as the pressure in atomic fluids, Monte Carlo and Molecular Dynamics are equally effective: both require about the same amount of computer time to attain similar levels of statistical precision. However, Molecular Dynamics more efficiently evaluates such properties as the heat capacity, compressibility, and interfacial properties. Besides configurational properties, Molecular Dynamics also provides access to dynamic quantities such as transport coefficients and time correlation functions. Such dynamic quantities cannot generally be obtained by Monte Carlo, although certain kinds of dynamic behaviour may be deduced from Monte Carlo simulations (Baumann, 1993). Molecular dynamics also offers certain computational advantages because of the deterministic way in which it generates trajectories. The presence of an explicit time variable allows us to estimate the length need for a run: the duration must be at least several multiples of the relaxation time for the slowest phenomenon being studied. No such

convenient guide is available for estimating the length required for a Monte Carlo calculation. Finally many kinds of small errors in a molecular dynamics program tend to accumulate with time and so become apparent as violations of conservation principles; in contrast, subtle errors in a Monte Carlo program may not be so obvious in the output. As a result, DSMC should be used with some care as inappropriate application may easily lead to non-physical results.

Rigid body dynamics

The idea of Rigid-Body Dynamics is complementary to the idea of Molecular Dynamics. While Molecular Dynamics simulations are always based on the evaluation of interaction forces, *Rigid-Body Dynamics* (sometimes also called *Contact Dynamics*) is based on the opposite idea: In the Rigid - Body (RB) Dynamics formulation, the interaction forces are determined from consistency requirements referring to the behaviour of the particles upon their contact, assuming however no penetration (whereas in MD the force models are determined by penetration assumptions). With much higher numerical effort Rigid-Body Dynamics allows for highly realistic simulation of systems comprising very stiff particles of complicated shape, which exhibit slow dynamics. However, as a direct consequence of disregarding material properties we have to sacrifice the uniqueness of the contact forces. Thus, the algorithm does not necessarily compute the physically-correct sets of contact forces of a many-particle system, but one out of many (in general out of an infinite set of contact forces). Therefore, it cannot be assured that the system behaves in a physically-realistic way. Rigid-Body Dynamics has also been applied to granular systems, where frictionless smooth spheres have been simulated. As a result, RB is useful only in cases where stiff particles and static (or semi - dynamic) behaviour is under investigation. A practical description of the application of Rigid-Body Dynamics to systems of spheres is presented by Unger et al (2002).

Other methods

Other important methods are, Cellular Automata (CA) and Bottom to Top Reconstruction (BTR) which however are either restricted to certain types of problems (mostly heap formation and avalanche investigation) or limited to simulation of static behaviour. In Table 2.1 are summarized the key advantages and limitations of these simulation methods. A detailed assessment is found, for example, in Poschel & Schwager (2005).

Table 2.1 Advantages and limitations of granular material simulation methods

Method	Advantages	Disadvantages
Event - Driven	Purely algebraic calculations Powerful for granular gases	Not realistic simulation of solids System parameters dependent Only dynamic state simulation of sphere shaped particles
Soft - Sphere Molecular Dynamics	Particle with complicated shape Dynamic and static conditions More efficient than MC for statistics Access to dynamic quantities (transport coefficient etc)	Small system size due to computational effort
Direct Simulation Monte - Carlo	More efficient than ED Realistic for granular gases Easier to code than MD Easier than MD for complicated intermolecular forces	Further simplifying assumptions are required Less computational advantages than MD due to stochastic way Small errors lead to non-physical results
Rigid - Body Dynamics	More realistic simulations for stiff particles of complicated shape	High computational cost
Other methods		Often restricted to certain types of problems

2.5 Angle of repose

Granular matter is often imagined in the form of a sand-pile. Indeed, the formation of sand-piles is not only an everyday experience but an event relevant to many practical applications also. One of the primary properties (macroscopic parameters) of granular matter, indicating the inter-particulate friction and characterizing their flow behaviour (flow ability, avalanching, stratification and segregation) is the angle of repose (Ileleji & Zhou 2008). Whatever is the method of approach, the angle of repose can be considered to be the bifurcation point after which the material alters its behaviour from solid-like to fluid-like and thus considering to be one of the most critical parameters of bulky ship cargo (IMO 2012). To state it simpler, it is the maximum slope angle of a non - cohesive (i.e. free - flowing) granular material. It has been found that, it strongly depends on material's properties, such as particles' density and size (Zhou et al, 2001).

The most common methods for measuring the angle of repose have been presented initially by Train 1958 and are still the same, although different researchers present slightly different approaches (Poschel & Schwager 2005):

The *fixed funnel and free standing cone method* (Newman 1953) comprises of a funnel with its tip at a given height above graph paper (the end of the stem is cut perpendicular to the axis of symmetry) through which the granular material is poured till the heap formed reaches funnel's tip. The angle of the heap is calculated from the height and the mean diameter of the base of the heap.

In *fixed bed cone method* (Nelson 1955) the diameter of the base is of fixed size (e.g. a circular disc) and the funnel through which material is poured can be raised vertically until a maximum height (maximum cone height). The angle of the heap formed, is calculated from the height and the diameter of the heap. A general drawback of these two methods is the collapse of heap before the end of experiment which results to larger base diameter and thus larger angles. Especially in Nelson's method, increase of particle momentum (e.g. by falling from a different point) leads to increase of collapse incidents. In order to overcome these limitations different variations of these methods have been presented (e.g. Train 1958).

The *tilting box method* firstly introduced by Takahasi (1934), consists of a rectangular box filled with material and tilted until the free surface of material starts moving. The angle between tank's bottom and horizontal plane, when the material presents motion, is assumed to be the angle of repose. Even though the size of the box was not described by Takahasi further research proved that its size is essential for experiment accuracy. As a rule of thumb, the width of the tank has to be at least $\frac{1}{3}$ of tank's length, while materials depth has to be at least 20 particle diameters.

The *revolving cylinder method* measures the maximum angle that a plane inside a half-filled hollow cylinder makes with the horizontal upon rotation. In addition to these well-established tests methods, a lot of other (either alternates or new) methods have been introduced, having several advantages and limitations.

The *pile (or cliff) collapse method* (Lee & Hermann 1993) is one of the most referred both by experimental and numerical works. According to that method a pile of material is formed inside a tank which right wall after material reaches stability, is moved quickly, thus material under gravitational forces starting to flow. The angle of material with horizontal plane is measured and assumed to be the angle of repose. Although the method has been shown to predict angles close to that of different methods, because of materials behaviour, several issues like non-homogeneity of cliff's angles have been raised. Holsapple (2013) used

this method in order to explain geophysical phenomena of resting piles in lower than the angle of repose angles (difference between 12 and 15 *deg*).

Finally the *method of “sand pile discharge”* is used mostly due to its simplicity, by a lot of scholars (Li et al 2005). The method is based upon the discharge of a pile when a part of tank’s bottom is suddenly moved and material starts flowing into a second (empty) tank. The part of the bottom could be at the corner or right in the middle (side or central discharge, respectively).

An interesting challenge is to understand the dependence of avalanching upon physical parameters of the system (e.g. moisture content, particle diameter, wall - particle friction etc) either by experimental (Dorbolo 2005) or by numerical (Maleki et al 2008) methods. It has been found that the critical angle, when avalanching occurs, strongly depends on material’s properties, such as particle density and size (Zhou et al, 2001); and also on tank’s depth (Zhou & Zhang 2009). The reader is referred to the work of Ileleji & Zhou (2008), where an extended critical literature review on angle of repose research progress can be found. Despite though the great efforts, scholars often object to the usefulness of the angle of repose as a flow property (Jenike 1964). As an example, Holsapple (2013) in his recent work proved that the statement that a pile formed by granular material is stable prior reaching the angle of repose and unstable afterwards is not even close to reality. Based both on an analytical investigation of a Mohr-Coulomb model of friction and numerical experiments, he showed that material’s behaviour is different when motion is involved, in the sense that angle of repose is a static parameter but when material is already under motion different parameters have to be taken into account. Having similar objections, two decade ago, Purutyan et al. (1999) suggested that there has to be a distinction between efforts that provide qualitative and quantitative results, including angle of repose in the former category that “*at best may help you find differences between samples but will not help you design the vessel*”.

IMO’s Solid Bulk Cargoes Code

According to IMO’s Solid Bulk Cargoes Code (IMO, 20012a), it is required to determine the angle of repose, as well as various other properties of the cargo (see Table 2.2). The angle of repose is indicative of non-cohesive cargo stability and its value establishes which provisions of the Code should apply.

Table 2.2 Recommended test methods according to the IMSB Code (IMO, 2012a)

Test method	Properties identified
Flow table, penetration and shipboard test	TML and FML of a cargo that may liquefy
Tilting box and shipboard test	Angle of repose
Trough test	Self - sustaining exothermic decomposition of fertilizers containing nitrates
Test of resistance to detonation	Propagation of detonation
Self-heating test	Self - heating for car coal

The recommended test method is the so called “tilting box method” which is suitable for non-cohesive granular materials with a grain size not greater than 10 *mm*. A standardized box (600 *mm* long, 400 *mm* wide and 200 *mm* high) is filled with the material to be tested and the tilting mechanism is then activated, with rate of tilting approximately 0.3 *deg/s*. It is stopped as soon as the material begins to slide.

Anticipating difficulties in handling the tilting rate of the box, IMSBC describe a second alternative method, identified as the “shipboard test method”. According to this, a quantity of the material (2 *l*) is poured out of a flask onto a sheet of rough - textured paper, in such a way that a starting cone is formed. A smaller quantity (1 *l*) of the material sample is then poured very carefully from a height of a few *mm* above the cone, by revolving the flask slowly and around the top of the cone. As a result of the pouring, an almost symmetric cone is formed. The angle of repose is the angle between the cone and the horizontal plane, measured at half height. When measuring, care should be taken that the protractor does not touch the cone; otherwise this may result in sliding of the material which would spoil the test. The angle has to be measured at four places around the cone, about 90 degrees apart. This test should be repeated two more times and the average of twelve measurements is the measured angle of repose (± 0.5 *deg*). Even though these two methods are adequate for static angle of repose identification, they are largely empirical and they cannot handle situations where the dynamic motion of the cargo is dominant.

2.6 Behaviour of granular material under prescribed vibration

2.6.1 Vertical (heave) vibration

Vertical vibration of granular material has been the most investigated kind of excitation due to its importance for the industry and thus its economic impact. A large number of experimental and numerical tests have been conducted last in the decades, in order to

understand the plurality of interesting phenomena, some of which have not been explained yet. Physical (e.g. Wassgren et al 1996) as well as numerical (e.g. Rapaport 1998) experiments are easily built and maintained, since the standard granular material vibration experiment consists of a container (most of the times rectangular or cylindrical) subjected to vertical harmonic oscillations. Depending on setup parameters (excitation frequency and amplitude, tank width and filling height), they can give rise to the formation of qualitatively different patterns, where particles behave as an unstructured "cloud", as a coherent mass, with various other possible states found in between.

By far the most investigated case is that of shallow particle beds (e.g. filling ratio less than 4) where, depending on the depth of particles, the bed, according to many authors (e.g. Wassgren et al 1996 and Jaimes et al 2002) exhibits three states : "Newtonian-I," where the vertical concentration of particles changes very little during a vibration cycle; "Newtonian-II," where a dense layer of particles accumulates on the vibrating surface on each vibration cycle while the remainder of the particles bounce around randomly; and lastly, "coherent-expanded" where particles begin to move as a coherent mass which expands and contracts considerably during each vibration cycle. Eshuis et al (2007) have further expanded these three states to five, although their additional states are, in reality, the intermediate layers between the three states mentioned before. Specifically, these authors experimentally observed five discrete states, depending on excitation's frequency and bed's depth. For low vibration frequency the material behaves like a solid that is never detached from the tank. Small increase of frequency leads to downward acceleration that exceeds gravity. Thereafter, bed reaches a detachment point and bounces like a ball would do. Further increase of the frequency leads to the undulations state (also called "arching" or "ripples" by other scholars) where bed behaves like a gas and shows standing wave patterns, similar to vibrating string. Increase of the frequency further drives material behaviour to enter the Leidenfrost state where a cluster of slow particles is floating on top of a dilute layer of fast particles. When higher frequency is considered, the bed enters a gaseous state where every particle is moving randomly throughout the tank. Lastly, for slightly larger depths and for the frequency range of bouncing bed and Leidenfrost states, the material enters the extensively studied by many authors (e.g. Gallas et al 1992, Paolotti et al 2004) convection state, where some particles are more agile than the surrounding, and by creating an open area they lead to convection rolls inside the material. The transition phenomena observed by the authors are graphically presented by the means of a phase diagram for different vibration amplitudes. It is shown that, increase of amplitude leads to larger Leidenfrost and smaller undulations state, in such a

way that, for high enough values of amplitude (e.g. 4 mm in their work), the undulations almost disappears, giving its place to the Leidenfrost state.

According to the categorization of Wassgren et al (1996), when the vibration frequency of the tank is increased above a certain value (Bachman 1940 worked on calculation of this bifurcation point value), lead particle-bed behaviour transitions to what is called a "coherent condensed" or "deep bed" state. In this state, particles move as a coherent mass on the one hand; but on the other, they remain fairly compact throughout the cycle of vibration. Although less investigated, deep particle beds present a set of very interesting phenomena, including heap formation, surface waves, and arches.

Being one of the first observed phenomena (see Faraday 1831) heap formation is the phenomenon where, after a critical value of acceleration amplitude is reached, the free surface of material begins to form a heap either in the centre (Laroche et al 1989) or at one of the two corners, depending on initial conditions (Jaimes et al 2002). Although the phenomenon attracted a lot of attention, the mechanism of heaping is not yet fully understood.

Considering free surface waves, two distinct phenomena have been reported: the first one has to do with travelling surface waves from the lowest point of the heap up the slope to the peak, that appear during the heaping phenomenon (Pak & Behringer 1993, Behringer, 1993). These waves, that don't interfere with the continuous avalanche of particles, increase in length and decrease in height as they travel up the slope and eventually disappear at the peak. The second one has to do with localized surface waves that appear when the acceleration level exceeds the heaping formation region (Melo et al 1994). Depending on excitation frequency, these waves present a great variety of resonance frequencies leading to a variety of wave patterns (such as stripes and squares). Although the mechanism of this phenomenon is also not well understood yet, it is assumed (e.g. Fauve et al. 1989) that it is similar to the Faraday instability (Miles & Henderson, 1990, Spandonidis & Spyrou 2012). Lastly, the arching phenomenon that appears at the bottom of the material (an arch is established), occurs for even larger acceleration values, due to differences in the oscillation phases between several sections of the bed. An interesting observation is that the phenomenon is apparent only after the motion of the particle bed undergoes a period doubling bifurcation (Douady et al., 1988).

2.6.2 Lateral (sway) vibration

Although less investigated than vertical oscillation, a rich variety of interesting macroscopic phenomena, such as convection, segregation and compaction, appear when a rectangular tank, filled with granular material, is shaken transversely. The convection phenomenon has been investigated both experimentally and numerically (e.g. Metcalfe et al 1997). The base of this phenomenon is the same as in the vertical vibration. The most investigated phenomenon in horizontal vibration is, due to its enormous importance in many industrial processes, that of segregation (or Brazil nut effect as it is also known). The phenomenon occurs when particles of different sizes are horizontally vibrated. It has been shown (e.g. Kudrolli 2004) that particles have the tendency to segregate rather than to mix. Finally, compaction is the result of a variety of pattern formation phenomena occurring when different sized or shaped particles are agitated (Aranson & Tsimring 2009). Secondary observation phenomena, like the swelling effect (that is, vibrational motion of the surface of material in the vertical direction with extremely low period) have been reported also (Poschel & Rozenkranz 1997). Some effort has also been given in the observation of structure formation, especially for horizontally driven shallow granular material (Krengel et al 2013).

2.7 Coupled ship-cargo motion

Micro-scale modelling of granular material transported through the oceans inside ship holds had not appeared before the current work. A category of interesting works, however in a neighbouring field, have dealt, for example, with the dynamics of sloshing granular cargos in silo vehicles (e.g. Fleissner et al 2009). But they have not presumed any link to the ship motion problem. However, as already said, the use of SPH methods for modelling the behaviour of liquids in ship tanks is a related field and in this, several works have appeared in the past, since high impacting pressures on tank walls constitute a perennial operation hazard. Faltinsen & Timokha (2009) provided an in depth presentation of analytical and numerical models for the coupled fluid motion in a tank. Moreover, in Monaghan (2005) is found a review of commonly applied SPH techniques.

2.8 “Weakly wet” granular materials

While by investigating dry granular matter we can understand their behaviour at fundamental level, it is unlikely to find any truly dry material out of the laboratory environment. Instead, most “dry” granular materials are wet, either due to environmental

humidity or due to storage conditions (e.g. rain, moisture etc). Thus, at a macroscopic level, the properties of granular media are drastically modified due to particles' contact with liquid state (Gladkyy & Schwarge 2014).

A lot of experimental works have been conducted, mainly in order to understand the static properties of such materials (e.g. Tegzes et al 1999, Betz et al 2003). Herminghaus (2005) presented a review of the dynamics of wet granular materials. Wondering what keeps sandcastles standing; Hornbaker et al (1997) have investigated the dependence of the angle of repose on oil thickness.


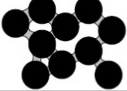
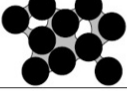
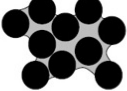
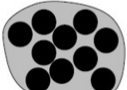
Liquid content	State	Schematic diagram	Physical description
No	Dry		Cohesion between grains is negligible.
Small	Pendular		Liquid bridges are formed at the contact points of grains. Cohesive forces act through the liquid bridges.
Middle	Funicular		Liquid bridges around the contact points and liquid-filled pores coexist. Both give rise to cohesion between particles.
Almost saturated	Capillary		Almost all the pores are filled with the liquid, but the liquid surface forms menisci and the liquid pressure is lower than the air pressure. This suction results in a cohesive interaction between particles.
More	Slurry		The liquid pressure is equal to, or higher than, the air pressure. No cohesive interaction appears between particles.

Figure 2.2 Schematic and physical description of material state based on its liquid content (source: Mitarai & Nori 2006).

Following a series of experiments, Mitarai & Nori (2006) investigated the differences between dry and wet granular media. Their main findings were that, wet granular media show larger surface angle and larger yield shear stress larger than their dry counterparts. In addition, they proved that wet media show enhanced hysteresis compared with that of dry cargos. Based on their findings, they concluded that, in contrast to dry granular media that are treated as one state, wet granular media may be distinguished in four different regimes, based on the liquid content: “Pendular”, “Funicular”, “Capillary” and “Slurry” state. Figure 2.2, borrowed from Mitarai and Nori (2006), presents in a schematic way the physical description of each state.

In general, there are two ways to simulate the fluid in wet granular media that falls into funicular, capillary and slurry states (Clement 2010): a) discretising and solving fluid equations on a lattice (e.g. Lattice Boltzmann method) and b) modelling the fluid as a finite

number of “particles” which move within a framework of various flow conditions [e.g. Dissipative Particle Dynamics (DPD) and Smoothed Particle Hydrodynamics (SPH)]. Zhang et al (2016) presented an interesting numerical approach for the study of nickel ore slurry sloshing in a rolling partially loaded prismatic cargo hold based on the volume of fluid (VOF) method and the non-Newtonian Herschel-Bulkley and Bingham equations. They further used their model in order to monitor the dynamic viscosity of the nickel ore slurry and investigate the critical baffle height with regard to the sloshing-induced moment and the elevation difference of the free surface at two sides of the cargo. Comparisons of numerical results were in good agreement with experiments.

While study of these three states would be normally one of the future steps of our investigation, in the current work we have mainly focused on the pendular state, where the effects of environmental humidity and the interaction of fluid can be modeled by means of an attractive capillary force simulating the liquid bridge between the two grains. We refer to these granular media as “weakly wet” in order to distinguish them from the other three states.

Gomez et al (2012) focused their investigation on the dynamics of avalanches of weakly wet granular media. In their work they carried out experiments with spherical particles of different diameters in the range of 0.5 -2 mm in order to measure the angle of repose and the maximum angle of stability after the collapse. Starting from dry granular material, they gradually increased the amount of humidity and tested the differences in dynamic behaviour of material with humidity levels up to 90%. They proved that the measured angles increase with the increase of humidity.

In parallel with the experimental efforts, due to additional difficulties arising when wet matter is considered (Richefeu et al 2006), a lot of numerical simulations of wet granular matter have been reported. The work of Lian et al (1998) was the first attempt to integrate capillary forces into a DEM model. By performing simulations for two agglomerates, they focused their work on kinetic energy dissipation. Since then several Capillary Bridge force models have been presented (e.g. Mikami et al 1998, Weigert & Ripperger 1999, Willett et al 2000, Rabinovich et al 2005, Soulie et al 2006). Zhu et al (2007) presents an inclusive review of capillary force amongst others non-contact particle force models (van der Waals, electrostatic etc). In addition they provide an extended review of particle - fluid interaction forces and flow.

“Molecular dynamics” simulation results have been presented by Richefeu et al (2006) and Anand et al (2009). They both worked with an altered version of Mikami’s et al (1998) model and focused on the tilting process of granular matter. More recently, Oger et al (2013),

using the Molecular Dynamics method and the linearly decaying, with distance, capillary force model presented by Charlaix & Ciccotti (2010), they replicated Gomez et al's (2012) experiments. It was shown that, simulations with humidity rate below 70% are in good agreement with experimental results. Furthermore, Gladkyy & Schwarge (2014), by means of the Molecular Dynamics method, investigated the differences between the four most profound capillary force models, achieving good coincidence with experimental data.

2.9 Granular material behaviour computing in Graphical Processing Unit

Despite the great progress in computing power, the need for huge amounts of memory and processing capability permits only simulations of some thousands, or hundred thousands, particles, from a few seconds to a few minutes; thus restricting the capability of simulating more realistic scenarios. Two methods are used by the silicon industry in order to increase processing speed: a) maximizing clock frequency (shorter time for each computation) and b) minimizing latency (more work per step) but both have been proven to have reached their upper limit, mostly due to hardware limitations and increase of power consumption (Kirk & Huw 2010). Based on supercomputer facilities, simulations with multi-million particles have been published (Perilla et al 2015).

The use of a Graphics Processing Unit (GPU) seems to be capable of eliminating parallel computing limitations while maintaining most of its advantages. Presentation of the key elements of General Purpose GPU (GPGPU) Architecture is presented in Appendix A. GPGPU computing emerged at early 90s. Since then, a tremendous increase in the design and implementation of algorithms for non-graphics applications using GPGPU programming has taken place. Data Mining & Analytics (Cavuoti et al 2013), Medical Imaging (Eklund et al 2013), Finance (Fernandez et al 2013), Fluid dynamics (Vanka 2013), Electromagnetics-Electrodynamics (Gupta et al 2013) and Seismic processing (Liu et al 2013) are only some examples of important scientific areas involving GPGPU programming.

A lot of effort has been conducted in order to accelerate Molecular Dynamics simulations by means of GPGPU, although the vast majority of that effort has been given for biomolecule simulations. However also, a lot of effort has been spent in order to incorporate GPU capability into the most popular scientific molecular dynamics software packages. In Table 2.3 are listed some of the leading molecular dynamics software packages that incorporate GPU programming capability.

Table 2.3 Molecular Dynamics software packages involving GPGPU programming

Application	Description
Abalone	Molecular dynamics of biopolymers for simulations of proteins, DNA and ligands
ACEMD	GPU simulation of molecular mechanics force fields, implicit and explicit solvent
AMBER	Suite of programs to simulate molecular dynamics on biomolecule
DL-POLY	Simulation of macromolecules, polymers, ionic systems, etc
CHARMM	MD package to simulate molecular dynamics on biomolecule.
GROMACS	Simulation of biochemical molecules with complicated bond interactions
HOOMD-Blue	Particle dynamics package
LAMMPS	Classical molecular dynamics package
NAMD	High-performance simulation of large molecular systems
OpenMM	Library and application for molecular dynamics for HPC with GPUs
* Data taken from NVIDIA's Popular GPU Accelerated Applications Catalog (http://NVIDIA.com)	

Anderson et al (2008) presented performance analysis of general-purpose Molecular Dynamics code that runs on several GPU processors. They have found that up to 100x speedup performance over a common CPU code could be achieved depending on implementation techniques. Based on an Nvidia GeForce 8800 GTX processor, Stone et al. (2007) achieved a performance of almost 100x speedup simulating large biomolecules, based on a procedure linking CUDA implementation of MD directly into NAMD that allows distribution of code across a cluster of nodes with GPUs. Furthermore Stone et al (2010) presented a Hybrid MD code capable of executing GPU code in a CPU cluster proving that although CUDA is very different in programming logic than Message Passing Interface (MPI) (used for distributed memory cluster), they can cooperate for the implementation of a Molecular dynamics code. As shown a cluster of nodes, each with a GPU, could be constructed consisting what is known as Hybrid high performance computing. Brown et al (2011) discussed about limitations and future directions for improving performance on hybrid or heterogeneous computers.

2.10 Non-spherical particle research

Simulation of granular matter through Discrete Element Methods (DEM) is of significant interest in the last decades, leading to an exponential increase of published scientific works in this area (Zhu et al 2007). Despite the importance of these works, the spherical representation

of grains has certain limitations (Poschel & Schwager 2005). Experimental (e.g. Schellart 2000) and numerical works (e.g. Matuttis et al 2000, Cleary & Sawley 2001) proved that dry granular materials present different values of internal friction and cohesion for different rounding and sphericity, while particle shape is a control variable for static (e.g. packing fraction), quasi-static (e.g. angle of repose) and dynamic (e.g. hopper flow) systems. The great challenge in DEM simulation thus, is to incorporate other than spherical representations for particles. A review of the early approaches on simulation of non-spherical particles by means of the molecular dynamics method has been presented by Allen et al (1989), while a complete review of works published the last two decades has been presented by Lu et al (2015). The latter unveiled the growth of scientific efforts on the simulation of non-spherical particles which is representative of the importance of the field. They further focused on challenges that such an approach is faced and also, on the advantages and disadvantages of the different methods of 2D and 3D non-spherical particle shapes in DEM.

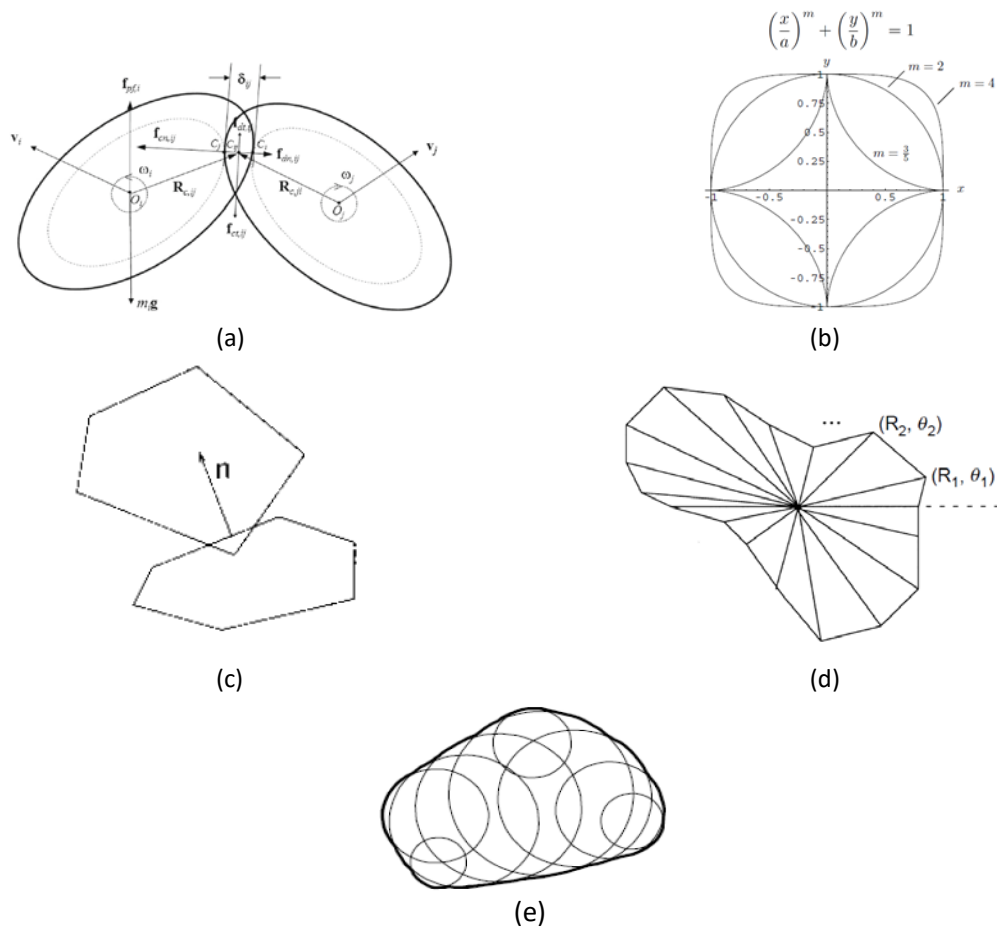


Figure 2.3 Graphical representation of the major non-spherical DEM approaches: a) elliptical, b) super quadric c) polygon, d) Discrete Function Representation and e) multi-element method. (sources: a) Zhou et al 2014, c-d) Hogue 1998, e) Ashmawy et al. 2003).

2.10.1 Non-spherical DEM approaches

Two are the main categories of non-spherical particle simulation approaches: single element (Figure 2.3 a-d) and the multi-element (Figure 2.3e) representation, each of them having specific advantages and limitations. A general drawback of both categories compared to the spherical representation is the higher computational effort.

Single - element particles

The simplest non-spherical particle shape investigated was the elliptical. The method was introduced by Ting (1991) and Rothenburg & Bathurst (1991). It was further improved by many authors both for the 2D (e.g. Ting et al 1995, Tzaferopoulos 1995) and the 3D (Wynn 2009, Zheng et al. 2013) case. Significant improvement of the contact resolution of this method has been done by Lin & Ng (1995) when a new geometric potential algorithm was presented instead of the geometric intersection approach) that was proved to be computationally more efficient. While the use of the ellipse is a step towards the simulation of non-spherical particles, it is representative of only a few real particle shapes, and thus it cannot be very useful for investigating more complex cases. In order to, partly at least, overcome this limitation, Williams & Pentland (1989) replaced the classical equation of the ellipse with that presented by Barr (1981) for super-quadrics. The method was adopted as a more general approach that could provide accurate results for a wide range of particle shapes (from ellipses to cubes) by many authors (e.g. Cleary et al., 1997, Wellmann et al., 2008, Portal et al., 2009). The two major problems that have been reported for this method are that: a) due to nonlinearity of the equations, contact resolution based on the determination of the intersection of the two functions demands a lot of computational effort (Lu et al 2014) and b) Lin & Ng (1995) proved that there is an error in determination of the contact normal. Furthermore a third problem is that while the range of shapes is large is far from realistic. Working towards overcoming this limitation Peters et al (2009) contracted an equation using the sum of multiple ellipsoids in order to describe a single element. This method was proven to be efficient but provided further contact resolution problems. The use of multiple super-quadrics has been also discussed by Hogue (1998).

In parallel to the previous described methodologies, a different approach has been followed, based on the polygon (or polyhedron for 3D cases) description of particles. Pioneers of this method were O'Rourke et al (1982), Walton (1983) and Cundall (1988) while a lot of effort has been given by modern scholars (e.g. Boon et al. 2012, Nassauer et al.

2013, Hopkins 2004) to further improve its efficiency. The great advantage compared to ellipses and super-quadrics is that particles are allowed to have corners (non-smooth particles) and may have arbitrary shapes (Hoge & Newland, 1994); thus are not symmetrical. The great limitations of the method are the non-realistic contour of the particles and the difficulty on identification of the contact normal especially in the case of corner to corner penetration. Feng & Owen (2004) presented an Energy based normal contact model, but the effectiveness of this method depends on selection of the energy function.

Williams & O'Connor (1995) introduced an alternative method to the previously discussed Continuous Function Description (CFR) methods. Their methodology, which is now known as Discrete Function Representation (DFR), is based on the discretization of the contour surface of a particle into several points; thus treating the particle as a cluster of points that have specific coordinates and are assigned to a reference frame. In their initial work they presented a four step contact detection which was based in the heap-sort algorithm (neighbour list) for the spatial sorting and comparison of reference frames of two colliding particles for contact resolution. Several methods of discretization of the implicit function (e.g. Fourier or wavelet based) were discussed by these authors (Williams & O'Connor 1999). Discretization of the surface contour was conducted on Cartesian coordinates. Important advantage of this methodology is that it may be extended to any shape described by a combination of one or more continuous functions or to even arbitrarily shaped particles.

By the use of polar coordinates Hogue (1998) presented an alternative to the DFR method. Based on her previously polar description of arbitrary shaped particles, she described a methodology consisting of two steps and further extended the method to 3D case particles. In her case, the points are not assigned to any frame, however contact resolution is achieved either: a) by using polygonal techniques when the function of the particle is unknown and thus the points are connected through straight lines or b) by using the implicit function to check whether a point lies inside or outside the contour.

Munjiza et al (1995) presented a slightly different approach where the discretized points were assigned not only their coordinates but also the connection information with their neighbours. This method seems to be suitable for realistic shape particles but the implementation of the algorithm is complicated. As mentioned by Hogue (1998), DFR methods are advantageous due to their ability to simulate realistically shaped particles (from smoothed to sharp edged), but their efficiency depends on the discretization (point density, number etc). Despite that; they have almost exclusively been used for simulation of arbitrary shaped or super-quadric particles. Lu et al (2012) evaluated the performance of DFR against

CFR modelling of super-quadric particles. Performing several tests he concluded that a) there is an excellent agreement between the results of the two methods when a specific number of points is used (e.g. more than 40 for a cubic particle) and B) the two algorithms present comparable efficiency. In a more recent approach, Dong et al (2015), focusing on the problem of the contact analysis for particles of arbitrary shape, they presented a new methodology for the calculation of the overlap information. Their method is based on the discretisation of the area of a 2D particle into small square cells and the exact calculation of the overlapping for different particle orientations. The data were added to a dedicated, for each particle, library, used upon need in order to provide the overlap area based on a Taylor series expansion. While the method proved to work efficiently, it either needs a huge amount of computational power in order to update the library during simulation; or it restricts the research to certain pre-calculated shape scenarios.

Multi-element particles

A different approach in order to simulate non-spherical particles is by using multiple spherical elements combined together in order to make one particle. The spherical elements are allowed to overlap in such a way that, by a combination of spheres with different diameter and positioning, almost any smoothly shaped particle form can be created. The methodology was introduced by Favier et al (1999), extending a previously described methodology by Taylor & Preece (1992) which was based on spherical elements that were not allowed to penetrate to each other but they were connected together to form a non-spherical particle (often referred as third methodology (e.g. Lu et al 2015)). Since then, this methodology has attracted a lot of attention, mainly because of three issues: a) the extension of an algorithm written for spherical particles is straight forward, b) a lot of realistic shapes (eg rice, corn, pellets etc) can be achieved with a small amount of spherical elements (eg Chung & Ooi 2006); and more importantly, c) contact resolution is unproblematic and easy to be achieved since, at any instant, only contacts between spheres are under evaluation.

While most of the works conclude that this method can provide accurate results (eg Hohner et al 2011), the artificial roughness inserted to the problem as a result of the multi-sphere connection (wavy surface contour) leads to unrealistic multiple contacts between two particles (Kruggel et al 2012, Markauskas et al 2010, Abbaspour et al 2004). Kodam et al (2009) suggested that the contact forces need to be altered (eg non velocity-dependent damping force) in order for the particle to produce realistic motion. Furthermore, the calculation of the mass and the moment of inertia for the particle is difficult. Working on this

issue, Parteli (2013) suggested a method of calculation of these parameters, though it has been only shown to be efficient for 2D cases. Following a different way from all the other scholars, who either reconstruct a multi-element particle from a surface contour provided by scanning (MRI, laser, etc); or construct a multi-element particle based on a predefined lattice, Mollon & Zhao (2012), presented a method of non-spherical particles generation based on spectral Fourier methods, for the description of the surface contour. Their methodology, initially discussed by Das et al (2008) for the simulation of sand particles, while still having the previously discussed problems, allows the simulation of extremely realistic particles. A general drawback of multi-element method is that, in order to achieve more realistic particle shapes, a lot of spherical elements have to be used increasing thus the computational cost.

2.10.2 Realistic shape descriptors

Being one of the fundamental geometrical properties of an object, shape, has been judged to be amongst the most difficult to quantify. Following the description of Blott & Pye (2008) shape is a subset of object's morphology amongst with surface texture and can be further divided into several different aspects with *form*, *roundness*, *irregularity* and *circularity*² having the greatest importance. A lot of effort has been spent towards quantifying all these aspects. The results however, whilst satisfactory for particular cases, they cannot be characterized as generic. Moreover, sometimes they appear as even contradictory (for a full review on this see Blott & Pye 2008). In addition, due to the improvement of DEM methods and the need for more realistic granular matter simulations, some efforts to reconstruct realistic material shapes based on morphology measurements have been noted in the last few years. A brief summary of the most profound (in the sense of frequency of citation from other scholars) shape descriptors is given below.

Shape and Angle Factor Descriptors

Sukumaran & Ashmawy (2001) presented a method deriving from a 2D projection of the scanned material surface. This projection was subsequently approximated by a polygon, while, in association with it, a distortion diagram was constructed, which was a plot of distortion angles against the cumulative sampling interval. While the use of this diagram in their methodology was to help calculate the shape and angular factors, i.e. the two parameters that describe the deviation of a particle from a perfect sphere, the diagram itself can be easily

² For a specific particle shape: *form* is defined by the ratios of its linear dimensions; *roundness* describes its angularity or sharpness; *irregularity*, defines the deviation of its edges from smooth shaped edges (eg line or curve); and *circularity* describes the degree to which it approximates a sphere (Sneed & Folk 1958).

used also in order to reconstruct the particle shape. Ashmawy et al (2003) used a range of such diagrams and then, by means of multi-element DEM, to simulate liquefaction effects. The great disadvantage of this method is that, it presumes an already existed library of scanned particles.

Fourier Descriptors

The idea of describing the particle shape by means of Fourier analysis was introduced by Ehrlich & Weinberg (1970). According to their method, the surface contour could be initially transformed into polar representation and then mathematically expressed in a Fourier series. More specifically, with respect to a suitable centre of the particle, the surface contour can be described as indicated below (Eq. 2.1):

$$R(\theta) = R_0 + \sum_{i=1}^N [A_n \cos(n\theta) + B_n \sin(n\theta)] \quad (2.1)$$

where $R(\theta)$ is particle's radius at angle θ ; N is the number of harmonics; and A_n, B_n are respectively, the *cos* and *sin* amplitudes of the n^{th} harmonic component. R_0 is the magnitude coefficient for $n = 0$ and it can be selected so that to coincide with the radius of a specific reference circle (Bowman et al., 2001).

The great problem, according to Fong et al (1979), of this representation is its incapability to handle re-entrance points; that is, to simulate irregular particles that have two or more points on the surface for the same angle. In order to overcome this limitation in their work, instead of (R, θ) pairs, the particle's profile was parametrised by its arc length l and change of slope $\varphi(l)$ from the slope at a randomly selected starting point. The method was shown to be capable of producing particles with complicated shapes, but there were limitations due to the introduction of some artificial parameters.

Rosler et al (1987) provided an insight into the relation between Fourier coefficients and shape parameters of the particle. Furthermore, Diepenbroek et al (1992) managed to relate the first harmonics with particle morphology. Specifically, after extensive experimentation, they concluded that, the amplitude of each one of the 24 first harmonics can be related with specific shape characteristics. They related the first descriptor with circularity, the second with elongation, the 3rd to 8th with irregularities (eg squareness etc) and the rest with roundness. The goal of their effort was that, for the first time, a connection between Fourier descriptor and real measurement values appeared possible (e.g. Meloy 1997). Meloy (1997) proved that there is a linear relation (on a log-log plane) between a descriptor's number and

its amplitude, for harmonics above the 8th. Mollon & Zhao (2012) described a similar relation for harmonics between 3rd and 8th, thus reducing the analysis on defining simple spectra only for descriptors 2, 3 and 8 (in their analysis they assumed that the first descriptor equals to 0)

Fractal Descriptors

Methods based on the idea of *fractal* geometry have been used during the last two decades in order to reproduce mathematically the surface of irregularly-shaped particles (e.g. Orford & Whalley 1983). Although different authors follow different paths, the core of the methodology lies in the assumption that the shape of a particle can be approximated by a series of equilateral polygons (Kennedy & Lin, 1992). A relation between the perimeter P of a particle and the length S of each polygon side (step length) was developed by Mandelbrot (1967). The M-R plot (also known as Richardson plot) for each particle is given as the plot of the $\log P$ against the $\log S$ (Figure 2.4 left). The slope of the linear curve (β) is linearly connected with the dimension of the *Fractal* (D) by $D = 1 - \beta$ and used as an indicator of shape irregularity (greater slope corresponds to more irregularly shaped particles).

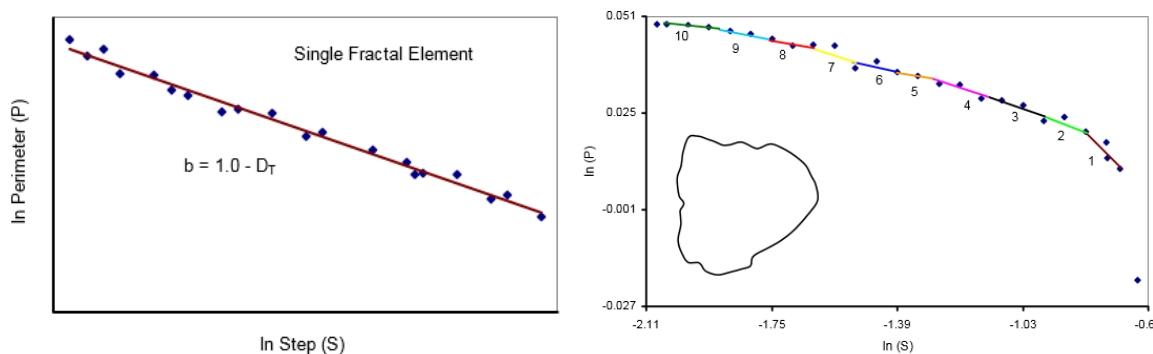


Figure 2.4 M-R plots for Single *Fractal* Element (left) and sedimentary particle using multiple *Fractal* elements (right). (sources: a) Orford & Whalley 1983, b) Kennedy & Lin, 1992).

The general drawback of this approach is that, only symmetrical particles may be represented. In order to overcome this problem, the technique of using two different dimensions (that actually is translated to different linear segments of the M-R plot) are used, each one of them being descriptive of a different layer of the shape. The smallest step length segment is descriptive of the surface texture; while the other of the gross shape of the particle (Flook, 1979). Kennedy & Lin (1992), using a lot of different linear segments, concluded that the use of fractal analysis can provide, more or less, the same results with the method of Fourier descriptors (Figure 2.4 right). This technique was employed subsequently by many authors in order to reproduce realistic particle shapes (eg Maria & Carey 2002 used fractal analysis to quantitatively characterize the shape of volcanic particles).

Chapter 3: Objectives

The general objective of this work is stated below:

To contribute to the establishment of a fundamental modelling approach for predicting the dynamic behaviour of granular cargos transported in ship holds. This means, to develop capability for predicting the conditions of occurrence of cargo shift, instigated by wave loading on the hull and the subsequent dynamic behaviour of the coupled ship – cargo system.

The particular objectives, and associated research tasks, are:

- a. To review the suitable mathematical modelling techniques and then select a mathematical model that should be capable of simulating efficiently the semi-static and dynamic behaviour of a large number of spherical (at first step) particles, inside a 2D tank forced to oscillate in the roll, sway and heave direction.
- b. To investigate the influence of tank scaling and identify critical parameters affecting the behaviour of cargo under various excitations. Special focus needs to be given on the investigation of the angle of repose, due to the importance of this quantity for ship safety.
- c. To optimize the developed numerical algorithm in order to be capable to simulate a larger number of particles.
- d. To address coupled ship motions in waves, for a ship having loose granular cargo tanks and further investigate the influence of cargo shift upon ship's stability.
- e. To consider how the mathematical model can be improved for dealing with the effect of environmental humidity on the grains, so that, its influence on ship stability can be assessed.
- f. To develop capability for handling irregularly-shaped particles and to conduct investigation on shape's influence upon the semi-static and dynamic behaviour of cargo.
- g. To experimentally reproduce key numerical findings.

Chapter 4: Basic Mathematical Model

The adopted modelling approach is explained in this chapter. Its pillar is the “Molecular Dynamics” method which presents some distinctive advantages already singled out in *Chapter 2*: it can simulate both semi-static and fully dynamic motions; it is time efficient and its application is not restricted to specific materials or states, as do other competing methodologies. In the following paragraphs are discussed the modelling, validation and verification of particle interaction forces on the basis of extensive comparative studies.

4.1 Molecular Dynamics simulation

Molecular Dynamics (MD) Method [referred also as Discrete Element Method (DEM)] is associated with three general elements: developing a mathematical model, using the model for simulation and analyzing the simulation outcome. In Figure 4.1 are illustrated these steps.

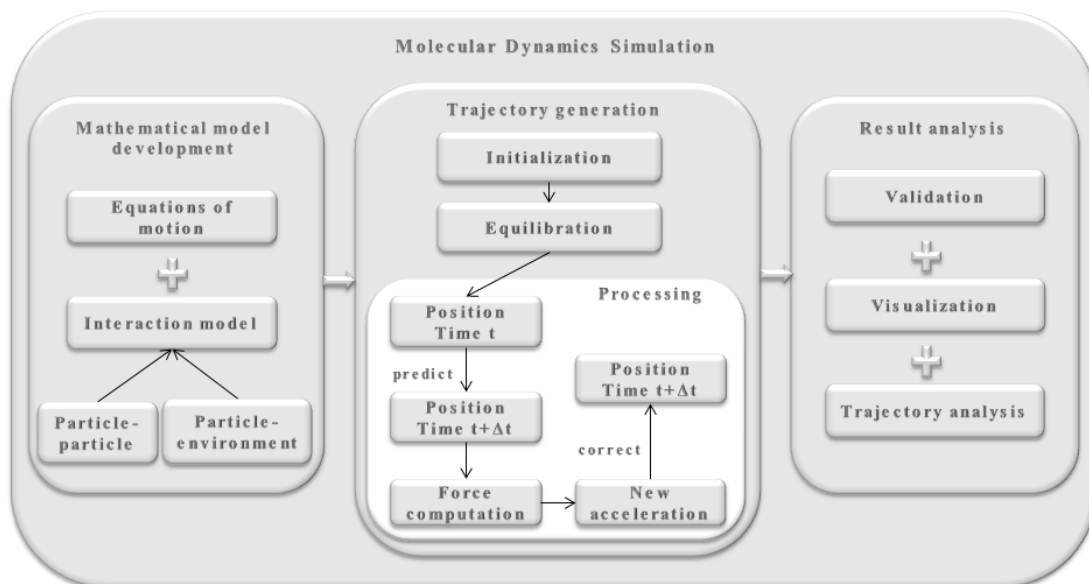


Figure 4.1 Molecular dynamics simulation

Model development includes selection of intermolecular and molecular – environment interaction forces and derivation of appropriate equations of motion. In our case, granules are considered as smooth spherical objects with diameters that could be either fixed or varied within some range. They can be translated (horizontally and/or vertically) and/or rotated on a perpendicular plane. At this specific stage we shall assume that the granules are completely dry although at a later chapter the effect of humidity will be introduced.

The implemented calculation scheme is based on the method of Poschel & Schwager (2005). Whilst other options had also been available, such as LAMMPS (Plimpton, 1995), they were not adopted due to their limited capability in providing a connection of pair style parameters (stiffness, damping) to material properties identified from experiments (such as density, Young's modulus, and the coefficient of restitution) as well as movable tanks.³

Trajectory generation refers to the paths of a large number of particles and it is divided into three major steps: initialization, equilibration and production. Of the large number of available finite - difference schemes, Gear's (1971) predictor - corrector was used which is suitable for MD due to its numerical stability. For computational time efficiency a *Neighbour List algorithm* (e.g. Verlet, 1967) may be introduced that, for each particle i , it retains a number of neighbouring particles lying within a predefined distance from i . As a result the list identifies those particles that contribute to the force on particle i . Neighbours detection is, however, not trivial. All pairs of close particles have to be considered, irrespectively of particle velocity or size (common issues of concern for the two main algorithms: *Verlet List* and *Linked Cell*). Even one collision pair miscalculation could lead to serious consequences for the validity of the simulation results (Poschel & Schwager 2005).

The *simulation results* are processed in order to assess the computed trajectories and moreover, to determine the quantities that are representative of the targeted collective phenomenon (e.g. shift of cargo's centre of mass). For trajectory visualization we have employed the open-source multi - platform ParaView 3.12 (Sawley et al, 2007) whose flexible and intuitive front - end graphical user interface (GUI) is amenable to complex and "fine-grained" data manipulation.

4.1.1 Coupled ship-cargo motion implementation

A key element in the coupled roll-granular cargo problem formulation is the feedback from the ensemble of discontinuously moving particles to the ship's body. Such abrupt particle movement is a characteristic of container-body motions receiving external excitations predominantly of low frequency, with some higher frequencies appearing in the excitation from time to time. Such sudden motion of the cargo constitutes the main contributing factor for a ship to acquire large roll bias, a state wherefrom capsizes becomes imminent. In general, in terms of dynamics, the particles behave like oscillating masses interacting with each other and also, in unison, with the hold they are transported wherein. As a matter of fact, significant

³A very recent upgraded version (LIGGGHTS) seems to overcome this deficiency.

quantities of energy can be exchanged between the particles and the carrying body in a rather intermittent manner. These effects of interaction take the problem out of the convenient field of rigid body dynamics where ship stability studies are customarily performed. Figure 4.2 depicts Molecular Dynamics's processing step for the case of coupled ship-cargo simulation.

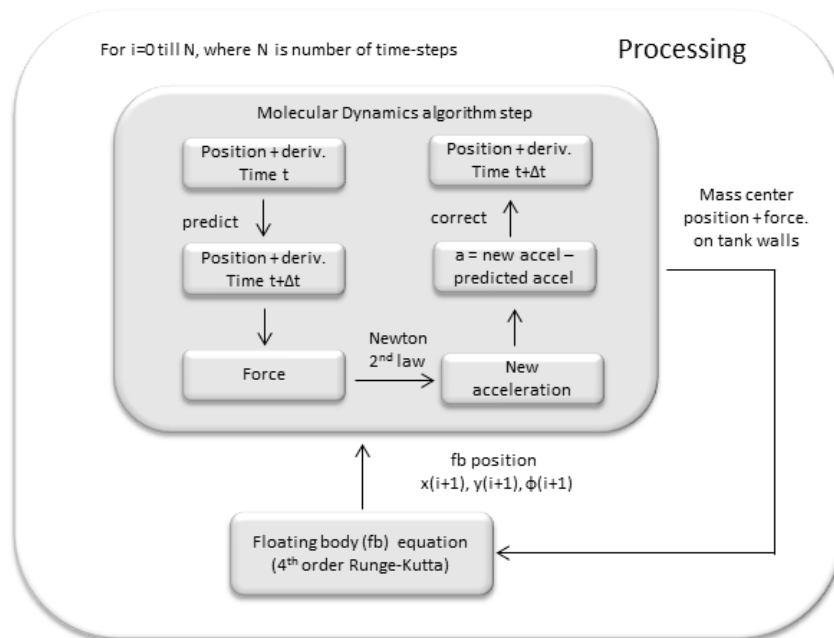


Figure 4.2 Molecular Dynamics's processing step for the case of coupled ship-cargo simulation.

As easily understood, two different problems need to be tackled simultaneously: The first is the prediction of the wave-induced ship motion; and the second is the prediction of the motion of the granules inside the hold. By means of the Molecular Dynamics method we predict the trajectory of each individual particle, assumed to interact with all its neighbouring particles through non-linear elastic and frictional forces. Collision forces are computed for each particle pair and at every time step. Then, the forces that act on the side plates of the hold and the position of the cargo mass centre can be deduced.

Newton's equation is applied for the ship motion problem incorporating however the nonlinear molecular dynamics model of the granular material. It is solved at each time step by a 4th order Runge-Kutta scheme, with forces/moments considered due to inertia (including the "added" hydrodynamic one), hydrodynamic damping, restoring, "Froude-Krylov" and the impacting load due to possible particles' impact with side walls.

4.2 Interaction forces

4.2.1 Dry granular solids and aggregates

The force acting on each particle i due to the interaction with all its neighbouring particles is given by:

$$\mathbf{F}_i = \sum_{j=1, j \neq i}^N \mathbf{F}_{ij} \quad (4.1)$$

where the force between two interacting particles \mathbf{F}_{ij} is given by:

$$\mathbf{F}_{ij} = \begin{cases} \mathbf{F}_{nor} + \mathbf{F}_{tan} & , \xi > 0 \\ 0 & , \xi \leq 0 \end{cases} \quad (4.2)$$

and ξ is the penetration distance between two particles (with radii R_i and R_j) given by:

$$\xi = \max(0, R_i + R_j - |\mathbf{r}_{ij}|) \quad (4.3)$$

Along the normal to the line of contact of particles during collision, have been considered nonlinear elastic and frictional forces (F_{nor}); while transversely it was assumed acting a purely frictional force (F_{tan}) [see Figure 4.3]. Considering these two forces, several options are available. A few popular schemes are summarized in Table 4.1 and Table 4.2, as identified in Schafer et al (1996). Other, more complicated, schemes also exist, which however are used rarely (e.g. Zhou et al 2001).

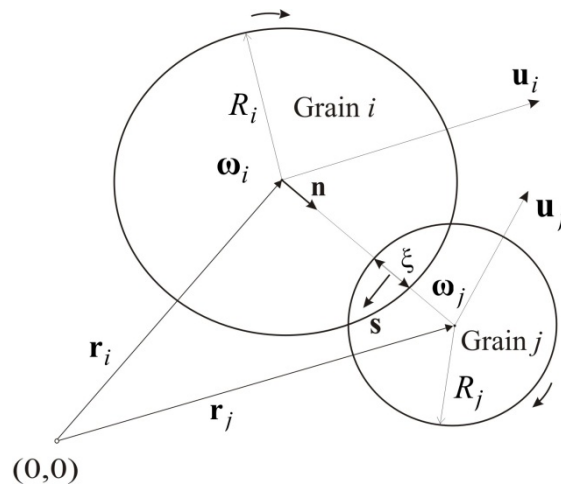


Figure 4.3 Grains penetration.

Table 4.1 Popular normal force (F_n) schemes applied in simulations of granular materials.

<i>Model</i>	<i>Comments</i>
$F_n = -k_n \xi - \gamma_n \dot{\xi}$	Linear model - only slow change of kinematic condition of particles
$F_n = -k_n \xi^{3/2}$	No viscous damping term
$F_n = -k_n \xi^{3/2} - \gamma_n \dot{\xi}$	No realistic results for low or high impact velocity
$F_n = -\tilde{k}_n \xi^{3/2} - \gamma_n \xi^{1/2} \dot{\xi}$	More realistic, however still empirical model
$F_n = \begin{cases} k_1 \xi, \dot{\xi} \geq 0 \\ k_2 (\xi - \xi_o), \dot{\xi} < 0 \end{cases}$	Suitable when plastic deformation occurs (ξ_o is the permanent plastic deformation)

More specifically, for the normal force we adopted the dissipative Hertz - type force for viscoelastic materials, proposed by Brilliantov et al (1996):

$$F_n = \tilde{k}_n \xi^{3/2} + \gamma_n \xi^{1/2} \dot{\xi} \quad (4.4)$$

where γ_n is a damping constant, whose value is connected to the radii of the spheres and \tilde{k}_n is the non-linear stiffness of a spring. F_n is connected to the elastic properties and to the radii of the spheres through the expression:

$$\tilde{k}_n = \frac{2Y\sqrt{R^{eff}}}{3(1-\nu^2)}$$

$$\frac{1}{R^{eff}} = \frac{1}{R_i} + \frac{1}{R_j} \quad (4.5)$$

Y stands for Young's Modulus and ν for the Poisson ratio. R^{eff} is the effective radius of the colliding particles. The choice of this model is based on a combination of its own merit and the other models limitations. Specifically, the linear spring-dashpot model (first model of Table 4.1) is restricted only to slow changes due to its inherent linear nature. The second one ("Hertz model") ignores the dissipation of energy during contacts. This limitation can be overcome by adding ad hoc a viscous damping term into the model. In the third model (dissipative-Hertz type model) the damping term is linear and although it can produce more realistic results compared to the previous models, it produces unrealistic results when it comes to high - impact - velocity collisions (Taguchi, 1992 as referred in Schafer et al, 1996). This unrealistic behaviour is avoided when the dissipative term obtains the nonlinear form of the fourth model ("Brilliantov's model"). This model was originally developed for stiff

particles as is the case of our investigation. The fifth model reflects a plastic deformation approach (which is not our case) and it ignores the dissipation of energy.

As for the transverse force, the following model by Haff & Werner (1986) was adopted:

$$F_t = -\min(\gamma_s |u_s|, \mu |F_n|) \cdot \text{sign}(u_s) \quad (4.6)$$

γ_s is shear damping constant; u_s is the shear velocity component that for a 2D case is expressed as:

$$u_s = (\mathbf{u}_i - \mathbf{u}_j) \cdot \mathbf{s} + \omega_i R_i + \omega_j R_j \quad (4.7)$$

μ stands for the dynamic friction coefficient and \mathbf{s} is the unit vector that, for contact between spheres, it is along the perpendicular to the line of contact. This model combines the strengths of the first two transverse models of Table 4.2 (the Coulomb and viscous friction model) without their limitations. Kuwabara & Kono (1987) argued that simulation results based on Equation 4.4 are in good agreement with experimental results when γ_s receives high values (e.g. 20N s/m).

Table 4.2 Popular transverse force (F_t) schemes applied in simulations of granular materials.

<i>Model</i>	<i>Comments</i>
$F_t = -\mu F_n \cdot \text{sign}(u_s)$ u_s is shear velocity component μ is dynamic friction coefficient	Discontinuous at $u_s = 0$
$F_t = -\gamma_s u_s$ γ_s is shear damping coefficient	Unrealistic results for nearly normal and nearly grazing impacts Difficult to obtain the value of shear damping experimentally
$F_t = -\min(\gamma_s u_s , \mu F_n) \cdot \text{sign}(u_s)$	Combination of above two Popular choice
$F_t = -\min(k_s u \zeta , \mu F_n) \cdot \text{sign}(\zeta)$ ζ is displacement k_s is tangential stiffness	Higher computational effort needed Difficulties in code initialization

Particles' motions are governed by Newton's second law for translational and rotational motions:

$$\begin{aligned}
m_i \frac{d^2 \mathbf{r}_i}{dt^2} &= \sum_{j=1, j \neq i}^N \mathbf{F}_{ij}(\mathbf{r}_{ij}, \mathbf{u}_i, \mathbf{u}_j, \boldsymbol{\omega}_i, \boldsymbol{\omega}_j) \\
J_i \frac{d(\boldsymbol{\omega}_i)}{dt} &= \sum_{j=1, j \neq i}^N \mathbf{M}_{ij}(\mathbf{r}_{ij}, \mathbf{u}_i, \mathbf{u}_j, \boldsymbol{\omega}_i, \boldsymbol{\omega}_j)
\end{aligned} \quad (4.8)$$

The force \mathbf{F}_{ij} and the torque \mathbf{M}_{ij} acting at some time instant on a particle i of mass m_i and of tensorial moment of inertia J_i , are functions of the distances \mathbf{r}_{ij} of the particle i from some other particle j that is in proximity. If spherical particles are only considered, their angular orientation does not enter the calculation because orientation is in this case indifferent for the generated forces. Since for the purpose of our work we are restricted to two-dimensional systems, both the angular orientation of a particle and its moment of inertia are reduced to scalar values. Appendix B presents a detailed description of the adopted integration scheme for the 2D case.

4.2.2 Implementation of humidity

Let us consider now wet granular media that are in the so called “pendular state”; that is, the liquid content (due to environmental humidity) appears forming a liquid bridge between the two particles after their contact. In general (Richefeu et al 2006), the capillary force between two particles is an attraction force that can be obtained by integrating the Laplace-Young equation, a nonlinear partial differential equation that relates the capillary pressure difference sustained across the interface between two static fluids, (water and air in our case) to: a) the gap between particles (δ_n), b) the liquid bond volume (V_b), c) the wetting surface tension (γ_s), d) particle-liquid-gas contact angle (θ) and, e) the effective radius of the particles R^{eff} .

However, in order to be used in DEM simulation, many authors presented explicit capillary force functions that, while uncorrelated with the liquid bond volume, they have been shown to be accurate enough (Zhu et al 2007). In Figure 4.4 is illustrated in a graphical way the liquid bridge formed after particles’ collision.

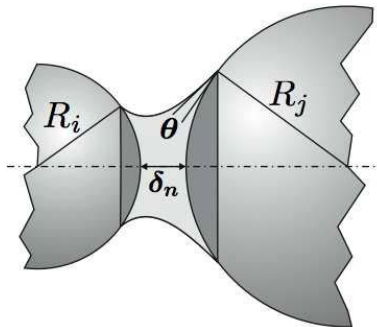


Figure 4.4 Particle condition after collision (source; Richefeu et al 2006).

In almost all models it is assumed that, for relatively small (compared to particles radii) overlap ($\delta_n \leq 0$) the amplitude of the capillary force can be given by:

$$f_0 = -2\pi \gamma_s \cos \theta R^{eff} \quad (4.9)$$

$$\frac{1}{R^{eff}} = \frac{1}{R_i} + \frac{1}{R_j} \quad (4.10)$$

At the contact point ($\delta_n = 0$) the capillary force has the greatest value. For positive values of gap ($\delta_n \geq 0$) it is assumed that the attraction force declines as the gap is increased. Two different approaches describing the decrease of the adhesive force when two particles are moving apart after the collision have been presented: a) The exponential (e.g. Richefeu et al 2006) and b) the linear (e.g. Charlaix & Crassus 2005), both with advantages and limitations. Following Oger et al (2013) we adopted the linear approach described by:

$$F_{cap} = - \begin{cases} f_0 & , \text{ for } \delta \leq 0 \\ s \cdot \delta + F_m & , \text{ for } \delta > 0 \end{cases}$$

$$\text{where } F_m = f_0(a_0 + a_1\sqrt{r_k} + a_2r_k) \text{ and } s = -\frac{f_0}{r_k} \quad (4.11)$$

a_0, a_1, a_2 are constants with numerical values given by Crassous et al (2011). r_k is the equilibrium curvature radius of the interface (Kelvin radius) and is linked to the humidity rate parameter. Selection of this force representation has been made for two reasons: firstly, because experimental data for the case of our interest (avalanches) were available; and secondly, because the methodology has been shown to produce accurate results (Oger et al 2013).

4.3 Systems of coordinates

Each particle's motion is monitored from an earth-fixed coordinate system, whose origin is placed at hold's bottom left corner (ZOY) when this had its initial upright position. System yKz is also placed initially at hold's bottom left corner; but this one follows the motion of the hold in such a manner that its z -axis is always perpendicular to hold's bottom. A third coordinate system aPb is assumed to be at the centre of rotation of the vessel (which in the current study coincides with the middle point of the ideal flat free surface). This coordinate system follows vessel's rotation. In Figure 4.5 systems yKz and aPb are depicted with solid lines.

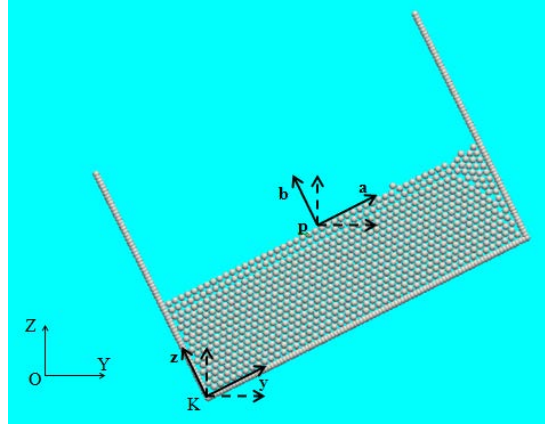


Figure 4.5 The three different coordinate systems (solid lines) and their irrotational equivalents (dashed lines) are being depicted.

4.4 Model verification

In order to verify our results, that is, to ensure that the code runs correctly given the equations of the model, we performed reliability tests as proposed by Haile (1997). Specifically:

- a) we checked conservation principles during both the initial equilibration and the subsequent execution of the code;
- b) we monitored the systematic and the statistical error.

In Table 4.3 is summarized the outcome of the performed tests. The calculated uncertainties are standard deviations of the average (total energy and internal energy) at a 95% confidence level.

Table 4.3 Performed tests for reliability of the code

<i>Type of test</i>	<i>Comments</i>	<i>Deviations</i>
Conservation Principles	Constant number of particles in time In equilibrium condition, total kinetic energy is constant and equally partitioned in Cartesian components.	< 0.5%
Statistical error *	Reproducible averages within statistical uncertainties for different initial conditions Stable instantaneous values	< 2%
Systematic error *	Same code - different PC	0.2-2%
	Same code - different compiler	0.2-2%

* All runs were for 2000 particles, time-step $\Delta t = 0.0001$. Averages were accumulated over 200.000 time-steps. The quantities studied are total energy and internal energy.

4.5 Validation

Verification tests such as those referred previously are only necessary conditions for satisfactory predictions, but they are not sufficient for proving accuracy relatively to the behaviour of the corresponding physical system. Validation of the code should involve comparison of characteristic obtained results with experimental data. However, there is lack of experimental data for the considered low frequency range (when it comes to low frequency excitation the literature is very poor) and the specific materials of interest (most of the scientific research is based on specific kind of material such as cellulose acetate, glass, aluminium and steel spheres). To overcome this difficulty, at this stage two different kinds of validation tests were performed.

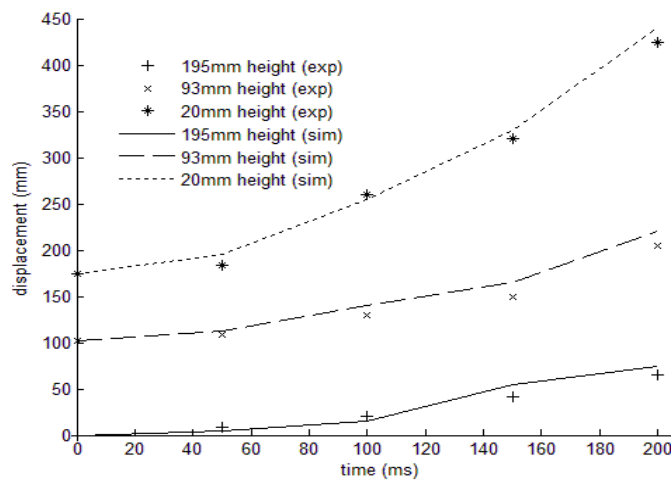


Figure 4.6 Comparison of simulation results to experimental data when a two dimensional stack is in guided fall.

To test code's output when nearly static or low dynamic behaviour is investigated, we have used the two dimensional stack in guided fall test, proposed by Duran (2000). According to that test aluminium particles (1.5mm diameter) are stacked in a regular triangular arrangement into a 2D vertical cell. The width of the cell is 3.6 cm and the height of the stack is varied between 0.15 and 19 cm . The bottom of the cell is blocked by a spring-loaded metal plate that can be dropped rapidly (with initial acceleration $3g$). As a result, the stack starts flowing and the altitude at the top of the pile as a function of fall time for various pile height is measured. Figure 4.6 presents experimental and simulation results for three different heights of the stack.

Furthermore, in order to evaluate the results when extreme dynamic behaviour is investigated, we performed the 2D horizontal shaken granular matter test proposed by

Poschel & Rozenkranz (1997). According to these authors, when a rectangular container (6 cm width) filled with granular material is shaken harmonically in the horizontal direction, with amplitude A and frequency f , for certain intervals of the parameters A and f , time - dependent variation of the volume of the material (0.1 mm diameter), and hence of its overall density, is observed. This effect, which is called the swelling effect, can be measured by recording the filling height (height of material at the middle of the free surface). In Figure 4.7 are shown records of the swelling frequency F , as a function of the frequency of forcing, for filling height 15 mm, obtained from our simulation and also from the experiments of Poschel & Rozenkranz (1997).

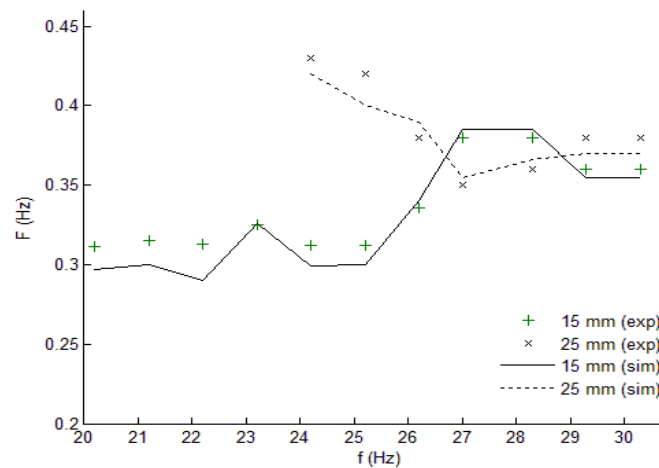


Figure 4.7 Comparison of simulation results to experimental data. Testing of granular matter involving horizontal shaking, for various filling heights in tank.

As indicated in both cases, the simulation results are in good agreement with the experiments. The main reason for the differences between the experimental and numerical data is believed to be related to the friction between walls and spheres that was not known exactly. Working in the same manner for several stack heights we calculated a standard deviation of about 7% between simulations and experiments. Based on the stability of the MD method (low error propagation rate) we considered such deviation value to be noncritical; in the sense that, the realism of the gained results is not disturbed. As a matter of fact, we felt that we can proceed to the main numerical experiments planned for the current investigation.

For the validation of the coupled motion results we relied on separate validation of the two sub-algorithms. Concerning the ship motion equation, results for “empty hold” and for “hold with solid (frozen) cargo” were compared against similar experimental results obtained by Rogenbake & Faltinsen (2003) and by Murashige & Aihara (1998), indicating that the

algorithm performs very well with a standard deviation less than 1%. Furthermore for wet granular matter results we relied on Oger et al (2013) validation showed that for humidity rates below 70% the deviation of simulation results from experimental data is less than 2%.

Chapter 5: Granular Flow under Prescribed Tank Motion

In this chapter several materials consisted of circular particles are investigated numerically in term of how easily they can exhibit a “fluid-like” behaviour. Two different tests are performed in order to investigate the dependence of granular flow upon a) particles’ properties (density, radius etc) and b) system configuration (initial free surface, tilting and filling ratio). Furthermore, the dependence of particles flow tendency upon their distance from the rolling point is considered. The usually ignored low frequency range is of prime interest here as it is the one encountered in ship motions. Lastly, by direct simulation we investigate the various facets of the scaling problem, for a rectangular tank that is partly filled with granular material and conclusions are drawn about the influence of scaling on the exhibited motions.

5.1 System Definition

As stated earlier, this work is driven from the desire to understand (and develop capability for predicting) phenomena of granular cargo movement in ships subjected to wave loading. However, a complete solution for this problem is rather elusive at present. Realistically, a step-by-step approach and a number of simplifying assumptions will be need to be made for realizing progress. Specifically for the work described in this chapter, the following assumptions have been made:

- external excitation is “prescriptive” (i.e. it is not affected by granular material’s response) and it is also harmonic,
- any effects due to moisture of the particles are neglected,
- the granular flow is considered as 2-dimensional,
- the particles are spherical and monosized. In fact, as a 2-d flow case is assumed, the particles are essentially discs of infinitesimal width that have been placed in a container of infinitesimal thickness.

Under these terms, materials consisted of four different types of particles will be investigated, broadly corresponding (e.g. in characteristic size and physical properties) to conventional materials of the real world. The properties of the investigated materials are identified in Table 5.1.

The horizontal motion performed by the granules is the key point of interest of this work. Excitation frequency and amplitude is selected in such a way to correspond to real sea case scenarios for the scaled tank (Appendix C presents a detailed description of the adopted scaling technique). Based on particles' diameter and density, "material A" could be associated with copper and "material B" with iron ore, two of the most common bulky materials. "Material C" however is a rather artificial one from the perspective of its transportation inside ship holds. It was selected merely for including in the investigation a very heavy material (its particles' diameter and density would associate it, in fact, with "gold ore"). Of course, the other parameters (Young modulus, Coulomb friction, etc) should also receive their true values in order to achieve accurate simulation results. "Material D" could associate with cellulose acetate spherical particles, a material that is widely used in scientific investigations of granular matter and will be further discussed in the next chapters.

Table 5.1 Particles' properties

Material	A	B	C	D
Diameter, d (mm)	3	2	1	6
Mass, m (g/cm ³)	1.98	4.45	17.8	17.8
Poisson ratio, ν	0.28	0.28	0.28	0.28
Young modulus, Y (N/m ²)	3.2×10^9	3.2×10^9	3.2×10^9	3.2×10^9
Coulomb friction, μ	0.25 - 0.5	0.25 - 0.5	0.25 - 0.5	0.25 - 0.5
Shear damping, γ_s (N s/m)	20	20	20	20

5.2 Dependence of granular flow on particle's properties

Two different tank configurations have been selected in order to understand in comparative manner the behaviour of these three materials. The tanks are partly filled by 2000 particles. In the first configuration the tank width is fixed at 19.2 cm. As the material weight is kept the same, this results in different h/l ratios. The key feature of the second configuration is geometric similarity. It is achieved by adjusting container's width to a certain multiple of the particle's diameter: i.e. a proportional relation between tank's width/height and particle diameter (d) was assumed. The size of each tank was determined from the relations: $l = 60d$ and $h = 20d$.

Three different simulation results are produced per tank configuration. Firstly, in order to determine the *angle of repose*, based on the tilting box test (IMO 2012a), we tested the

response of the free surface under certain rates of tilting. Furthermore, we monitored the movement of the granules' mass centre for various tilting rates and pure sway and heave oscillations. We assumed harmonic external excitation of the form $n_2 \sin(2\pi f_2 t)$ and $n_3 \sin(2\pi f_3 t)$, where n_2, f_2 are the horizontal and n_3, f_3 the vertical excitation amplitude and frequency, respectively. Then giving to n_2 and n_3 a constant value (10 cm) we investigated system's behaviour as the frequency is varied. In Appendix D a study based on the alternative according to IMO (2012a) method for measurement of the angle of repose (shipboard test method) is presented.

5.2.1 Slow tilting of tank – identification of angle of repose

Identical tanks

In Figure 5.1 (up) are illustrated the three materials before the tilting had started. From there on a 3°/s tilting rate was introduced. In Figure 5.1 (down) the tanks are shown in time instants right after the free surface started to flow. It is deduced that the angle of repose is larger for material A and smaller for material C (heavier with smaller size particles).

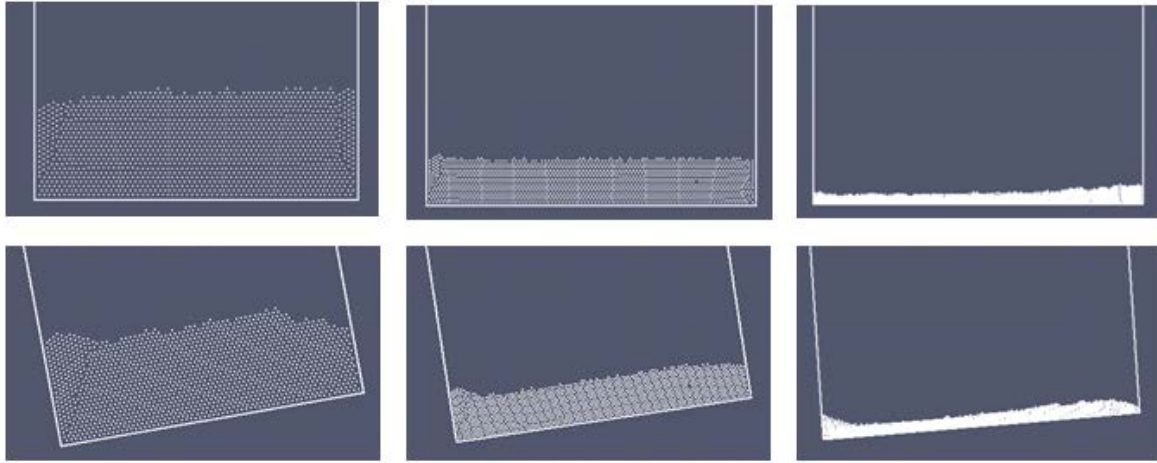


Figure 5.1 Different time instants of the slowly tilted tank, for material A (left), B (middle) and C (right) in the case of the 1st tank configuration. Up: Tanks at the beginning of the test (0 s). Down: Tanks' state when the free surface granules begin to flow (at 6 s, 5.5 s and 3.9 s, from left to right).

Geometrically similar tanks, scaled to particles' size

Burkalow (1945) had experimentally observed that, increase of density yields a smaller angle of repose. Doroblo (2005) found that the angle of repose becomes higher as the ratio of tank width to particle diameter is lowered. Zhou & Zhang (2009) observed that the angle of repose becomes larger with the increase of particles' diameter. These qualitative statements

are in good agreement with the findings of our numerical experiments, described in detail below.

In Figure 5.2 are shown collectively the tanks at different time instants of a tilting experiment with rate $2^\circ/\text{s}$. To facilitate the comparison, we superimpose three comparable results in one picture: the white particles correspond to material C, the blue to material B and the green to material A. Beside simply noting when the free surface flows, by using a simulation method we can also systematically study the dynamic behaviour of the materials in comparison to each other when their critical angle values are crossed.

Following the most common definition of angle of repose (IMO 2012a); and considering that the critical angle has been reached only when the free surface starts to continually flow like a fluid (thus excluding initial reordering of the free surface), it is observed that, Material C starts to flow at a lower angle than material B, which in turn flows earlier than material A. As indicated in Figure 5.2.d, up to about 11s the free surface of material A is practically unmovable. On the other hand, by then, the angle thresholds had already been exceeded for the other two materials (8.5 and 11 s after the tilting had begun, for material C and B respectively). Because of the tank scaling applied for this scenario, the difference in the critical angle values is likely to be owed to the difference of particle densities (the smaller the density, the larger the angle of repose).

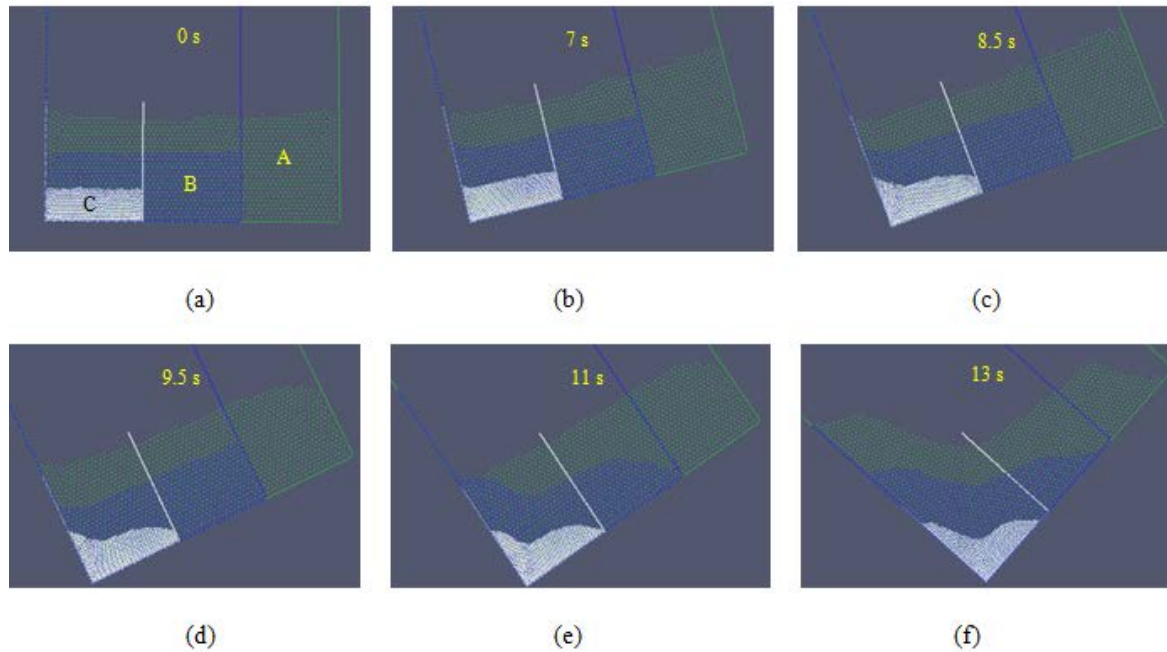


Figure 5.2 Snapshots of the state of the tanks as the tilting progresses. Different time instants of tank tilting, for material A, B and C in the case of the 2nd tank configuration.

By further examining Figure 5.2 it is deduced that, the transition from the static to the dynamic state is not performed in one step (i.e. as soon as a critical angle is exceeded) but the material exhibits, for a range of angles, “stick – slip” behaviour. Soon after the tilting begins, the free surface starts to flow (however at different instant for each material) but only for a while, until a small heap of particles is formed (Figure 5.2 b and c). This initial flow seems to obey the qualitative rule that, the lower density leads to a larger angle s . After heap formation, the free surface stops flowing. However, it starts to flow more massively when another critical angle has been reached. We interpret this angle as the one associated with the angle of repose.

5.2.2 Motion under horizontal (sway) and vertical (heave) excitation

As discussed in *Chapter 2*, a rich variety of interesting macroscopic phenomena such like convection, segregation and compaction appear when a rectangular tank, partly filled with granular material, is shaken horizontally. Among all these phenomena what interests us is that of fluidization; that is the transformation of materials behaviour after a critical point of a system's variable (most commonly excitation frequency and amplitude) has been reached, from solid like to fluid - like behaviour .

Identical tanks

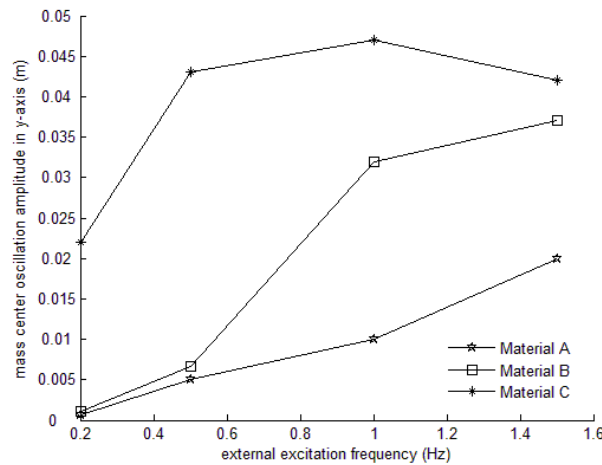


Figure 5.3 Steady oscillation amplitude of mass centre under horizontal oscillation.

The steady amplitude of oscillation performed by the centre of mass of material A (red), material B (green) and material C (blue), under horizontal harmonic oscillation with frequency ranging from 0.2 to 1.5 Hz , is presented in Figure 5.3. In Figure 5.4 is shown the horizontal and vertical movement of the mass centre for two different excitation frequencies (0.2 Hz is indicated with dashed and 1.5 Hz with solid line).

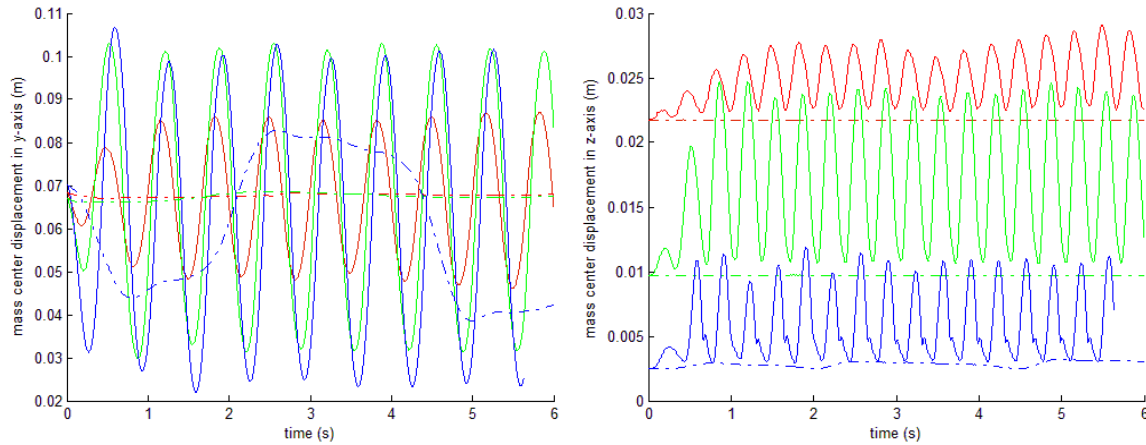


Figure 5.4 Horizontal (left) and vertical (right) movement of centre of mass of material A (red), B (green) and C (blue), under sway oscillation with two different excitation frequencies: i) 0.2 Hz (dashed line), ii) 1.5 Hz (solid line). Tank width is 19.2 cm .

As far as horizontal excitation is concerned, it is shown that for $f_2 = 0.2\text{ Hz}$ the mass centres of materials A and B appear as practically insensitive. This implies that the particles follow the movement of the tank. As the frequency is increased, the mass centre starts to oscillate both along the y and z axes, with a period close to that of the external excitations period in the y axis and close to half of it in the z axis. As expected, under high frequency external excitation the free surface moves almost like a fluid and patterns of high amplitude waves are noticed. In addition, the oscillation is definitely larger for material C, which thus appears to be more sensitive to external excitations. As indicated by Figure 5.3, even for a frequency as low as $f_2 = 0.2\text{ Hz}$, the granules of material C move, however in a rather intermittent pattern. This movement resembles a stick - slip phenomenon, at multi-particle level, rather than of a smooth oscillation.

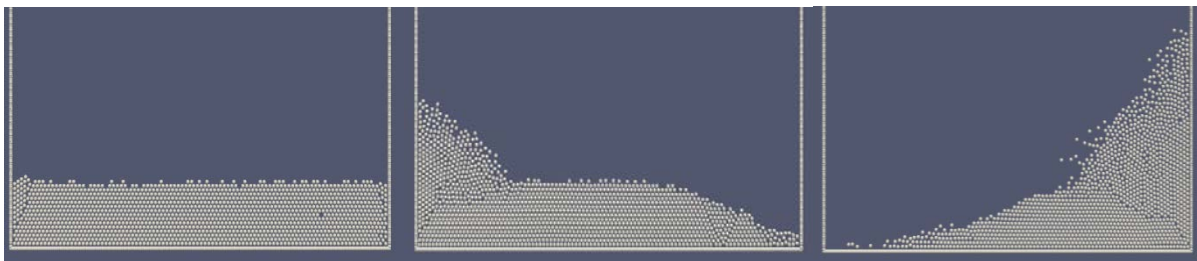


Figure 5.5 Time instants of motion of material B, for excitation frequency 1.5 Hz (horizontal). Left: beginning of the motion. Middle: time instant between the beginning and the instant of maximum amplitude. Right: instant right after the maximum amplitude is reached and the tank moves to the left for the first time.

Comparison in terms of mass centre oscillation amplitude between materials A, B and C shows that, the smaller diameter (and so the height of the material in the tank) corresponds to a lower resonance frequency. As a general remark, the decrease of particle diameter leads

(event though the density is increased) to easier material flow. Characteristic snapshots of the exhibited motion of material B are shown in Figure 5.5.

When the tank is vertically vibrated with low excitation frequency, the mass centre follows the tank's movement (Figure 5.6). However, for excitation frequency $f_3 = 1.5 \text{ Hz}$, B material's mass centre starts to oscillate along the z axis. Moreover, A and C materials' centres oscillate both along the y and z axes. Thus, a critical value of frequency exists, after which a wavy free surface occurs. It seems that this critical frequency depends not only on particle size, but also on particle density and on the tank - height - to - width ratio. The larger particles (for fixed material weight) are associated with larger oscillation amplitude (Figure 5.6). This is expected due to differences in the height – to-width ratio (Jaeger et al., 1996). It is notable that the mass centre did not remain at the middle of the tank but it was shifted along the y and z axes.

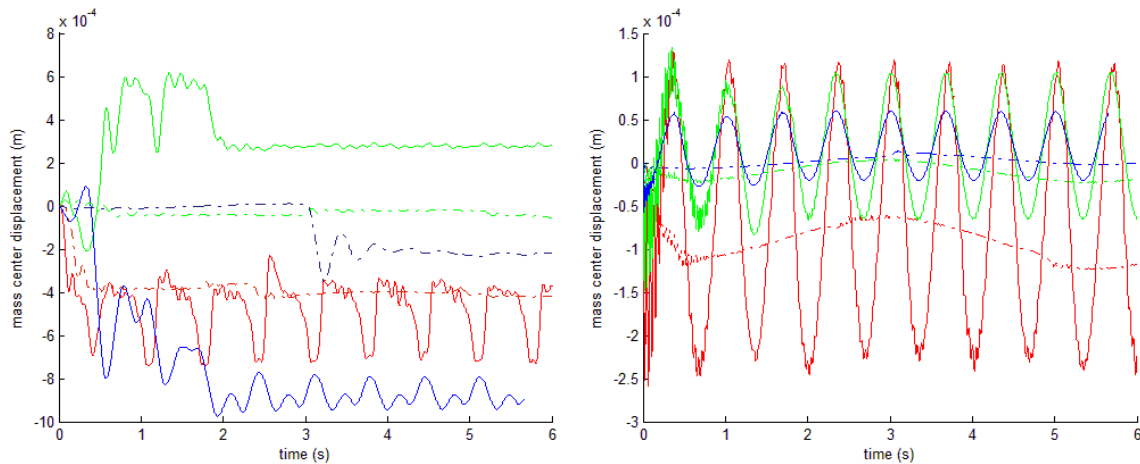


Figure 5.6 Horizontal (left) and vertical (right) movement of centre of mass of material A (red), B (green) and C (blue), under vertical oscillation in two different excitation frequencies: i) 0.2 Hz (dashed line), ii) 1.5 Hz (solid line). The tank width is fixed.

Geometrically similar tanks, scaled to particle size

In Figure 5.7 is presented the movement of the mass centre at a low and at a relatively high excitation frequency. The behaviour of the three materials is qualitatively similar when they are excited horizontally in harmonic manner. It is summarized as follows: for low frequencies the mass centre is practically insensitive to the excitation. By frequency's increase, the mass centre starts to oscillate in both the y and z axes, with a period whose ratio, in relation to excitation's period, is close to 1 for the y axis and close to $\frac{1}{2}$ for the z axis. The motion resembles that of a fluid. Material A begins to exhibit such fluid - like oscillation at a higher frequency than material B that, in turn, is less responsive than material C (Figure 5.8).

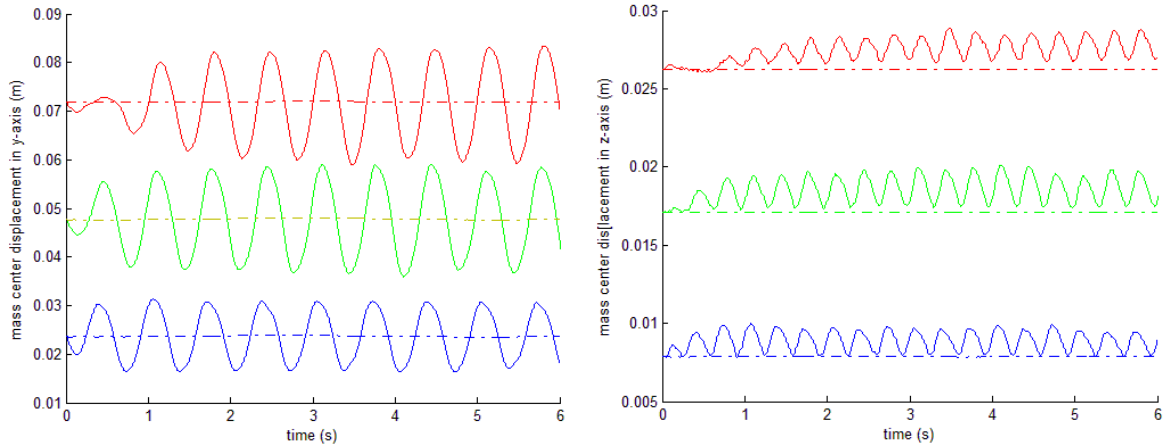


Figure 5.7 Horizontal (left) and vertical (right) movement of centre of mass of material A (red), B (green) and C (blue) under sway oscillation in two different excitation frequencies: i) 0.2 Hz (dashed line), ii) 1.5 Hz (solid line). Tank's height to width ratio value is fixed.

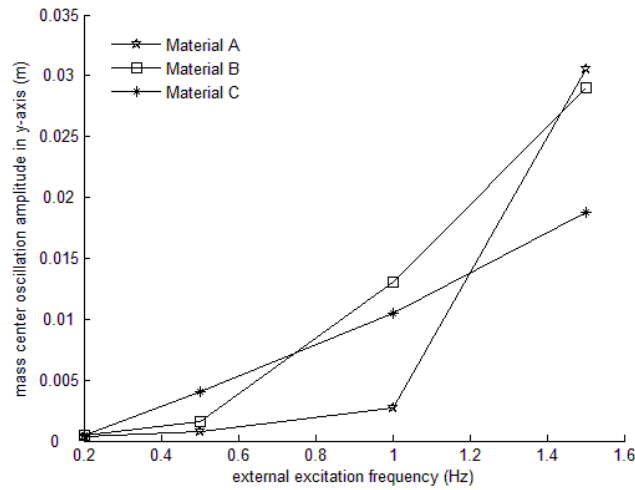


Figure 5.8 Steady oscillation amplitude of centre of mass under horizontal harmonic excitation.

Furthermore, the centre of mass of material C oscillates at a frequency closer to the excitation frequency, compared to that of A and B. A characteristic example of the exhibited motion of the particles is presented in Figure 5.9.

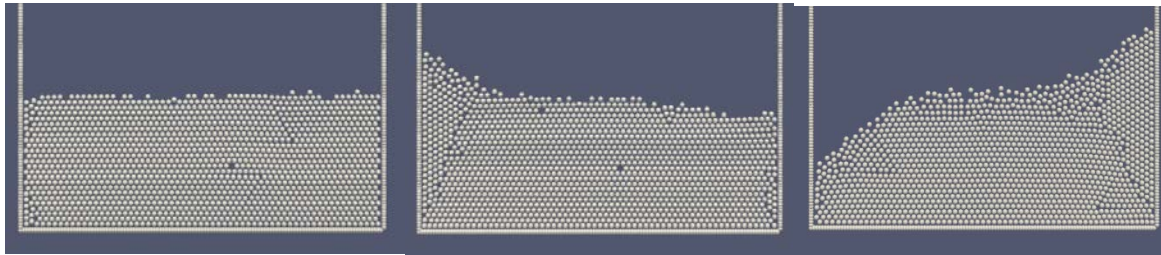


Figure 5.9 Status of particles of material B under horizontal harmonic excitation with frequency 1.5 Hz . Left: beginning of the motion. Middle: time instant between the beginning and the instant of maximum amplitude. Right: instant when the maximum amplitude is reached for the first time.

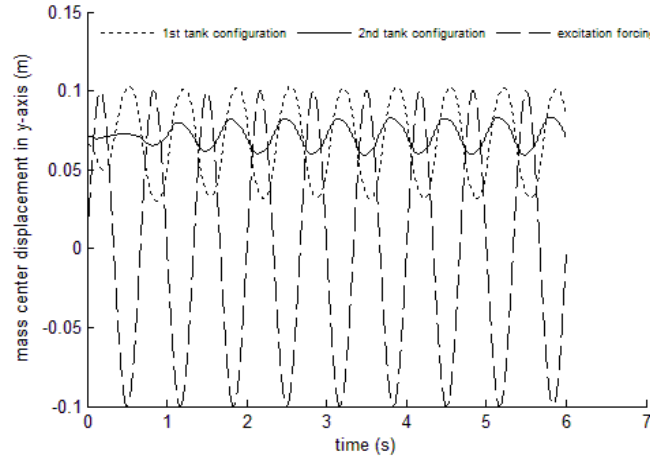


Figure 5.10 Behaviour of B material's centre of mass, for the two tank configurations (horizontal vibration, $f = 1.5 \text{ Hz}$). The phase between response and excitation appears to be almost 180° .

The oscillation amplitudes are in general quite similar, around the range of frequencies where each material begins to visibly oscillate. In lower excitation frequencies the oscillation of material C is larger than that of A or B. As frequency is raised, A's oscillation becomes slightly larger than B's or C's. The phase difference between excitation and centre of mass response is, at steady state, almost 180° (Figure 5.10).

In vertical oscillation of low to moderate frequency, however, (and similarly to what was observed in the tests with the first tank configuration), the mass centre appears practically fixed. For excitation frequency $f_3 = 1.5 \text{ Hz}$ and higher, the mass centre begins oscillation along both the y and z axes. This frequency threshold is practically invariant, irrespectively of particle size. However, the movement became smoother as particles' size was reduced

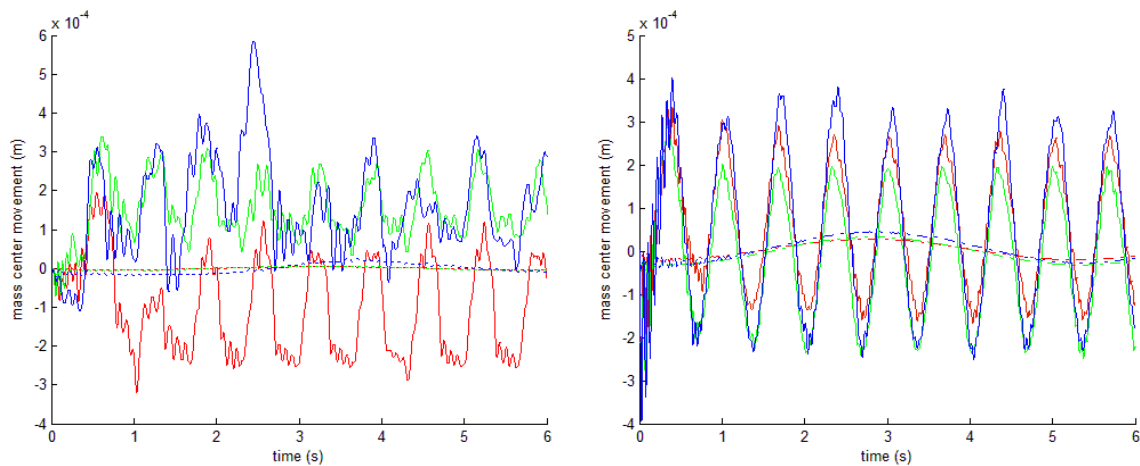


Figure 5.11 Horizontal (left) and vertical (right) movement of mass centre for material A (red), B (green) and C (blue) under vertical (heave) harmonic excitation with frequency: 0.2 Hz (dashed line); 1.5 Hz (solid line). The number of particles is the same while tanks are scaled to particle size.

In Figure 5.11 is shown the movement of the mass centre in two frequencies that lied well apart (0.2 and 1.5 Hz). The curves have been recentralized so that the initial mass centres fall on the axes origin.

5.3 Dependence of granular flow on system's configuration

Before taking the step towards a full material-ship-coupled-motion investigation, it is essential to perform a number of further preliminary studies based on prescribed tank excitation, in order to understand the sensitivity of behaviour upon certain choices of system configuration. Semi-static and fully dynamic conditions are considered. The tests are organized in three categories as described below:

Firstly, the formation of heaps on the free surface and the stick - slip behaviour, both linked to the initiation of cargo shift, are distinctive phenomena receiving detailed attention.

Then, behaviour is examined in slow tilting tests, with variation of the following factors:

a) Initial free surface configuration: as it is practically impossible to have an exactly identical free surface configuration at the beginning of different simulation runs, it is required to assess the quantitative effect that this factor bears on the tendency for cargo shifting.

b) Side-wall height: in contrast to IMO's (2012a) description of the tilting box test, where a tank with height just equal to material's depth is used, realistically the tank height should exceed material's depth. Thus, any difference in the pattern of shift due to the presence of high side walls has to be assessed.

c) Filling ratio: similarly to the case of liquid cargo, possible variations of material's flow due to material's depth need to be investigated.

d) Tilting rate: as it is intended to use this model for exploring the coupled ship - cargo motions in realistic scenarios, tilting rates different than those proposed in the context of the tilting box test (IMO 2012a), would be useful to be examined.

The final category of tests includes roll oscillations, for various locations of the roll centre. It is remarked that our attention is not restricted only on the prediction of the usual macroscopic parameters, like *the angle of repose* (that is the maximum slope angle of non-cohesive, i.e. freely-flowing, granular material), but it is set rather on understanding granular material behaviour when tilting is applied, before and after threshold parameter values are reached. From this work it is revealed that, whilst the angle of repose is the established critical parameter that is currently used for characterizing material behaviour, it should be

used in complementary manner to some other influential parameters, such as the “angle of collapse” or the initiation of stick-slip phenomena.

5.3.1 Dependence of angle of repose on initial free surface configuration

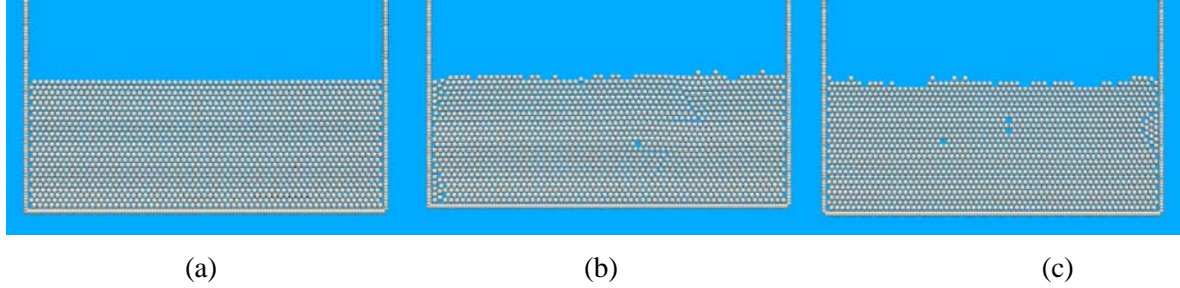


Figure 5.12 Three different initial free surface configurations: a) undisturbed free surface (left), b) slightly disturbed free surface (middle) and c) disturbed free surface (right).

We examined the effect on the apparent angle of repose for three different surface initializations. In the first, the particles are compacted to an extent that void spaces are minimized as much as possible and also the free surface is almost completely flat. The third case is a somehow naturally occurring free surface: the particles are thrown uniformly from a height and they are left to arrange themselves in the tank. The second is an in-between case which however can be associated with the reasonably smoothed surface requested by the regulations. Material B (with $d = 2 \text{ mm}$) was used and the tank width was 19.2 cm as in the previous section. The three considered initial surfaces are seen in Figure 5.12.

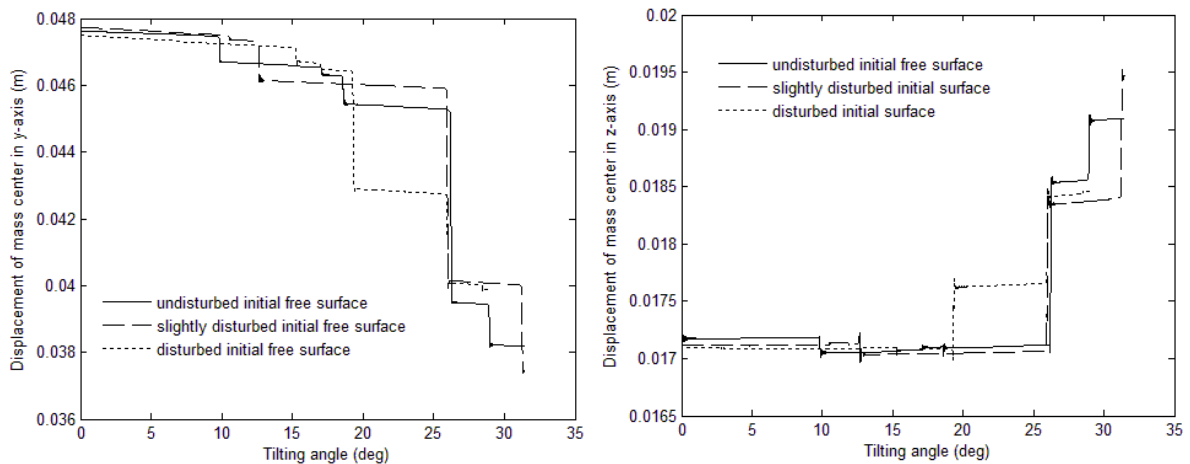


Figure 5.13 Displacement of B material's centre of mass, for tilting rate $0.3^\circ/\text{s}$. Comparative study for three different initializations. Sufficiently high tank walls are assumed.

The obtained movements of mass centres during the application of gradual tilting are summarized in Figure 5.13. The tilting rate was the recommended IMO value of $0.3^\circ/\text{s}$ (IMO 2012a). A stepped response is a remarkable feature of the behaviour. The largest step could

be associated with the angle of repose while earlier small steps are more relevant to heap formation. It is notable that the model predicts almost the same value for the angle of repose, irrespectively of the initial free surface configuration, although it is obvious that the material behaves in a very different way prior reaching this value. When the disturbed free surface configuration is considered, the initial heap formation is substantial and one might erroneously associate it with the angle of repose.

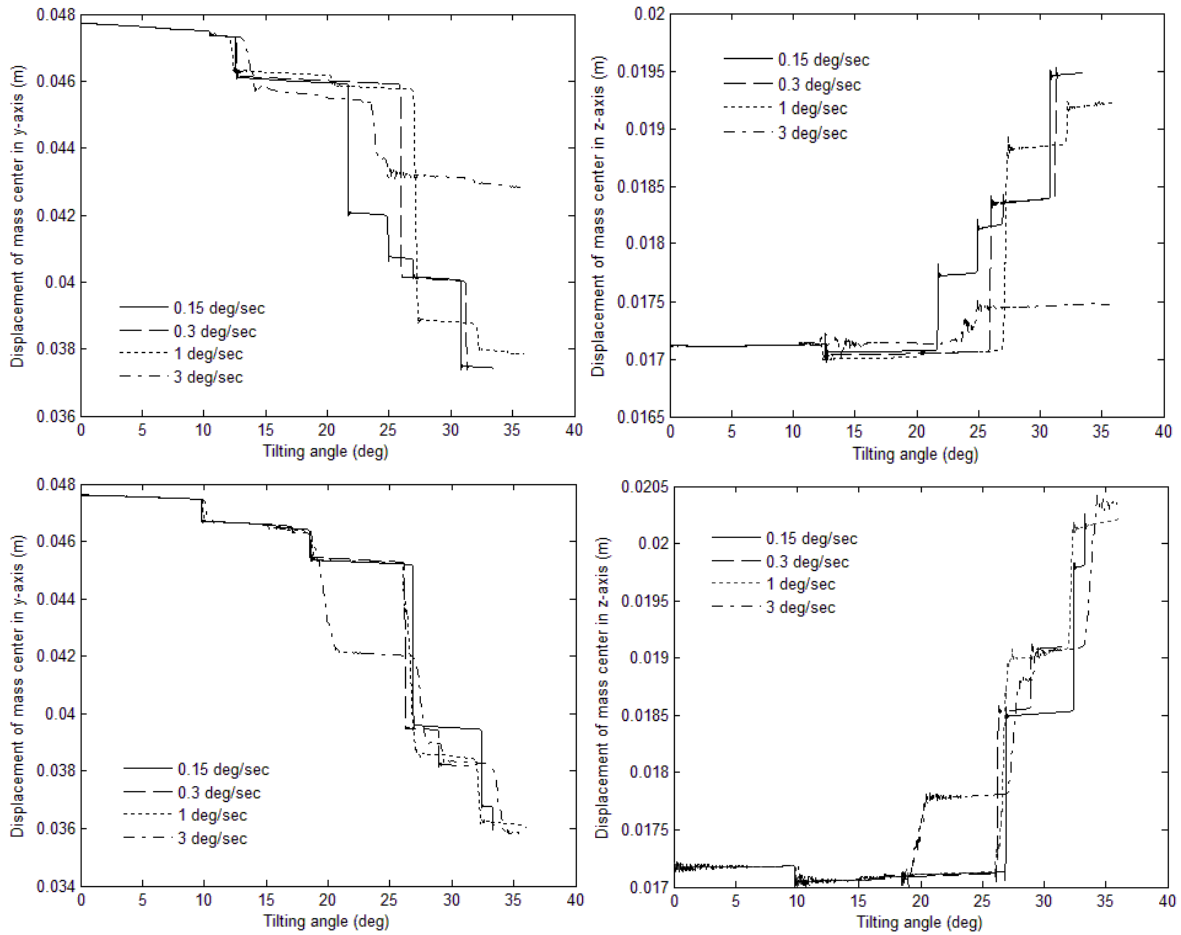


Figure 5.14 Displacement of B material's centre of mass, for different tilting rates when the free surface is a) slightly disturbed (upper), b) absolutely undisturbed (lower).

We were further interested to see how this picture is determined by the tilting rate. In Figure 5.14 can be seen the movement of the mass centre for the different tilting rates. If the free surface is initially in a slightly disturbed state (upper), then a faster tilting (eg $3^\circ/\text{s}$) leads to smoother movement of the particles; while lower rates lead to violent movement when the critical angle is approached. Furthermore, the lower tilting rate incurs smaller angle of repose; however the critical angle for heap formation seems to be almost the same for every rate. On the other hand, when the initial free surface is flat, the material behaves in the same manner, irrespectively of the tilting rate, if this is small enough ($0.15 - 1^\circ/\text{s}$). As a result,

almost the same angle of repose is predicted for the different tilting rates. What differs in this case is that, the initial heap is formed in two different time steps.

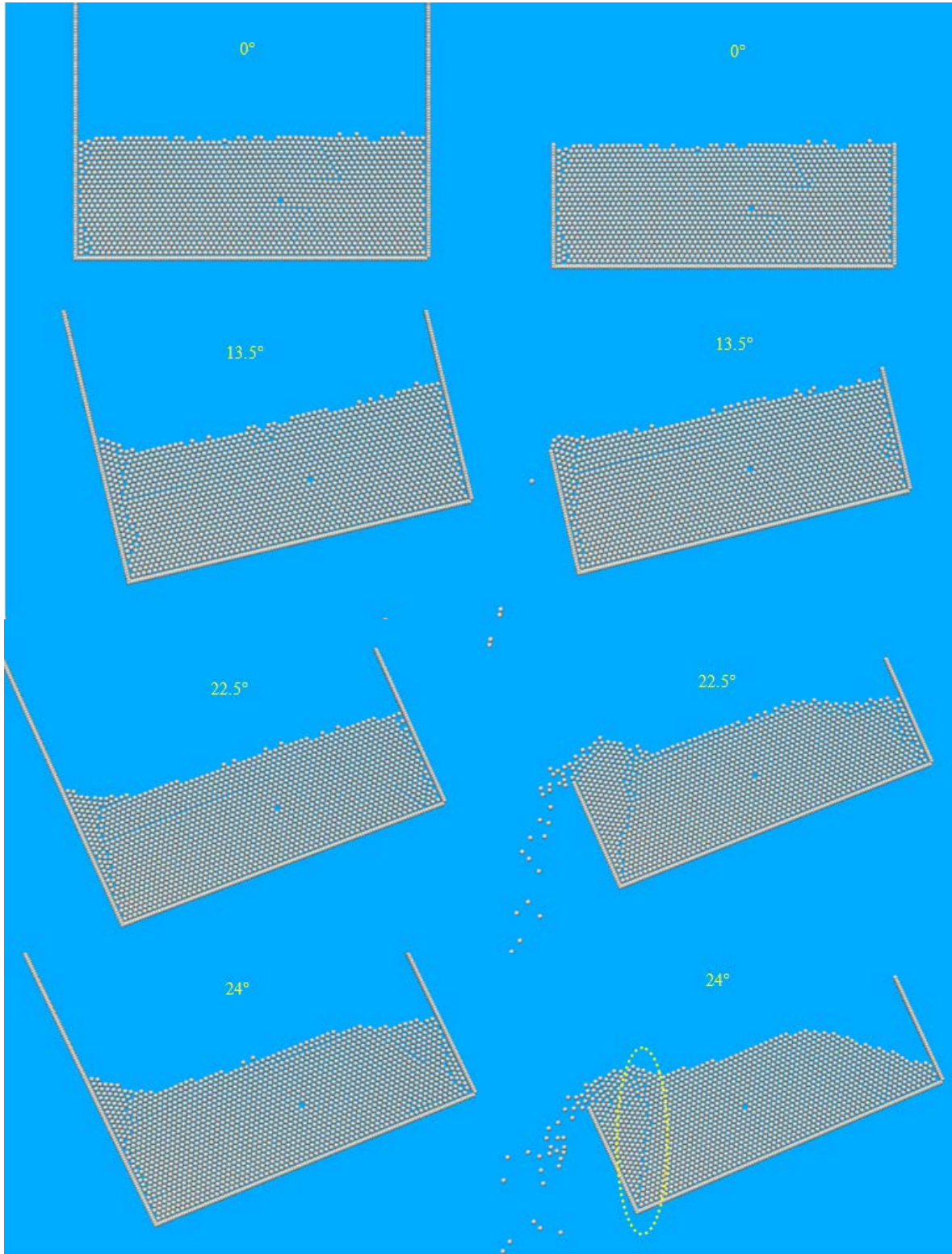


Figure 5.15 Snapshots of B material particles during tilting, with rate of rotation $3^\circ/\text{s}$, for two different cases: a) tank with sufficiently high-sided walls (left), b) tank with side wall height equal to material's height (right).

5.3.2 Dependence of angle of repose on side wall height

In a subsequent step, the exact tilting test described by IMO (2012a) was simulated, removing the side walls of the tank above the height covered by the particles, as shown in Figure 5.15 (right). We compared the behaviour of the particles in these two tanks before and after flow had begun. A slightly disturbed free surface configuration was used.

As evidenced from Figure 5.15, no matter whether the upper side walls are removed, there is still heap formation. The corresponding critical angle seems to be near to the one predicted for the tank with the higher sides. Qualitative differences in material behaviour between the two configurations appear, however, after that point. Further increase of tilt of the lower tank leads to a point where the free surface starts to flow and the material is spilled outside the tank. For that angle, the free surface of the high - sided tank does not appear moving yet and, by the time its angle of repose is reached, a lot of material has already left the tank with the low sides.

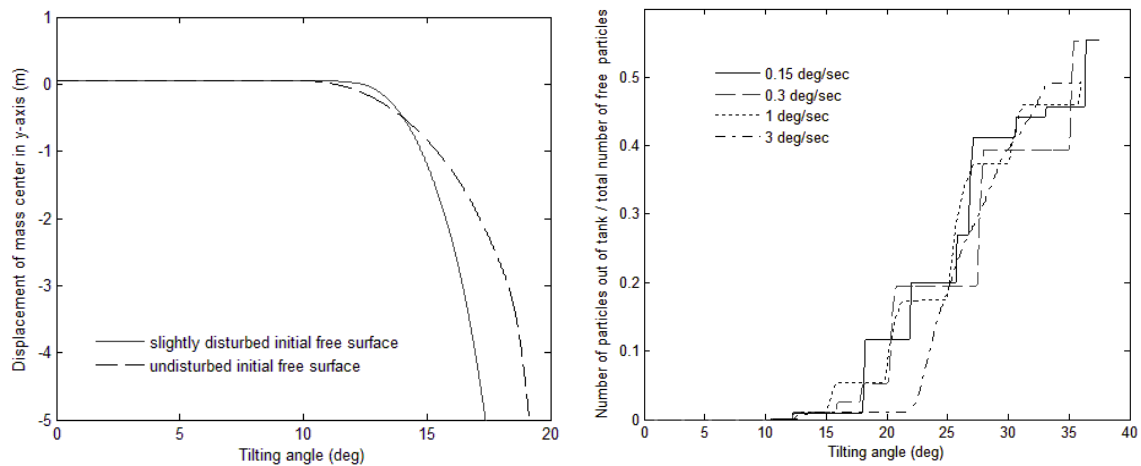


Figure 5.16 Behaviour of the particles during tilting with rate $0.3^\circ/\text{s}$ in the low-sided tank, monitored by two different macroscopic indices: a) Displacement of centre of mass (left) b) Ratio of particles leaving the tank to total number of free - to - move particles (right).

In Figure 5.16 is presented diagrammatically, in quantitative terms, the above discussed behaviour. Soon after spilling begins, the mass centre moves very far. However, because of spilled particles participation in the numerical calculation of the mass centre, no other useful information can be extracted from this diagram. Then, we calculated the number of spilled particles in every time step. In Figure 5.16 (right) is presented the ratio of the number of spilled particles to the total number of movable particles, for each time step during the tilting. Notably, for high tilting rates ($3^\circ/\text{s}$) the loss of particles appears to be continuous, while for low tilting rates it is a stepped process. There is an angle after which particles leave the tank,

nonetheless the escape rate is low and only a small percentage (almost 2%) has left until a further critical angle is reached where the escape rate shows a sharp upturn. We associate this phenomenon with the definition of the angle of repose. Comparison of this value against the one predicted for the corresponding case where the tank had high sides, indicates that, for the few numerical experiments that we performed, it presents a lead that is between 1.7° and 6.8° , depending on the tilting rate.

5.3.3 Slow tilting of tanks with different filling

A new series of numerical tests was started, in an attempt to understand the dependence of system's behaviour upon tank's filling ratio. A tank with 60 cm width, partly filled with spherical grains of Material D, was selected. In addition, three different tilting rates (0.3, 0.5 and 1 deg/s) were successively applied. The aim was to identify possible variations in the prediction of the angle of repose and any connections with phenomena of dynamic behaviour taking place at the micro scale of the particles (e.g. the difference in the stick-slip behaviour etc).

In the case of liquid cargo, the flow at resonant condition is different for shallow, intermediate and finite liquid depth. According to Faltinsen & Timokha (2009) shallow depth is defined as $h/l < 0.1$, intermediate as $0.1 < h/l < 0.25$ and "finite" as $0.25 < h/l < 1$. The boundaries of course are not strict. In what follows we adopted the same terminology for material depths. It has to be noted though that, in contrast to a multimodal approach applied for the prediction of fluid motion dynamics (eg Faltinsen & Timokha 2009), our particle-based methodology is capable of handling all kind of material depths without any change in the mathematical model.

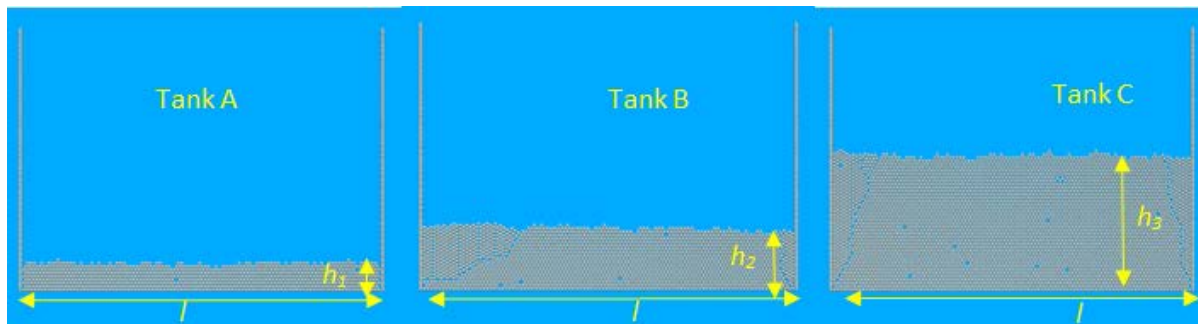


Figure 5.17 Three similar tanks were used for the numerical experiments. While the tank length is the same, material's height inside the tank is varied, leading thus to different filling ratios.

In Figure 5.17 are illustrated the three different filling ratios that we have set under investigation. In tank A, the filling ratio was chosen such that, material's depth in the tank to

be characterized as shallow $h_1/l_1 \approx 0.075$). A filling ratio $h_2/l_2 \approx 0.15$ was chosen for tank B, so that the latter to represent an intermediate depth case; while, for tank C, a ratio $h_3/l_3 \approx 0.37$ was set, to have a finite material depth case.

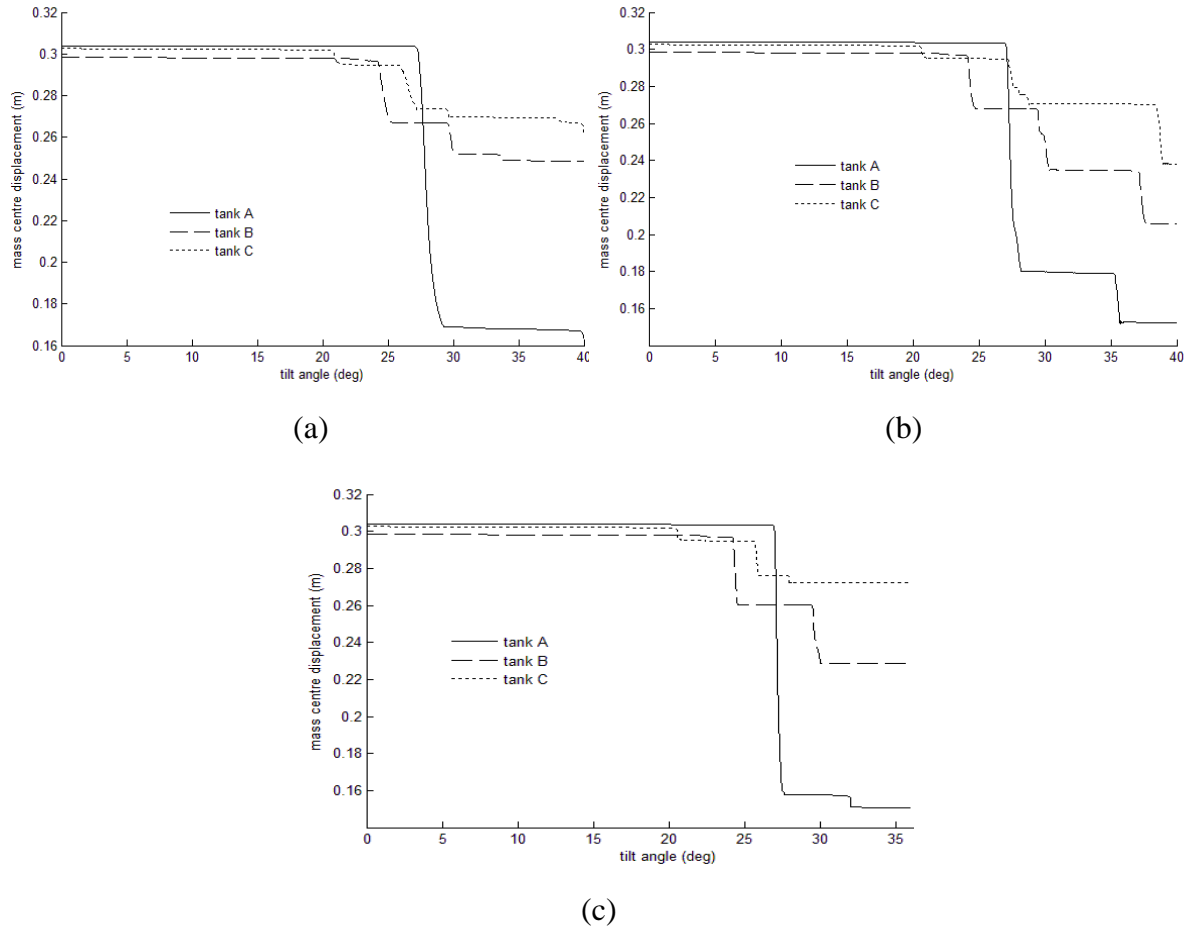


Figure 5.18 Mass centre displacement for the three tanks, under different tilting rates: a) 1 deg/s, b) 0.5 deg/s, c) 0.3 deg/s.

In Figure 5.18 are presented some characteristic results for the mass centre of the material inside the three tanks, for the three tilting rates (1, 0.5 and 0.3 deg/s, respectively). Visual inspection of material inside *tank C* indicated that, from the beginning of the motion and till the critical angle is reached, the material remains stable, in the sense that it does not move at all (except some minor motion occurring in free surface caused by initial rearrangement of the particles). After the critical angle has been reached, the material starts flowing almost like a fluid and this phenomenon is repeated, in a stick-slip manner, as the angle is increased further. However, only the upper layers of the material play a role in the flow while the bottom part stays unchanged (stable solid behaviour). This conclusion applies for the first and the second critical angle. A comparison between material behaviour inside *tank C* and inside the same tank but with larger filling ratio, points out that the same amount of material (almost

fifteen layers) avalanches each time, whatever the filling ratio. In contrast, inspection of material inside *tank A* after the critical angle has been reached indicated that the whole body of the material participates the motion. At the end of the motion the material has been displaced in such a manner that, only the down left corner of the tank is filled. For intermediate depths the material behaves in a similar manner with that of shallow depth, tending to behave like one of finite depth as filling ratio increases. That is the lower layers tend to stay motionless but due to friction effects they finally participate the motion.

Thus, three were the key findings of this investigation:

a. Larger filling ratio leads to smaller angle of repose. Specifically, angles of repose close to 21, 24 and 27 *deg* were predicted for finite, intermediate and shallow depth, respectively. The change in the angle is significant (almost 3 *deg* between *tanks A-B* and *B-C* and 6 *deg* between *tanks A-C*); thus the filling ratio has to be taken into account whenever such experiments take place. In a step further, we investigated the predicted angle of repose for higher filling ratios (0.5, 0.4 and 0.6). The results confirm that, below the intermediate filling range, one can safely predict an almost constant angle of repose (close to 21 *deg* with 5% deviation) for different material depths. On the other hand, for filling ratios inside the intermediate and shallow depth regions a different value of the angle of repose, ranging between 30 and 22 *deg*, was predicted each time a numerical experiment was realised.

b. The stick-slip phenomenon is more distinguishable (in the sense that the steps of mass centre displacement take place in a more homogenous manner) when intermediate depths are considered. For *tank A* and *tank C*, the stick-slip phenomenon is a rather minor one, with a single avalanching realised in a big shift. For *tank B* there is not a clearly distinguishable point of shift, the material behaving in a similar way for a multiplicity of successive critical angles. An explanation for the difference between *tanks A, C* on the one hand and *tank B* on the other, is that, for *tanks A* and *C* only a few particle layers participated in the flow; while for *tank B* practically the whole body moved inside the tank.

c. The angle of repose does not seem to depend strongly on the tilting rate (of course, within the relatively low rates applied in the tests). Some small variations occur nevertheless, tending to predict, one would have anticipated, slightly larger angles for larger tilting rates. This leads to the general suggestion that, irrespectively of the depth of material considered (shallow, intermediate or finite) for low tilting rates (close to 0.3 *deg/s*) the predicted angle of repose is almost fixed within a deviation up to about 7%.

5.3.4 Investigation of material's hysteretic behaviour

Going one step further, we investigated material's "hysteresis". Right after the angle of 40 deg has been reached, the tilting rate was reversed (depending on the scenario, from 0.3, 0.5 and 1 deg/s to its negative equivalent). In this way the tank started to rotate in the opposite direction (clockwise in our case) until it returned to its initial horizontal position (0 deg).

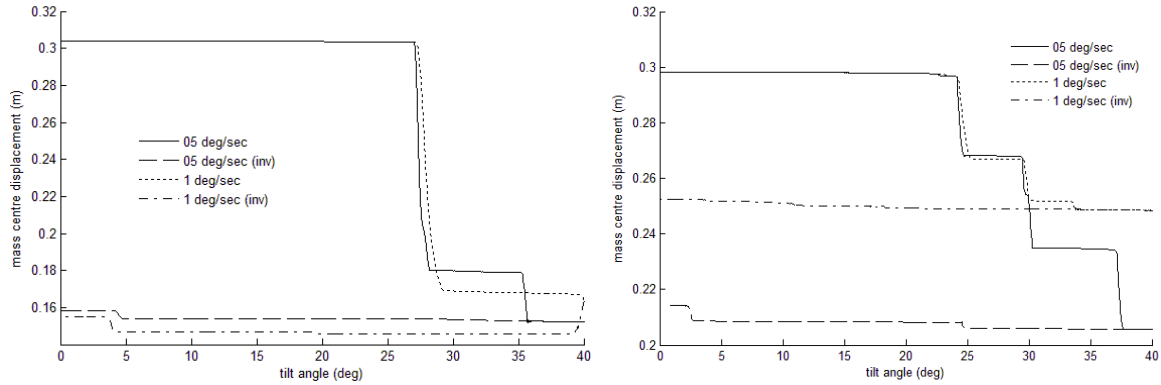


Figure 5.19 Hysteretic behaviour of material inside tank A (left) and B (right)

In Figure 5.19 are presented cases of material's mass centre displacement inside *tank A* (left) and *B* (right), for several tilting rates. Moreover, in Figure 5.20 appear time-shots targeting the final material position for the same tanks, respectively. It is apparent that significant hysteresis is present, in the sense that the material displays a very small tendency for returning to its initial state as the tank is brought back to the upright position, at the end almost sustaining the position it had when tilting angle of 40° was reached.

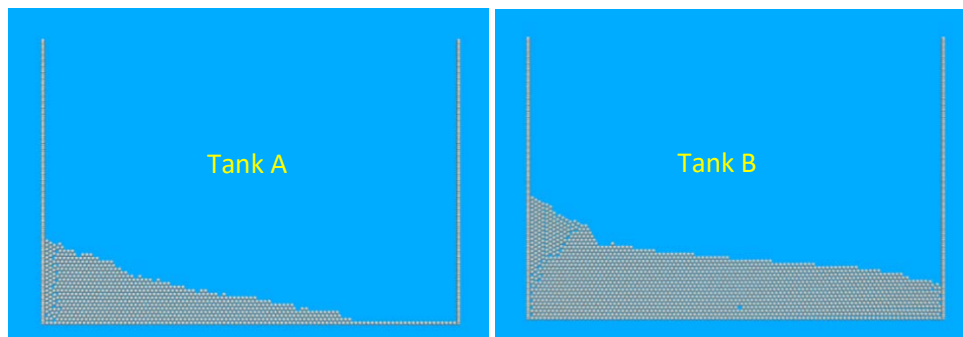


Figure 5.20 Time shots from final material position after reverse motion with tilting rate -1 deg/s .

To investigate the hysteretic behaviour further, the experiment was repeated, this time with the tank's tilting direction switched from anti-clockwise to clockwise right after material collapse occurred (e.g. at 24 degrees for tank B). In Figure 5.21 is shown the material's mass centre's displacement when using *tank A*, for 1 deg/s tilting rate. It is confirmed that, as soon

as the material settled to its final position after the collapse, it stays there despite the opposite rotational motion applied to the tank.

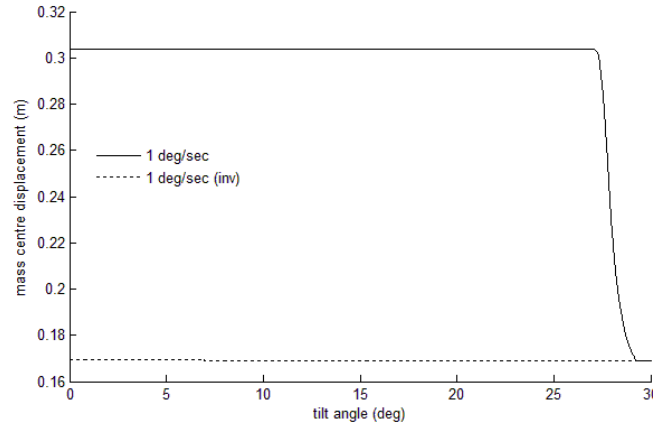


Figure 5.21 Mass centre's displacement in tank A for 1 *deg/s* tilting rate. The tank alters its tilting rate from anticlockwise to clockwise right after material collapse occurs. It is shown that despite the opposite rotational motion, material inside the tank settled to its final position after the collapse.

5.3.5 Granular material flow depending on the position of the roll centre

In order to investigate variations in the cargo's dynamic response depending on the distance of the roll point from the bottom of the tank, four sets of different numerical tests were performed. Material D was selected for this test. The excitation frequency range was 0 - 1.3 *Hz* and the imposed roll amplitude was between 0 and 30 *deg*.

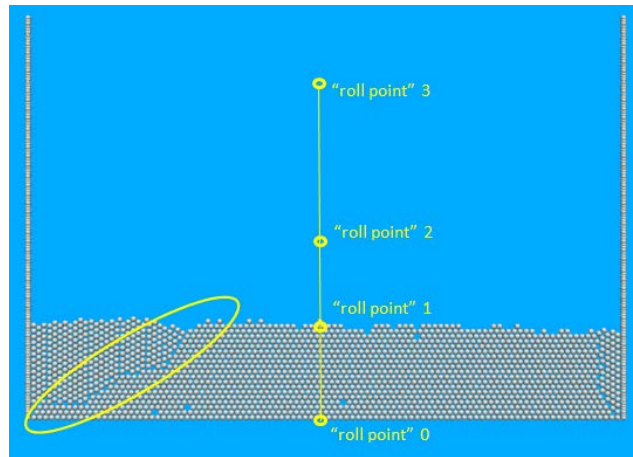


Figure 5.22 Initial separated material part.

All roll points were placed on the perpendicular line crossing tank's bottom through its middle point. In the first test, the vertical distance of "roll point 0" from the bottom was 0 m (the "roll point 0" was just in the middle of tank's bottom). In the second, the distance was 10 *cm* ("roll point 1"), in the third 20 *cm* ("roll point 2") and in the fourth 50 *cm* ("roll point 3"). The locations of the roll points are shown in Figure 5.22. A qualitative description of the

observed material behaviour is given below, side-by-side with a more quantitative analysis deriving from the monitoring of the material's centre of mass:

a. For small excitation amplitudes (up to 10 *deg* roll) material's behaviour was found to be independent of the distance, from tank bottom, of the roll point.

b. Increase of excitation amplitude (to 20 *deg*) leads however to different material behaviour. For roll point 0 and excitation frequency 0.7 *Hz*, even though the material remains motionless and at steady state, it rearranges itself during the transition time in such a manner that, the initially separated part (circled in Figure 5.22) disappears. For excitation frequency 1.1 *Hz*, the upper layers of material start moving periodically. Two surfing waves (quite small however) appear at the upper corners of the material (free surface corners). In Figure 5.23 is presented the displacement of the mass centre for every case (roll points 0 to 3) considered, for excitation frequency 1.3 *Hz*. Concerning roll point 1, a small oscillation has been noted. Whereas for roll points 1 and 2, the material remained motionless. For roll point 3 the oscillation of mass centre becomes very large (five times larger than the one around roll point 0). The frequency of response is very close to the excitation frequency in both cases.

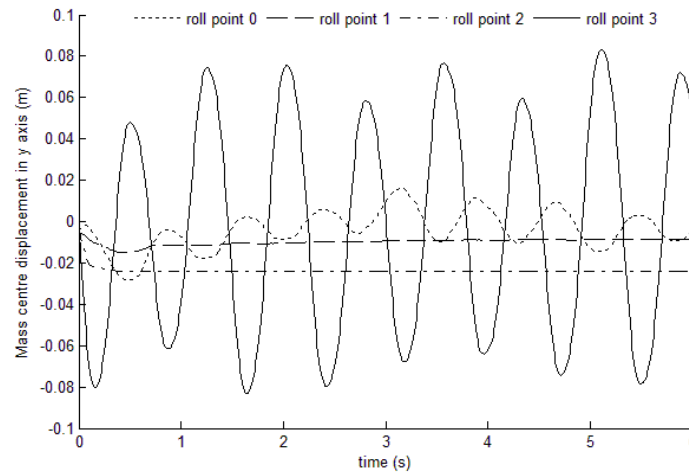


Figure 5.23 Displacement of material's centre of mass, for various roll centres. The excitation frequency is 1.3 *Hz* and the amplitude is 20 *deg*.

c. For large enough excitation amplitude (30 *deg*) the material behaves in a different way. This time, even for excitation frequency as low as 0.1 *Hz*, the material starts to move almost like a fluid, right after the angle of the tank exceeds the computed angle of repose of the material (24 *deg*). In reference to roll point 0, after the initial movement, the material remains stack at the one side of the tank, till a critical angle has been reached where a violent motion is triggered: the material shifts with high velocity from the one side of the tank to the other and this mode of motion is periodically repeated. As the excitation frequency is

increased, the phenomenon becomes stronger. In particular, for 0.5 Hz , a small jet appears after the final fall of material. The described violent motion disappears however when the excitation frequency surpasses 0.5 Hz . For these frequency values, only the upper layers of the material participate in the periodic motion. For excitation frequency above 0.9 Hz , the phenomenon is less violent but a number of particles move almost like a gas above the material. For roll points 1 and 2, the material behaves in a way similar to that experienced for rotations around roll point 0, although behaviour is actually a lot smoother. When it comes to roll point 3, for excitation frequencies between 0.1 and 0.9 Hz , the behaviour is observed to be similar to that found for the other roll centres. However, for higher frequencies it behaves like a fluid with large response amplitude. All material layers participate in the motion. The phenomenon is intensified with the increase of the excitation frequency. In Figure 5.24 is illustrated, in a more quantitative manner, the different behaviour exhibited at low and high excitation frequency. Once again, the response frequency is close to the external one. The flat step-like form of the curve in the upper figure (0.3 Hz) corresponds to the fact that, for a portion of the cycle, some material remains relatively stable at the one side, before falling abruptly to the other; and so forth.

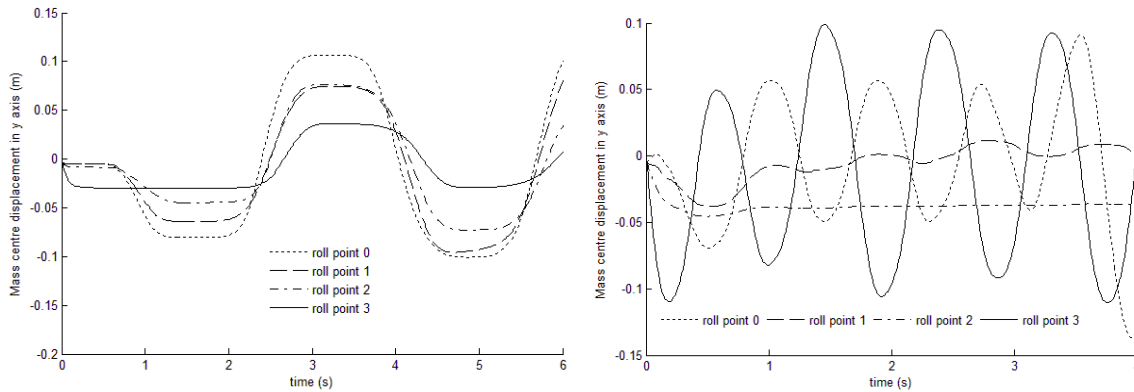


Figure 5.24 Material's behaviour for different roll centres. The excitation frequency is 0.3 (left) and 1.3 (down) Hz while the amplitude is 30 deg .

It is apparent thus that, a larger distance of the roll centre from the tank bottom has, as one would have expected, a mitigating effect on the exhibited material dynamics; hence the behaviour of material when the roll centre 0 is used is smoother than that when roll centres 1, 2 and (partly) 3. In contrast, when the distance is large enough for the tank to exhibit substantial motions mostly in the sway direction and to lesser extend in heave (Figure 5.25), the particles experience higher acceleration giving rise to a “fluid-like” material behaviour.

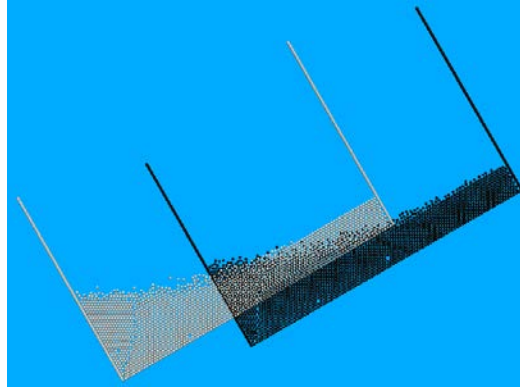


Figure 5.25 Tank's displacement (30 deg and 0.1 Hz) when rollpoint 0 (white) and 3 (black) are considered.

5.4 Scaling effects

Here, geometrically similar containers of three different sizes are investigated, assuming horizontal harmonic vibration of the container. In another type of test is investigated the avalanching phenomenon of the free surface during slow tilting, in containers of different size. Specifically:

We consider a mobile, rectangular, smooth and rigid tank, filled partly by dry granular material. The origin of the coordinate system is placed at the left side of tank's bottom. Tank is free to move in any possible direction, depending on the desired excitation. Following Schafer et al (1996) and basically what is a standard practice, our tank walls are built of particles, to model surface roughness. Motion of the walls is prescribed and it can be periodic or random. Cellulose acetate spheres with diameter 3 mm were used. Table 5.2 summarizes the material properties.

Table 5.2 Numerical values for particle coefficients.

Parameter	Value	Parameter	Value
Diameter (mm)	3	Young modulus (N/m^2)	3.2×10^9
Density (gr/cm^3)	1.319	Coulomb friction	0.25
Poisson ratio	0.28	Shear damping ($N s/m$)	20

* Cellulose acetate particles

Three different tank configurations (tank A, B and C in Figure 5.26) are employed in order to investigate how the scaling affects the dynamic behaviour of the material inside the tank. Considered tank widths are: $l_1 = 6 \text{ cm}$ for tank A, $l_2 = 15 \text{ cm}$ for tank B; and $l_3 = 18 \text{ cm}$ for tank C. The height-to-width-ratio has been fixed ($h/l = 0.256$).

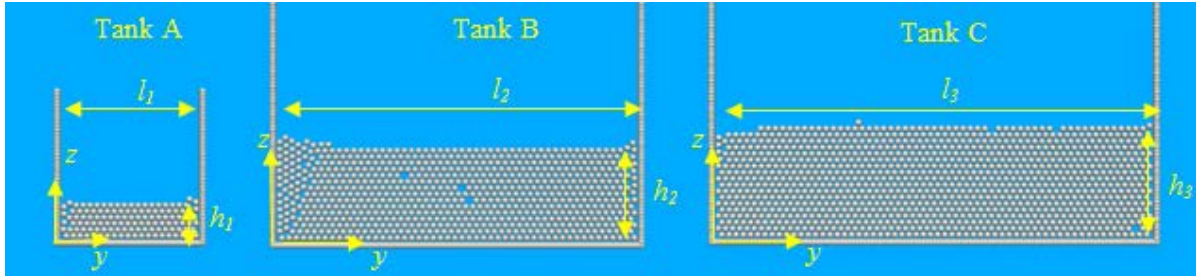


Figure 5.26 The height-to-width-ratio h_i/l_i , ($1 \leq i \leq 3$) is fixed to a constant value.

Two different simulation results, per tank configuration, are produced. Firstly, we monitored the movement of the mass-centre for various pure harmonic sway tank oscillations. A wide range of excitation frequencies and amplitudes is investigated (0 - 3.7 Hz and 0 - 4 cm, respectively). Based on these simulations, diagrams in comparative form are created depicting material's dynamic behaviour in the three tanks. Furthermore, to determine whether the angle of repose is affected by the scaling, we have examined the response of the free surface by monitoring the initiation of the avalanching phenomenon.

5.4.1 Horizontal motion under sway excitation

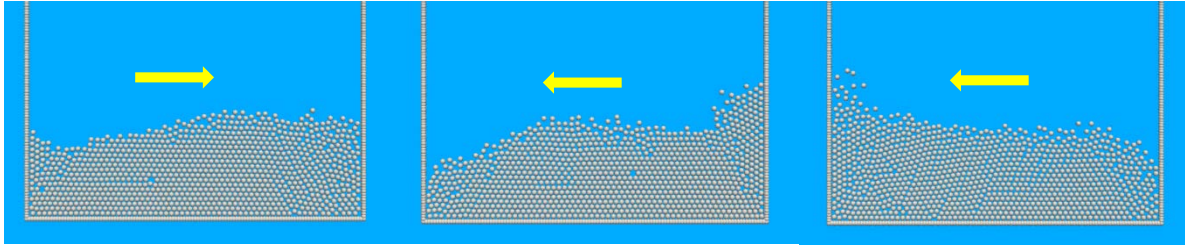


Figure 5.27 Motion of material inside tank C (excitation frequency 1.5 Hz). Left: time instant little after the beginning of the motion; middle: time instant when the maximum amplitude is reached for the first time; right: time instant after tank crosses the initial point for the first time.

In Figure 5.27 are presented time instants of material's motion inside tank C (large) for a case where this critical point has been exceeded. In order to investigate differences between the dynamic behaviour of the same material inside different tanks, we performed a great number of simulations for each tank configuration varying the excitation frequency and amplitude. The displacement of material's mass-centre both in y and z -axis were captured and graphically presented. In Figure 5.28 material's mass-centre displacement inside tank C, for different excitation frequency and excitation amplitude 4 cm is depicted. There is a critical frequency value close to 1.2 Hz after which the material starts to behave almost like a fluid.

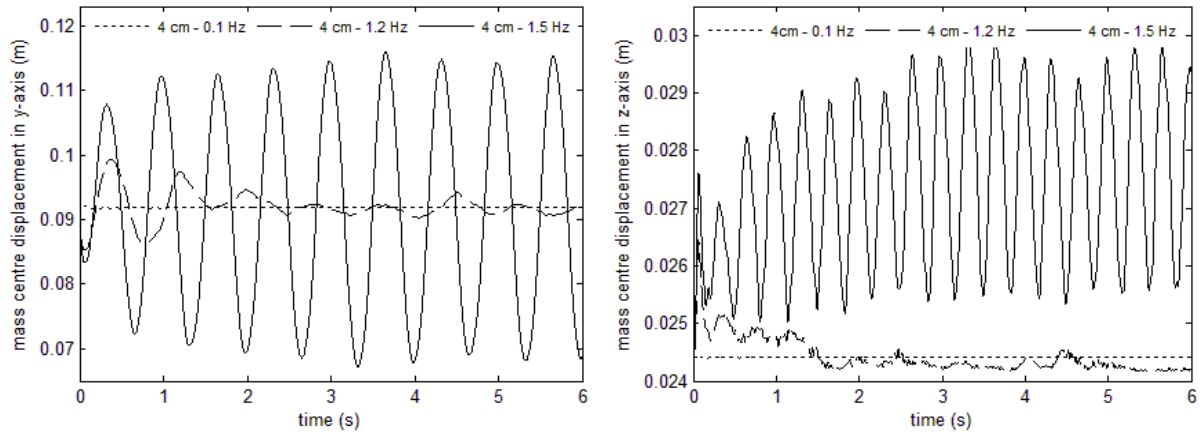


Figure 5.28 Horizontal (left) and vertical (right) movement of material's mass-centre inside tank C under sway oscillation for three different excitation frequencies (excitation amplitude is 4 cm).

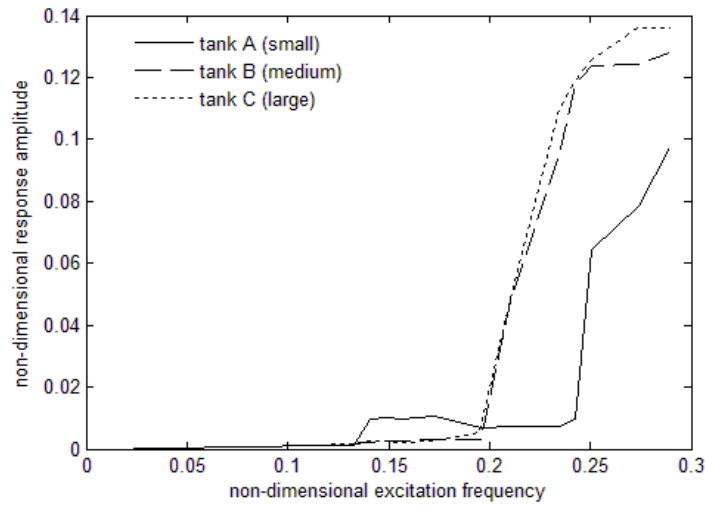


Figure 5.29 Mass centre response for various excitation frequencies.

By proceeding in a similar manner for more than 300 simulations (for the three tank configurations) we are able to demonstrate the dynamic behaviour of the material inside the tank in the frequency region near to the critical (bifurcating) point. In Figure 5.29 is shown the mass-centre response amplitude y'_{0i} for various frequencies ω'_i . The prime indicates a non-dimensionalised quantity ($y'_{0i} = y_{0i}/l_i$, $\omega'_i = \omega_i \sqrt{l_i/g}$). The excitation amplitude n'_i ($n'_i = n_i/l_i$) had a fixed value for all cases.

For low frequencies the material moves with the tank; but for higher values it starts to flow. What is interesting is that, A tank's bifurcating point appears at a much higher frequency than that of the other two tanks. Another interesting observation is that, in the A tank there is a second critical point where some limited avalanching is realised, located at lower frequency. The mass-centre shift, realised between these two critical points, is relatively small. These observations inspire the suggestion that, there must be a critical tank

beam, after which the scaling effect becomes insignificant since the material behaves in an almost identical manner irrespectively of tank size. This difference is believed to be due to the fact that friction plays a more crucial role when the size is small and the particles are few.

5.4.2 Slow tilting of the tank – identification of angle of repose

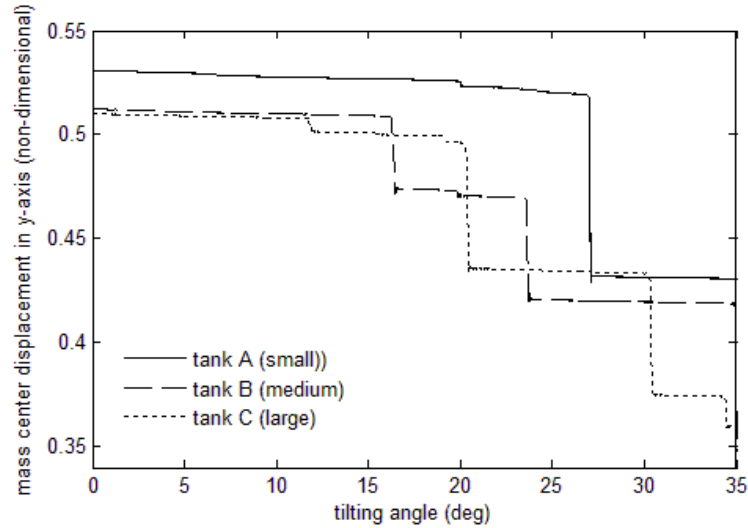


Figure 5.30 Displacement of centre of mass for a tilting rate $0.3^\circ/\text{s}$. Comparative study for three tank configurations. High tank walls are assumed.

In Figure 5.30 is presented the displacement of the centre of mass along the *y-axis*, in relation to the tilting angle, for the three tank configurations. A slight offset of the initial centre of mass is noted for all three tanks, owed to some slight free surface disorder which is a natural occurrence and thus no effort was made for removing it. As the tilting begins, and up to about an angle of 15° , the particles on the surface show a tendency to be realigned. Also, a small heap is formed adjacently to the wall furthest from the rotation centre (this matter is investigated further in the next chapter). Thereafter, the material behaves like a solid, soon however another critical angle is reached where, suddenly, the material behaves almost like a fluid. It returns again to a solid - like behaviour, till the next critical angle is reached. Hence, a stick-slip phenomenon is the dominant feature of the behaviour. In the two smaller tanks the material exhibited a stepped (staircase like) transition. We have identified as angle of repose the first critical angle, although this is a matter that should be further considered.

Following Lee & Hermann (1993) we repeated each numerical experiment 12 times, for slightly different initial free surface configurations. Each angle value appearing in Figure 5.31 is the mean angle over the 12 experiments and the error is the mean square sample-to-sample fluctuation. As noticed, there is a slight dependence of angle of repose on tank's

beam, in the sense that the smaller the tank the larger the predicted value. Additional tests have been performed with much wider tanks. It is observed that beyond a critical beam, the predicted angles of repose are practically the same.

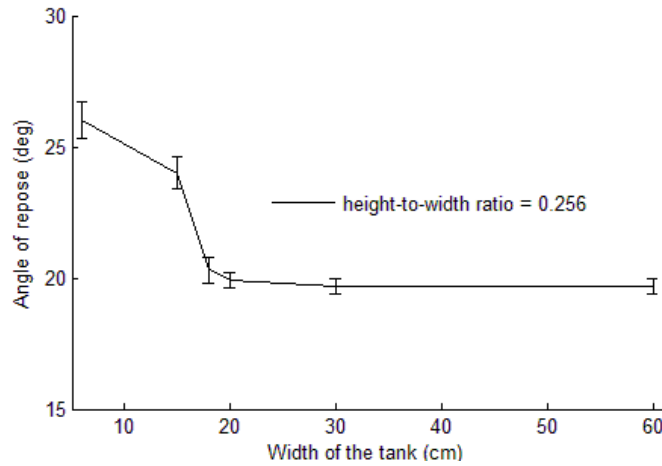


Figure 5.31 The angle of repose against the width of the tank for constant height-to-width ratio.

5.5 Concluding remarks

The Molecular Dynamics method was applied for studying stick - slip phenomena in the behaviour of excited granular matter, for the purpose of gradually building up capability for simulating the motions of bulky cargos transported in ship holds. Two series of tests were performed for exploring the dependence of the granular flow upon particles' properties and system configuration. In the first series, the participating materials consisted of spherical monosized particles with diameters 1, 2 and 3 mm, having properties (e.g. density) relevant to common bulky ship cargos. The considered excitations were: a) slow or fast tilting; b) horizontal or vertical harmonic vibration. It was noticed that the material with the smallest particle size and the highest density tended to flow more easily. Some dependence of system's macroscopic behaviour (resulting in different values of critical angles) from free surface's initial state was noticed. This matter deserves a dedicated statistical study in the future.

In the second series, slow tilting experiments were performed, varying: a) the initial free surface configuration, b) the side walls height, c) the filling ratio and d) the tilting rate. Also, roll motion experiments were performed. When side tank walls were as low as material's height, flow was enacted earlier, in comparison to a similar phenomenon occurring in a tank with high side walls. This difference in angle was found to be between 1.7 to 6.8 deg, depending on the tilting rate. Another interesting observation was that, a small heap formation seems occurring quite consistently, at an angle of tilt that precedes the angle of

repose. Such a formation seems quite independent of the tilting rate and the tank wall height. Also, a larger filling ratio leads to a lower angle of repose, in the sense that, the material with the largest filling ratio tends to flow more easily. Some dependence of the stick-slip realisation upon the filling ratio was also observed. Also, the material is more sensitive to roll excitations as the distance of roll point from tank's bottom decreases.

Lastly, the rather obscure, up to now, problem of scaling of granular matter was addressed, focusing on the transition from semi-static to dynamic behaviour, by considering three geometrically similar small size containers. Cellulose acetate spheres with 3 *mm* diameter were selected for these tests. The tanks were successively i) vibrated in sway assuming prescribed harmonic external excitation and ii) tilted with low tilting rates. As far as the horizontal vibration is concerned, the target was the initiation of the phenomenon of fluidization. Observations lead to the conjecture that, a critical container size exists beyond which the material behaves in an almost identical manner irrespectively of container's size. Friction appears to play a greater role in the smaller sizes, hence the observed difference in the dynamic behaviour of the smaller from the larger tanks. Furthermore, rotation of the three tanks at a low rate (0.3 *deg/s*), indicated that, the critical angle where avalanching of material's free surface appears, is dependent on tank's width. Specifically, the smaller tank leads to later beginning of avalanching. If however the tank's beam is sufficiently large, avalanching begins at practically the same value, irrespectively of tank size.

It is remarked that that the investigations described here are purely numerical and whilst verification and validation procedures have been applied, practical use of the simulation results produced from the current model would require a more extensive and systematic association of the model with experimental methods.

Chapter 6: Code Parallelization in CUDA Environment

In the current chapter two different General Purpose Graphical Processing Unit (GPGPU) implementations, using either CUDA runtime Application Program Interface (API) only, or a combination of CUDA runtime and the Thrust API, are presented. We consider, once more, a mobile, rectangular, and rigid tank, filled partly by some dry granular material. The particles are monosized spheres of diameter 6 *mm* and mass 0.148 *gr*. By applying the tilting box method we monitor the shift of material's mass-centre along the y-axis of the tank (Figure 4.5), for a rate of tilting applied in several cases earlier (3 *deg/s*). Verification and numerical validation are discussed. The main driver of this effort is to examine the feasibility of simulating large systems by using a CUDA implementation and to investigate, in a quantitative manner, our algorithm's performance. Furthermore, a discussion on the restrictions of GPGPU for granular material applications is provided, along with suggestions on the direction of future efforts.

6.1 Implementation

Each CPU and GPU test was performed on a Dell Aurora R3 workstation with a 3.4 *GHz* Intel core i7 processor with 8 GB RAM running Windows 7. The GeForce GTX 400 family of GPUs that was used is based on NVIDIA's Fermi architecture. With 7 streaming multiprocessors, each containing 48 steaming processors (thus containing a total number of 336 cores), the GeForce GTX 460 SM is composed of a highly parallel processor employing superscalar execution, a technique that allows sequential instructions from a program to be executed in parallel, for optimal performance, improving latency in addition to throughput. Each SP can fulfil 2 single precision fused multiply-add (FMA) operations per cycle. It is capable of handling 65,535 parallel thread blocks, each of them may consisted of a maximum number of 1024 threads. Thus, for the purpose of our investigation (granular dynamics using molecular dynamics simulation) the GTX 460 GPU theoretically is capable of handling a maximum number of 6.7 million particles (of course the actual number gets smaller both due to hardware and software limitations). As for most GPUs, GTX 460 uses the PCIe 2.0x16 data bus for communication with the CPU. We firstly built the code using the lower runtime API and then, using only the two Thrust vectors *thrust/host vector* and *thrust/device vector*,

we replaced the necessary algorithmic steps, calculating both performance and speed in the resulted simulation.

Although several techniques splitting the code in more than one kernels (eg Walters et al 2008) have been presented, leading to several advantages and limitations, we restricted our code to a single kernel solution which is beneficial for speed of execution due to limited need for communication between different kernels, when no further optimization techniques are incorporated. The kernel, sequential for each particle, predicts its position, calculates the forces between particles and corrects the position values. Due to the great number of thread blocks and threads per block, for the purpose of the current work where simulations with no more than 50,000 particles were performed, each particle corresponds to a different thread, leading to an absolute parallel implementation for every time step (this is further supported due to absence of necessity for inter particle communication at each step).

Table 6.1 Pseudo-code for MD simulation without thrust library.

Step	Description	Execution
1	Insert initialization file*	Host
2	Transfer data to constant GPU memory (Time, time-step, material properties)	
3	Allocate memory for particles on GPU	
4	Transfer particle data (position + derivatives) to global GPU memory	
5	For all time-steps do:	
6	Launch integrate kernel (__global__ function)	Device
7	Set forces to zero (__device__ function)	
8	Predict particle position + derivatives (__device__ function)	
9	Calculate Forces (__device__ function)	
10	Correct particle position + derivatives (__device__ function)	
11	Synchronize threads	
12	Transfer particle data from GPU to CPU	Host
13	for all particles do	
14	Calculate mass centre position + derivatives	
15	end for	
16	Export data to a .dat file	
17	Update GPU memory	
18	End for	
19	Free CPU memory	

* A .dat file containing particles' properties and position information + integration data (time time-step etc). Because vector data cannot be directly transferred between CPU and GPU further transformation is needed after initialization of the algorithm.

In order to guaranty the appropriate execution of the code at each step; that is the finish of each step before the next one starts running, thread synchronization is incorporated. Table 6.1 presents the pseudo-code for our GPU implementation of the Molecular Dynamics algorithm. The GPU kernel is expressed in lines 6-12, while the rest lines express the

sequential part of the implementation. For the purpose of the current work no neighbour list algorithm is added as the appropriate algorithm for the specific problem (granular material dynamics) is under evaluation.

Table 6.2 summarizes the differentiations of the implementation when Thrust API is used. As shown the actual device code remains the same while the sequential part of it presents two major changes: a) the transfer of particle data from CPU to GPU and b) the allocation of memory on GPU are automatically executed by Thrust.

Table 6.2 Table 4. Pseudo-code for MD simulation using thrust library

Step	Description	Execution
1-2	Same as Table 3	
3	Use thrust library to copy particle data from CPU to GPU	Host
4	Allocate memory for particles on CPU and point to “device vector”	
5	For all time-steps do:	
6-12	Same as Table 3	Device
13-18	Same as Table 3 – no need for step 19 (free CUDA memory)	Host

* Differences between this and table 3 code occur mainly in format of the transferring data. In the case where thrust library is used particles are simply transferred as vectors without further transformation.

6.2 Numerical verification/validation of the algorithm

Two different kinds of tests have been performed, similar to those proposed by Haile (1997), in order to verify the code. Firstly, we have checked conservation principles during both the initial equilibration and the subsequent execution of the code and secondly we monitored the statistical error. The systematic error could not be monitored due to lack of hardware variety.

Table 6.3 Performed code verification tests

Type of test	Comments	Deviations
Conservation Principles	◦ Constant number of particles in time	< 0.5%
	◦ In equilibrium condition, total kinetic energy is constant and equally partitioned in Cartesian components.	
Statistical error*	◦ Reproducible averages within statistical uncertainties for different initial conditions	< 2%
	◦ Stable instantaneous values	

* All runs were for 15560 particles and time-step $\Delta t = 0.0001$. Averages were accumulated over 200.000 time-steps. The quantities studied are total energy and internal energy.

The outcome of the performed tests is summarized in Table 6.3. As shown, the code behaves in a very stable manner; very similar to that presented for the CPU-based code. In addition, numerical validation tests were executed.

Anderson et al (2008) managed to quantify the corresponding deviation of simulation trajectories for single and double precision modes, on the CPU and the single precision GPU calculations, from a baseline generated by LAMMPS running on a single processor. It was shown that single precision calculations on the CPU are slightly less precise with the trajectories starting to diverge at 1000 time steps while the GPU single precision implementation is no worse than the CPU, diverging at exactly the same point. The tests performed were based on an Nvidia GeForce 8800 GTX Ultra processor which, as a member of the G80 GPU family, supports only CUDA compute capability⁴ version 1.0 that does not have double precision floating point capability. According to NVIDIA (2009) the Fermi architecture has been specifically designed to overcome this limitation; up to 16 double precision fused multiply-add operations can be performed per SM, per clock

In order to numerically validate the results of the code, two kinds of tests were performed: a) we run the code without changing the default value of compute capability (1.3) that is enabled when running CUDA through Microsoft Visual Studio (version Ultimate 2013), through which the double type gets demoted to float by default and the double-precision math functions are mapped to their single-precision equivalents (CUDA C programming guide); and b) we changed the compute capability value to 2.0, thus enabling the double precision floating point handling. The corresponding results were compared with those from single and double precision CPU codes, respectively (Figure 6.1).

As shown in Figure 6.1, both the results of double precision and the single precision GPU code are in good agreement with the corresponding results of their CPU counterparts. It is also shown that both GPU and CPU single precision codes have a rather expected deviation from their double precision equivalent. Nonetheless, it is shown that the critical angle calculated by all codes (single and double precision CPU and GPU) is almost the same.

⁴ The *compute capability* of a device is defined by a major revision number that corresponds to the core architecture and a minor revision number that corresponds to an incremental improvement to the core architecture, possibly including new features (NVIDIA 2012)

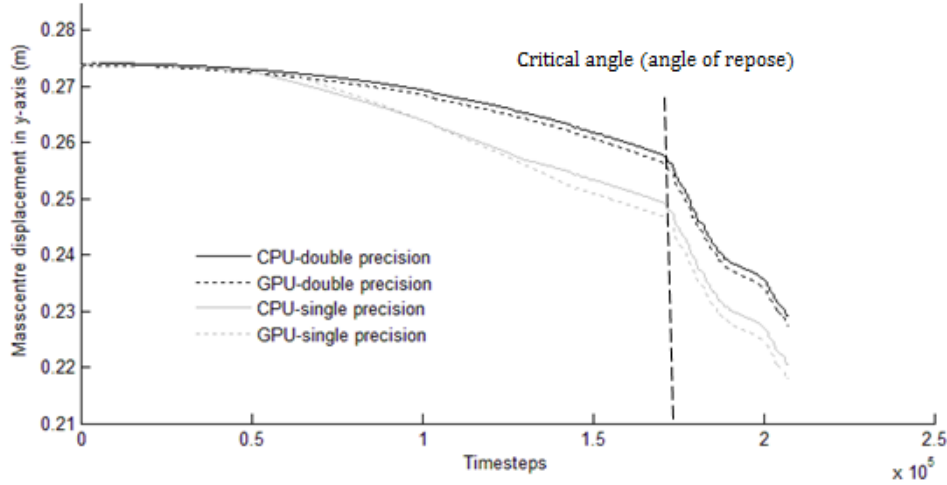


Figure 6.1 Comparison of CUDA_C simulation results against similar CPU code, both for single and double precision floating point handling.

In Figure 6.2 are shown quantitative results of deviations between GPU (single and double precision) and CPU (single precision) code predictions. The deviation is computed as the difference of mass centre displacements along the y axis, per time step. The difference is further divided by a particle's diameter to obtain a non-dimensional value of the deviation.

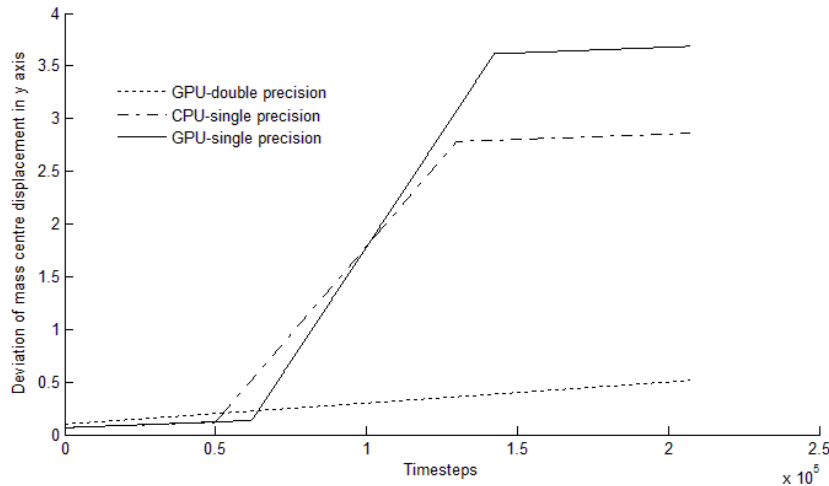


Figure 6.2 Mass centre displacement along y-axis for the GPU and single precision CPU codes are compared against that of double precision CPU code calculating the corresponding deviation.

The deviation between GPU and CPU code, expected due to the different way calculations are executed, is limited enough and our GPU results should be considered as accurate (deviation less than 2%). The deviation between single and double precision code was found to be very close to that found by Anderson et al (2008) and it can be considered as non-important. It is noted that, for the verification and validation study we have relied on the CUDA_C code that incorporates the Thrust library.

6.3 Performance results

In what follows a comparative analysis focused on simulation times, for code executed in CPU only and CPU-GPU (CUDA), is given. As was the case for the numerical validation tests two different code implementations were tested: single precision GPU and double precision GPU, each compared with its CPU counterpart. Furthermore two different simulation times were captured: time needed for kernel execution (the actual GPU part without memory allocation and data transfer) at each step and time needed for the execution of the entire algorithm (only the MD loop and the total runtime, including any start-up/shutdown, respectively). The times extracted were compared with that of the CPU analogue and the run speedup (e.g. 100X CPU time) is presented. Different initial files were used with a variety of particle numbers (from 1000 to 50,000). Only the code with Thrust API was considering for comparison due to its slightly better performance as shown in Figure 6.3 for the case of double precision code.

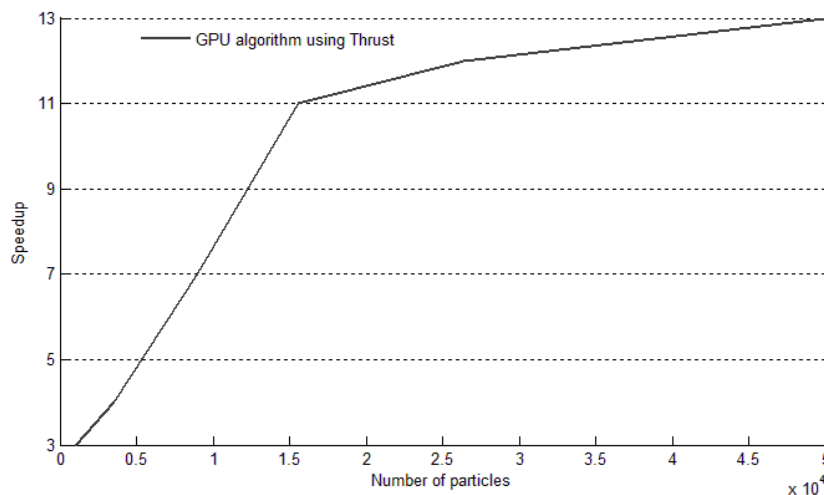


Figure 6.3 Speedup of total runtime, including any startup/shutdown using Thrust library compared to CUDA runtime API. As shown a 13x speedup occurs for 50000 particle simulation.

More than 5 executions were performed for each scenario (particle number, floating point precision) each of them incorporating different number of thread blocks (and consequently threads). As shown in Figure 6.4 for the case of double precision -15,560 particles simulation, both kernel and algorithm execution time varies for different thread blocks. Although it was impossible to find an exact mathematical model predicting the best number, as a “rule of thumb” it was found that too few or too many thread blocks lead to less performance. In our comparative results only the maximum speedup values are presented.

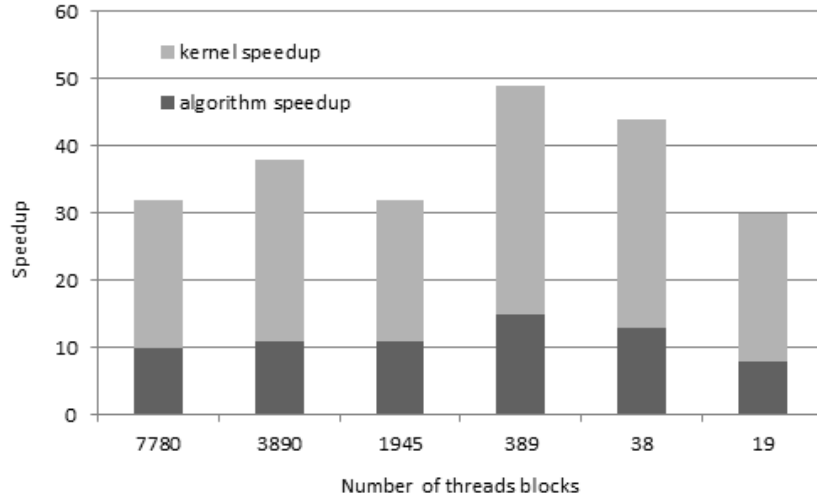


Figure 6.4 Time speedup for the case of double precision -15,560 particles simulation, both for kernel and algorithm execution.

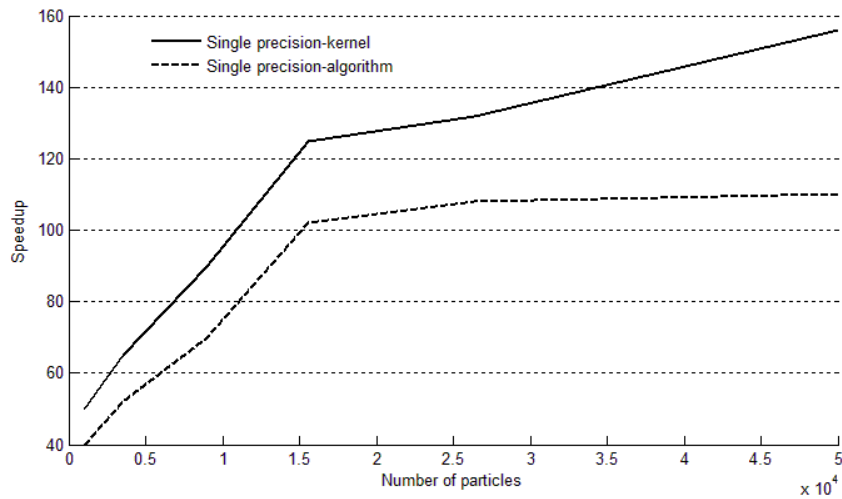


Figure 6.5 Speedup of total runtime, including any startup/shutdown (dashed line) and MD loop (solid line) run using Thrust library and single precision floating points.

In Figure 6.5 the performance of single precision code both for kernel execution and entire algorithm is presented. As shown the GPU implementation may lead to a maximum speed-up of almost 160x for kernel and 110x for algorithm execution for large number of particles. As expected less number of particles leading to less speedup. Practically for the implementation of our code (no neighbour list) execution of CPU code with more than 20,000 particles is almost impossible and thus the evaluated time was theoretically calculated through first 2000 time-steps.

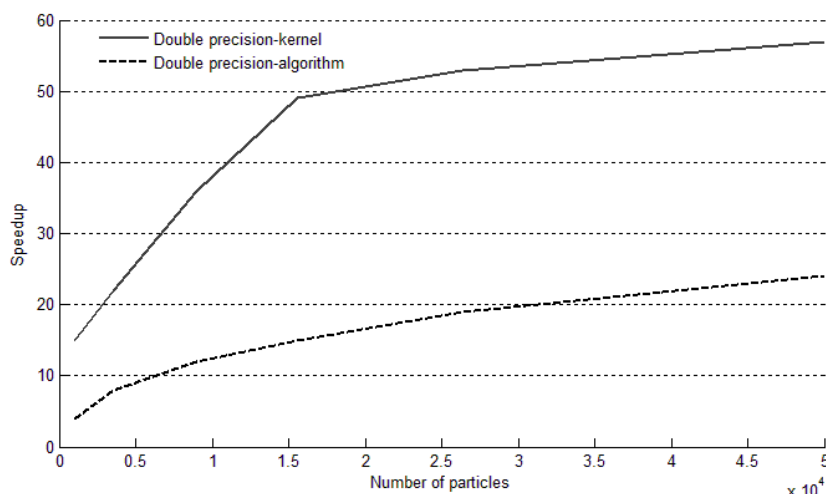


Figure 6.6 Speedup of total runtime, including any startup/shutdown (dashed line) and MD loop (solid line) run using Thrust library and double precision floating points.

Similarly to the previous case, the performance of double precision code, both for kernel and algorithm execution, are presented in Figure 6.6. Once again the simulation time using GPU is less than that using only CPU, but in this case the algorithm speedup reaches the maximum value of almost 25x for 50,000 particles. Comparing though the two curves in Figure 9 it can be understood that this limited speedup value, occurs partly due to reduced kernel performance but mostly due to the large contribution of sequential part of the code in total simulation time.

6.4 Discussion

From what was analysed in the previous paragraph it is obvious that the GPU implementation of the code is leading to a processing speedup by a value up to 150x. Even though certain barriers, like in precision and the in right choice of thread blocks, have been indicated, these are known problems occurring for every GPGPU implementation. Practically, these barriers only confirm that, granular material dynamics could be added to the list of scientific areas that benefit from GPU processor speed-up, having more or less the same limitations as every other scientific field, especially molecular dynamics simulation (eg for biomolecules). Optimization algorithm techniques, such as splitting the kernel to two or introducing a hybrid GPU-CPU cluster could improve even more the time efficiency of the algorithm, although every optimization effort has to be performed with scepticism as it could even destroy the initial algorithm performance (Brodtkorb et al 2013).

In addition though, a major issue for discussion has been raised: how much precision we can afford losing in order to execute our algorithms faster. To state it differently, as was

shown, the improvement of speed comes with a precision cost. By adopting only single precision floating points in order to benefit from the faster execution, the precision is inferior compared to that of the CPU code simulation results. Therefore, both computational precision gain and the deviation from experimental results should be considered in a GPU implementation. To be able to separate these two effects, it is essential to employ selected “CPU scenarios” for “benchmarking” of the GPU code. In our case, both the single precision and double precision GPU codes, despite predicting slightly different displacements of the mass centre, they are nevertheless capable of predicting almost identical values of the angle of repose. Thus, the benefit of single precision performance could be reaped for the sake of gaining computational efficiency. This benefit would be of great importance when coupled material-ship motion is under investigation due to the need for even more computational capacity. Of course, in a more dedicated work it could be investigated the deviation of the predicted angle against the computational gain, when an enormous number of particles is considered, by this way evaluating any possible performance thresholds that may exist. Furthermore, computational tests with a Kepler architecture would be of a great importance, due to its ability of more accurately handling double precision floating points.

6.5 Concluding remarks

Starting from a sequential molecular dynamics code written in C++ for the purpose of granular material simulation, a GPU implementation using either CUDA runtime API or CUDA runtime and the Thrust API was presented. The results point to the direction that, an algorithm implementation of the latter type, produces improved performance. Even though a single kernel approximation was followed; thus no optimization technique was adopted, comparison between CPU and GPU simulation results showed that a speedup of up to 150x could be reached when the graphics processor is used and the proper set of threads-thread blocks is selected. This speedup is much less when double precision floating points are considering, although it may be improved when less export data are needed. Comparatively results proved that the use of GPGPU in order for simulating ship cargo shift is not only essential when a lot of particles are under investigation but it could be more than vital, when large scaling tanks or even coupled phenomena are under consideration.

Chapter 7: Coupled ship - cargo motion in regular beam seas

In this chapter we take a step further, to study how the ship and the granular material behave, as a combined system, under the effect of harmonic wave excitation on the hull. Our objective is to understand how the interaction of the material with the ship can aggravate safety, so that an effective tool could be created in the future for assessing the severity of this interaction. At present, the study has been restricted to the assumption of regular beam sea waves propagating in deep water and exciting a barge with rectangular cross section at whose interior is a rectangular tank partly loaded with granular material. Several further simplifying assumptions are applied on the ship motion model. In the first stage of the investigation, the barge is allowed to rotate only around a fixed (in space) longitudinal axis, hence it possesses only one degree of freedom (for roll motion). At second stage, the model is upgraded to a heave - sway - roll model, so that the motions of the freely floating barge can be simulated when meeting, transversely, harmonic waves (3-DOF approach). In reality of course, this model, as well as the initial simpler one, possess thousands of degrees of freedom due to the independent movement of the cargo particles.

The humidity of the particles is another issue looked into in the current chapter. The coupled motions are investigated with the 3DOF model, in a comparative manner, for dry and for humid cargo.

7.1 System definition

When the 1-DOF approach is applied, the roll centre is considered as fixed (this is point P in Figure 7.1). On the other hand, three different systems of coordinates are used in the 3 DOF approach, which have already been described in *Chapter 4* (they are shown again in Figure 7.1).

In what follows, only the dynamics on the yz plane is under investigation, due to the 2D assumption associated with the developed granular material algorithm. The barge model is assumed to be long enough (greater than 2 m) compared to her height (0.3 m) and beam (0.34 m). Linear wave theory, transverse harmonic waves (“beam sea”), small wave height related to the wave lengths (although this condition is not always strictly respected and values up to

$H/\lambda < 1/18$ were also tested), wave length much larger than the barge's beam and zero forward speed of the barge, are also assumed.

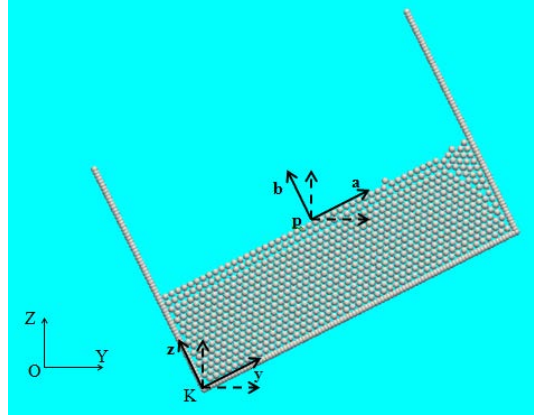


Figure 7.1 The three different coordinate systems (solid lines) and their irrotational versions (dashed lines).

The hold is filled with smooth spherical particles made of cellulose acetate, having diameter 0.3 cm , such that, particle parameters (friction, stiffness etc) coincide with those experimentally measured by Foerster et al (1994). With the material inside, the draught is (at initial position) 0.11 m . The material height-to-width-ratio is 0.37 which corresponds to the “finite” material depth case discussed in *Chapter 5*. Following the tilting table method (IMO 2012), the critical angles triggering cargo shift were determined. When relatively slow rates are applied (less than 1 rad/s), two critical angles, at about 25 and 42 deg , are identified.

7.2 Single Degree of Freedom - Roll

7.2.1 Equation of motion

The barge is allowed to rotate around a longitudinal axis cutting vertically its middle section at a fixed point P shown in Figure 7.1. Ship motion is predicted by solving Newton's equation at every time step. The hull is considered receiving loads due to inertia, hydrodynamic damping, restoring (with consideration of time varying centre of mass of cargo) and the impacting moment due to possible particles' impact with hold's side walls. Vessel's roll motion can then be described, used a rather simplistic 1-DOF mathematical model, as follows:

$$(I + \delta I)\ddot{\phi} + B_1\dot{\phi} + B_2\phi|\phi| + M_R = mg GM Ak r \cos(\omega t) + M_{cargo} \quad (7.1)$$

φ is the absolute roll angle, r is the effective wave slope, I and δI are, respectively, the roll moment of inertia and the added moment of inertia, B_1 and B_2 are the linear and the quadratic roll damping coefficients. δI and B_1 are, in general, frequency-dependent while B_2 was assumed here as frequency independent (Delorme et al 2006).

M_R is the restoring moment (Vidic & Jensen 2009) calculated as the sum of three moments (M_B due to buoyancy, M_S due to ship's weight and M_C due to cargo's weight) with reference to the fixed axis of rotation (Eq. 7.2).

$$M_R = M_B + M_S + M_C$$

$$M_B = \rho g r_b V_s, \quad M_S = m_s g r_s \quad \text{and} \quad M_C = m_c g r_c \quad (7.2)$$

In the above, m_s , m_c correspond to the mass displacement due to unloaded ship's and cargo's weight, respectively, while V_s is the submerged volume surface. The distance between unloaded ship's centre of gravity and point P (origin of local coordinate system) is known; thus the position of ship's centre of gravity (r_s) is easily calculated based on knowledge of the roll angle. The position of the centre of buoyancy ($r_b = \sqrt{x_B^2 + y_B^2}$), with respect to the local coordinate system, is calculated at every time-step, on the basis of ship's geometry and for the rectangular barge of our case is given by:

$$x_B = \begin{cases} \frac{l(6T + l \tan \varphi)}{12T} & \varphi \leq \alpha_1 \\ \frac{x}{3} & \alpha_1 < \varphi < \alpha_2 \\ \frac{1}{3} \sqrt{\frac{2lT}{\tan \varphi}} & \alpha_2 \leq \varphi < \frac{\pi}{2} \end{cases}, \quad y_B = \begin{cases} \frac{48T^2 + l^2 \tan^2 \varphi}{24T} & \varphi \leq \alpha_1 \\ \frac{y}{3} & \alpha_1 < \varphi < \alpha_2 \\ \frac{\sqrt{2lT \tan \varphi}}{3} & \alpha_2 \leq \varphi < \frac{\pi}{2} \end{cases}$$

$$\alpha_1 = \tan^{-1} \left(\frac{2T}{l} \right), \quad \alpha_2 = \tan^{-1} \left(\frac{h}{2lr} \right) \quad (7.3)$$

l , h and T stand for barge's width, height and draught, respectively while r for the barge's to sea's density ratio. A detailed description on the calculation of this distance can be found in Spyrou (2015) and Sakelariou (2013). The distance of cargo's gravity centre (r_c) in local coordinate system is numerically calculated at every time-step, based on the instantaneous location of the centre of gravity of each free-to-move particle (x_i, y_i) according to Eq. (7.4).

$$r_c = \frac{\sum_{i=1}^N m_i \sqrt{x_i^2 + y_i^2}}{\sum_{i=1}^N m_i} \quad (7.4)$$

m_i stands for the mass of particle i and N for the total number of the free-to-move particles inside the hold.

Moreover, the impact moment M_{cargo} is calculated by:

$$M_{cargo} = \sum_{i=1}^K M_i \quad (7.5)$$

where M_i is the moment due to the contact force F_i , calculated on the basis of Eq. (4.1), acting on a particle i of the tank wall. This force is produced by interaction with neighbouring cargo particles having, with respect to particle i , nonzero relative velocity (Spandonidis & Spyrou, 2015 & 2016). K is the total number of hold's wall particles.

In Figure 7.2 is shown the calculated GZ curve [$GZ = M_R / [(m_s + m_c)g]$] for calm water, considering rotation around point P, when the vessel was loaded with *solid cargo*; that is, cargo with the same weight and position of mass centre as those of the granular cargo, but without ability of its particles to move.

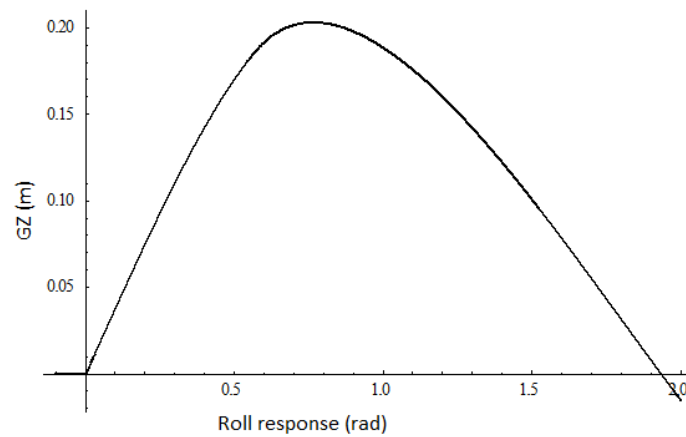


Figure 7.2 The GZ curve in calm water as calculated numerically from the algorithm.

At preliminary stage, the barge was left to balance in calm water. In this way, the draught of the barge and its initial roll angle were calculated for several slightly different initial free surface configurations. The roll response of the barge in free roll is presented in Figure 7.3 (left). In Figure 7.3 (right) is presented the single-sided amplitude spectrum of the roll response after the Fast Fourier Transformation has been applied on the roll response. The natural frequency had a value close to 0.78 Hz (4.9 rad/s). The corresponding eigenperiod of the barge lies within acceptable (for real case scenario after considering the scale ratio) limits, close to 1.28 s .

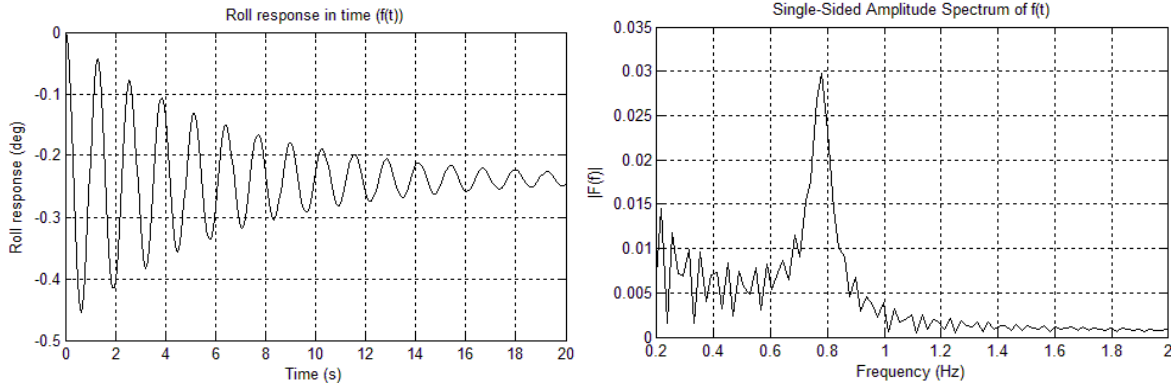


Figure 7.3 Roll response of the barge for free oscillating motion (left) and the single-sided amplitude spectrum of this response after Fast Fourier Transformation (right).

In what follows, the excitation frequency has been normalized with the undamped system's natural frequency. Thus, the roll response is depicted in relation to the non-dimensional frequency factor $\sigma = \omega/\omega^*$, where ω and ω^* are the encounter and natural frequency, respectively.

7.2.2 Case study

The vessel was free to move only in roll, with an external excitation owed to the effect of waves of certain amplitude and frequency. At this specific stage we assumed dry cargo with its weight equalling that of the vessel itself (i.e. the weight of the carrier was considered as comparably insignificant).

Two kinds of numerical experiments were performed. The first was basically a benchmark, where the vessel was loaded with *solid cargo*. It was tested in several harmonic excitations. Analysis of these results provided a good indication for the most significant frequency region where further investigation should be carried out. The second series involved tests with actual granular cargo. The wave frequency and amplitude regions of interest were 3-6.5 rad/s ($\sigma = 0.61 - 1.33$) and 0.5 - 2.5 cm, respectively.

In Figure 7.4 are shown some comparative examples of barge's behaviour, for four different frequency values, with wave amplitude fixed at 1 cm. The key findings of this investigation are the following:

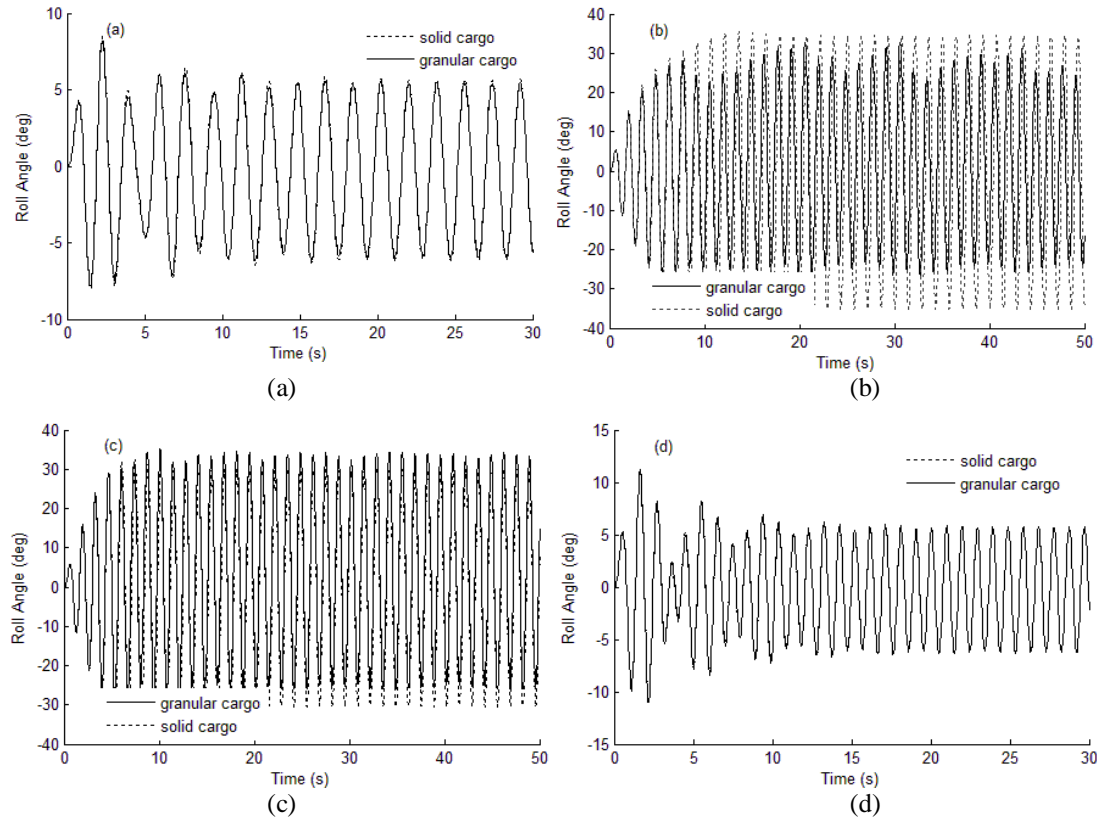


Figure 7.4 Comparison of response of frozen and granular cargo. The excitation amplitude s is fixed at 1 cm and the frequency varies as follows: a) 3.5 rad/s ($\sigma = 0.71$), b) 4.4 rad/s ($\sigma = 0.9$), c) 4.7 rad/s ($\sigma = 0.96$) and d) 6.5 rad/s ($\sigma = 1.33$).

a) For wave frequency values below 3.5 rad/s ($\sigma = 0.71$) and above 6 rad/s ($\sigma = 1.22$), barge's response is of low importance (see Figure 7.4 (a) and (d)). After a short transient, a peak roll angle of no more than 5 deg was reached. Since the granular material did not perform any substantial motion, barge's behaviour did not depend on whether the cargo was movable.

b) For wave frequency values between 3.5 and 6 rad/s , the barge entered a resonance region. For solid cargo (see Figure 7.4b), the peak of roll amplitude appeared at frequency 4.4 rad/s ($\sigma = 0.9$) and a maximum roll angle of approximately 36 deg was reached. With the cargo in granular form, the system showed a tendency to move less, the motion becoming however more intense beyond a frequency threshold value about 4 rad/s ($\sigma = 0.82$). The peak roll angle reached was less than 30 deg . The lower response is explained as follows: whilst the granular material reaches the first critical angle of heap formation, the phase of cargo's movement opposes that of the vessel, and thus the overall motion is reduced. The calculation of moments indicated that, the moment due to shift of cargo's mass centre, and not the moment due to impact against the walls, is the primary cause of this effect.

c) Further observation of Figure 7.4b led to additional findings. Firstly, the motion of

the vessel with the granular cargo has become asymmetrical. Local movement of particles around the one end of the free surface, led to a lower absolute roll peak when the hold rotated clockwise. Secondly, for certain values of wave frequency, the steady-state is characterized by more than one frequency. As confirmed from Figure 7.4b and c, where a 50 s simulation result is shown, this phenomenon is not transient but it represents the true long-term response. The last observation is better depicted in Figure 7.5, where the vessel's response phase portrait for wave amplitude 1 cm and frequency 4.4 rad/s ($\sigma = 0.9$) is presented.

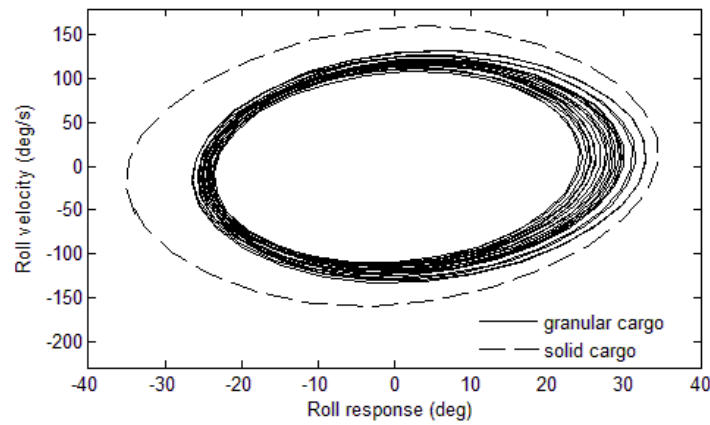


Figure 7.5 Phase plots of vessel response (model scale) when carrying solid (dashed line) and granular (continuous line) cargo, for wave amplitude 1 cm and frequency 4.4 rad/s ($\sigma = 0.9$).

d) Inside the resonant region and after a critical value of 4.7 rad/s ($\sigma = 0.96$), the two systems produce almost identical mean roll responses. Despite though their macroscopically similar behaviour, the initial movement of the granular cargo during the transient stage gives rise to larger roll. For the case of 4.7 rad/s (Figure 7.4c), both systems oscillate with mean roll amplitude of 30 deg. But for the granular cargo, an almost 2 degree dynamic roll bias is incurred, generating a higher absolute roll peak. These findings are summarized in Figure 7.6.

For wave amplitudes between 0.5 and 1.5 cm, our simulations yielded that the behaviour remains qualitatively similar to that obtained for 1 cm wave (no diagram shown). In Figure 7.7 appear comparisons at the two ends of the investigated region of wave amplitude [0.5 cm (up) and 1.5 cm (down) - wave frequency, respectively, 4.5 and 4.3 rad/s (σ : 0.92 and 0.88)]. Notably, for wave amplitude 1.5 cm, the granular cargo case is associated with smaller response but with a “clear” second frequency existing in the steady state due to material’s displacement.

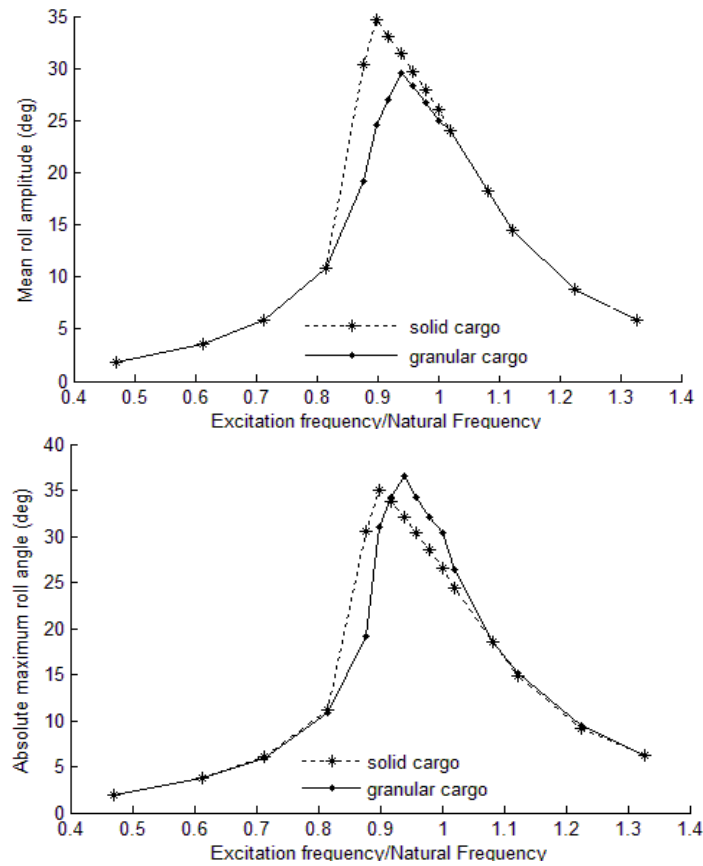


Figure 7.6 Mean roll amplitude (up) and absolute maximum roll angle (down), for 1 cm roll excitation amplitude.

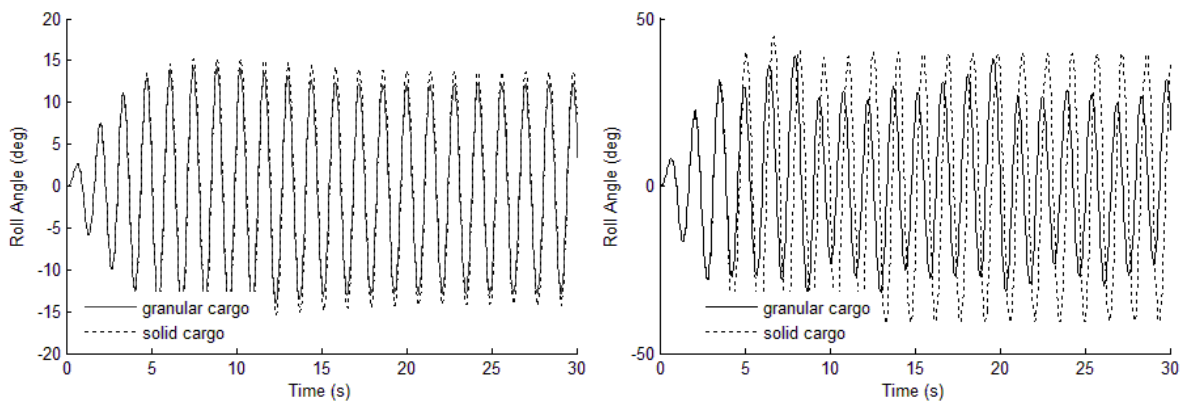


Figure 7.7 Comparison of response of solid and granular cargo: (left) excitation amplitude 0.005m and frequency 4.5 rad/s ($\sigma=0.92$); (right) excitation 0.015 m and frequency 4.3 rad/s ($\sigma=0.88$).

e) Further increase of the excitation leads however to a substantially different behaviour (Figure 7.8): for wave amplitude 1.7 cm and frequency 4.5 rad/s ($\sigma=0.92$), the material inside the hold moves in such a way that the barge cannot return towards the upright position and capsize is finally realised.

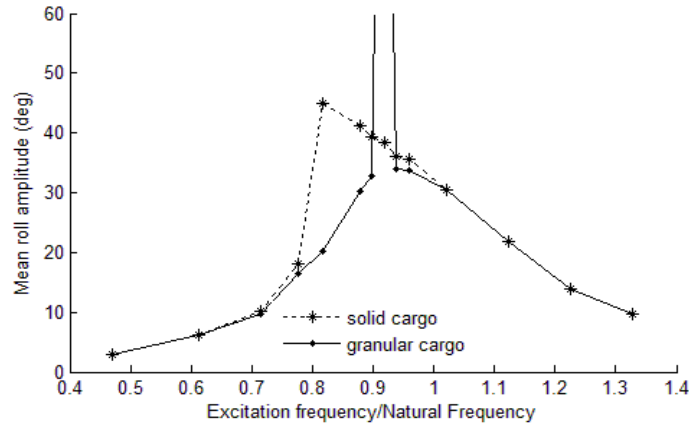


Figure 7.8 Mean roll amplitude for wave amplitude 1.7 cm.

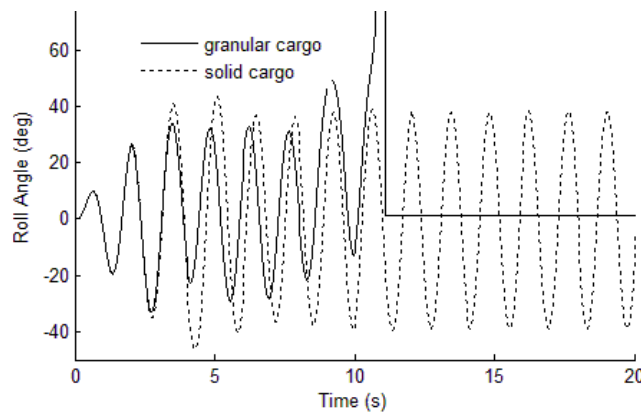


Figure 7.9 Comparison of response for the solid and granular cargo cases, when the wave amplitude is 1.7 cm and the frequency is 4.5 rad/s ($\sigma=0.92$). Vessel capsizes in the case of the granular cargo.

To investigate to greater depth this unexpected behaviour, we have looked into the first seconds of its realisation. In Figure 7.9 are depicted, in comparative manner, the first 20 seconds of the motion, for the two systems. At about the 10th second, the barge with the granular cargo capsized. As will be explained next, this is not a purely numerical instability of the code but in fact, it is owed to shifting of the cargo inside the hold. Whilst the barge initially behaved in a similar manner to the 1 cm wave amplitude case (that is, smaller mean roll angle and quasi-steady state response), soon a large peak value suddenly emerged (almost 45 deg). This is above the material's second critical angle associated with its angle of repose. In the ensuing cycle the roll angle grew even further and capsizing finally occurred. Visual inspection of the cargo inside the hold indicated that, due to high acceleration, significant amount of material was displaced to the one side, remaining there during the two roll cycles before the capsizing (see the simulation snapshots of Figure 7.10).

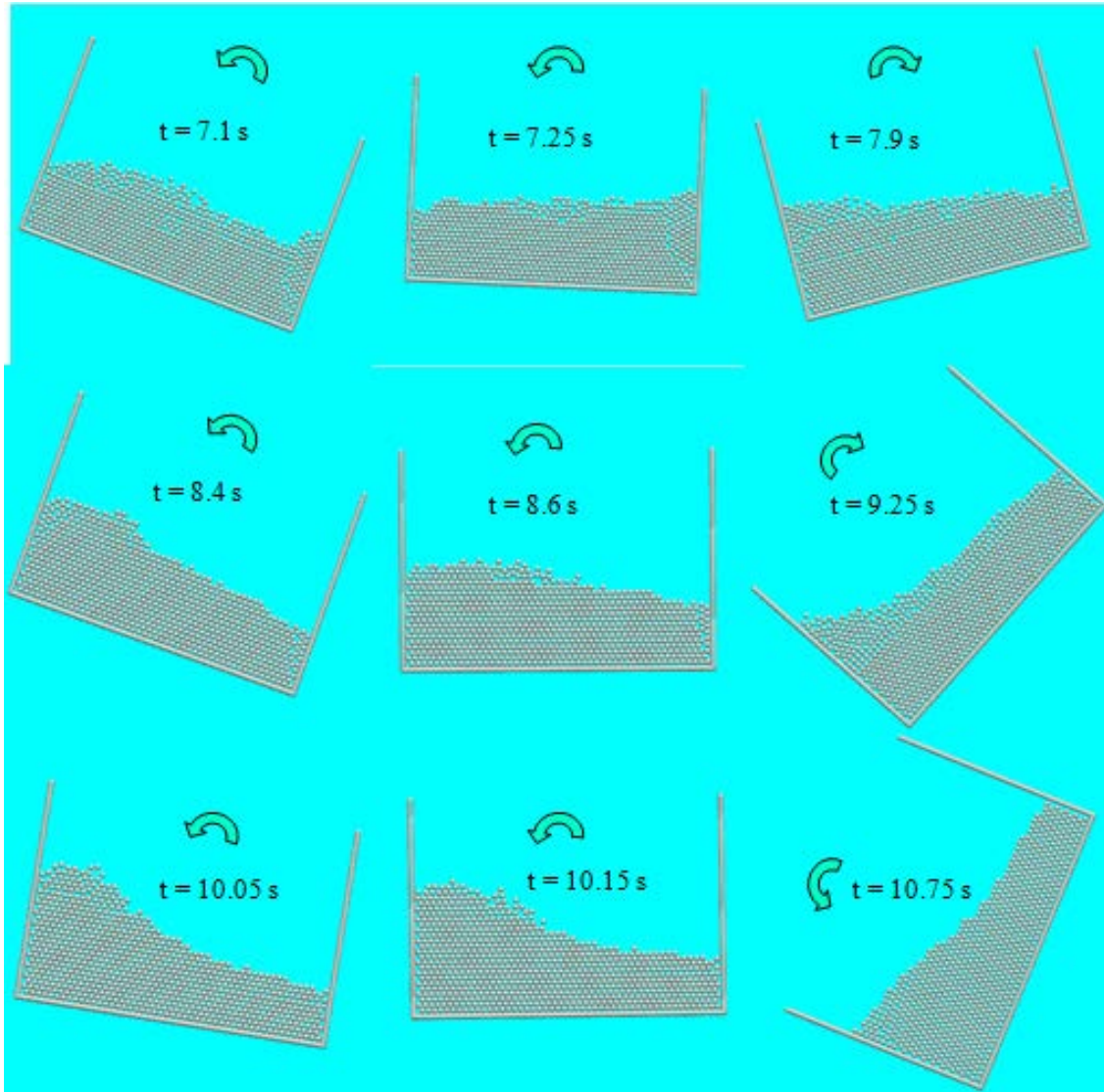


Figure 7.10 State of the cargo inside the hold during the three last roll cycles before capsizing: 6th, 7th and 8th (upper to lower, respectively). The creation of a substantial roll bias due to cargo's shift to port is noticed.

For wave amplitudes higher than 1.7 cm, a qualitatively similar behaviour was observed. Figure 7.11 depicts vessel's response phase portrait for wave amplitude 1.9 cm and frequency 4.3 rad/s ($\sigma = 0.88$). As was the case before, vessel's steady state response is characterized by more than one frequency. For slightly larger wave frequency material inside the hold moves in such a way that once again capsizing is finally realised. In Figure 7.12 the mean roll amplitude of the barge for wave amplitude 1.9 cm is presented. As shown capsizing at this occasion occurs for a wider frequency range (between 4.4 and 4.7 rad/s ($\sigma = 0.9 - 0.96$)). Material inside the tank presents a qualitative similar behaviour with that presented in Figure 7.10.

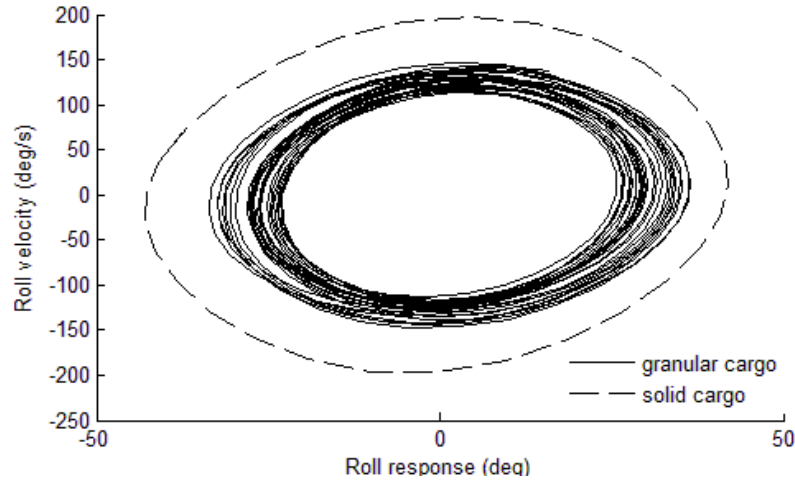


Figure 7.11 Phase plots of vessel response (model scale) when carrying solid (dashed line) and granular (continuous line) cargo, for wave amplitude 1.9 cm and frequency 4.3 rad/s ($\sigma=0.88$).

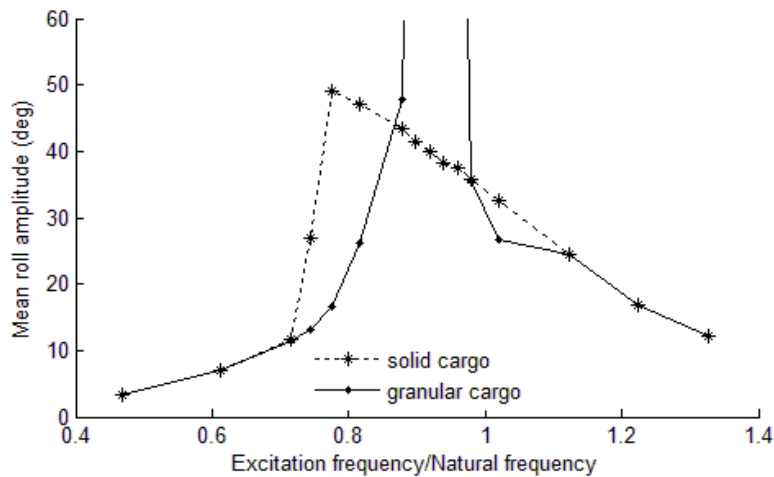


Figure 7.12 Mean roll amplitude for wave amplitude 1.9 cm.

7.3 Three degrees of Freedom (Roll - Sway - Heave)

7.3.1 Equations of motion

At second stage, an improved model is developed in order to study how the ship and the granular material behave, as a system, when the barge is able to react in the heave, sway and roll directions (3DOF). Newton's approach for the differential equations of motion of a vessel free to move in sway, heave and roll (3 DOF), taking into account the inertial system discussed in *Chapter 4* and zero initial conditions for barge's position and velocity was followed. The corresponding forces and moment can, in general, be decomposed following Schmitke (1978). The coupling due to cargos weight is taken into account through the calculation of the hydrostatic forces. The analytical description of the mathematical model is

provided in Appendix E. As shown there, the wave induced ship motion (undisturbed wave assumption) may be described by the system of Eq. (7.6) which is solved in time, coupled with the nonlinear molecular dynamics model of the granular material:

$$\begin{aligned}
 (M + A_{22})\ddot{y} + B_{22}\dot{y} + A_{24}\ddot{\phi} + B_{24}\dot{\phi} &= -\rho\nabla_0 A\omega^2 \sin(\omega t) + F_y^{cargo} \\
 (M + A_{33})\ddot{z} + B_{33}\dot{z} + \rho g A_{WPZ} &= \rho g A_{WP} \cos(\omega t) - \rho\nabla_0 A\omega^2 \cos(\omega t) + F_z^{cargo} \\
 (I + A_{44})\ddot{\phi} + B_{44}\dot{\phi} + A_{42}\ddot{y} + B_{42}\dot{y} + M_x^{HS}(\phi, \alpha) &= -IAk\omega^2 \sin(\omega t) + M_x^{cargo} \quad (7.6)
 \end{aligned}$$

Here ϕ is the “absolute” roll angle, M the ship mass and I her roll moment of inertia with respect to an axis passing from the centre of undisturbed free surface (point P in Figure 7.1). F_y^{cargo} , F_z^{cargo} and M_x^{cargo} correspondingly stand for the impact forces and moment generated by the particles’ contact with nonzero relative velocity with hold’s wall. $M_x^{HS}(\phi, \alpha)$ stands for the restoring moment calculated numerically as the sum of the three moments due to buoyancy, ship’s and cargo’s weight, taking account of the absolute roll angle (ϕ) and the slope (α) of the incident wave. Calculation of these roll restoring moments is conducted at every time-step, based on buoyancy, hull gravity centre and cargo mass centre positions, in the local coordinate system, similarly to what was described in the previous section. A_{ij} and B_{ij} are the frequency-dependent added mass and damping coefficients of the hull. Since we focus on the steady state response of a symmetric body subjected to a regular incident wave, memory effects are neglected (see Appendix E).

For the purpose of the current work $A_{33}, A_{22}, A_{24}, A_{42}$ and $B_{33}, B_{22}, B_{24}, B_{42}$ are calculated from Vugts’ (1971) diagrams of hydrodynamic coefficients for rectangular tanks that were extracted using the strip theory and experimental measurements. A_{24}/B_{24} and A_{42}/B_{42} are equal due to the symmetry of the hull. In order to incorporate these diagrams into our algorithm we initially performed samplings with small frequency step and afterwards we calculated suitable fitting curves using 4th degree polynomials. In this way we achieved calculation of the hydrodynamic coefficients for the specific frequency, each time prior the numerical calculation of system response. This approach is judged to be accurate due to the fact that the investigated frequency range of this work has been limited in the close proximity of the roll natural frequency, where the coefficients are either almost fixed (heave and sway cases) or follow a simple algebraic equation.

The roll centre of this system is not fixed, unlike that for the 1-DOF case. However, for free rotation in calm water, up to moderate angles, where vertical balance of gravity and

buoyancy is maintained, the centre of rotation would again be point P of Figure 7.1, located on the waterline. This is due to the vertical sides to free surface of the hull. Thus, the GZ curve in calm water calculated from the algorithm should be the same as before until deck is submerged or bottom's edge emerged (Figure 7.2).

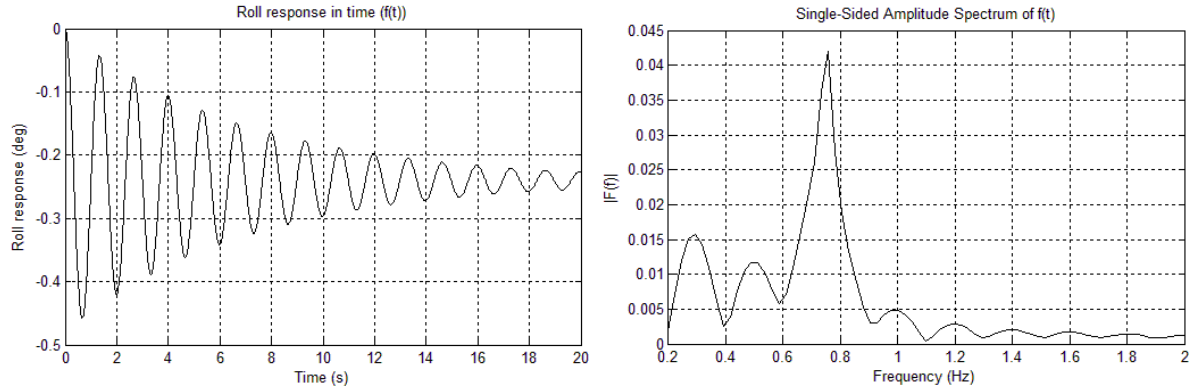


Figure 7.13 Roll response of the barge for free oscillating motion (left) and the single-sided amplitude spectrum of this response after Fast Fourier Transformation (right).

As was the case for the single degree of freedom model, initially we calculated the eigenperiod and the corresponding natural frequency of the system, by allowing the barge to freely oscillate (after a small initial perturbation). The roll response of the system is presented in Figure 7.13 (left). The period of oscillation was measured to be close to 1.35 s (natural period) thus the corresponding natural frequency had a value close to 0.74 Hz (or 4.65 rad/s). In Figure 7.13 (right) is presented the single-sided amplitude spectrum of the roll motion after Fast Fourier Transformation has been applied on a typical record of freely decaying roll. In order to investigate any unrealistic situation due to the cosine term in Eq. (7.6) in Appendix F system's dynamic behaviour is compared with that after initialization of the propagation wave.

Following a similar approach as for the presentation of our findings for the single degree of freedom motion, in what follows the excitation frequency has been normalized with the natural frequency of the undamped system. Thus the roll response is depicted in relation to the non-dimensional frequency factor $\sigma = \omega/\omega^*$, where ω and ω^* are the encounter and natural frequency, respectively.

7.3.2 Dry cargo

It is recalled that the focus of our investigation is not only on the detailed behaviour of the granular material inside the tank, but mainly on the influence of this behaviour upon vessel's dynamic response. Once again, the first series of testing involved a free-to-move vessel

loaded with *solid cargo*; that is cargo with the same weight and mass centre with those of the granular cargo, but with no possibility for its particles to move independently. Analysis of these results provided a good feeling of the most significant frequency region for further investigation. The second series involved tests with *granular cargo*. The wave frequency and amplitude region of interest, turned to be in the region of 3 to 6 *rad/s* ($\sigma = 0.64 - 1.3$) and 1.5 to 3 *cm*, respectively.

For wave frequency values below 3.9 *rad/s* ($\sigma = 0.84$) and above 5.5 *rad/s* ($\sigma = 1.2$), barge's response is of low significance: After a short transient period, a peak roll angle no more than 5 *deg* was reached. Since, in these frequency regions, the granular material did not perform any substantial motion relatively to the tank, barge's behaviour did not depend on whether the cargo was movable.

For wave frequency values, though, between 3.9 and 5.5 *rad/s* ($\sigma = 0.84 - 1.2$) the barge was in a resonance region. For increasing values of wave amplitudes the key findings inside that region are as follows:

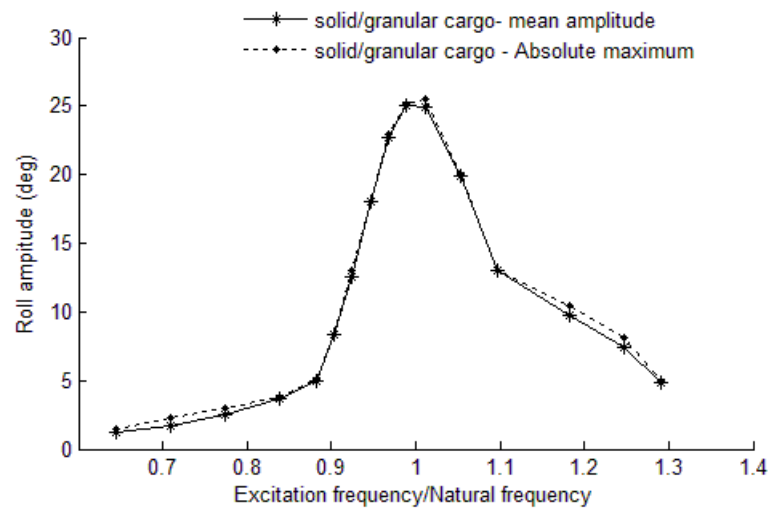


Figure 7.14 Mean (solid) and absolute (dotted), roll amplitude for 1 *cm* excitation. Both systems (solid and granular cargo) have the same dynamic behaviour.

a) For small excitation amplitudes and up to a value close to 2 *cm*, the response of the *solid* and *granular* systems (transient and steady state) is identical. This is why both the mean roll and the absolute maximum roll response in Figure 7.14 are interpreted with the same line for *granular* and *solid* cargo. Furthermore, the mean roll amplitudes (measured on the basis of two successive maxima) receive the same values with the actual maximum angles, for the two systems (coincidence of the solid and dotted line in Figure 7.14). This results from the fact that, the two systems present symmetry in their response between the port and starboard

side. Whilst this is an expected result for the *solid* system, in the case of the *granular* system it means that the particles either haven't shown any tendency of moving at all, or their movement was so small that it was insufficient for breaking the symmetry.

b) Excitation amplitude of 2 cm seems to represent a critical point for system's behaviour. The roll response of the barge is close to cargo's angle of repose; thus cargo's upper particle layers start moving. In Figure 7.15 is shown a characteristic comparison between the roll responses of the two systems, for two different excitation frequencies. For excitation frequency 4.1 rad/s ($\sigma = 0.88$) it is observed that, while the mean amplitude of oscillation is smaller than that of the barge with solid cargo, due to cargo shift the barge reaches larger roll angles to the one side. It has to be noted also that, for relatively large values of excitation frequency (inside the resonance area) the response of the system shows a difficulty on reaching the steady state condition. Thus we measured the amplitude in approximate manner. This feature of the motion becomes even starker as the excitation amplitude is increased.

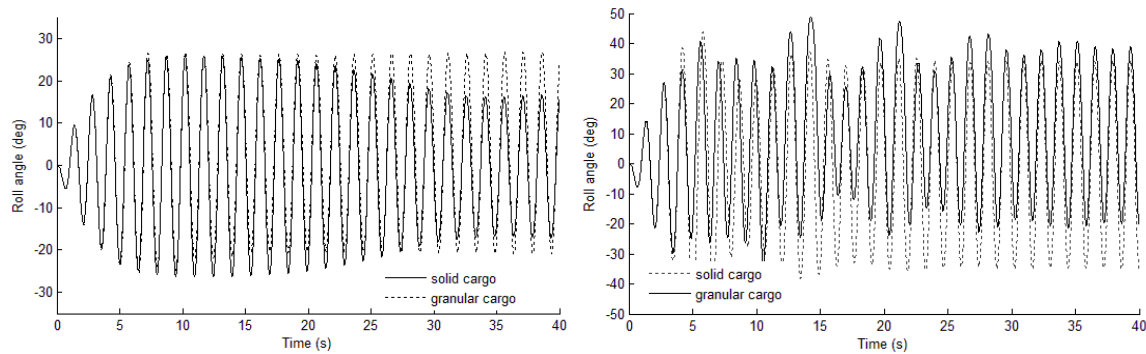


Figure 7.15 Roll response of ship for excitation amplitude of 2 cm and excitation frequency 4.2 (left) and 4.5 (right) rad/s ($\sigma = 0.92$ and 0.97, respectively).

In Figure 7.16 is depicted the barge's roll response for 2.5 cm wave excitation amplitude. As is apparent, the peak response amplitude of the *granular* system has been shifted to the right, compared to that of the *solid* system. Consequently, while the mean roll amplitude is smaller for the *granular* system (Figure 7.16 upper), there is a frequency region where the peak response amplitude is higher than that of the *solid* system (Figure 7.16 lower); implying that, some significant part of granular cargo has flown towards the one corner of the tank, giving rise to this symmetry breaking.

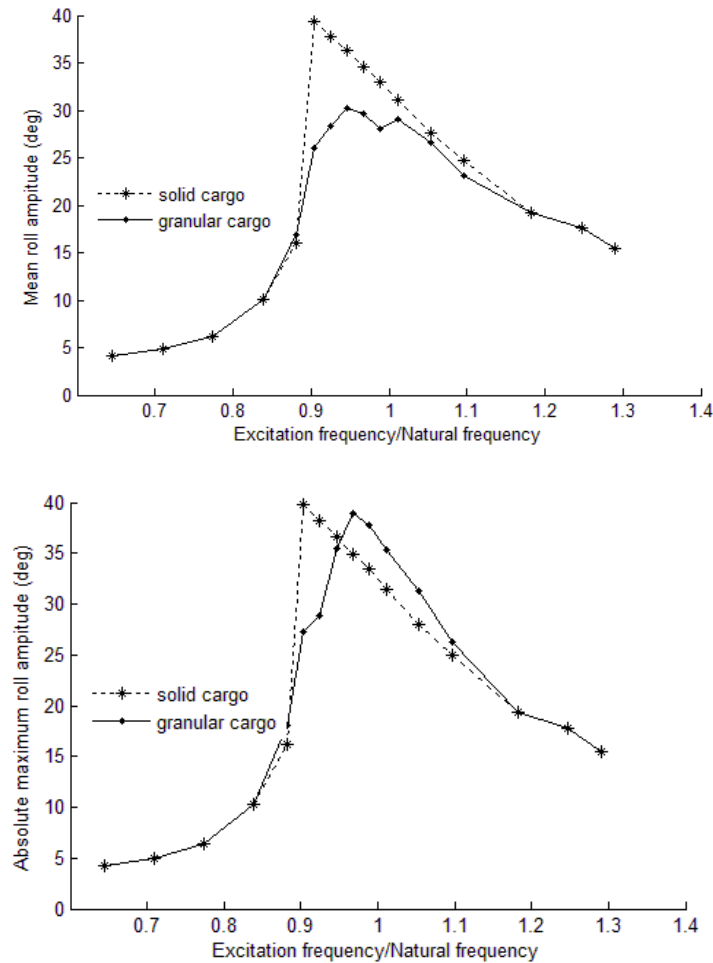


Figure 7.16 Mean roll amplitude (up) and absolute maximum roll angle (down), for 2.5 cm roll excitation amplitude.

c) For higher values of excitation however, the system is driven to a substantially different behaviour. As shown in Figure 7.17, for a wave amplitude 2.7 cm and frequency 4.5 deg/s ($\sigma=0.97$), the material inside the hold moves in such a way that the barge cannot return towards the upright position and capsizing is finally realised. In Figure 7.18 is depicted, in comparative manner, the roll response of the barge (scaled for illustration purposes) and the mass centre displacement of the *granular* media, for frequency 4.5 rad/s. Just before the 18th second, the material inside the tank flows in such a way that the barge is unable to return to the stable position and consequently she is driven to capsize.

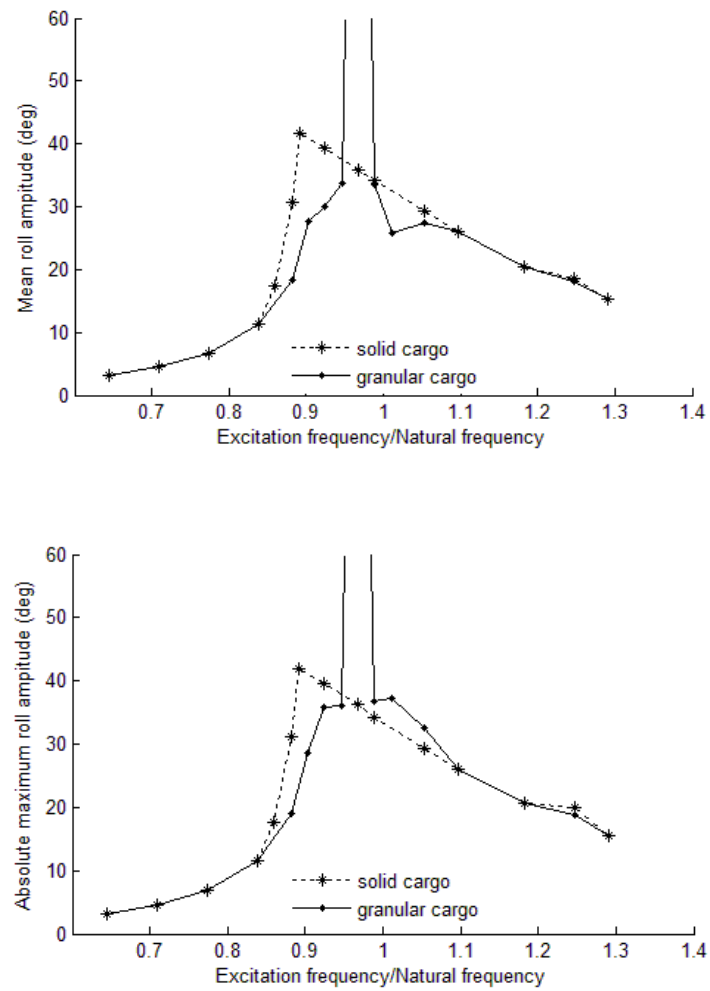


Figure 7.17 Mean (up) and absolute (down), roll amplitude for 2.7 cm excitation.

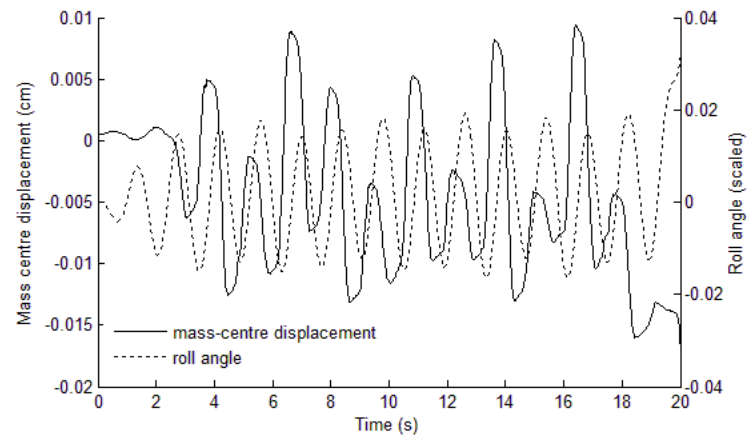


Figure 7.18 Mass centre displacement of granular media (solid) and scaled (1:2000) roll amplitude (dotted) for 2.5 cm excitation.

Further increase of excitation amplitude (no more than 3 cm) leads to similar findings (Figure 7.19).

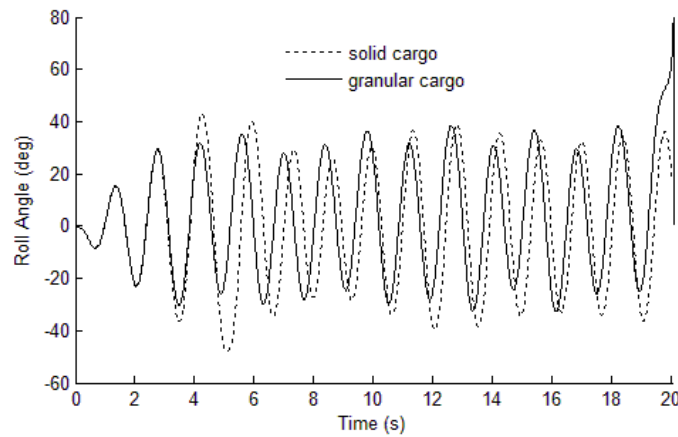


Figure 7.19 Mean (solid) and absolute (dotted), roll amplitude for 3 cm excitation. Solid marker corresponds to bulk while open to solid cargo.

7.3.3 Implementation of humidity

In the next stage we focused on the behaviour of wet granular media, confined however to the assumption of *pendular state*; that is, the liquid content (due to environmental humidity) appears establishing liquid bridges between couples of neighbouring particles, after their contact. As discussed in *Chapter 4*, the capillary force between two particles is an attractive force and in order to be used in DEM simulation, many authors presented explicit capillary force functions that, while uncorrelated with the liquid bond volume, have been proved to be accurate enough (Zhu et al 2007). In our case, a linear model for the decrease of the adhesion force when two particles are moving apart, after collision, has been adopted (Oger et al 2013).

In a series of numerical experiments based on the titling box method, following the same mathematical modelling for the capillary force with that described in *Chapter 4* for pendular state, in Lambrou (2015) it was found that, some differentiation between dry and wet cargo's dynamic response exists only when large enough rates of humidity have been assumed. Specifically, it was shown that, for humidity levels lower than 60%, the dry and wet cargo have practically identical behaviour. This conclusion was in good agreement with the findings of experiments that we performed, briefly outlined in *Chapter 9* (see also Koromila et al 2013). Furthermore, based also on comparisons between numerical and experimental results, Oger et al (2013) concluded that this model can provide accurate results only for humidity rates lower than 70%. The results presented below concern a value of 1.47 nm for

the r_K , that for our case corresponds to humidity rate close to 70%. For lower values of humidity, hardly any difference between dry and wet cargo was found occurring.

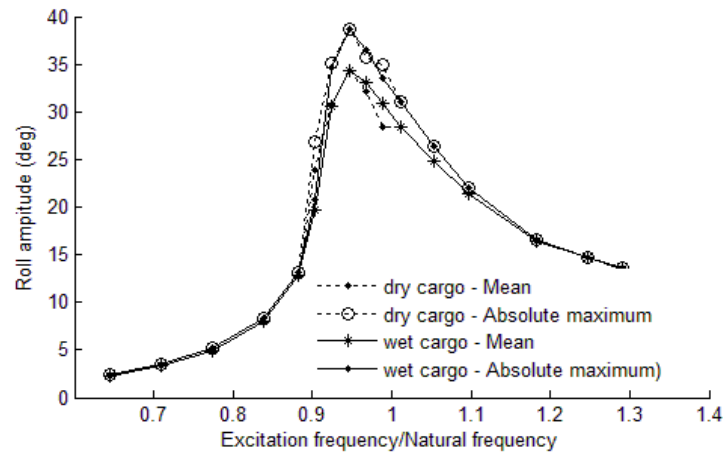


Figure 7.20 Roll response of ship with wet and dry bulk cargo for excitation amplitude 2 *cm*.

Working at the same frequency and amplitude region as for the dry cargo investigation, it was found that, for less than 2 *cm* wave amplitude, wet and dry cargo barge responses coincide at every excitation frequency. Figure 7.20 depicts this coincidence for a 2 *cm* wave excitation amplitude.

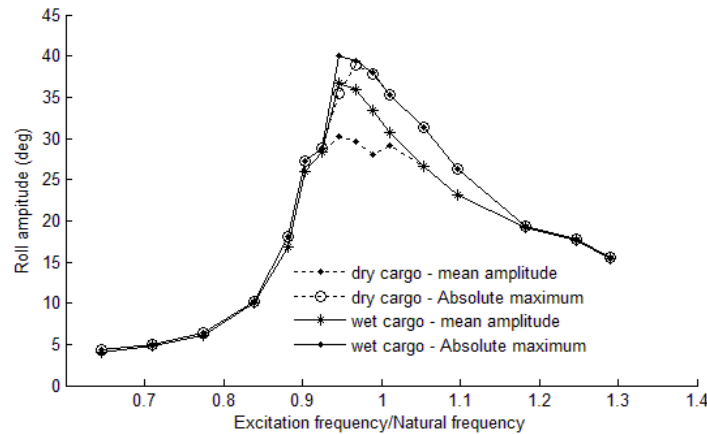


Figure 7.21 Mean amplitude and absolute maximum roll response of ship with wet and dry bulk cargo, for excitation amplitude 2.5 *cm*.

For larger values of excitation amplitude, the barge with wet cargo seems to behave slightly differently compared to its dry cargo counterpart. More specifically, when the barge enters the resonance frequency region, the material inside the tank in the case of wet cargo is more kinetic, that is, it flows more easily, and thus the barge performs larger oscillations. As a result, even though the absolute maximum value for the two systems is almost the same, the mean value for the case of wet cargo is larger. The reason behind this behaviour is the fact

that, the wet cargo appears as less prone to the hysteresis phenomenon, and thus, the shift of the material is not permanent. The same behaviour continues for larger values of excitation amplitude. In Figure 7.22 is depicted the previously discussed difference between the responses of the two systems [with wet (solid) and dry (dotted) cargo], while in Figure 7.23 is depicted the motion of the centre of mass of the two cargos, when excitation amplitude and frequency had a value of 2.7 and 4.7, respectively.

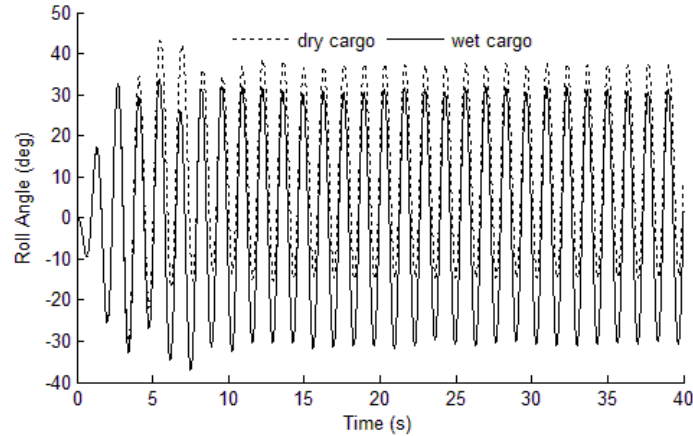


Figure 7.22 Roll response of ship with wet (solid) and dry (dotted) bulk cargo for excitation amplitude 2.7 cm and frequency 4.7 rad/s.

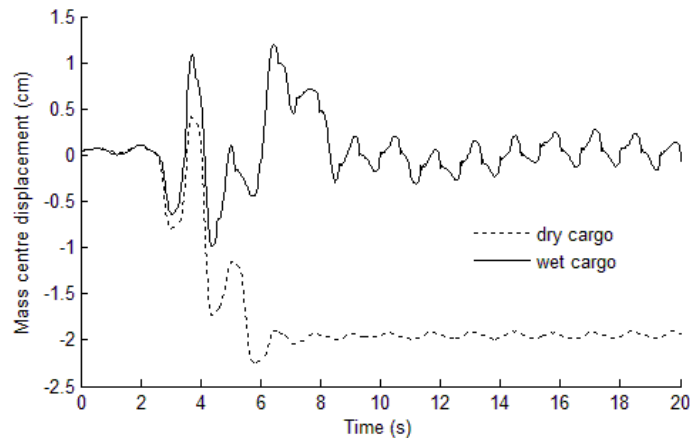


Figure 7.23 Movement of centre of mass when cargo is dry (dotted) and wet (solid) for wave frequency 4.7 rad/s (σ close to 1). Wave amplitude has a fixed value of 2.7 cm.

Despite the fact that the wet cargo proved to be more agile, we didn't identify any specific frequency and/or amplitude of excitation that leads the vessel to capsizing (other than that for the dry cargo).

7.4 Concluding remarks

A step towards a systematic numerical investigation of the coupled granular-material-and-vessel motion in regular beam seas was described. Several values of wave amplitude and frequency were applied on a scaled barge, partly filled with spherical particles of granular material in order to capture her response. Special attention was paid to the comparison of the results against corresponding cases where the cargo behaved like a rigid body, i.e. it is insensitive to vessel's oscillations.

Initially the vessel was allowed to move only in the roll direction, macroscopically performing a restricted 1-DOF motion. Later, the vessel was allowed to move in sway, heave and roll directions performing thus a 3 DOF motion. In the case of granular cargo and for wave amplitudes below a certain limit, vessel's motion is generally milder. The vessel carrying the granular cargo appears as even more stable, even though it appears having some difficulty to reach steady state. For higher wave amplitudes, an interesting region appears where, as a result of cargo's movement, the vessel shows larger response, in some cases being of sufficient intensity for bringing-in capsizes. Further consideration of this behaviour revealed that, it is related with a shift of the roll resonance peak value. Comparison of barge's response when filled with wet and dry cargo has shown that, below a critical limit of wave amplitude, hardly any difference can be noticed. Above this limit, the wet cargo becomes however more agile, leading eventually the barge to capsize sooner, but in the same frequencies that the barge with dry cargo capsizes too.

Chapter 8: Cargo with Irregularly-Shaped Particles

In this chapter a method to investigate the effect of particles' shape on the dynamics of the cargo (and eventually of the containing body) is presented. A Fourier descriptor method was developed for the construction of arbitrarily-shaped particles. Moreover, the single element Discrete Function Representation (DFR from now on) method (Hogue 1998) was adopted as the contact detection algorithm. Basic validation of our algorithm was carried out by considering the spherical particle limit and comparing the semi-static and dynamic responses of such a material with those predicted by the classical Molecular Dynamics method (Continuous Function Representation - CFR from now on). These comparisons have shown that, DFR results are accurate when the number of nodes is above some threshold. It is encouraging that, the results we obtained for our irregularly-shaped particles were in good agreement with those obtained by other scholars. Based on these results, conclusions about the accuracy of the spherical particle assumption and also, about the dynamic behaviour of irregularly-shaped particles have been drawn.

8.1 Methodology description

According to Williams & O'Connor (1995), the four principal elements of a general Discrete Element Method (DEM) Analysis are: a) Object generation, b) Contact detection, c) Physics and d) Visualization. These elements are assembled in the pipeline shown in Figure 8.1. A detailed description for the first two elements of our methodology is given next, followed by brief remarks concerning the last two elements.



Figure 8.1 Discrete Element Method (DEM) Analysis Pipeline.

8.1.1 Object generation

Main focus of the work described in this chapter is, the behaviour of a cargo comprised of slightly non-spherical particles, for various harmonic excitations. A concern, though, was also how to build a methodology that would be capable, in the longer term, of handling

arbitrary particle shapes with maritime interest. Two additional requirements were thus imposed:

- a) Generation of particle shapes that are shown to be realistic and relevant as much as possible for the maritime field. To achieve this, measurable shape parameters should be defined in association with each particle type;
- b) Particles' geometry should depend upon a function featuring random parameter(s) so that different shapes within a class (i.e. for the same shape parameters) can be created.

Inspired by what is the standard technique for the simulation of irregular ocean waves (Fourier representation based on energy spectra) we developed a Fourier-series-based particle shape representation, which however, as we found out, it had been used also to represent non-spherical particle shapes in the past by the name “Fourier descriptor method” by Beddow & Philips (1975). Specifically, the distance of a point on particle's contour from a defined particle centre is:

$$R(\theta) = R_0 + \sum_{i=1}^N [D_n \cos(n\theta + \delta_n)] \quad (8.1)$$

R_0 is the radius of a spherical particle whose as the perturbations can be considered our particles. Perturbation amplitude parameters D_n are called Fourier Descriptors while δ_n is the phase angle of the n^{th} harmonic. As discussed by Mollon & Zhao (2012), D_2 describes the elongation of the particle, thus it is one of the most important descriptors. Das (2007) suggested that descriptors D_3 to D_8 define the main irregularities of the particle contour while higher order descriptors express the roughness of the particle's surface. Meloy (1997) proved that, for sand particles, descriptor values decrease linearly with the descriptor number in a \log - \log scale. Based on this finding, Mollon & Zhao (2012) assumed the following expressions for the Fourier Descriptors in order to generate realistic packing for discrete modelling of granular materials:

$$\begin{aligned} D_n &= 2^{\alpha \log_2(n/3) + \log_2(D_3)} \quad \text{for } 3 < n < 8 \\ D_n &= 2^{\beta \log_2(n/8) + \log_2(D_8)} \quad \text{for } n > 8 \end{aligned} \quad (8.2)$$

In their work the coefficients α , β were assumed receiving the constant value -2, although this was basically for illustrative purposes and no sufficient justification was

provided. In general, these parameters express the slope (in a *log-log* scale) of the relation descriptor number and descriptor value (Meloy 1997).

In Figure 8.2 are presented two different particles created using Equations 8.1 and 8.2. The two particles have the same Fourier descriptors (Figure 8.2 up-left), but phase angles are randomly selected from a Random Number Generator (Figure 8.2 up-right). It is observed that the obtained shapes of particles are arbitrary (within the class) due to the uncertainty inserted by the phases of the harmonic components (Figure 8.2 down).

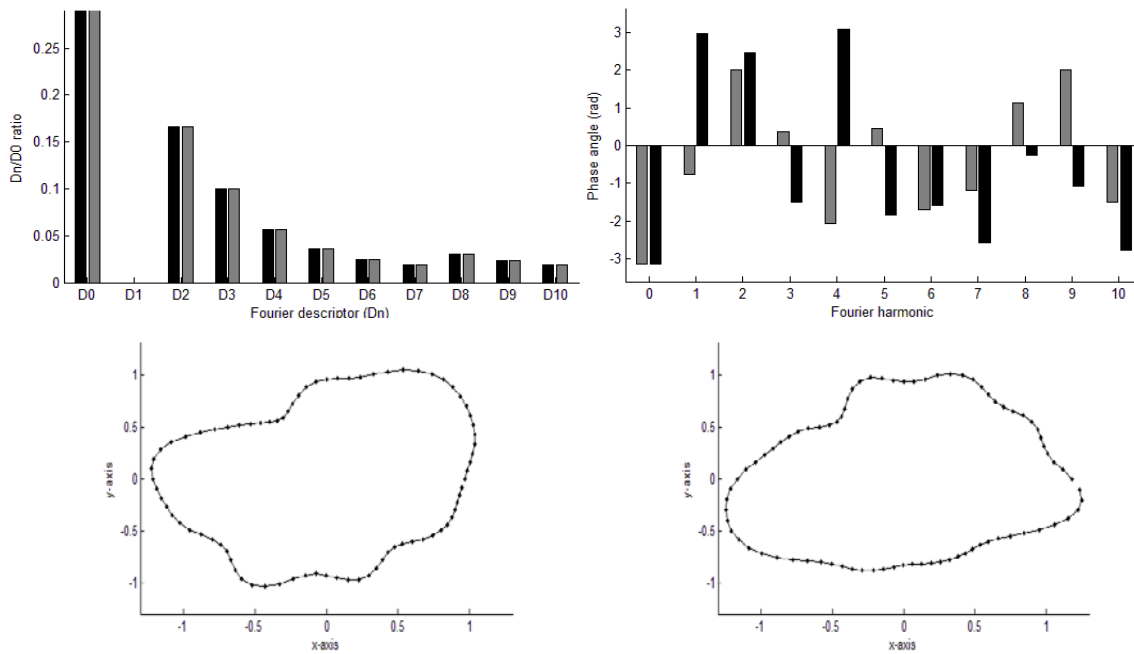


Figure 8.2 Two different arbitrarily-shaped particles created as perturbations of the same spherical (circular) particle. The same Fourier Descriptors (up-left) but randomly chosen harmonic phases (up-right) have been used. Left particle corresponds to grey while right to black distribution.

In Figure 8.3 examples of particles of common ship cargos transported in bulky form (grains and sand) inside ships are depicted. Beneath each picture, the graphical representation of the corresponding particle based on the Fourier Descriptor method is provided. Fourier Descriptors and their phase angles were selected in such a way that graphical representation to be as close as possible to the depicted particles.

The qualitative comparison of pictures and representations gives a feeling about the good potential of the method to describe realistically a variety of non-spherical particles. It has to be noted that, in the case of wheat, both side and top view of the particle are provided, due to the special form of this material. Combination of these two sides will lead to realistic wheat shape representation when 3D particles will be considered in a future extension of this work.

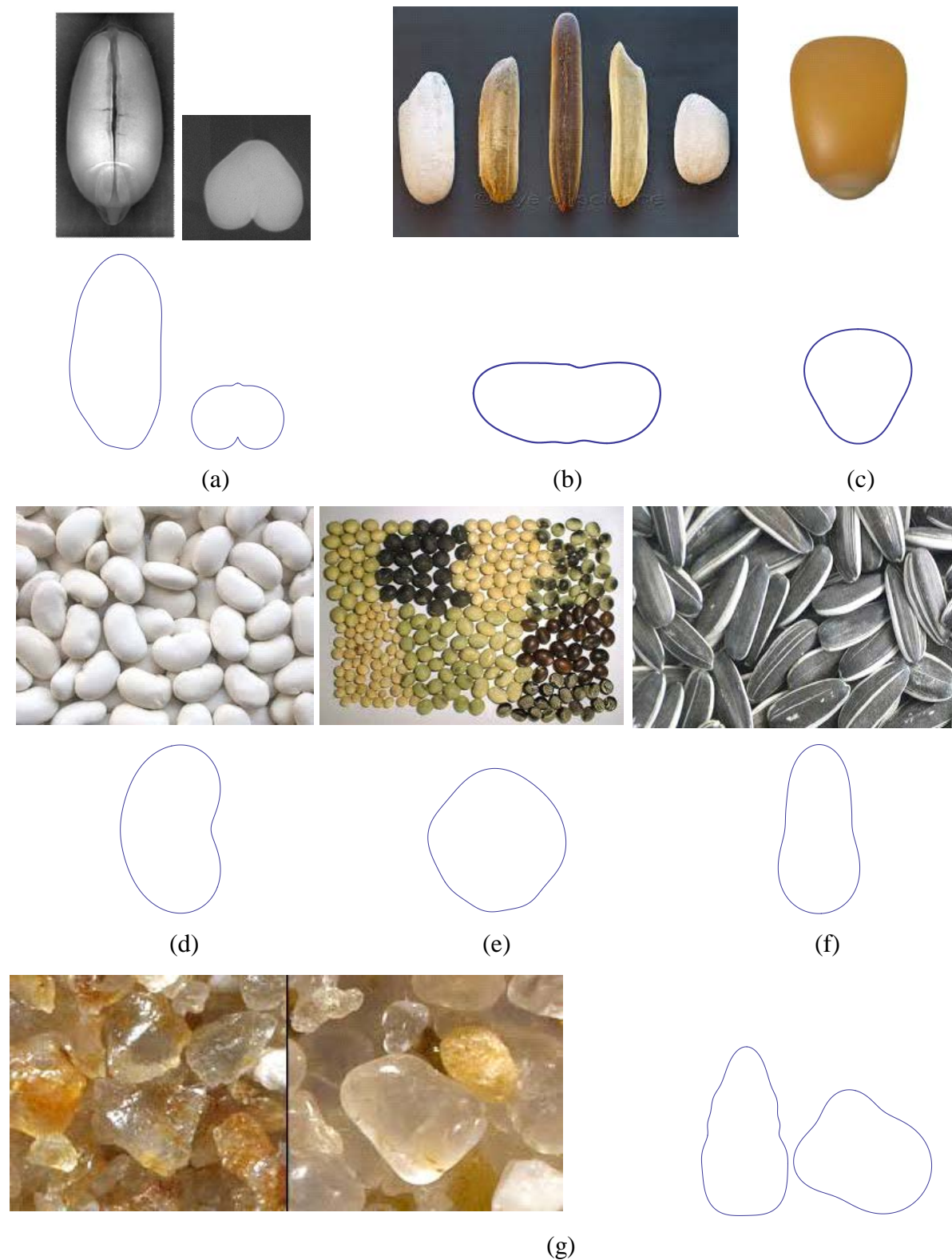


Figure 8.3 Representation by the “Fourier Descriptors Method” of conventional cargos transported in bulky form: a) wheat (similar to barley), b) rice, c) corn, d) beans (common white), e) soybeans, f) sunflower seeds, g) sand. (Sources: a) Demyanchuk et al (2013), b) <http://eyeofscience.de>, c) <http://bluetrack.com>, d-f) <http://agropol.gr>, g) <http://sandatlas.org>)

Considering all the above, it can be deduced that the Fourier Descriptor Method fulfils all our requirements:

- c) almost every smooth shape can be produced,
- d) the distribution of descriptors is linked to real measurements of geometrical features of a particle; and,
- e) the random choice of the phase of each harmonic provides the opportunity to generate slightly different shapes that obey the same shape description.

In addition, this method provides two more major advantages:

- f) it is based on an implicit function and a polar description of the particle, something very useful for future extensions of the method,
- g) moment of inertia and centre of mass can be easily calculated.

8.1.2 Contact detection

For the purpose of contact detection the DFR method described by Hogue (1998) has been used. This is quite convenient due to the featured polar description of the irregular shape through Fourier descriptors which is compatible with our method of producing a particle's geometry by perturbing a sphere. In fact, this explains also why we have applied discretization of the surface contour during particle's generation.

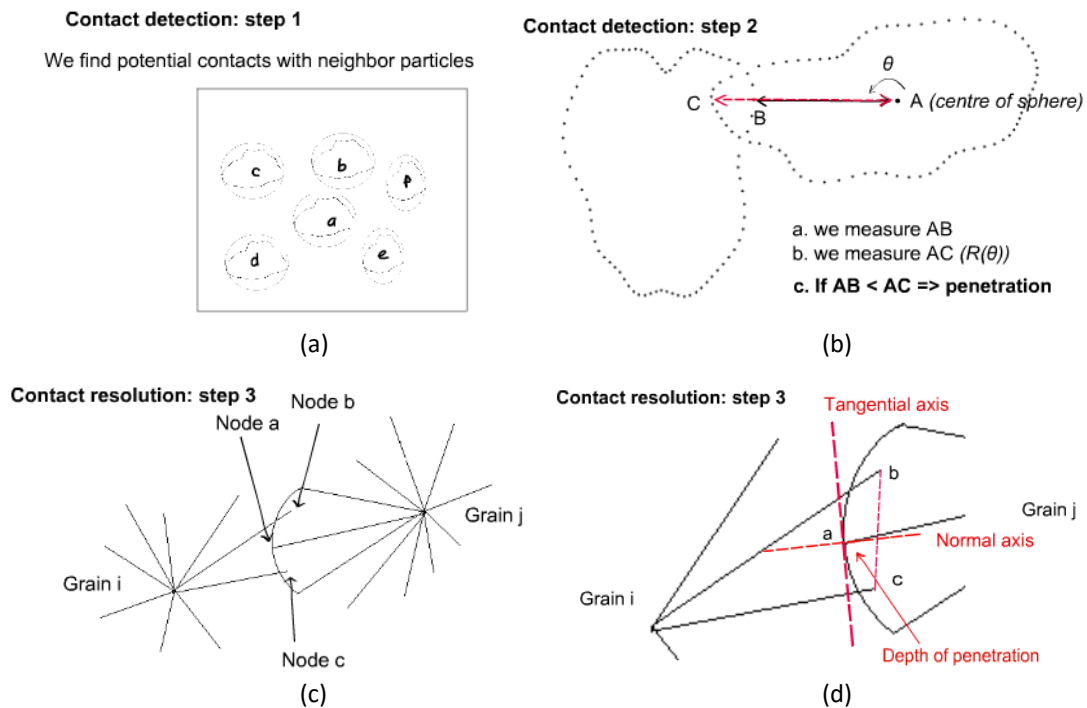


Figure 8.4 Contact detection and resolution between two discretized irregularly-shaped particles.

As described in Figure 8.4, the collision analysis consists of three distinctive steps:

- a) Initially, the algorithm searches for contacts between the circumscribed circles of all particles. Contact detection is, thus, at this stage, similar to that followed for spherical particles. Outcome of this first step is a set of potentially colliding particle pairs.
- b) During the next step, all potentially colliding particle pairs are cross-checked in order to investigate whether a collision actually occurs. In order to do that, the distance between centre of particle j and every node of particle i is measured (AB in Figure 8.4b). Based on the angle that corresponds to AB (θ in Figure 8.4b) the distance of the centre of particle j from its contour is further measured (AC in Figure 8.4b). Comparison of these two distances, provide information about collision and depth of penetration. This is the most time - consuming step and its outcome is a set of colliding particle pairs.
- c) The last step involves contact resolution for each one of the colliding particle pairs. During this stage, determination of collision details (that is, depth of presentation and direction of the normal/tangential axis of the repulsive force) is being conducted. These details will be entered as input to the calculation of particle trajectories performed in the “Molecular Dynamics” algorithm.

In Table 8.1 is shown the pseudo-code followed for contact detection and resolution of a contact between particles i and j .

Table 8.1 Pseudo-code for DFR MD simulation

Action	Description
1	Calculate distance of j particle's centre from i particle's nodes (d_{nj})
2	Calculate the angle between the centre of particle j and each node (θ_n)
3	Compare this distance with the distance of j particle's centre from its contour at this specific angle (R_θ)
4	If $d_{nj} < R_\theta$, the node is found inside particle j , hence a collision has been detected
5	Calculate the node with the greatest penetration (if more than one nodes involved)
6	Based on information about the tangential of the contour on this node, calculate the vertical distance between the node and the line connecting the two neighbouring nodes of particle i (ζ_i)
7	Repeat steps 1-6 for all j particle nodes and find ζ_j
8	Penetration distance, ζ , is the maximum of the two distances ζ_i and ζ_j
9	The normal direction of the repulsive force is assumed to be perpendicular to the tangential of the contact point.

A novel element of the current approach is that, the contact forces are calculated on the basis of the real geometric characteristics of the contact, assuming that, at their contact point, the two particles have the same tangential (which is often the real case). A limitation accruing from this is however that, the method cannot be used for simulating particles with high degree of irregularity and angularity.

8.1.3 Physics and visualisation

Whilst the focus has been set on the first two elements of the DEM pipeline, it is important to refer to the available choices for the contact forces and the visualization techniques. In order to make a direct comparison with our previous numerical experiments, we have based our effort on the non-linear Herzian contact force introduced by Brilliantov et al (1996) for the normal force and Haff & Werner's (1986) assumption for the tangential force. While more delicate contact force models could be followed (eg Lu et al 2012) incorporating different visco-elastic properties for normal and contact forces, these were judged to add to our numerical experiments, at first sight, unnecessary complication, especially for this stage of model development. A possible improvement in the future would be the replacement of these forces (especially the tangential assumption) by another model directly related to the penetration area. Calculation of each particle's mass and moment of inertia is conducted during system's initialization phase, based on particle's density (uniform density with same value as for spherical particles). At this stage the irregularly shaped particles are treated as polygons constructed by N triangles; where N is the number of nodes on particle's surface. In addition, each particle's position of gravity centre is assumed to coincide with polygon's centroid.

Furthermore, the software package ParaView has been employed for the visualization of the generated particles. In contrast, though, to the spherical case where well established filters for the visualization of the particles exist, in this case customized filters must be constructed. This is a demanding task outside of the immediate scope of our current effort, thus we have been content with the visualization, merely, of the centres of mass. As a matter of fact, each particle was represented by a single point. While missing details about particle packing and contact resolution, such an approach was found, nonetheless, to be very helpful when material's dynamic behaviour was under investigation.

8.2 Validation results and discussion

Validation of the DFR algorithm was based on three benchmark simulation tests of spherical particles:

- a) Investigation of angle of repose,
- b) Prescribed sway oscillation test,
- c) Coupled fluid-vessel-material motion.

Simulation results were compared with similar, experimentally validated, results based on CFR methods. The intention was to investigate the stability and robustness of the algorithm, as well as, to evaluate its accuracy and calculate the critical number of nodes below which results are not within acceptable limits.

8.2.1 Investigation of semi-static behaviour: angle of repose

The slightly altered tilting box method (having high-sided tank walls), described in *Chapter 5* has been imitated for the evaluation of algorithm's accuracy to predict material's semi-static behaviour. 2000 cellulose acetate spherical particles of 3 mm radius and well-known characteristics (Schafer et al 1996) are placed, with regular ordering, inside a rectangular 2D tank. The width of the tank was 0.3 m and the height of the free surface of the material from tank's bottom was 0.11 m. Tank's side walls were high enough (0.4 m) to ensure that all particles remain inside the tank during the experiments. The tank is assumed to be hinged at the left bottom corner, free to rotate anti-clockwise with different tilting rates varying from 0.3 deg/s (which is the recommended by IMO rate) to 10 deg/s. DFR numerical experiments were performed with particles of 36, 80, 120, 180, 360 and 500 nodes, leading to a maximum number of 1,000,000 nodes.

During the initial preparation of the tank it was noticed that, depending on the particles' number of nodes, a different free surface configuration was obtained. It is recalled that, in *Chapter 5*, we found that the angle of repose shows some weak dependence on the free surface configuration. In order to take this dependency into account, each numerical experiment was repeated several times (12 times except for the 500-node particles where only 3 repetitions were performed), then the mean value and standard deviation of the obtained angles were determined.

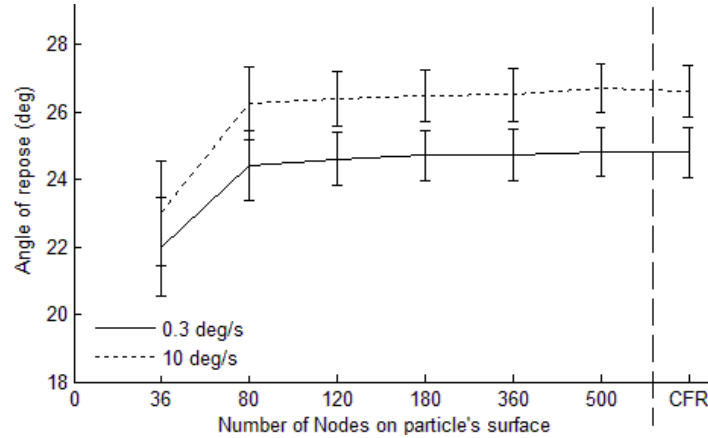


Figure 8.5 Predicted angle of repose according to CFR and DFR (with various node numbers) methods. The tilting box method is performed for two different tilting rates (0.3 and 10 *deg/s*).

In Figure 8.5 are summarized the results of numerical experiments for DFR, providing also a comparison with corresponding results based on CFR DEM. As the two applied tilting rates are vastly different, they provide a good basis for assessing the adequacy of discretization. When particle's contour is discretized by more than 120 nodes, the calculated by the DFR method angle is very close to that calculated by CFR DEM (deviation less than 0.5%). The number of 80 nodes seems to be the threshold of acceptance, since, for such number, DFR results in slightly larger predicted angles, with a calculated deviation from the real value close to 2%. When less than 80 nodes are considered, this deviation is amplified quite rapidly. For example, when the surface contour is discretized by 50 nodes, a difference close to 2 degrees (deviation close to 8%) between the calculated by DFR and CFR DEM has been found.

8.2.2 Dynamic behaviour – sway oscillation

In the second kind of numerical experiment performed, the tank was forced to oscillate in prescribed sway motion. We kept the same tank dimensions and filling ratios, as before, while we assumed harmonic oscillation of the tank, with the amplitude and frequency of this oscillation serving as the control parameters. Three different amplitudes were tested (2, 5 and 10 *cm*), while the frequency range was between 0.2 and 2 *Hz*. Once again, experiments of the same specification were repeated for particles comprised of 36, 80, 120, 180, 360 and 500 nodes. The dynamic responses of cellulose acetate particles, predicted by DFR simulations, were under evaluation, calculating the shift of the material's mass-centre inside the tank, at every time-step.

In Figure 8.6 are contrasted the predicted mass-centre displacements obtained by 120-node-particle DFR and CFR simulations. Excitation amplitude 5 cm and a frequency 1.8 Hz are applied. As shown, after an initial transient period where the material inside the tank rearranges itself, the two methods predict similar dynamic behaviour.

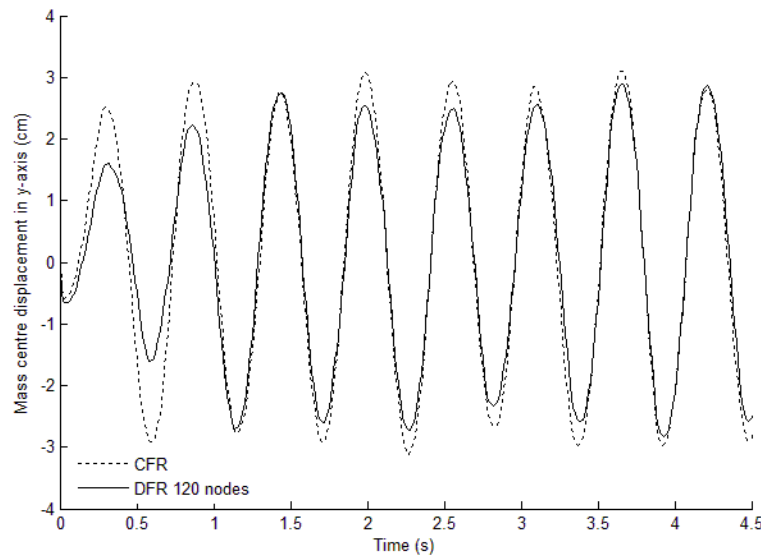


Figure 8.6 Mass-centre displacement (*y*-axis) when DFR with 120-node-particles (solid) and CFR (dotted) simulation is used. Excitation amplitude 5 cm and frequency 1.8 Hz are considered.

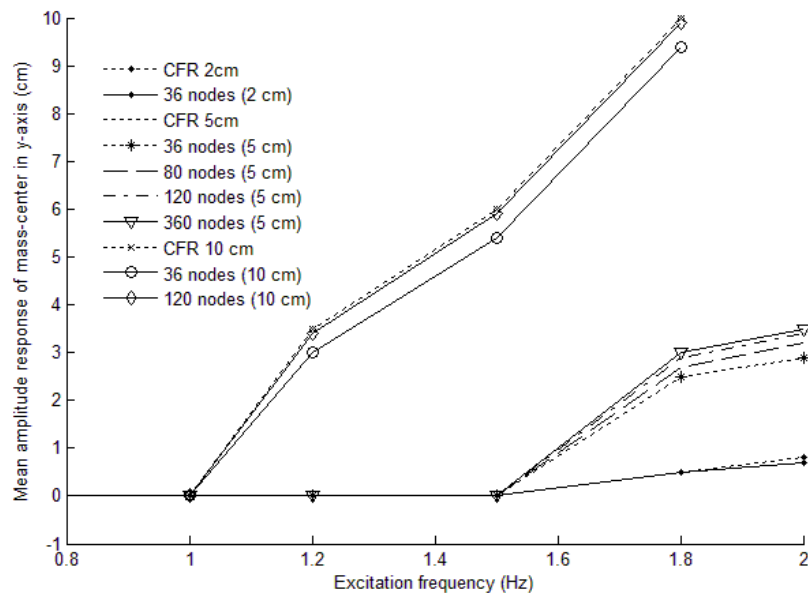


Figure 8.7 Mean amplitude response of mass-center (along the *y*-axis) for different values of excitation frequency. The tank is forced to oscillate with a prescribed motion.

Working in a similar manner for every DFR case, Figure 8.7 was produced, where the mean amplitude response of the mass-centre (along the *y*-axis), for different values of

excitation frequency, is graphically presented. Each DFR simulation outcome is presented against its CFR simulation analogue. Two are the principal findings:

- a) For more than 120 nodes, the dynamic behaviour of the particles is almost identical with that obtained from CFR simulation (the results for more than 360 nodes are not included in Figure 8.7).
- b) As the nodes become fewer than 100 however, an increasing deviation between DFR and CFR simulation results is noted. Quantitatively, the deviation amounts to less than 0.5% difference for more than 120 nodes, 2% for 80 nodes and 7% for 36 nodes.

8.2.3 Coupled fluid-ship-material motion in 3 DOF

Feeling confident that DFR simulation with more than 120-node particles leads to accurate results both for semi-static and dynamic tests, a third kind of numerical test was performed. This time a scaled barge hold model, with same shape and dimensions with the tank used during the previous experiments, was assumed. The rectangular barge was allowed to move in 3 degrees of freedom (DOF) under the effect of harmonic “beam-sea” waves. In *Chapter 7*, based on an identical configuration, we evaluated the effect of the granular material’s motion on barge’s response. It was shown that, the dynamic behaviour of the material becomes influential when waves with amplitude more than 2 *cm* are considered.

The numerical experiments were performed, hence, for the DFR model with 120 nodes. Wave amplitude of 2 *cm* and frequency in the range between 3 and 6 *rad/s* were selected. In Figure 8.8 is shown the barge’s mean roll response amplitude when CFR (dotted line) and DFR with 120 nodes (solid line) simulations are realised. Comparison of the two curves confirms that the DFR model with 120 nodes per particle can be successfully applied for coupled ship-cargo simulations.

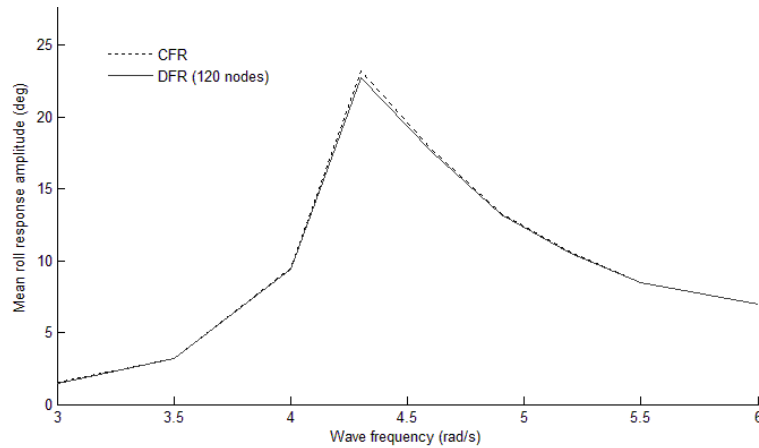


Figure 8.8 Mean roll response amplitude of the scaled barge model when wave amplitude of 2 cm and frequency range between 3 and 6 rad/s is considering. CFR (dotted line) and DFR (solid line) with 120 nodes are considering.

8.2.4 Discussion

Before leaving this section it is important to answer three questions that may have reasonably arisen by now:

- a. What did we prove by these three experiments?

The numerical experiments conducted for the spherical particles showed that DFR with more than 120 nodes can provide accurate enough results compared with same predictions of CFR simulation; that is, the DFR and CFR methods yield very similar results. The accuracy, though, against experimental results has to be separately investigated.

- b. Does it mean that we can perform experiments with irregular shaped particles?

The earlier proven validity of DFR simulation for the limiting case of spherical particles does not necessarily mean that the algorithm can provide accurate results for irregularly shaped particles in general. What was proven is that the algorithm is robust and stable when lots of nodes are considered. Thus, any variation from spherical shape has to be i) small enough in order not to enter into some unexpected numerical instability due to the algorithm and gradually get unreasonably increasing values and ii) be validated through comparison against experimental and/or well established numerical results.

8.3 Numerical experiments with irregularly - shaped particles

Our methodology was further applied for numerical experiments with irregular shaped particles. Each particle was constructed as a perturbation of a spherical particle with radius

R_0 3mm. In order to take into account the essence of the previous discussion, each particle's contour was discretized by 200 nodes. A rectangular tank with same dimensions as before was filled with 2000 free-to-move particles and two different series of experiments were conducted, investigating the dependence of material's behaviour upon the Fourier descriptors and the phase angles of the harmonics, respectively.

8.3.1 Dependence of the angle of repose upon the Fourier Descriptors

In order to investigate the dependence of material's behaviour upon the Fourier descriptors, we constructed particles that had only one nonzero descriptor at each time. In Figure 8.9 are presented some examples of obtained particles when the most important Fourier descriptors D_2, D_3, D_4 and D_8 are considered. The corresponding phase is also zero since, any other value of the harmonic phase at this occasion would simply result in the rotation of the particle around its own axis. The descriptor values are normalized against the radius R_0 which is the radius of the initial spherical particle. As shown, nonzero D_2, D_3, D_4 or D_8 Fourier descriptors result to ellipse-, triangle-, square- or octagon-like particle shapes, respectively.

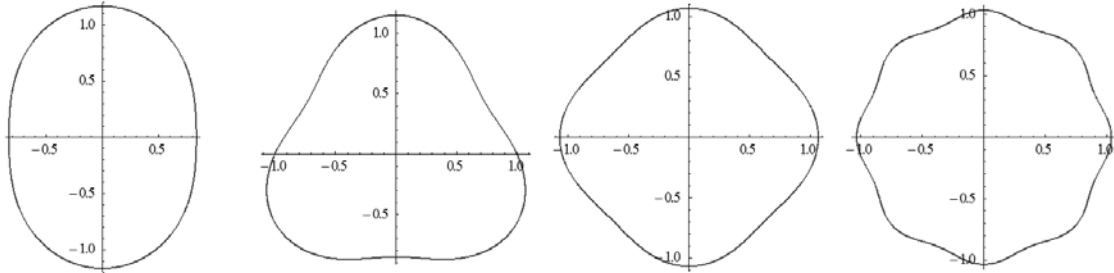


Figure 8.9 Particle shapes described by Fourier representation of a perturbed spherical particle when only one descriptor (D_n) is nonzero. From left to right: D_2, D_3, D_4, D_8 .

Four series of “tilting box method” numerical experiments were conducted, with inclination rate of 10 deg/s. All particles had the same, single nonzero, descriptor value per numerical experiment. The second and third descriptor were allowed to take any value in the range of 0-0.5 mm, while the fourth and eighth in the range of 0-0.2 mm. The initial orientation of the particles was random, controlled through the phase which was set randomly by means of the uniform distribution. Each experiment was performed 12 times in order for the mean value and the standard deviation of the angle of repose to be calculated.

In Figure 8.10 is summarized, in a graphical way, the dependence of the angle of repose on the descriptor value. The angle of repose has been normalized by the one predicted for spherical particles. Three are the main results:

- a) Larger descriptor values lead to less kinetic particles and thus to a larger angle of repose. This result is in good agreement with Lu et al (2012).
- b) For relatively low values of descriptors (e.g. for D_n/D_0 values less than 2) the dynamic behaviour of a bulk material consisted of spherical particles is very similar to that of irregularly shaped particles (normalized angle of repose value close to 1). This means that the spherical particle assumption could be quite accurate for predicting the dynamic behaviour of cargo consisted of slightly irregularly shaped particles.
- c) Deviation of the predicted angle of repose values between similar experiments is large enough (about 10 %). This is mainly due to the initial difference in particles packing between different simulations. As shown, this deviation is large for the case of D_2 where the vertical orientation of the particles is crucial for the determination of the angle of repose. It is even larger in the case of D_3 and D_4 where the triangularity of the particles leads to totally different initial packing configurations.

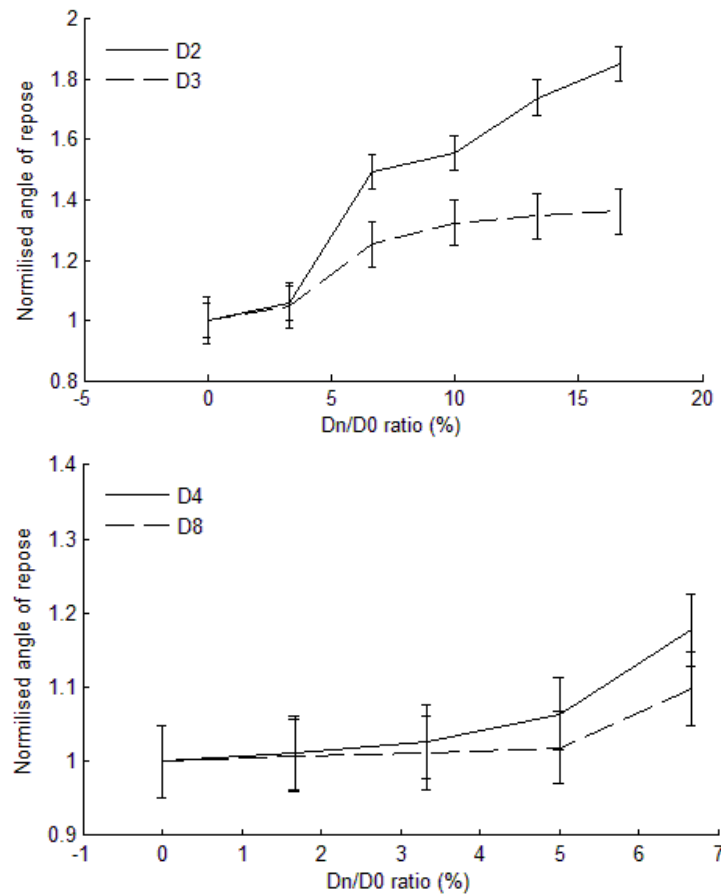


Figure 8.10 Predicted angle of repose when only one descriptor (D_n) is nonzero.

8.3.2 Dependence of angle of repose on phase angle distribution

Two categories of particles were constructed: a) in the first, only very small values of the Fourier Descriptors were used. In this way the particle's contour was very close to that of an ideal spherical particle but with some degree of anomalies on its surface. b) In the second category, the Fourier descriptors had larger values. Specifically, D_2 , D_3 and D_8 were selected so that the particle's shape to be far from that of a spherical particle.

In Figure 8.11 is graphically presented the corresponding distribution of Fourier Descriptors. In Figure 8.12 are depicted sample particles from each category, contrasted with a spherical particle.

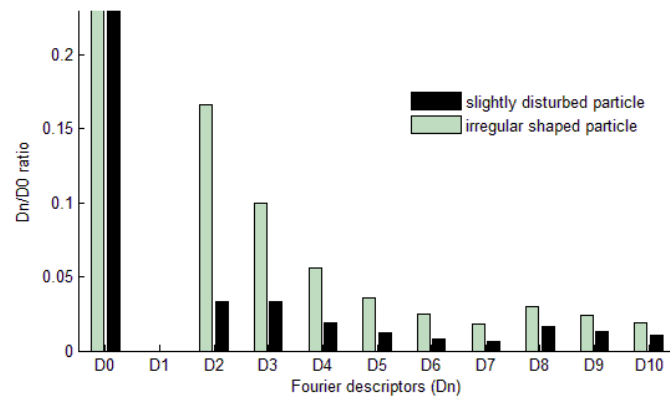


Figure 8.11 Distribution of Fourier descriptors for the two categories of particles: a) slightly disturbed spheres (black) and b) fully irregular (grey).

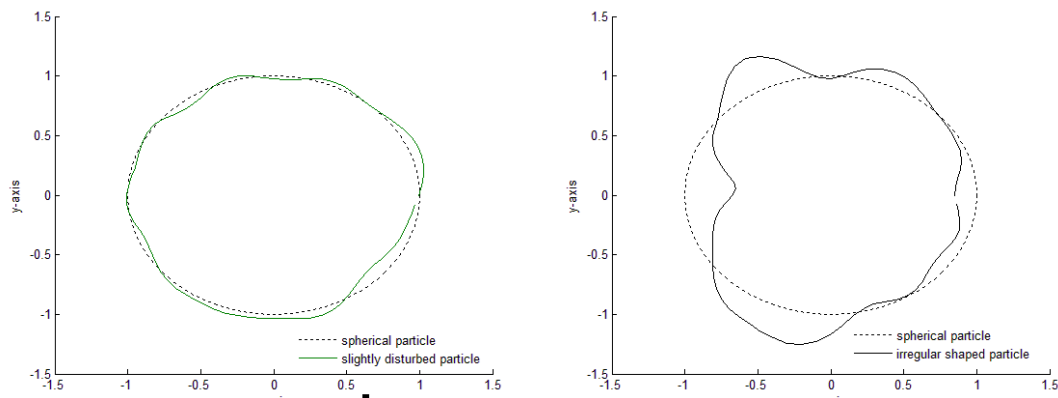


Figure 8.12 Examples of slightly disturbed (left) and irregular shaped (right) particle, compared with a spherical particle (dotted line).

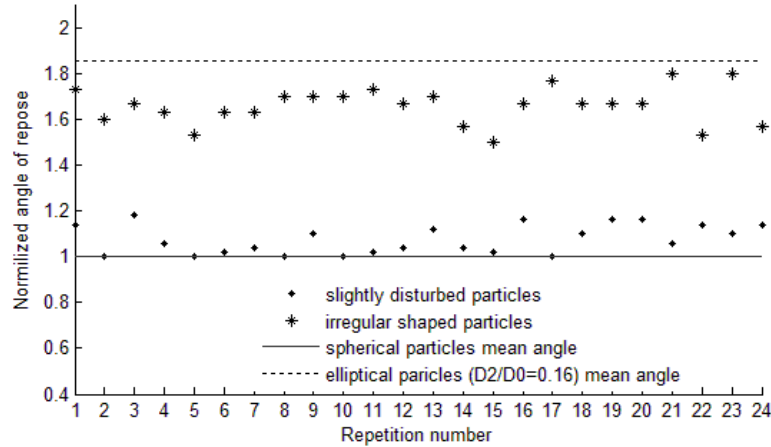


Figure 8.13 Predicted angle of repose for fixed Fourier descriptors (D_n) and various randomly chosen harmonic phase angles. The solid line corresponds to the mean angle of repose for spherical particles, computed by CFR; and the dotted line to the mean angle of repose for particles having D_2 as the only non-zero value descriptor ($D_2/D_0 = 0.16$). The value of the angle of repose for the case of slightly disturbed particle is depicted with a dot while for the case of irregular shaped particle with a star.

We constructed 25 different initial configurations of the tank for each category, by keeping the descriptor values fixed and allowing the phase angles to take any arbitrary value within a specific range between different configurations; that is, all the particles of each configuration were identical but different than every other configuration's. The titling table method was further applied with a tilting rate 10 deg/s and the angle of repose value was calculated as the angle where the material, for the first time after the initial transient period, started to flow. In Figure 8.13 is summarized the outcome of these experiments. The values are presented in sequential order without taking any care for clustering these values.

It is noticed that, for slightly disturbed spheres, the predicted angle of repose is very close to that predicted for spheres. Actually, there is a small deviation to slightly higher values but this deviation is inside the statistical error range. The outcome is totally different when particles from the second category are considered. In that case, the numerical experiments showed that the material inside the tank is less agile than spherical particles and has a mean value of angle of repose 1.7 times higher. This value is closer to that predicted for the elliptical particles. A second interesting finding is that the deviation of the predicted values between different experiments is very large. As shown, for different experiments, the angle has a value in the range of 1.4 to 1.8 times higher than that of the spherical particles. The highest value was predicted for experiments #21 and #23 which were intentionally selected to have 0 and π phase angles for all harmonics (non-random selection).

8.3.3 Shipboard test method

Going one step further, we investigated the effect of particles' shape upon the angle of repose, using the "shipboard method" detailed in IMO (2012a). Specifically, we repeated the numerical experiments described in Appendix D for the case of spherical particles, using the slightly disturbed spheres presented in Figure 8.12. The funnel was partly filled with 2500 particles and then it was allowed to move in the vertical direction with low velocity (2.5 *cm/s*), so that, the funnel's tip remains all the time very close to the top of the formed pile (at approximately 2 *cm* distance). Once again, the test was repeated 12 times. In Figure 8.14 are presented, in a comparative manner, the results for irregularly shaped and spherical particles. It is obvious that the shape affects the predicted angles. Specifically, the mean value of the predicted angle of repose for the non-spherical particles is about 2.5 *deg* higher than the one predicted for spherical particles on the basis on the same method. In addition, it is found that the predicted angle by the "shipboard test method" for the irregular particles is 4 *deg* lower than that predicted by the tilting box method, for the given material. This result is in good agreement with the reference value of 3 *deg* that IMO (2012a) suggests as the difference between the angles predicted by the two methods (the angle predicted by the "shipboard method" has always lower value).

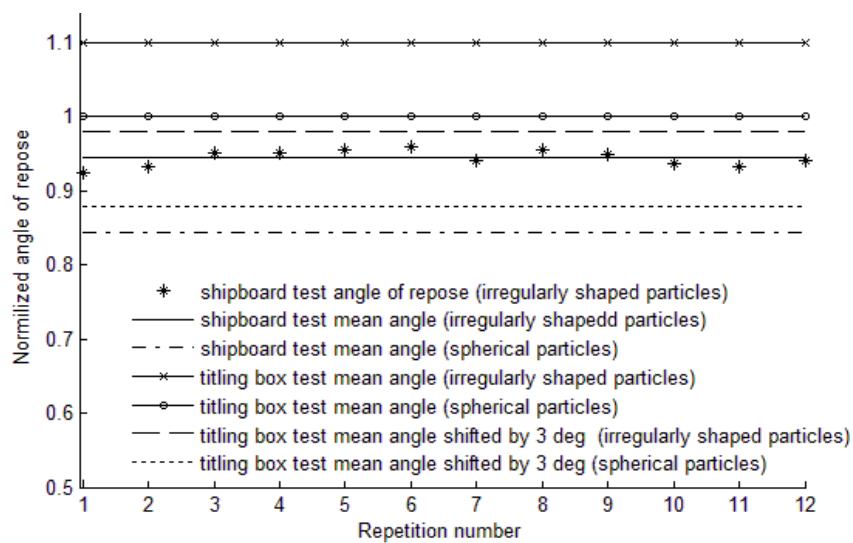


Figure 8.14 Predicted angle of repose for spherical and irregularly shaped particles by the alternative "shipboard" test method.

8.4 Concluding remarks

A single element method for investigating the dynamic behaviour of arbitrarily-shaped particles was presented. The new method combines the Fourier Descriptor Analysis for the representation of particle's shape, with the Discrete Function Representation Technique for the contact resolution. The time expense of the algorithm proved to be a challenging issue and additional optimization techniques need to be investigated in the future for improving efficiency.

Validation of the algorithm was based on comparisons against numerical experiments with spherical particles. Different kinds of experiments, examining semi-static and dynamic behaviour, were conducted. The predicted results were compared with those predicted by the Molecular Dynamics algorithm of *Chapter 3*. As found, the results of the two algorithms are in good agreement when a sufficient number of nodes is used for the discretization of the particle's surface contour. Specifically, it was shown that for more than 120 nodes the results are almost identical, while for less nodes there is a significant deviation (eg 8% for less than 50 nodes).

Two different series of experiments were conducted, investigating the dependence of material's behaviour upon the Fourier descriptors and the phase angles of the harmonics. Results of the first series showed a strong dependence of the angle of repose especially on the second and third descriptor (D2 and D3, respectively). The results are in good agreement with results of similar numerical experiments conducted by other scholars (eg Lu et al, 2012). Based on the results of the second series, we may deduce that a spherical particle representation can provide accurate enough predictions when the physical shape of the particles is slightly irregular (deviation 5%). But for very irregular shapes of particles, the prediction of this angle is strongly connected to the packing of the material inside the tank.

Chapter 9: Experimental reproduction of key results

Validation of our numerical results in the previous chapters was primarily based on experimental or numerical tests presented by other scholars. Although very useful for our investigation, this kind of validation involves a basic restriction: they are, in many cases, different than those needed for our work. As a matter of fact, we have proceeded to the experimental reproduction of our main numerical findings. Our motivation on this stage is twofold: a) to examine the efficiency of the algorithm to predict in a qualitatively manner the behaviour of granular materials and b) to evaluate its accuracy on providing quantitative results. In addition liquefaction of granular materials in a rectangular container has been experimentally investigated. The intention was to develop some qualitative understanding on how liquefaction comes about for materials of different properties.

9.1 Experimental Setup

The NTUA “shaking table” equipment, with capability of motion in 6 degrees of freedom enabling deterministic as well as random vibrations of large amplitude, was used (Figure 9.1). Six time histories represent the input (prescribed) motions that are applied on the moving table platform and hence on the tank: the three rotations (roll, pitch and yaw); and the three translations (surge, sway, and heave). Motions can reach $\pm 30 \text{ deg}$ and $\pm 0.5 \text{ m}$. An interface program reads these time histories and computes the required actuator movements that set in the prescribed motion the table platform. Calibration/ measurement of table’s motion is achieved by real time PID loops controlling the six actuators and by use of a table-mounted Miniature Attitude Heading Reference System (AHRS) with GPS that reports to the main PC the exact position of the table at any time. Dynamic data acquisition software enables interactive setting of measuring conditions and sensor information.

For the execution of experiments we used a rectangular tank made from non-coloured Perspex of 20 mm thickness and dimensions: 34 cm length, 23 cm width and 15 mm height. A Greek variety of Chickpeas (*Cicer arietinum*) with particles’ diameter varying in the range of 4 - 12 mm and mean weight of 0.145 gr was selected as granular material cargo (Figure 9.2 left). Selection of this material was mainly based on its shape that could be described as perturbed sphere (Figure 9.2 right) and provides the opportunity to accomplish both of our tasks.

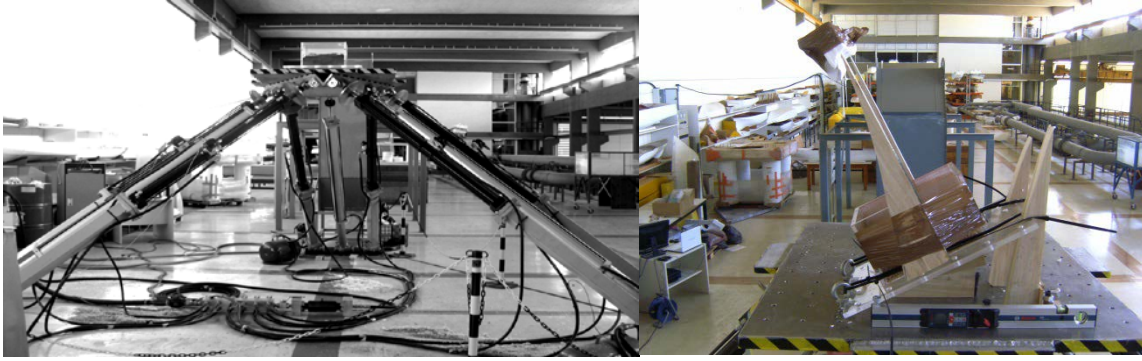


Figure 9.1 Experimental setup: a) the 6 DOF shaking table and b) tank monitoring configuration.



Figure 9.2 A Greek variety of Chickpeas (*Cicer arietinum*) with particles' diameter varying in the range of 4 - 12 mm were selected as granular material cargo.

To examine the behaviour of this material we performed several experiments with prescribed motion of the tank in sway, heave and roll axis. It was shown that, within the frequency/amplitude range of our setup, the material is practically insensitive to the external excitation. Thus, we have restricted our investigation on semi-static behaviour following the tilting box method described by IMO (2012). It has to be noted that, since our experimental apparatus has a 30 *deg* limitation and the material starts flowing after that angle has been reached; a wooden wedge was used in order to give an initial inclination of 27.5 *deg* to the tank. This way, angles close to 55 *deg* could be reached.

9.2 Evaluation of qualitative efficiency of simulations

A series of tests were conducted in order to evaluate the qualitative efficiency of our algorithm to predict granular material's behaviour. Each time, all but one critical parameter were kept fixed; that is, only the tilting rate, filling ratio, tank width or free surface configuration was changing each time. Each test was repeated 6 times and the mean values and standard deviation of critical angles were calculated. It was found that, in every case, the

experimental results were in good agreement with the numerical predictions; meaning that, the experimental reproduction of key results confirmed the validity of our suggestions, deriving from numerical studies, about granular material behaviour and its dependence upon critical parameters.

9.2.1 Response of granular material under slow tilting

Initially, we focused the investigation on material's response when a slow tilting rate (0.5 deg/s) was applied on the tank. The height to-width ratio was close to the value 0.3. The tank could move from its initial position up to an angle of 45 deg anticlockwise and 27.5 deg clockwise (passing thus from the 0 deg position). In Figure 9.3 is illustrated the status of material inside the tank at three different time instants, for two of the six tests performed in total. The selection of these two was based on the difference of their initial free surface configuration. For the upper case the surface was almost horizontal; while for the lower case its initial configuration was slightly uneven.



Figure 9.3 Slightly disturbed (up) and disturbed (down)

As shown in Figure 9.3, the transition from the static to the dynamic state is not reached in one step (i.e. as soon as a critical angle is exceeded) but the material exhibits, for a range of angles, a “stick – slip” behaviour. Until a tilting angle value of 37 deg has been reached, the free surface of material is practically not moving (left). After that angle, the free surface starts to flow but only for a while, until a small heap of particles is formed (middle). After this heap formation, the free surface stops flowing; however it starts to flow more massively

when another critical angle, considered to be the angle of repose, has been reached, at 41.3 deg (right).

It is notable that, almost the same value for the angle of repose was measured, irrespectively of the initial free surface configuration, although the material behaves in a very different way prior reaching this value. When the disturbed free surface configuration is considered, the initial heap formation is substantial and one might erroneously associate it with the angle of repose. Interestingly, after the angle of repose has been reached and while the tank continues its slow tilting, the granular material starts behaving in the same manner irrespectively of the initial free surface configuration. That is, it continues its static behaviour until a second critical angle is reached where it starts flowing again.



Figure 9.4 Time shots of the tank with filling ratio 0.3 after a) the second critical angle of 48.5° and b) initial position for the second time, has been reached

In Figure 9.4 (left) is presented a time instant of the tank, right after the second critical angle of 48.5 deg has been reached. In Figure 9.4 (right) appears a snap-shot when the 0° inclination has been reached for the second time (i.e. the tank has returned to the horizontal position). It is prevalent that significant hysteretic behaviour is realised, in the sense that the material practically sustains the shifted configuration acquired when the 40° tilting had been applied.

9.2.2 Scaling effects

In order to investigate the effects of tank scaling upon material's behaviour we performed the same kind of testing to more than one tanks. Specifically three smaller tanks, with inner widths 10, 15 and 20 cm were used. The tilting box test was repeated six times for each one of the tanks with the same tilting rate (0.5 deg/s) but different filling ratio ($h/l = 0.2, 0.267, 0.3$). Due to the polymorphism of the particles (varying diameters) for the filling of the smaller tanks the Quota Sampling Method has been used. Specifically the particles of

the larger tank were grouped according to their diameter. Each group was assigned a specific weight number calculated as the ratio of the number of the particles of the group to the total number of particles. The smaller tanks were filled by random selection of the proper number of particles from each group based on its weight. Every repetition of the experiment was performed with different sample that was constructed with the same methodology in order to eliminate the possibility of erroneously selection of particles during the random selection process. In Figure 9.5 is presented, in a graphical way, the mean value of the angle of repose as the tank width is increased. The standard deviation has been calculated as the mean square sample-to-sample fluctuation.

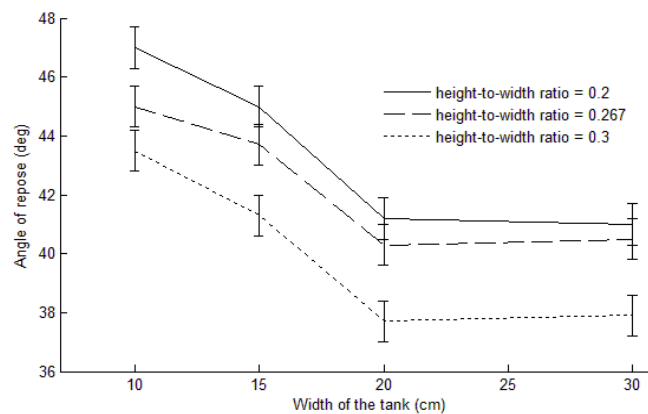


Figure 9.5 Mean value of the angle of repose as the tank width is increased.

As noticed, for smaller than a critical value of tank width (20 cm) there is a dependence of angle of repose on tank's width, in the sense that the smaller the tank the larger the predicted value. After that critical value, the same value for the angle of repose was measured.

9.2.3 Different filling ratios and tilting rates

Based on the results of the previous paragraph the larger tank (30 cm inner width) was used for the rest of our tests. As a next step, the dependence of system's behaviour upon filling ratio and tilting rate was investigated. Five different height-to-width ratios ($h/l = 0.2, 0.267, 0.3, 0.4, 0.467$) and three different tilting rates (0.5, 1 and 5 deg/s) were tested. Filling ratio was chosen in such a way that, material's depth inside the tank to be characterized as *intermediate* in the first two, as *critical* in the third and as *finite* in the last two cases. This characterization follows the convention when liquids free surface sloshing is under investigation (Faltinsen & Timokha 2009). It is recalled here that, for liquid cargos, the critical depth ($h/l \approx 0.33$) corresponds to that depth where strong changes in liquid's

behaviour occur, for excitation frequencies close to the lowest natural frequency. In Figure 9.6 are presented three of the five different filling ratios that have been under investigation.

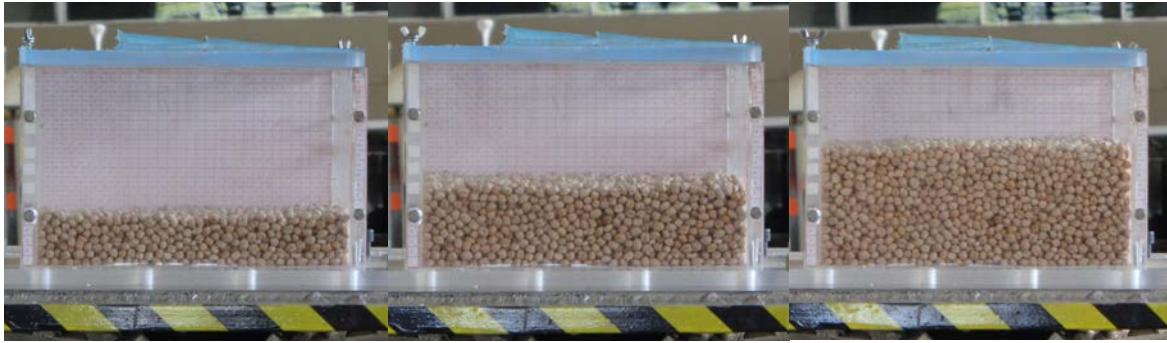


Figure 9.6 Three of the five different filling ratios under investigation: 0.2, 0.3 and 0.467 from left to right respectively.

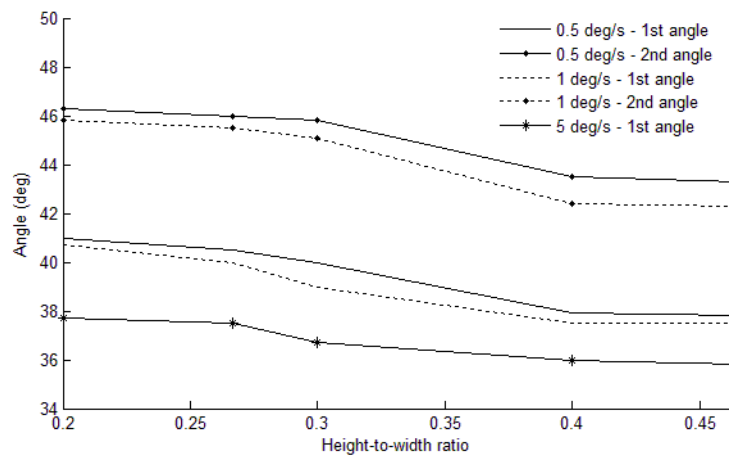


Figure 9.7 Dependence of critical angles upon height-to-width ratio for three different tilting rates. The 1st angle corresponds to angle of repose while 2nd to next critical angle.

Figure 9.7 summarizes the measured results for all filling ratios and tilting rates. Both the mean value of the angle of repose (1st angle) and the next critical angle (2nd angle) have been included. Three are the key findings of this investigation:

- Below finite depth area larger filling ratio leads to smaller angle of repose. The variance of the measured angle between different scenarios has a significant value, which in some cases equals to almost 3 degrees. In contrast, for higher values of filling ratios (above finite depth area) the measured angle of repose seems to be fixed and in-dependent of material's depth.
- For finite depth only the upper layers of material are moving. For smaller filling ratios some layers at the bottom of the tank tend to stay motionless, but due to friction effects they start flow after a while and thus all layers finally participate the motion. This means that for intermediate depth two distinct large displacements can be

measured when the critical angles have been reached, in contrast to the finite depth case, where two small displacements of material occur. As a result stick-slip phenomenon is more obvious for intermediate material depths. Figure 9.8 presents the displacement of the material right after the first material flow has been stopped.



Figure 9.8 Displacement of the material right after the first material flow has been stopped for two different filling ratios (0.2 and 0.467, left and right respectively) and tilting rate 0.5 deg/s .

- c. Small tilting rates result to the same angle of repose, although small variations occur (slightly larger angles for larger tilting rates). For larger tilting rates the measured angle is significantly smaller. Material on this occasion starts flowing when a critical angle, close to that of heap formation has been reached and stops flowing only after the 2nd critical angle have been crossed. Thus the stick-slip behaviour of the material between the angles of heap formation, angle of repose and 2nd critical angle is practically non-existent.

9.3 Evaluation of simulation results' accuracy

In order to analyse the accuracy of our algorithm on providing quantitative results, we compared our experimental results with similar derived by simulations. A tank with same dimensions with that used for experimental tests was numerically constructed and partially filled with particles up to a depth of 12 cm . Materials consisting of spherical or irregular shaped particles were assumed. In order for our simulation to be as much realistic as possible we focused on three topics: a) particle size distribution, b) particle shape and c) particles' properties.

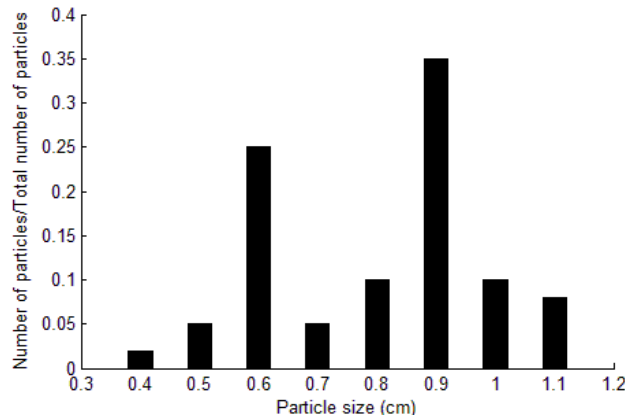


Figure 9.9 Particle size distribution used in experiments.

Figure 9.9 graphically presents the size distribution of the particles in our experimental material. Due to the elliptical-like shape of the particles the dimension of their maximum axis was measured. As shown more of the 60% of the particles have size of 0.6 or 0.9 *cm* and the rest of them are distributed between these two values.

Initially the tank was filled with spherical particles that followed the same with experimental material size distribution. Furthermore the tank was filled with irregularly-shaped particles that were constructed using the Fourier Descriptor - Discrete Function Representation (FD-DFR) method presented in *Chapter 8*. Two different irregularly-shaped particles were constructed as perturbations of spherical particles with diameters 0.6 and 0.8 *cm*. Granular cargo inside the tank had an analogy of particles equal to 35.2 - 64.8, with larger particles being the majority. Figure 9.10 (left) presents the distribution of the two sets of Fourier Descriptors. Figure 9.10 (right) presents an example of the shape of these materials.

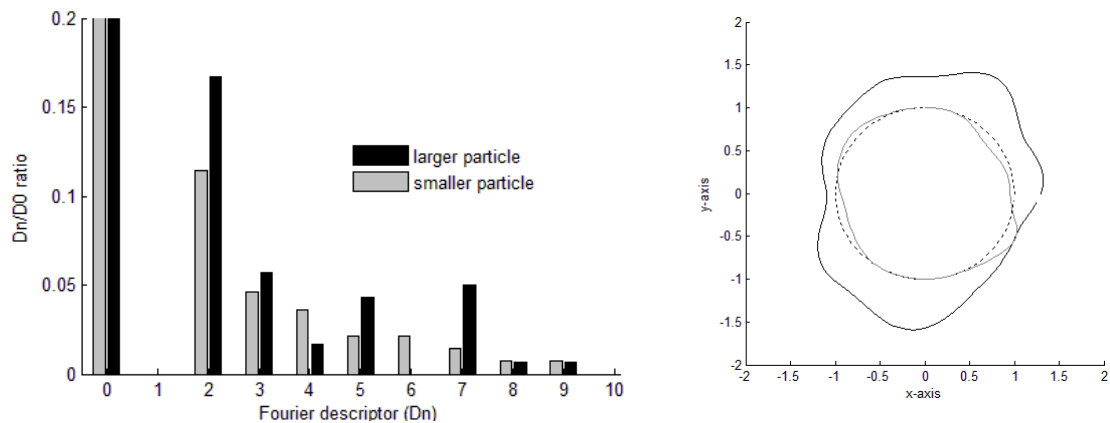


Figure 9.10 Distribution of Fourier Descriptors (left) and general form (right) of the two kinds of irregular shaped particles used for the simulations. Dotted line corresponds to the spherical particle.

In addition the properties of the particles were selected to be close to that of chickpeas that is: a) the mass of each particle was equal the corresponding mass of the real material (0.147 gr for smaller and 0.18375 gr for larger particles) and b) the friction coefficient close to 0.3 as suggested by Tavakoli et al (2002).

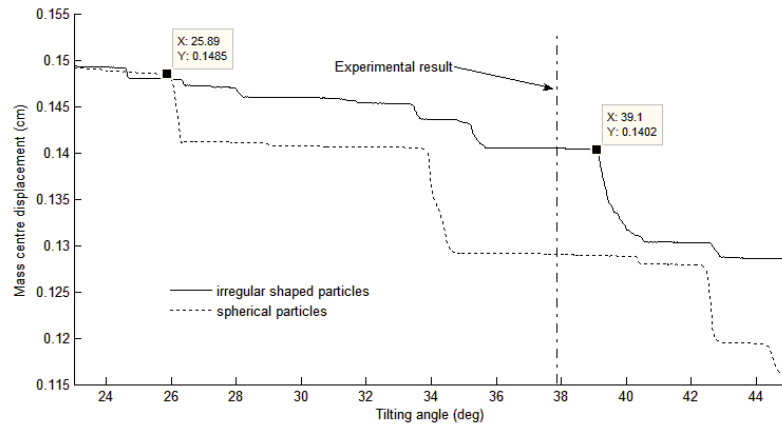


Figure 9.11 Mass-centre displacement for spherical and irregular shaped particles under slow tilting ($0.5^\circ/\text{s}$) of the tank.

Figure 9.11 describes the displacement of the mass centre of the two granular cargos (with spherical and irregular particles) when the tank is tilted with a rate of 0.5 deg/s . The angle of repose predicted for each case is noted, as well as the mean value of the experimental tests. As expected, due to the majority of elliptical-like particles, the predicted angle in the case of spherical particles is lower than the experimentally measured value. Specifically, the predicted angle is 13 degrees lower. In contrast, the predicted angle of repose in the case of irregularly-shaped particles is closer to the experimentally measured one (the predicted angle was found by 1.3 degree larger).

Furthermore, we repeated the same numerical experiment 24 times with different initial particle configuration each time (same Fourier descriptors but different phase angles for each particle). In Figure 9.12 are summarized the results, presented in a serial manner according to the order of execution of the test. The predicted values of angle of repose (star points) were consistently higher than the experimentally measured values, with a mean deviation of 9%. This deviation is explained to be the outcome of three effects: a) the simulations were two-dimensional in contrast to the three-dimensional experiments, b) particle shape and size distribution was close but not exactly the same with the actual material and c) the particle parameters have to be fine-tuned to the specific situation.

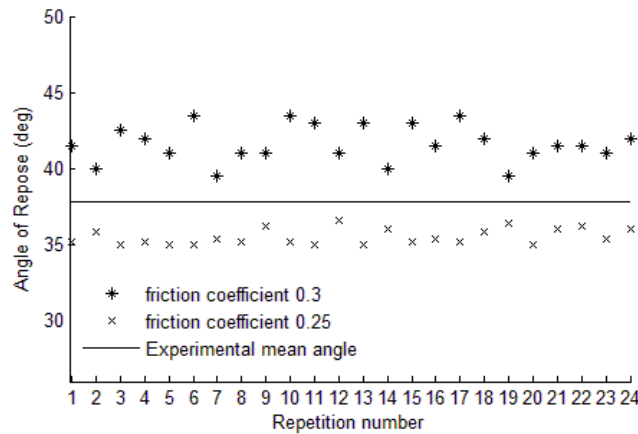


Figure 9.12 Comparison of experimental and numerical values of angle of repose.

To investigate further the last factor, we considered the response of the granular cargo when a slightly lower value of friction coefficient (0.5) was assumed (according to Markowska et al (2016) friction coefficient is related to grain's moisture level). As shown in Figure 9.12 (x points), the predicted mean value although lower, was closer to the actual value, with mean deviation of 7.2%. It is suggested that the accuracy of the algorithm can be optimized by fine-tuning of the friction coefficient.

9.4 Experimental investigation of cargo liquefaction

Two different materials (sand and olive pomace) in several moisture content scenarios were tested (moisture content expressed as ratio of material's mass). Harmonic forcing in a range of frequencies and amplitudes has been applied. The work was initiated on 2012 when two general cargo casualties occurred in Greece (Erol Senkaya and Agios Gerasimos, both carrying olive pomace). Results were presented by Koromilla (2013) as partially fulfilment of her thesis and furthermore by Koromila et al (2013).

Used materials and procedure of investigation

In the case of sand the specific gravity of the tested sample was 1.386t/m^3 and the average diameter, as found from analysis with an optical microscope, was 0.5mm. On the other hand olive pomace's specific gravity was 0.52t/m^3 and the average diameter of particles 4.5mm.

In all tests, the tank was filled with material up to a height of 11.5 cm. Various moisture contents were examined, as detailed in the next paragraphs. For each type of material, two series of experiments were performed: one for roll and one for sway oscillations. The excitation was harmonic and the duration of each experiment was 30 s.

In addition, two angle-of-repose tests were performed for the olive pomace, at a moisture level close to 60%. The first test was performed for the unshaken pomace while the second was performed after intensive sway shaking and liquefaction appearance.

9.4.1 Results for sand

The initial moisture content of the sand was 0% and it was achieved by heating it in a furnace. The moisture level was later increased in steps, up to 40% of the total weight of the material. A wide range of excitation frequencies and amplitudes were applied. Specifically, for roll: 0.1 - 3.0 (Hz) / 2.09 - 22.2 (deg) and for sway: 0.6 - 3.0 (Hz) / 0.25 - 17 (cm). The key findings are summarised below. They were basically similar irrespectively of the direction of excitation (roll or sway).

a) There is a critical moisture level (at about 27%) below which the material behaves almost like a solid; in the sense that it follows container's motion without flowing, no matter what the external frequency and or amplitude value is.

b) Right after the critical moisture content is reached however, two phenomena emerge: for frequencies between 0.1-0.2Hz (in roll as well as in sway) the material forms a small heap with its peak appearing at the centre of the free surface, while a small amount of water appears at each side of the tank (Figure 9.13 left). For frequencies between 0.4 and 0.8 Hz for roll and above 1.2 Hz for sway oscillations a shift of sand to the sides of the container is formed while water appears in a thin layer at the top of the free surface (Figure 9.13 right).

c) Further increase of moisture means that the amount of water on the top increases too and, for low external frequency, it moves separately from the lower, solid like, material (Figure 9.14 left). The frequency range in which shifting of the sand underneath the water occurs, appears now at relatively lower values (e.g. 0.7 Hz instead of 0.8 Hz for the roll motion, see Figure 9.14 right). For higher excitation frequency the water layer enters a resonance area and moves following the corresponding natural mode (Figure 9.15). At the same time, the material underneath the water layer rearranges itself.

d) The time duration of the experiment seems to be directly related to the appearance of liquefaction. Increase of the duration leads to lowering of the frequencies where liquefaction first appears.

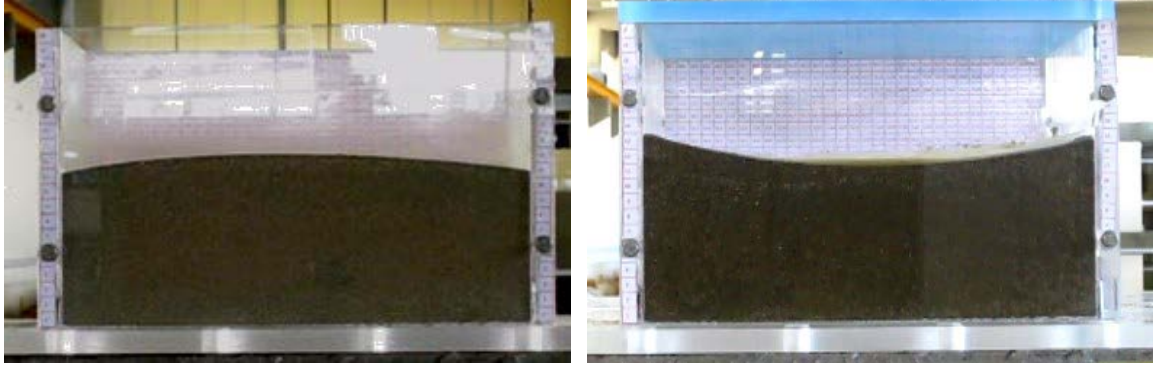


Figure 9.13 Sand with MC 27.5% after being excited in roll. Left) $f=0.15Hz$, $\varphi_{\max}=4.2deg$; Right) $f=0.5Hz$, $\varphi_{\max}=13.2deg$.

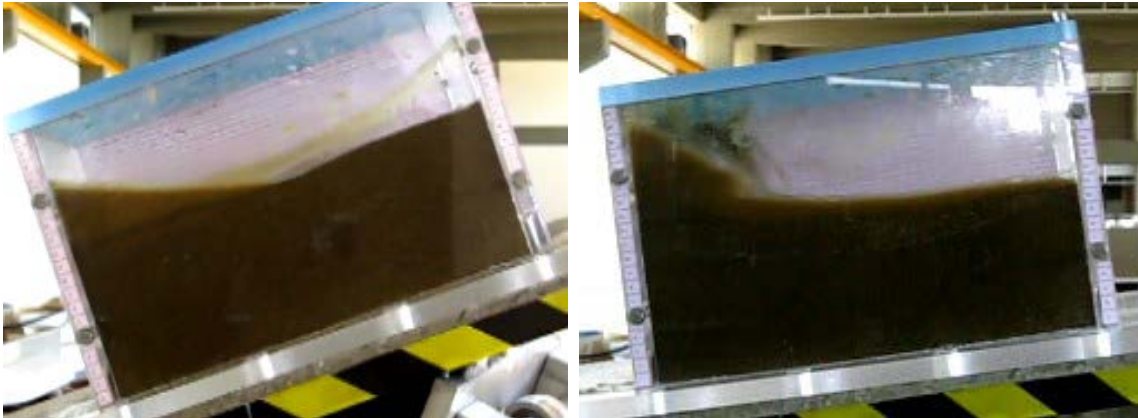


Figure 9.14 Sand with MC 40% excited in roll: Left) $f=0.1Hz$, $\varphi_{\max}=22.2deg$. The upper water layer is the only part that moves; Right) $f=0.8Hz$, $\varphi_{\max}=9.05deg$.

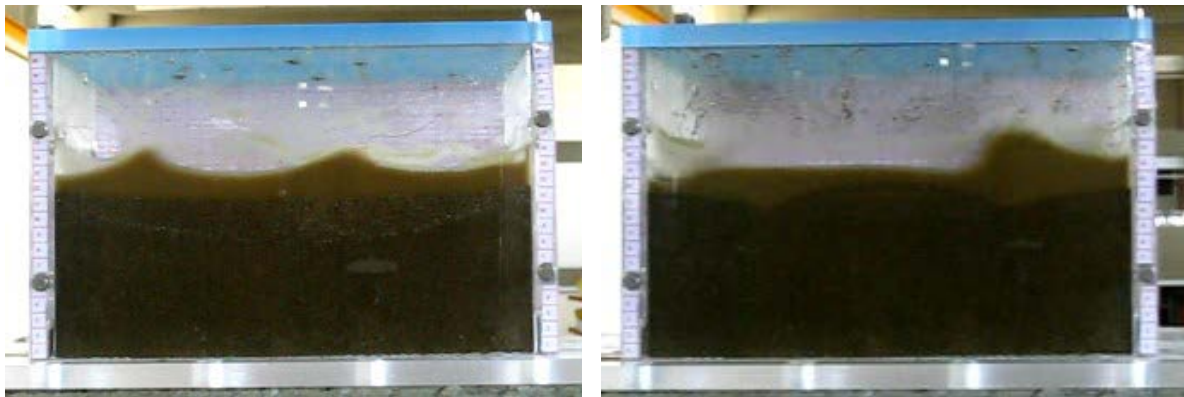


Figure 9.15 Sand with MC 40% excited in high frequency - small amplitude sway. Left) $f=2.5Hz$, $a=2.37cm$; Right) $f=1.4Hz$, $a=4.3cm$.

9.4.2 Results for olive pomace

The olive pomace used for our experiments was supplied from two different olive mills in Greece (one in Corfu and one in Kalamata). We worked with samples of “dry” and “wet” olive pomace, having moisture content that is commonly found when such a material is transported by sea. The focus of our work now turned from the identification of the critical moisture level, to the differences of material’s behaviour in realistic moisture scenarios for

this material's transportation. Similarly to the dry sand, dry pomace behaves like a solid too, basically following container's motion. For the wet olive pomace however, two phenomena should be noted:

- Moisture diffusion from specific areas of moisture concentration (black areas inside the material appearing in Figure 9.16) towards the entire material body through the formation of moisture layers, leading to a jelly like motion of the material.
- Excitation at frequencies above 1.0 Hz leads to noticeable shift of a portion of material to the sides of the container.

To examine the change in the semi-static behaviour of the olive pomace before and after liquefaction occurrence, comparative tilting tests were conducted.

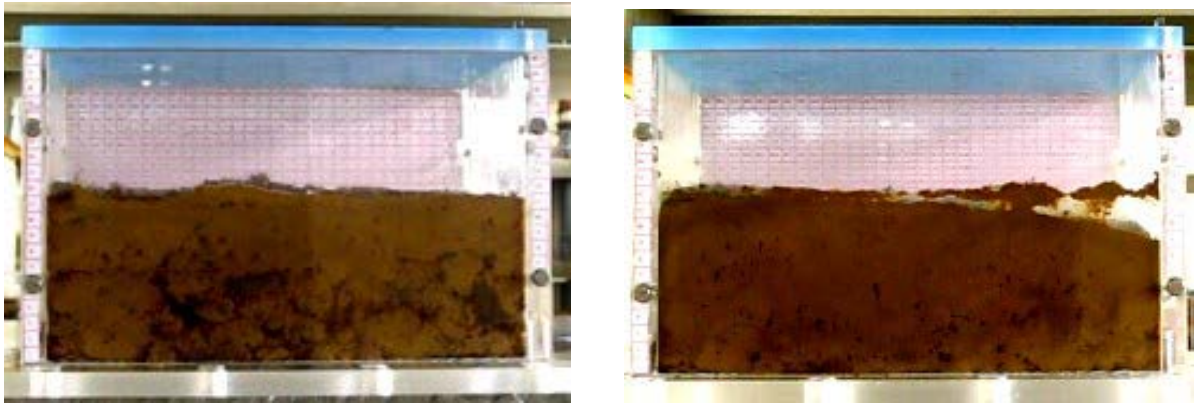


Figure 9.16 Wet olive pomace (left) before; and (right) after the application of sway excitation ($f=2.2\text{Hz}$, $A=4.3\text{cm}$).

In accordance to the tilting box test method prescribed in IMBSC (IMO 2012a), the tank was tilted with rate 0.3 deg/s . Due to physical limits (container's height) the tilting stopped when 30 deg was reached. In the second test where the material had already been shaken and liquefaction had been established, the material started to move earlier (by about 10 deg). However, due to the moisture, the flow observed is not the typical for angle of repose. Here, the entire body of material has tended to move and not only some portion of it near to the free surface.

9.5 Concluding remarks

By applying an established experimental technique (the “tilting box method”), the behaviour of chickpea grains inside a three-dimensional rectangular tank has been investigated. Focus was initially given on the reproduction of numerical investigation's key findings, in order to evaluate qualitatively the effectiveness of our simulation method to

predict principal aspects of the behaviour of granular matter. The numerical predictions were found in good agreement with the experimental results.

In addition, the results obtained from the experiments were compared against numerical results in order to evaluate the accuracy of our simulation in providing quantitative accuracy. Whilst the prediction from our simulations is close to the experimental values, a deviation about 10% has been found. This deviation is assumed to be normal due to the differences between the experimental and numerical apparatus (e.g. three dimensional experiments compared to two dimensional numerical results) and the uncertainty on the specific particle parameters. An interesting observation was that, right after the critical angle has been reached, initially the inner part of material starts flowing, drifting after a while its neighbours. Thus upgrade of our algorithm in order to be capable of simulating 3D particles should be conducted before any further investigation.

Lastly, a step towards a systematic investigation of the liquefaction phenomenon, based on experimental procedures, was presented. Roll and sway oscillations were applied on a scaled container containing two commonly transported materials (sand and olive pomace). Results indicated that, below a moisture level limit, materials wet materials behaved very similar to their dry counterparts. For further increase of moisture, oscillation of short duration under critical frequency led to a water layer formation at the top of the material.

Chapter 10: Conclusions

10.1 General overview

Cargo shift and liquefaction has become a great concern for the safe carriage of dry bulk over the past 10 years (INTERCARGO 2016). The recent improvement of international regulations concerning the loading and stowage of ship cargos in bulky form was the result of, almost entirely, empirical considerations, a fact implying the lack of a fundamental theoretical framework for the problem (IMO, 2012). Indeed, approaches using micro-scale modelling of cargo particles' motion and considering their interaction with the moving ship under wind/wave excitations are practically non-existent. A probable reason is because such a task is very demanding, calling for an interdisciplinary approach for overcoming the often fragmented nature of scientific efforts. As well known, coupled ship motions affected by liquid sloshing have been extensively studied in the past, since high impacting pressures on tank walls constitute a perennial ship operation hazard. For granular cargos behaviour however, the authors could not identify comprehensive research efforts of similar standing and hence, a fundamental approach had to be devised.

Initially, a mathematical model for the simulation of particles' movement in a tank was developed, starting from the properties of the elementary granules that make up a material of interest and then incorporating laws for their mutual interactions. The model was "two-dimensional" and it was kept generic enough so that, potentially, prediction of the behaviour of realistic granular cargos can be achieved in a variety of situations. The algorithm was focused on studying scaling effects and stick - slip phenomena influencing the behaviour of granular matter. Initially we restricted our scope to the case of prescribed harmonic external excitation. Validation of the code for nearly static and highly dynamic responses indicated that the simulation results are in good agreement with available experimental data.

At next step the algorithm was improved, by combining it with standard models of ship motion in regular beam seas, in order to study how the ship and the granular material behave, as a system, when the tank is able to move in the heave, sway and roll directions. Our intention was to understand how the coupling between material and ship works and whether such a coupling can be responsible for safety critical phenomena in vessel's response.

A number of additional improvements were also implemented, in successive steps. Firstly, the effect of humidity on the coupled motion was modelled. Secondly, a GPU

implementation using either CUDA runtime API or CUDA runtime and the Thrust API and was completed, in order to improve computational efficiency. Thirdly, a single element method was developed for investigating the dynamic behaviour of particles with arbitrary shape. This method combines Fourier analysis for the representation of particle's shape and Single-Particle Discrete Element Method for the contact resolution.

Experimental reproduction of our key findings indicated that the algorithm can efficiently predict the behaviour of granular cargo although certain limitation on its quantitative accuracy has been found, mainly due to uncertainty on particle parameters and of course the limited scope of a 2D approach. In what follows, the outcome of our analysis for each one of the research questions is presented. The usefulness and restrictions of the model are further discussed and the chapter concludes with suggestions about next steps of our research.

10.2 Outcome of investigation

In the introductory chapter six different research questions were raised that lead our investigation to specific direction. In what follows each research question and the corresponding outcome answer based on our analysis is given.

1. What are the critical parameters that influence the behaviour of a bulky cargo inside a tank forced to move in prescribed motion?

It was noticed that the material with the smallest particle size and the highest density tended to flow more easily. Some dependence of system's macroscopic behaviour (resulting in different values of critical angles) from free surface's initial state was noticed. Investigation of behaviour in the case where side tank walls were as low as material's height indicated that, substantial flow is realised earlier in comparison to a similar phenomenon occurring in a tank with high side walls. This difference in angle was found to be between 1.7° to 6.8° , depending on the tilting rate. Another interesting observation was that, a small heap formation seems occurring quite consistently, at an angle of tilt that is smaller than the angle of repose. This formation seems to be quite independent of the tilting rate and the tank wall height. It was also noticed that larger filling ratio leads to smaller angle of repose in the sense that material inside tank with the largest filling ratio tended to flow more easily. Some dependence of system's macroscopic behaviour (stick-slip phenomenon) from filling ratio was also noticed. Lastly, it was shown that the material is more sensitive to roll excitation when the distance of the roll point from tank's bottom is decreased.

2. *What are the effects of tank scaling upon granular material behaviour?*

Investigation of scaling effects influencing the behaviour of granular matter was based on simulations relying on cellulose acetate spheres with diameter 3 mm inside tanks that were successively i) vibrated in sway assuming prescribed harmonic external excitation and ii) tilted with low tilting rates. As far as horizontal vibration is concerned, observations lead to the suggestion that a critical size of container exists after which the material behaves in an almost identical manner irrespectively of container's size. It is conjectured that friction plays a greater role in the smaller sizes, hence the apparent difference in the dynamic behaviour. Furthermore, tilting of the three tanks with a slow rate (0.3 deg/s), in order to identify the critical angle where avalanching of material's free surface appears, indicated that there is some dependence of this angle on tank's width. Specifically, it was observed that the smaller tank leads to a larger critical angle. Once again, after a critical tank width almost the same angle was predicted for every case.

3. *How does bulk cargo shift affect vessel's stability?*

Results for both single DOF (pure roll) and 3 DOF (sway, heave, roll) motion indicated that, although the same resonant region occurs for both systems, in the case of granular cargo and for wave amplitudes below a certain limit, the motion of the system is smaller. This leads to a system that is even more stable than its frozen counterpart, even though it appears to have some difficulty in reaching steady state. For higher wave amplitudes a new region appears where the vessel due to her cargo's movement, shows larger response and in some cases it capsizes. An effort to analyse this behaviour revealed that, this is related with a shift of the roll resonance peak value.

In addition, analysis of the numerical experiments for sway motion showed that when it comes to maritime interest the sway motion is insensitive of material's bifurcating behaviour. Apparently this behaviour occurs in higher frequency and/or amplitude regions, than that of the specific interest for sea keeping behaviour. However the bifurcating behaviour for slightly larger amplitude and frequency values were investigated and results showed that cargo behaviour has an effect on structures' motion. The kind of affection leads to the adoption of a mechanical analogy such as a non-linear frequency depending spring, similar to that used for liquid sloshing.

4. *How does environmental humidity affect cargo shift and ship stability?*

Comparison of barge's response, when filled with wet or dry cargo, has shown that, below a critical limit of wave amplitude, hardly any difference can be noticed. Above this limit the wet cargo becomes more kinetic. For our case study, this motion did not lead to capsize but it is believed that interesting results would appear when larger values of vessel-to-material-weight ratios are considered. Strangely, in both occasions the abrupt motion of the cargo was found to be responsible for capsize, but it was shown that it occurred slightly earlier than when the angle of repose was reached. This is assumed to be a consequence of acceleration and needs further research.

5. *How could we gain computational efficiency? What are the restrictions?*

Comparison between CPU and GPU simulation results showed that a speedup of up to 150x could be reached when the graphics processor is used and the proper set of thread blocks is selected. This speedup is much less, however, when double precision floating points are considered, although it may be improved when fewer export data is needed. The results indicated that, the use of GPGPU in simulations of ship cargo shift is not only essential when a lot of particles are under investigation, but it could be more than vital, when large tanks and coupling phenomena are under consideration.

6. *How does particle shape affect cargo shift and ship stability?*

Two series of numerical experiments were performed in order to investigate how the various terms in the Fourier series representation ("Fourier descriptors") as well as the harmonic phase angles, influences the angle of repose, respectively. Results on the first aspect showed a strong dependence of the angle of repose, especially on the second and third descriptor (D_2 and D_3 , respectively). That is, the angle of repose for elliptical particles is drastically larger than that of triangular particles, which on their turn flow in higher angles than square-shaped particles and spheres. Based on the results of the second series, we could assume that spherical particle representation provides an accurate enough prediction when slightly irregular particles are considered. However, for irregular particles, the prediction of this angle is strongly connected to the packing of the material inside the tank. These suggestions come in close agreement with our experimental results.

10.3 Discussion

As becomes evident from the above, a tool capable of simulating accurately dynamical response of a 2D vessel under coupled sea wave and dry cargo shift impact loads have been developed. A big question though, evolved from the very beginning of our research was:

How feasible is it to combine micro-scale modelling with ship motions in a practical framework of study?

Whilst certain restrictions affect the accuracy and efficiency of numerical methods in general, our simulation results proved to be very encouraging and showed that not only is feasible to combine micro-scale modelling with ship motions in a practical framework, but also this combination enables investigation of aspects that can hardly be approached by theoretical or experimental methods (for example measurements of individual particle trajectory, pressure distribution on tank walls, etc). Despite being a newly established approach in handling cargo shift related phenomena, further development of this (or similar) algorithm could be beneficial for the elimination of the risk involved in design and operation of bulk carriers. The three major elements of methodology's potential for investigation of coupled ship-cargo motions in a practical framework are its:

1. **Simplicity:** Discrete Element Methods are very popular for the simulation of granular materials. Based on modelling of cargo as a collection of individual particles that are only affected by external forces and torques and governed by Newton second law for their motion, Molecular Dynamics method avoids any differential algebraic equations. Thus simulation of very large number of particles is easily achieved.

2. **Modularity:** Within Molecular Dynamics method only collisions between pairs of particles are considered. Thus any surface (e.g. tank walls) is constructed by a series of particles with fixed coordinates and there is no need for geometrical representation of the tank. This enables coupling of our particle simulator with advanced Simulation tools (e.g. SPH simulators, Matlab/Simulink) using custom subroutines in C++. A TCP/IP interface between our algorithm and any external simulation tool enables the transfer of data both ways or even between more than two software packages (e.g. from SPH algorithm to our simulator and from our simulator to Simulink).

3. **Scalability:** One of the major advantages of the micro-scale approach is the ability to construct systems that can be easily modified in order to simulate more complicated systems. Based on specific routines and sub-routines written in C++ the algorithm is able to simulate a tank filled with particles or a barge with cargo inside her hold, or even a large bulk carrier with several dampers inside her partially filled holds. This scalability, in addition to enabling investigation of any real case scenario (system geometry, cargo particle shapes, wave loads, etc), allows in depth study of any potential corrective and/or preventive engineering solutions (e.g. dampers, tank shape, etc) related to vessel stability issues.

While though the micro-scale modelling is capable of providing useful results for cargo shift phenomena pertinent in maritime transportation it has also demonstrated a series of limitations. In order to overcome these limitations and looking at the greater picture, our further research focus should be on the improvement of the current algorithm, making it thus capable to realistically simulate the response of ship and cargo (dry or wet) for realistic sea wave scenarios. In the next paragraph our short and longer term goals are briefly presented.

10.4 Future work

As identified in the introductory Chapter (*Chapter 1*), our intention is the creation of an accurate tool for assessing the severity of coupling effects. In order to achieve our goals, four specific problems need to be tackled:

Simulation of 3D structure

The algorithm should be improved, so that results for three dimensional structures could be simulated. The problem can practically be approached by three different sub-topics: a) improvement of the “Molecular Dynamics” algorithm in order to describe three dimensional particles, b) implementation of new equation of motion that can provide response for the three dimensional particles and c) experimental verification of the algorithm. The third dimension is expected to provide slightly different results comparing to the 2D equivalent since different phenomena can appear in 3D tanks.

Coupled DEM - SPH algorithm.

The use of micro-scale modelling of cargo particles’ motion and their interaction with the moving ship under wind/wave excitations could be classified along with sloshing; with clear methodological analogies prevalent in particular when, for the latter, a smooth particles

hydrodynamics (SPH) modelling approach is applied. Our intention here is twofold: a) coupling of our algorithm with an SPH algorithm in order to investigate the influence of humidity on structure response. Our current approach is to adopt a force description for the capillary forces between particles after their collision. While though this method has been proven to be efficient (Oger et al 2013) it is restricted to pendular state; that is particles are held together by liquid bridges at their contact points but there voids between them are filled with air (Mitarai & Nori, 2006). MD-SPH coupling could allow the study of more general case where liquid and particles coexist inside the tank. b) Replacement of the analytical method of calculating wave impact on structure by the numerical force/moment feedback of an SPH simulation of sea. A Coupled DEM –SPH algorithm would provide two different feedback forces: one from inside based on the actual pressure on tank walls by the particles and one from outside based on the pressure of the hull from each liquid particle. This way our investigation would be independent of hull shape and more complicated structures could be studied.

Motion under realistic wave excitation

While the investigation of prescribed and single regular wave excitation that we have used so far in our research has provided useful results for understanding the coupled motion, our intention is to study more realistic sea state scenarios:

a) Study of the coupled motion when deterministic wave packets are applied. The upgrade of the algorithm in that occasion would be straightforward since the typical form of an irregular wave record might reasonably be represented by adding together a suitable assembly of regular waves.

b) Study of the coupled motion when stochastic wave excitation is applied. In order to improve fundamental understanding about homoclinic/heteroclinic phenomena associated with ship dynamic behaviour, last three years our team investigated how normal forms of the three considered bifurcations (heteroclinic tangency, homoclinic saddle connection and homoclinic to saddle-node connection, can be produced from the respective ship motion models. By establishing this connection the critical combinations of parameters, from a ship's perspective, should be revealed.

Irregularly-shaped particles simulation method optimization

As discussed before, the results of our study with more complicated particle shapes proved to be promising but, at the same time, computationally very costly. For this reason,

several possible improvements of computational efficiency have been investigated. This step can be of crucial importance when studying realistic cargos.

References

- Abkowitz, M.A. 1969. Stability and Motion Control of Ocean Vehicles. MIT Press, Cambridge, MA.
- Allen M.P., Frenkel D., Talbot J., (1989) "Molecular dynamics simulation using hard spheres", Computer Physics Reports, 9: 301–353.
- Abbaspour-Fard M. H., (2004) "Theoretical validation of a multi-sphere, discrete element model suitable for biomaterials handling simulation." Biosystems engineering 88(2): 153-161.
- Albert R., Albert, I., Hornbaker D., Schiffer P., & Barabási A. L. (1997) "Maximum angle of stability in wet and dry spherical granular media", Physical Review E, 56(6): R6271.
- Anand A., Curtis J.S., Wassgren C.R., Hancock B.C., Ketterhagen W.R., (2009) "Predicting discharge dynamics of wet cohesive particles from a rectangular hopper using the discrete element method(dem)", Chemical Engineering Science, 64: 5268–5275.
- Anderson A., Lorenz C. D. , Traveset C. D., (2008) "General purpose molecular dynamics simulations fully implemented on graphics processing units", Journal of Computational Physics 227(10): 5342-5359.
- Aranson, I.S., Tsimring, L.S., (2009) "Granular Patterns", Oxford University Press, Oxford.
- Argyriadis G (2015) "Investigation of the Capsize of cargo ship DYSTOS", Diploma Thesis, National Technical University of Athens.
- Ashmawy A.K., Hoang V.V., Sukumaran B. (2003) "Evaluating the influence of particle shape on liquefaction behaviour using discrete element modelling ." The Thirteenth International Offshore and Polar Engineering Conference. International Society of Offshore and Polar Engineers.
- Athanassoulis G. A., (2008) "Ship dynamics", NTUA publications, Athens (lecturer notes in Greek)
- Bachmann D. (1940) "Veifahrenstechnik" Z.V.D.I. Beiheft, 2: 43.
- Bagnold R., (1941) "The Physics of Blown Sand and Desert Dunes", Chapman & Hall, London.
- Barr A.H. (1981) "Superquadrics and angle-preserving transformations", IEEE Computer Graphics and Animation, 1: 11-23.
- Baumann G, Jobs E, Wolf D.E, (1993) "Granular cocktail rotated and shaken", Fractals, 1:767.

- Baxter G.W., Behringer R.P., Fagert T., Johnson G.A., (1989) "Pattern formation in flowing sand", *Physical Review Letters* 62 (24): 2825–2828.
- Beck R. F., Cummins W. E., Dalzell J. F., Mandel P., Webster W. C. (1989) "Motions in waves", in *Principles of naval architecture* edited by Lewis E. V., 3:1-188.
- Beddow J.K., Philips G.C., (1975) "Planseeber", *PulvermetaII.*, 23: 3 - 14.
- Behringer, R. P. (1993) "The dynamics of flowing sand", *Nonlinear Science Today* 3: 1-15.
- Betz F. (2003) "Managing technological innovation: competitive advantage from change", John Wiley & Sons.
- Blagoveshchensky S. N., (1962) "Theory of Ship Motions, edited by L. Landweber, Vol. 2", Dover Publications, New York, translated from the 1st Russian edition by T. Strelkoff and I. Strelkoff.
- Blott S. J., Pye K. (2008) "Particle shape: a review and new methods of characterization and classification", *Sedimentology* 55.1: 31-63.
- Bonfiglio L.U., Brizzolara S.T., Chrysostomidis C.H. (2011) "Added Mass and Damping of Oscillating Bodies: a fully viscous numerical approach", *Recent Advances in Fluid Mechanics, Heat & Mass Transfer and Biology*, 210-215.
- Boon C.W., Houlsby, G.T., Utili, S., (2012) "A new algorithm for contact detection between convex polygonal and polyhedral particles in the discrete element method", *Computational Geotechnics* 44: 73–82.
- Bowman E.T., Soga K., Drummond W. (2001) "Particle shape characterisation using Fourier descriptor analysis.", *Geotechnique* 51.6: 545-554.
- Brilliantov N. V., Spahn F., Hertzsch J.-M., Poschel T. (1996) "A model for collisions in granular gases", *Phys. Rev. E*, 53:5382.
- Brodtkorb A. R., Hagen T. R., Sætra M.L., (2013) "Graphics processing unit (GPU) programming strategies and trends in GPU computing", *Journal of Parallel and Distributed Computing*, 73(1): 4-13.
- Brown K. J., Sujeeth A. K., Lee H., Rompf T., Chafi H., Odersky M., Olukotun K. (2011) "A heterogeneous parallel framework for domain-specific languages", In *Proceedings of Parallel Architectures and Compilation Techniques (PACT) International Conference*, 89-100.
- Brown R., Richards J. C. (1970) "Principles of Powder Mechanics", Pergamon, Oxford, UK.
- Buchholtz V., Poschel T., (1994) "Numerical investigations of the evolution of sandpiles", *Physica. A*, 202: 390-401.
- Burkalow A. (1945) "Angle of repose and angle of sliding friction: an experimental study." *Geological Society of America Bulletin* 56.6: 669-707.

- Cavuoti S., Garofalo M., Brescia M., Paolillo M., Pescape' A., Longo G., Ventre G., (2013) "Astrophysical data mining with GPU. A case study: Genetic classification of globular clusters", *New Astronomy*, 26: 12-22.
- Charlaix E., Ciccotti M. (2010) "Capillary condensation in confined media", *Handbook of nanophysics: Principles and methods* ed. klaus sattler, 12-1.
- Charlaix E., Crassous J. (2005) "Adhesion forces between wetted solid surfaces", *Journal of Chemical Physics*, 122: 184701.
- Chung Y. C., Ooi J. Y. (2006) "Confined compression and rod penetration of a dense granular medium: discrete element modelling and validation", *Springer Berlin Heidelberg*.
- Cleary P., Ha J., Sawley M. (2001) "Modelling industrial fluid flow application using SPH." *Bifurcation and Localisation Theory in Geomechanics*, 125.
- Cleary P.W., Stokes N., Hurley J., (1997) "Efficient collision detection for three dimensional super-ellipsoidal particles", *Proceedings of 8th International Computational Techniques and Applications Conference*. Adelaide, Australia, 139–144.
- Clément C.P.A.R. (2010) "Multiscale modelling of fluid-immersed granular media.", *Diss. University of Nottingham*.
- Coppersmith S. N., Liu C. H., Majumdar S., Narayan O., Witten T. A. (1996) "Model for force fluctuations in bead packs", *Physical Review E*, 53(5): 4673.
- Crassous J., Ciccotti M., Charlaix E., (2011) "Capillary force between wetted nanometric contacts and its application to atomic force microscopy", *Langmuir* 27: 3468–3473
- Cummins, W. E.: The impulse response function and ship motions. *Schiffstechnik* 9, 101–109 (1962).
- Cundall P. A., Strack O.D.L, (1979) "A discrete numerical model for granular assemblies", *Geotechnique*, 29:47.
- Cundall P.A., (1988) "Formulation of a three-dimensional distinct element model – Part I. A scheme to detect and represent contacts in a system composed of many polyhedral blocks", *International Journal of Rock Mechanics and Mineral Science & Geomechanics*, 25: 107-16.
- Das, N., (2007) "Modelling three-dimensional shape of sand grains using discrete element method. " *Phd thesis submitted at University of South Florida*.
- Das N., Giordano P., Barrot D., Mandayam S., Ashmawy A.K., Sukumaran B. (2008) "Discrete element modelling and shape characterization of realistic granular shapes", In: *Proceedings of the 18th International Offshore and Polar Engineering Conference*. Vancouver, Canada, 525–532.

- Demyanchuk A. M., Grundas S., Velikanov L. P. (2013). "Identification of Wheat Morphotype and Variety Based on X-Ray Images of Kernels", in *Advances in Agrophysical Research*", book edited by Grundas S. & Stepniewski A., Intech, 223-269.
- Delorme L., Colagrossi A., Souto-Iglesias A., Zamora-Rodríguez R., Botía-Vera E., (2009) "A set of canonical problems in sloshing, Part I: Pressure field in forced roll—comparison between experimental results and SPH", *Ocean Engineering.*, 36(2): 168-178.
- Delorme L., Bulian G. , Souto-Iglesias A., (2006) "Coupling between sloshing and ship roll motion: Comparison between first order potential theory and SPH", *Proceedings of 26th Symposium on Naval Hydrodynamics, Italian Ship Model Basin (INSEAN), US Office of Naval Research (ONR)*, 17-22.
- Diepenbroek, M., Bartholoma, A., and Ibbeken, H. (1992). How round is round? A new approach to the topic 'roundness' by Fourier grain shape analysis. *Sedimentology*, 39, 411-422.
- Dong K., Wang C., Yu A. (2015) "A novel method based on orientation discretization for discrete element modelling of non-spherical particles." *Chemical Engineering Science* 126: 500-516.
- Dorbolo S. (2005) "Stability limit of a granular monolayer.", *European Physical Journal E*, 17(1): 77- 81.
- Douady S., Fauve S., 1988. "Pattern selection in Faraday instability", *Europhysics Letters*, 6: 221-226.
- Duran J. (2000) "Sands, powders, and grains: An introduction to the physics of granular materials", Springer, New York.
- Duran J., de Gennes P. G. , Reisinger A. (1999) "Sands." *Powders and Grains* Springer-Verlag, New-York.
- Duran J., Mazozi T., Luding S., Clement E., Rachenbach J., (1996) "Discontinuous decompaction of a falling sandpile", *Physical Review E* 53: 1923.
- Ehrlich R., Weinberg B., (1970) "An exact method for characterization of grain shape", *Journal of Sedimentary Petrology* 40(1): 205–212.
- Eklund A., Dufort P., Forsberg D., LaConte M.S., (2013) "Medical image processing on the GPU – Past, present and future", *Medical Image Analysis*, 17(8): 1073-1094.
- Ennis, B. J., Green J.,. Davies R. (1994) "The Legacy Of Neglect In The United-States", *Chemical Engineering Progress* 90(4): 32-43.
- Eshuis P., Van Der Weele K., Van Der Meer D., Bos R., Lohse D. (2007) "Phase diagram of vertically shaken granular matter", *Physics of Fluids*, 19(12): 123301.

- Faltinsen O. (1993) "Sea loads on ships and offshore structures Vol. 1", Cambridge university press.
- Faltinsen O.M., Timokha A.N., (2009) "Sloshing", New York: Cambridge University Press.
- Faraday M. (1831) "On a peculiar class of acoustical figures; and on certain forms assumed by groups of particles upon vibrating elastic surfaces.", Philosophical transactions of the Royal Society of London 121: 299-340.
- Farber R., (2011) "CUDA: Application Design and Development", Elsevier, Waltham.
- Fauve S., Douady S., Laroche C. (1989) "Collective behaviour s of granular masses under vertical vibrations." *Le Journal de Physique Colloques* 50.C3: C3-187.
- Favier J.F., Abbaspour-Fard M.H., Kremmer M., Raji A.O. (1999) "Shape representation of axi-symmetrical, non-spherical particles in discrete element simulation using multi-element model particles", *Engineering Computations*, 16(4): 467-480.
- Feng Y. T., Owen D. R. J. (2004) "A 2D polygon/polygon contact model: algorithmic aspects." *Engineering Computations* 21.2/3/4: 265-277.
- Fernández J.L., Ferreiro A.M., García-Rodríguez J.A., Leitao A., López-Salas J.G., Vázquez C., (2013) "Static and dynamic SABR stochastic volatility models: Calibration and option pricing using GPUs", *Mathematics and Computers in Simulation*, 94: 55-75.
- Fleissner F., Alessandro V., Schiehlen Wand Eberhard P., (2009) "Sloshing cargo in silo vehicles", *Journal of Mechanical Science and Technology* 23: 968-973.
- Flook A. G. (1979) "The characterization of textural and structural profiles by the automated measurement of their fractal dimensions", 2nd European Symposium on Particle Characterization, 591-599.
- Foerster S. F, Louge M.Y, Chang H, Allia K., (1994) "Measurements of the collision properties of small spheres", *Physics of Fluids* 6: 1108.
- Fong, S. T., Beddow, J. K., & Vetter, A. F. (1979) "A refined method of particle shape representation", *Powder Technology*, 22(1): 17-21.
- Frette V., K. Christensen A. M., J. Feder T. J., Meakin P., (1996) "Avalanche dynamics in a pile of rice," *Nature*, 379: 49-52.
- Gallas J. A. C., Herrmann H. J., Sokolowski, S., (1992) "Convection Cells in Vibrating Granular Media", *Physics Review Letters*, 69:1371-1374.
- Gear C. W., (1971) "Numerical Initial Value Problems in Ordinary Differential Equations", Prentice-Hall, Englewood Cliffs.
- Gladkyy, Anton, and Rüdiger Schwarze. "Comparison of different capillary bridge models for application in the discrete element method." *Granular Matter* 16.6 (2014): 911-920.

Goldhirsch I., 2010, "Stress, stress asymmetry and couple stress: from discrete particles to continuous fields". *Gran Mat* 12(3):239-252.

Gómez I., Ippolito I., Chertcoff R. (2012) "Characterization of wet granular media behaviour under different relative humidity conditions", *Powder Technology*.

Gupta M., Choudhary A., Pande N.A., (2013) "Accelerated Electromagnetic Field Simulation on Graphical Processing Unit by the Finite Difference Time Domain Method", *International Journal of Computer Applications* 70(27): 34-36.

Haff P. K., Werner B. T. (1986), "Computer simulation of the mechanical sorting of grains" *Powder Techn.*, 48:239.

Haile J. M., (1997) "Molecular dynamics simulation, elementary methods", New York: Wiley - Interscience.

Herminghaus S. (2005) "Dynamics of wet granular matter." *Advances in Physics* 54.3: 221-261.

Hogue C., (1998) "Shape representation and contact detection for discrete element simulations of arbitrary geometries" *Engineering with Computers* 15: 374-390.

Hogue C., Newland D., (1994) "Efficient computer simulation of moving granular particles", *Powder Technology* 78: 51-66.

Höhner D., Wirtz S., Kruggel-Emden H., Scherer V. (2011) "Comparison of the multi-sphere and polyhedral approach to simulate non-spherical particles within the discrete element method: Influence on temporal force evolution for multiple contacts", *Powder Technology*, 208(3): 643-656.

Holsapple, Keith A. "Modelling granular material flows: the angle of repose, fluidization and the cliff collapse problem." *Planetary and Space Science* 82 (2013): 11-26.

Hopkins M.A., (2004) "Discrete element modelling with dilated particles", *Engineering with Computers* 21: 422-430.

Hornbaker D. J., Albert R., Albert I., Barabási A. L., Schiffer P. (1997) "What keeps sandcastles standing?", *Nature*, 387(6635): 765.

Ileleji K. E., Zhou B. (2008) "The angle of repose of bulk corn stover particles." *Powder Technology* 187.2: 110-118.

International Association of Dry Cargo Shipowners (INTERCARGO) (2012) "Benchmarking Bulk Carriers 2011-12", London.

International Association of Dry Cargo Shipowners (INTERCARGO) (2016) "Bulk Carriers Casualty Report. The previous ten years (2005-2015) and the trends", London.

- International Maritime Organization (IMO), (1991) "International Code for the Safe Carriage of Grain in Bulk, International Grain Code", IMO publishing, ISBN: 9789280112757.
- International Maritime Organization (IMO), (1998) "Code of Safe Practice for Solid Bulk Cargoes (BC Code)", IMO publishing, ISBN: 9 92-801-1463-8.
- International Maritime Organization (IMO), (2012) "International Maritime Dangerous Goods Code (IMDG Code)", IMO publishing, ISBN: 978-92-801-1561-1.
- International Maritime Organization (IMO), (2012) "Solid Bulk Cargoes Code [IMSB Code 268(85)]", IMO publishing, ISBN: 978-92-801-1535-2.
- Jaeger H. M., Nagel S.R., Behringer R., (1996) "Granular solids, liquids and gases", *Reviews of Modern Physics* 68(4): 1259-1273.
- Jaimes J., Joseph G. G., Geffroy E., Mena B., Herrera-Velarde J. R. (2002) "Pattern formation in oscillatory granular flows", *Revista mexicana de física*, 48(6): 534-538.
- Jenike A. W. (1964) "Steady gravity flow of frictional-cohesive solids in converging channels." *Journal of Applied Mechanics* 31.1: 5-11.
- Johnson C. G., Gray J. M. N. T. (2011) "Granular jets and hydraulic jumps on an inclined plane." *Journal of Fluid Mechanics*, 675: 87-116.
- Kawaguchi T., (2010) "MRI measurement of granular flows and fluid-particle flows", *Advanced Powder Technology*, 21(3): 235-241.
- Kennedy S.K., Lin W.H. (1992) "A comparison of Fourier and fractal techniques in the analysis of closed forms." *Journal of Sedimentary Research* 62(5).
- Kodam M., Bharadwaj R., Curtis J., Hancock B., Wassgren C. (2009) "Force model considerations for glued-sphere discrete element method simulations", *Chemical Engineering Science*, 64(15): 3466-3475.
- Koromila I, (2013) "Experimental investigation of cargo liquefaction and impact on the stability of a bulk - carrier", Diploma Thesis, National Technical University of Athens.
- Koromila I., Spandonidis, C.C., Spyrou K.J., (2013) "Experimental investigation of cargo liquefaction and impact on the stability of a bulk - carrier", *Proceedings of 13th International Ship Stability Workshop, Brest*, 228-234.
- Krengel D, Strobl S., Sack A., Heckel M., Poschel T. (2013) "Pattern formation in a horizontally shaken granular monolayer", *Granular Matter* 15: 377-387.
- Krugger-Emden H., Sudbrock F, Wirtz S., Scherer V., (2012) "Experimental and numerical investigation of the bulk behaviour of wood pellets on a model type grate", *Granular Matter*, 14(6): 681-693.

Kudrolli A., (2004) "Size separation in vibrated granular matter", Reports on progress in Physics 67:209–247.

Kuwabara G, Kono K. (1987) "Restitution Coefficient in a Collision between Two Spheres", Japanese Journal of Applied Physics 26: 1230-1233.

Lambrou Christos (2015) "Micro-scale modelling of excited granular ship cargos inside humidity environments", Marine Science and Technology Master Course, School of Naval Architect and Marine Engineering, National Technical University of Athens.

Laroche C., Douady S., Fauve S., (1989) "Convective flow of granular masses under vertical vibrations", Journal de Physique France, 50: 699-706.

Lee J., Herrmann H.J. (1993) "Angle of repose and angle of marginal stability: molecular dynamics of granular particles", Journal of Physics, 26:373.

Li Y., Xu Y., Thornton C. (2005) "A comparison of discrete element simulations and experiments for 'sandpiles' composed of spherical particles", Powder Technology, 160(3): 219-228.

Lian G., Thornton C., Adams M. J. (1998) "Discrete particle simulation of agglomerate impact coalescence", Chemical Engineering Science, 53(19): 3381-3391.

Lin W-M., Collette M., Lavis D., Jessup S., Kuhn J. (2009) "Recent Hydrodynamic Tool Development and Validation for Motions and Slam Loads on Ocean-Going High-Speed Vessels", 10th International Symposium on Practical Design of Ships and Other Floating Structures Houston, Texas.

Lin, X. and Ng, T.T. (1995), "Short communication, contact detection algorithms for three dimensional ellipsoid in discrete element modelling", International Journal for Numerical Methods in Geomechanics, Vol.19, pp. 653-9.

Liu C H, Jaeger H M, Nagel S R. (1991) "Finite-size effects in a sandpile", Physical Review A, 43(12): 7091–7092.

Liu G., Liu Y., Ren L., Meng X. (2013) "3D seismic reverse time migration on GPGPU", Computers & Geosciences, 59: 17-23.

Lloyd A.R.J.M. (1989) "SEAKEEPING ship behaviour in rough weather", Ellis Horwood Limited, England.

Lu G., Third J.R., Müller C.R., (2015) "Discrete element models for non-spherical particle systems: From theoretical developments to applications", Chemical Engineering Science 127: 425–465.

Lu, G., Third J.R., Müller C.R., (2012) "Critical assessment of two approaches for evaluating contacts between super-quadric shaped particles in DEM simulations", Chemical Engineering Science. 78: 226–235.

- Lu, G., Third J.R., Müller C.R., (2014) "Effect of wall rougheners on cross-sectional flow characteristics for non-spherical particles in a horizontal rotating cylinder", *Particuology* 12: 44–53.
- Lumay G., Boschini F., Traina K., Bontempi S., Remy J.-C., Cloots R., Vandewalle N. (2012) "Measuring the flowing properties of powders and grains", *Powder Technology* 224: 19–27.
- Maleki H., Ebrahimi F., Oskoei E. N. (2008) "The angle of repose of spherical grains in granular Hele-Shaw cells: a molecular dynamics study", *Journal of Statistical Mechanics*, P04026.
- Mandelbrot B.B. (1967) "How long is the coast of Britain.", *Science* 156.3775: 636-638.
- Maria A., Carey S. (2002) "Using fractal analysis to quantitatively characterize the shapes of volcanic particles" *Journal of Geophysical Research*, 107(B11): 2283.
- Markauskas D., Kačianauskas R., Dziugys A., Navakas R. (2010) "Investigation of adequacy of multi-sphere approximation of elliptical particles for DEM simulations", *Granular Matter*, 12(1): 107-123.
- Markowska A., Małgorzata W., Józef W., (2016) "Influence of moisture on external friction coefficient and basic physical properties of Astoria variety wheat grain." *Technical Sciences* 19(1): 17-26.
- Matuttis H. G., Luding S., Herrmann H.J. (2000) "Discrete element simulations of dense packings and heaps made of spherical and non-spherical particles.", *Powder technology* 109(1): 278-292.
- Melo F., Umbanhowar P., Swinney H. L. (1994) "Transition to parametric wave patterns in a vertically oscillated granular layer", *Physical review letters*, 72(1): 172.
- Meloy T.P. (1977) "Fast Fourier transform applied to shape analysis of particle silhouettes to obtain morphological data", *Powder Technology*, 17: 27-35.
- Metcalf T., Knight J. B., Jaeger H. M. (1997) "Surface Patterns in Shallow Beds of Vibrated Granular Material", *Physica A*, 236: 202-210.
- Mikami T., Kamiya H., Horio M. (1998) "Numerical simulation of cohesive powder behaviour in a fluidized bed", *Chemical Engineering Science*, 53(10): 1927-1940.
- Miles J., Henderson D., (1990) "Parametrically forced surface waves", *Annual Review of Fluid Mechanics*, 22: 143-165.
- Mitarai N., Nori F., (2006) "Wet granular materials" *Advances in Physics* 55(1-2): 1-45.
- Mollon G., Zhao J. (2012) "Fourier–Voronoi-based generation of realistic samples for discrete modelling of granular materials." *Granular Matter* 14.5: 621-638.

- Monaghan J.J., (2005) "Smoothed Particle Hydrodynamics", Reports on Progress in Physics, 68: 1703-1759.
- Moon S.J., Shattuck M.D., Bizon C., Goldman D.I., Swift J.B., Swinney H.L., (2001) "Phase bubbles and spatiotemporal chaos in granular patters", Physical Review E, 65: 011301.
- Munjiza, D.R., Owen, N. and Bicanic, N. (1995), "A combined finite-discrete element method in transient dynamics of fracturing solids", Engineering Computations, 12(2): 145-74.
- Munro, M.C., Mohajerani, A., (2016) "Liquefaction incidents of mineral cargoes on board bulk carriers", Advances in Materials Science and Engineering, Article ID 5219474, 2016:1-20.
- Murashige S., Aihara K., 1998. "Coexistence of periodic roll motion and chaotic one in a forced flooded ship", International Journal of Bifurcation and Chaos 8:619-626
- Nassauer B., Liedke T., Kuna M., (2013) "Polyhedral particles for the discrete element method", Granular matter 15: 85–93.
- Nelson E. (1955) "Measurement of the repose angle of a tablet granulation.", Journal of the American Pharmaceutical Association 44(7): 435-437.
- Newman J. N. (2005) "Wave effects on vessels with internal tanks", Proceedings of the 20th International workshop of water waves and floating bodies, Lonyerbyen, Svalbard.
- NVIDIA (2009) "NVIDIA's Next Generation CUDATM compute architecture: Fermi", NVIDIA Whitepaper V1.1.
- NVIDIA (2012) "CUDA C Programming guide", NVIDIA Design Guide PG-02829-001_v5.0.
- O'Rourke J., Chien C.B., Olson T., Naddor D., (1982) "A new linear algorithm for intersecting convex polygons", Computer Graphics and Image Processing 19: 384–391.
- Oger L., Vidales A. M., Uñac R. O., Ippolito I. (2013) "Tilting process with humidity: DEM modelling and comparison with experiments", Granular Matter, 15(5): 629-643.
- Ogilvie T. F. (1964) "Recent progress toward the understanding and prediction of ship motions", 5th Symposium on naval hydrodynamics. Vol. 1. No. 2. Bergen, Norway.
- Orford J. D., Whalley W.B. (1983) "The use of the fractal dimension to quantify the morphology of irregular-shaped particles", Sedimentology 30(5): 655-668.
- Pak H. K., Behringer R.P. (1993) "Surface waves in vertically vibrated granular materials." Physical review letters 71(12): 1832.

- Paolotti D., Barrat A., Marconi U. M. B., Puglisi A., (2004) "Thermal convection in monodisperse and bidisperse granular gases: A simulations study", *Physical Review E* 69: 061304.
- Parteli E.JR. (2013) "DEM simulation of particles of complex shapes using the multisphere method: application for additive manufacturing." *American Institute of Physics Conference Proceedings*, 1542.
- Perilla J.R., Goh B.C., Cassidy C., Liu B., Bernardi R.C., Rudak T., Yu H., Wu Z., Schulten K., (2015) "Molecular dynamics simulations of large macromolecular complexes", *Current Opinion in Structural Biology*, 31: 64-74.
- Peters J.F., Hopkins M.A., Kala R., Wahl R.E., (2009) "A poly-ellipsoid particle for non-spherical discrete element method", *Engineering with Computers* 26: 645–657.
- Plimpton S., (1995) "Fast Parallel Algorithms for Short-Range Molecular Dynamics", *Journal of Computational Physics*, 117: 1-19.
- Portal R., Santos N., Sousa L., Dias J., (2009) "Contact detection of convex super-quadric using optimization techniques with graphical user interface" *Proceedings of the 7th EUROMECH Solid Mechanics Conference*. Lisbon, Portugal.
- Pöschel T, Rosenkranz D, (1997) "Experimental study of horizontally shaken granular matter — The swelling effect", *A Perspective Look at Nonlinear Media Lecture Notes in Physics*, 503: 96-109.
- Poschel T., Schwager T. (2005), "Computational Granular Dynamics", Springer – Berlin, Heidelberg.
- Purutyan H., Pittenger B.H., Carson J.W. (1999) "Six steps to designing a storage vessel that really works." *Powder and bulk engineering* 13(11): 56-67.
- Rabinovich Y.I., Madhavan S. E., Brij M. M. (2005) "Capillary forces between two spheres with a fixed volume liquid bridge: theory and experiment." *Langmuir* 21(24): 10992-10997.
- Radhika S. S., Leslie V. W., (2004) "Quasi-thermodynamics of powders and granular dynamics", *Physical Chemistry chemical Physics* 6: 5195-5202.
- Rapaport D. C. (1998) "Subharmonic surface waves in vibrated granular media", *Physica A: Statistical Mechanics and its Applications* 249(1): 232-238.
- Richard P., (2005) "Slow relaxation and compaction of granular systems", *Nature Materials* 4: 121–128.
- Richefeu V., Radjai F., El Youssoufi, M. S. (2006) "Stress transmission in wet granular materials", *The European Physical Journal E*, 21(4): 359-369.
- Rognebakke O.F, Faltinsen O.M., (2003) "Coupling of sloshing and ship motions", *Journal of Ship Research* 47: 208-221.

- Rösler R. Schneider H.A., Schuberth R. (1987) "Relation between particle shape and profile Fourier coefficients", *Powder Technology* 49: 255-260
- Rothenburg L., Bathurst R.J. (1991) "Numerical simulation of idealized granular assemblies with plane elliptical particles", *Computational Geotechnics*, 11: 315–329.
- Sakelariou A. (2013) "Deepening in floating equilibrium of symmetrical objects ", Diploma Thesis, School of Naval Architect and Marine Engineering, National Technical University of Athens.
- Savage S. B., Sayed M. (1984) "Stresses developed by dry cohesionless granular materials sheared in an annular shear cell", *Journal of Fluid Mechanics*, 142: 391-430.
- Sawley M, Biddiscombe J., Favre J. (2007) "Advanced visualization of large datasets for discrete element method simulations" *Proceedings of Discrete Element Methods Conference (DEM 07)*.
- Schafer J., S. Dippel, and D. E. Wolf. (1996), "Force schemes in simulations of granular materials" *Journal Physique I*, 6:5.
- Schellart W.P., (2000) "Shear test results for cohesion and friction coefficients for different granular materials: scaling implications for their usage in analogue modelling ", *Tectonophysics* 324: 1–16.
- Schmitke R, (1978) "Ship sway, roll and yaw motions in oblique seas", *SNAME Transactions*, 86: 26-46.
- Sellerio L., Mari D., Gremaud G. and D'Anna G., (2011) "Glass transition associated with the jamming of vibrated granular matter", *Physical Reviews E* 83(2-1):021301.
- Sneed E.D., Folk R.L., (1958) "Pebbles in the Lower Colorado River, Texas: a study in particle morphogenesis", *Journal of Geology*, 66: 114–150.
- Soulie F., El Youssoufi M. S., Cherblanc F., Saix C. (2006) "Capillary cohesion and mechanical strength of polydisperse granular materials", *The European Physical Journal E*, 21(4): 349-357.
- Spandonidis C., Spyrou J. (2012) "Use of granular material dynamics simulation for the study of cargo shift of ships", *Proceedings of 11th International Conference on the Stability of Ships and Ocean Vehicles*, 497-507.
- Spandonidis C. C., Spyrou K. J., (2013) "Numerical investigation of scaling effects on granular material dynamics", *Proceedings of 10th HSTAM international congress*, Chania, Greece.
- Spandonidis C. C., Spyrou K. J., (2013) "Micro-scale modelling of excited granular ship cargos: A numerical approach", *Ocean Engineering* 74: 22–36.

- Spandonidis C. C., Spyrou K. J., 2015 "Coupled granular material and vessel motion in regular beam seas", Proceedings, 12th International Conference on the Stability of Ships and Ocean Vehicles, Glasgow, 1133-114.
- Spandonidis C. C., Spyrou K. J., 2016 "Coupled vessel-dry-granular-cargo roll dynamics in regular beam seas", Ocean Engineering 120: 238 - 245.
- Spyrou K. J., 2015 "Dynamic Stability of Ships", Kallipos repository, Hellenic Academic E-books - Athens (in Greek).
- Stone J.A., Hardy D.J., Ufimtsev I.S., Schulten K., (2010) "GPU-accelerated molecular modelling coming of age", Journal of Molecular Graphics and Modelling , 29:116-125.
- Stone J.E., Phillips J.C., Freddolino P.L., Hardy D.J., Trabuco L.G., Schulten K., (2007) "Accelerating molecular modelling applications with graphics processors", Journal of Computational Chemistry 28: 2618–2640.
- Sukumaran B., Ashmawy A. K. (2001) "Quantitative characterisation of the geometry of discret particles", Geotechnique, 51(7): 619-627.
- Taguchi Y. (1992) "New origin of a convective motion: Elastically induced convection in granular materials", Physical Review Letters, 69(9): 1367.
- Takahasi K. (1934), Institute of Physical and Chemical Research, Tokyo; Scientific Papers, 540(26):11.
- Tavakkoli T., Kermani A. M., Khazaei J, (2002) "Effects of Normal Pressure, Sliding Velocity and Moisture Content of Chickpeas on Dynamic Friction Coefficient on Steel Surfaces", Journal of Agricultural Science and Technology, 4: 11-22.
- Taylor L. M., Preece D. S. (1992) "Simulation of blasting induced rock motion using spherical element models", Engineering computations, 9(2): 243-252.
- Techet A. H. (2005) "Design Principles for Ocean Vehicles", Massachusetts Institute of Technology, Department of Ocean Engineering.
- Tegzes P., Albert R., Paskvan M., Barabási A. L., Vicsek T., Schiffer P. (1999) "Liquid-induced transitions in granular media", Physical Review E, 60(5): 5823.
- Tejchman J., Gudehus G., (1993) "Silo-music and silo-quake experiments and a numerical Cosserat approach", Powder Technology, 76(2): 201-212.
- Themelis N. I. (2008) "Probabilistic Assessment of Ship Dynamic Stability in Waves", Doctoral Thesis, National Technical University of Athens, Greece.
- Ting, J. M., Meachum, L. and Rowell, J.D. (1995) "Effect of particle shape on the strength and deformation mechanisms of ellipse-shaped granular assemblages", Engineering Computations, 12: 99-108.

- Tigkas G. I. (2009) "Nonlinear Dynamic Analysis of the Course Instability of Ships in Wind and Waves", Doctoral Thesis, National Technical University of Athens, Greece.
- Ting, J.M.,(1991) "Anellipse-based micro mechanical model for angular granular materials", Proceedings of the ASCE Engineering Mechanics Specialty Conference. Columbus, USA, 1214–1218.
- Todd B.D., Evans D.J., Divis P.J., (1995) "Pressure tensor for inhomogeneous fluids", Physical Review E 52(2): 1627-1638.
- Toukan K., Rahman A., (1985), "Molecular-dynamics study of atomic motions in water", Physical Review B 31(5): 2643–2648.
- Train D., (1958) "Some aspects of the property of angle of repose of powders", Journal of Pharmacy and Pharmacology, 10: 127–135.
- Tuzun U., J. Baxter D., Heyes I., Hayati, Fredlund P., (1998) "Stratification in poured granular heaps", Nature, 391: 136.
- Tzaferopoulos M.A., (1995) "On the numerical modelling of convex particle assemblies with friction", Computer Methods in Applied Mechanics & Engineering 127: 371–386.
- Unger T., Brendel L., Wolf D. E., Kertesz J., (2002) "Elastic behaviour in contact dynamics of rigid particles", Physical Review E, 65:061305.
- Vanka S. P., (2013) "Freeman Scholar Lecture: Computational Fluid Dynamics on Graphics Processing Units", Journal of Fluids Engineering, 135(6): 061401-061401-23.
- Vassalos, D. (1992) "Physical modelling and similitude of marine structures", Ocean Engineering, Vol. 26(2): 111-123.
- Verlet L., (1967) "Computer 'experiments' on classical fluids. I. Thermodynamical properties of Lennard-Jones molecules", Physical Review A, 159: 98–103.
- Vidic-Perunovic, J., Jensen, J. J., (2009) "Parametric roll due to hull instantaneous volumetric changes and speed variations", Ocean Engineering, 36(12): 891-899.
- Vivanco F.,Rica S.,Melo F (2012) “Dynamical arching in a two dimensional granular flow”, Granular Matter 14(5): 563–576.
- Vugts J. H. (1971) "The hydrodynamic forces and ship motions in oblique waves", Nederlands scheepsstudiecentrum TNO.
- Walters J.P., Balu V., Chaudhary V., Kofke D., Schultz A., (2008) "Accelerating Molecular Dynamics Simulations with GPUs", Proceeding of ISCA 21st International Conference on Parallel and Distributed Computing and Communication Systems, 44-49.

- Walton O.R. (1983) "Particle dynamics calculations of shear flow", in Jenkins, J.T. and Satake, M. (Eds), *Mechanics of Granular Materials: New Models and Constitutive Relations*, Elsevier, Amsterdam, 327-38.
- Wassgren C. R., Brennen C. E., Hunt M.L., (1996) "Vertical vibration of a deep bed of granular material in a container", *Journal of Applied Mechanics* 63(3): 712-719.
- Weigert T., Ripperger S. (1999) "Calculation of the liquid bridge volume and bulk saturation from the half-filling angle", *Particle & Particle Systems Characterization*, 16(5): 238-242.
- Weinhart T., Thornton A., Luding S., Bokhove O., (2012) "From discrete particles to continuum fields near a boundary" *Granular Matter*, 14(2): 289-294
- Wellmann C., Lillie C., Wriggers P., (2008) "A contact detection algorithm for superellipsoids based on the common-normal concept", *Engineering Computations*, 25: 432–442.
- Willett C. D., Adams M. J., Johnson S. A., Seville J. P. (2000) "Capillary bridges between two spherical bodies", *Langmuir*, 16(24): 9396-9405.
- Williams J. C. (1976) "The segregation of particulate materials. A review." *Powder technology*, 15(2): 245-251.
- Williams J. R., O'Connor R. (1999) "Discrete element simulation and the contact problem", *Archives of Computational Methods in Engineering*, 6(4): 279-304.
- Williams J.R., O'Conner, R. (1995) "A linear complexity intersection algorithm for DEM simulations of arbitrary geometries", *Engineering Computations*, 12: 185-201.
- Williams J.R., Pentland A.P. (1989) "Superquadrics and modal dynamics for discrete elements in concurrent design", *Proceedings of 1st US Conference on the Discrete Element Method*, Golden, CO.
- Wong Y. S., Gan C.H., Wang C.H., (2005) "Study on Granular Dynamics in Vertically Vibrated Beds using Tracking Technique", *DSPACE@MIT, Singapore-MIT Alliance, MEBS*.
- Wynn E.J.W., (2009) "Simulations of rebound of an elastic ellipsoid colliding with a plane", *Powder Technology*, 196: 62–73.
- Zhang J., Wanqing W., Junquan H., (2016) "A numerical study of the effects of the longitudinal baffle on nickel ore slurry sloshing in a prismatic cargo hold." *Marine Structures* 46: 149-166.
- Zheng Q.J., Zhou Z.Y., Yu A.B., (2013) "Contact forces between viscoelastic ellipsoidal particles", *Powder Technology*. 248: 25–33.
- Zhou Y., Zhang G., (2009) "Effect of granular size on the angle of repose in the chute", *Science China Physics, Mechanics & Astronomy*, 52(4): 563-565.

Zhou Y.C., Xu B.H., Yu A.B., Zulli P., (2001) "A numerical investigation of the angle of repose of mono-sized spheres", *Physical Review E*, 64: 021301.

Zhu H.P., Zhou Z.Y., Yang R.Y., Yu A.B., (2007) "Discrete particle simulation of particulate systems: theoretical developments", *Chemical Engineering Science*, 62(13): 3378–3396.

Zhou Z. Y., Zou R. P., Pinson D., Yu A. B. (2014) "Angle of repose and stress distribution of sandpiles formed with ellipsoidal particles", *Granular Matter*, 16(5): 695-709.

Appendix A:

General Purpose Graphical Processing Unit Architecture

In Figure A.1 are presented the differences between the CPU and GPU architecture. As shown, even for multicore processors, CPU has limited amount of processing units; thus in order to speed-up an algorithm more processors are needed.

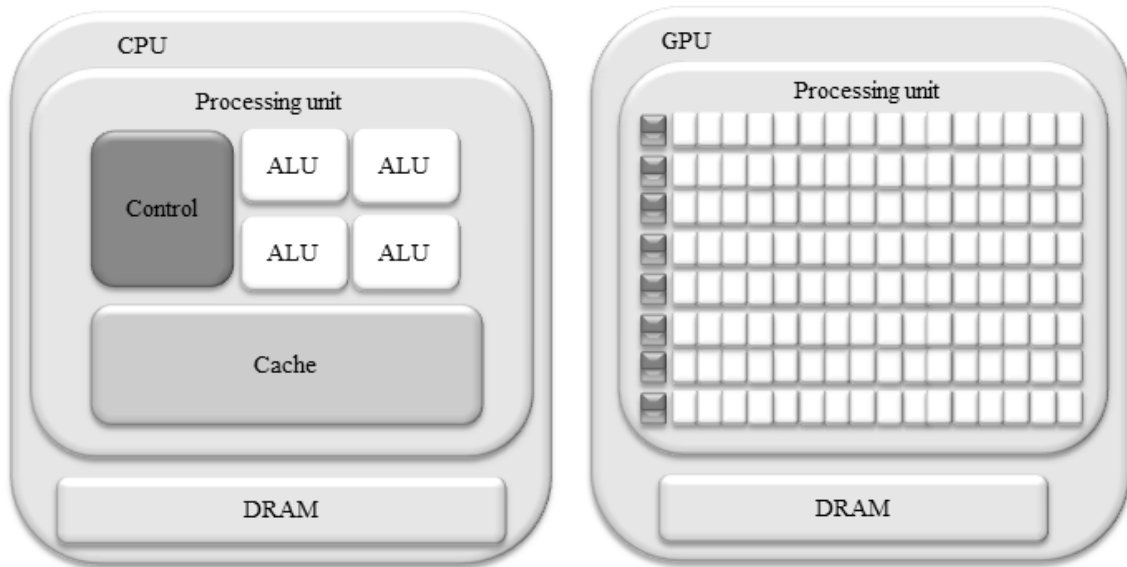


Figure A.1 Differences between CPU (left) and GPU (right) architecture.

On the other hand GPU, despite the lack of high cache memory and large control unit, has embedded thousands of ALUs, hundreds of processors and tens of thousands of concurrent threads that are capable of executing parallel arithmetic processes. Due to its simpler control hardware (that means more hardware for computations) modern GPUs are capable of handling a huge amount of parallel calculations, after data are transferred to its memory, thus optimizing processing throughput. The main advantages of this architecture are the low cost, impressive floating-point capabilities, high memory bandwidth, and low electrical power requirements (Farber 2011). This is the reason that, even though computer game industry drives GPUs evolution, its streaming architecture and programmability becomes more and more popular in scientific applications too.

A.1 CUDA and the NVIDIA GeForce GTX Architecture

To a CUDA programmer, the computing system consists of a host, which is a traditional central processing unit (CPU), such as an Intel architecture microprocessor in personal

computers today, and one or more devices (GPU) equipped with a large number of arithmetic execution units.

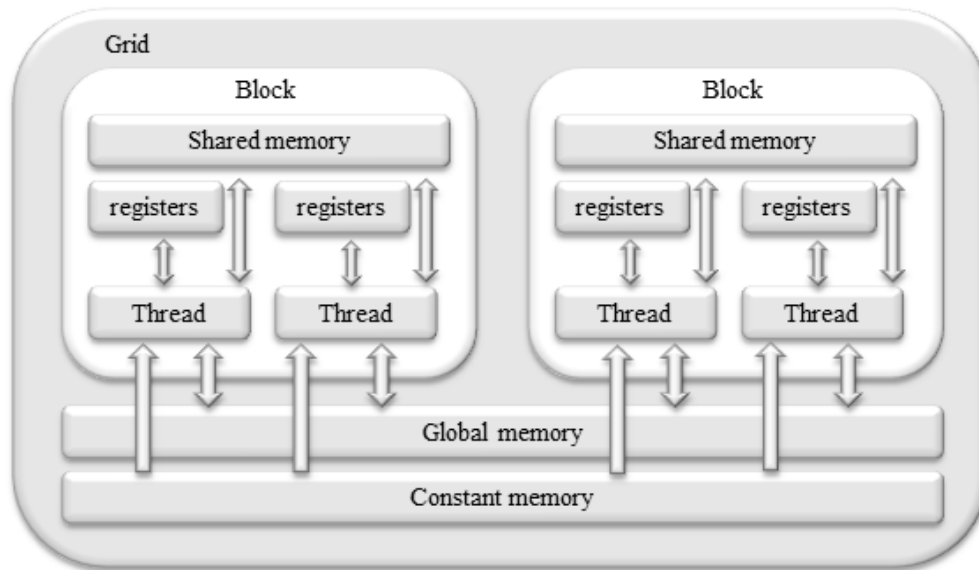


Figure A.2 GPU memory hierarchy

As shown in Figure A.2, each GPU incorporates a DRAM, referred to as global memory (read/write) and a constant memory (read only) that both are accessible by the host. In addition a software-managed cache known as shared memory (read/write) that is common to all threads per thread block, thread registers and local thread memory, both accessible only by each thread, are included in CUDA-capable GPU. Most of recent released GPUs have incorporated all of these features of the CUDA Architecture in order to be able of exceling computation in addition to performing well at traditional graphics tasks.

Figure A.3 presents the compiling process for a CUDA program (unified source code encompassing both host and device code) consisted of one or more phases that are either executed on host (serial phase) or device (parallel phase). The two phases are separated by the appropriate compiler (e.g. NVIDIA_ C compiler (nvcc)) during the compilation process. The host code is further compiled with a common compiler and thus running as an ordinary CPU process, while device code is compiled by the nvcc and executed on a GPU device. Emulation features in CUDA software development kit (SDK) or the MCUDA tool are also available when GPU devices are not CUDA-capable (Stratton 2008). Using NVIDIA Nsight Development Platform, building, debugging profiling and tracing of heterogeneous compute and graphics GPU application using CUDA C/C++ is able using Microsoft Visual Studio.

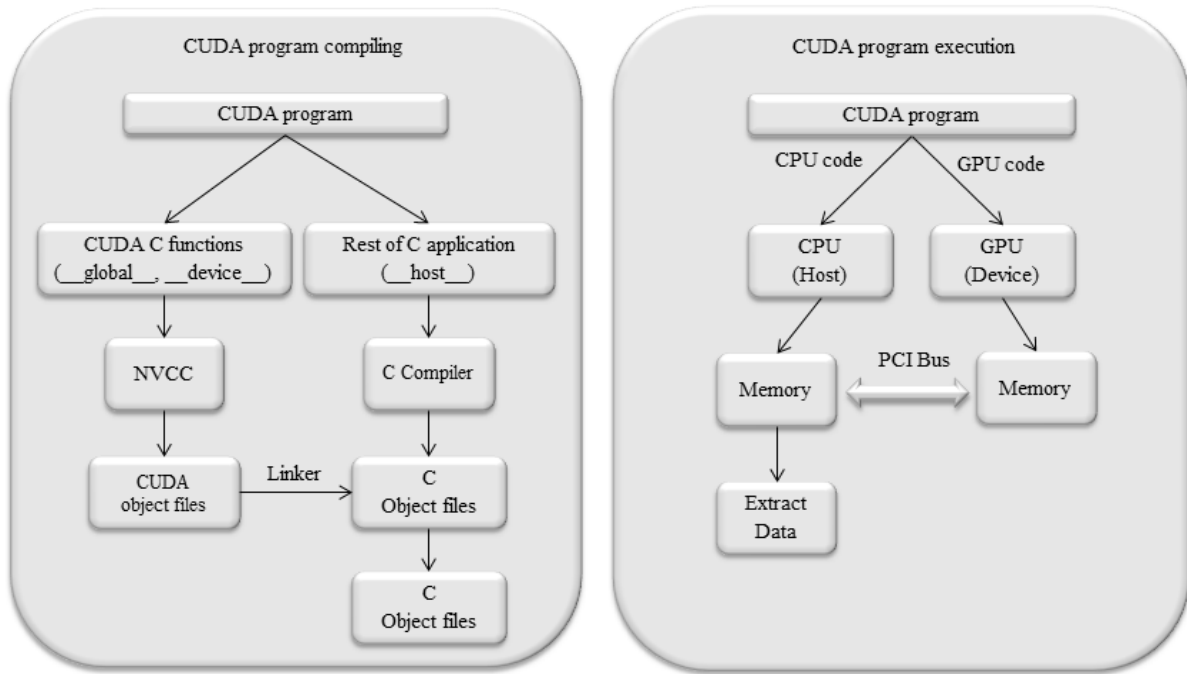


Figure A.3 Compiling (left) and execution (right) process for a CUDA code written in CUDA_C.

A.2 THRUST library

Depending on the amount of control programmer wishes to exert over the GPU, CUDA offers several APIs, such as the data-parallel C++ Thrust API, the runtime API, which can be used in either C or C++ and the driver API, which can be used with either C or C++, hierarchically referred from highest to lowest level, respectively (Of course different APIs exist for different languages but our work was based on CUDA-C language). As a general rule moving from lower to higher level API a programmer may benefit several ready to play methods that do more for him in the cost of allowing CUDA to make some decisions on his behalf. Based on the Standard Template Library (STL) Thrust has been shown to deliver high computational performance, generality, and convenience, quicker code development, easier to read source code, more maintainable and extendable programs and freedom to incorporate new hardware. On the other hand extend use of Thrust may isolate the programmer from the hardware (Farber 2011).

Appendix B: Trajectory Generation for the 2D case

The dynamics of a two dimensional granular particle i are governed by Newton's equation of motion for the centre-of-mass coordinates (x_i, y_i) and particle's (scalar) angular orientation(φ_i):

$$\begin{aligned} m_i \frac{d^2 x_i}{dt^2} &= F_x^i \\ m_i \frac{d^2 y_i}{dt^2} &= F_y^i \\ J_i \frac{d\omega_i}{dt} &= M_i \end{aligned} \tag{B.1}$$

The forces F_x^i, F_y^i are projections on the corresponding axes, of the total force, acting on the particle i at some time instant due to the interaction with its neighbour particles (as presented in Eq. (4.2)). M_i is the torque acting on particle i at the same time instant, m_i is its mass and J_i its (scalar) moment of inertia.

Table B.1 Pseudo-code for MD simulation.

Step	Description
1	Insert initialization file ¹
2	Insert excitation values ²
3	For all time-steps do:
4	Set forces to zero
5	Predict particle position + derivatives
6	Calculate Forces
7	Correct particle position + derivatives
8	for all particles do
9	Calculate mass centre position + derivatives
10	end for
11	Export data to a .dat file
12	End for

¹ A .dat file containing particles' properties and position + integration data (time time-step etc).

² Excitation values such as frequency and amplitude are entered via an interactive GUI

The irregularly shaped particles are treated as polygons constructed by N triangles; where N is the number of nodes on particle's surface. Calculation of each particle's mass and moment of inertia is based on particle's density (uniform density with same value as for spherical particles). In addition, each particle's position of gravity centre is assumed to coincide with polygon's centroid.

Of the large number of available finite - difference schemes, Gear's (1971) predictor - corrector was used which is suitable for MD due to its numerical stability. It has to be noted that for the purpose of our work a vector $\mathbf{r}_i(x_i, y_i, \varphi_i)$ was created in order to handle the coordinates and angular orientation in a single step. In Table B.1 is illustrated the pseudocode⁵ of our algorithm. As shown for the integration of Equation B.1 three steps are followed:

In the first step, the Gear algorithm predicts particles positions at time $t + \Delta t$ using a fifth order Taylor series based on positions and their derivatives at time t :

$$\begin{aligned}\mathbf{r}_i^{pr}(t + \Delta t) &= \mathbf{r}_i(t) + \Delta t \mathbf{u}_i(t) + \frac{1}{2} \Delta t^2 \ddot{\mathbf{r}}_i(t) + \dots \\ \mathbf{u}_i^{pr}(t + \Delta t) &= \mathbf{u}_i(t) + \Delta t \dot{\mathbf{r}}_i(t) + \dots \\ \ddot{\mathbf{r}}_i^{pr}(t + \Delta t) &= \ddot{\mathbf{r}}_i(t) + \dots \\ &\vdots\end{aligned}\tag{B.2}$$

In the next step, the algorithm calculates the force on each granule at time $t + \Delta t$ using the predicted positions. Based on this force and Equation B.1 a new value $\ddot{\mathbf{r}}_i^{new}(t + \Delta t)$ of each particle is calculated as well as the discrepancy between the two accelerations:

$$\Delta \ddot{\mathbf{r}}_i = \ddot{\mathbf{r}}_i^{new}(t + \Delta t) - \ddot{\mathbf{r}}_i^{pr}(t + \Delta t).\tag{B.3}$$

Finally, the algorithm corrects the predicted positions and their derivatives using the discrepancy between the predicted acceleration and that derived from the calculated force:

$$\begin{pmatrix} \mathbf{r}_i^{cor}(t + \Delta t) \\ \mathbf{u}_i^{cor}(t + \Delta t) \\ \ddot{\mathbf{r}}_i^{cor}(t + \Delta t) \\ \vdots \end{pmatrix} = \begin{pmatrix} \mathbf{r}_i^{pr}(t + \Delta t) \\ \mathbf{u}_i^{pr}(t + \Delta t) \\ \ddot{\mathbf{r}}_i^{pr}(t + \Delta t) \\ \vdots \end{pmatrix} + \begin{pmatrix} c_0 \\ c_1 \frac{1}{\Delta t} \\ c_2 \frac{1}{2} \\ \vdots \end{pmatrix} \frac{(\Delta t)^2}{2} \Delta \ddot{\mathbf{r}}_i\tag{B.4}$$

⁵ Pseudocode is an informal description of an algorithm intended for human rather than machine reading

Coefficients c_i depend on the algorithm and the order of differential equation and in our case are given by Poschel & Scwager (2005). Furthermore, in Table B.2 is presented the pseudo-code of our algorithm for the coupled ship-cargo problem. As discussed in *Chapter 4*, in addition to the Gear predictor-corrector algorithm for particles' trajectory generation, a 4th order Runge-Kutta scheme is solved at each time step for the ship motion problem and the impacting load due to possible particles' impact with hold's side walls.

Table B.2 Pseudo-code for MD simulation for coupled motion.

Step	Description
1	Insert initialization file ¹
2	Insert floating body's initial position
3	For all time-steps do:
4	Insert floating body's position for this timestep
5	Set forces to zero
6	Predict particle position + derivatives
7	Calculate Forces
8	Correct particle position + derivatives
9	for all particles do
10	Calculate mass centre position + forces on tank walls
11	end for
12	Calculate floating body's position for next time step (4 th order RK)
13	End for
¹ A .dat file containing particles' properties and position + integration data (time time-step etc).	

Appendix C:

Scaling technique

Due to space and budget limitations in most of the cases experiments (actual or numerical) with real size constructions are impossible. When it comes to maritime research, testing models are almost unavoidable. Even though testing models can provide suitable measurements generally easier than at full-scale, problems associated with scaling still exist. As a result, experiments based on scaled models have to be carefully planned in order to give realistic results.

Extensive discussion about scaling laws and techniques applied in marine structures can be found, for example, in Vassalos (1992). According to him, the basic principles of scaling laws for sea keeping or ocean engineering experiments may be summarised under three headings:

- a) Similarity, which involves geometric (similarity of shape), kinematic (similarity of motion) and dynamic (similarity of forces) similarities.
- b) Dimensional analysis, which involves extraction of non-dimensional excitation frequency and amplitude.
- c) Governing equations (e.g. ‘group theory’ approach)

Focusing on dimensional analysis, an effort to summarize our scaling approach is given below. Our aim is to further explain the choices that we have made in the main part of the work, regarding tank’s size and excitation parameters (amplitude, frequency). It has to be noted that, in the present section, only scaling laws that have to do with tank size and external excitation parameters are considered. Scaling effects of materials’ physical properties, such as particle diameter and friction, which would normally need further experimental investigation, are not discussed here (*Chapter 5* includes such approaches).

Scaling of excitation frequency and amplitude

Based on the specific dimensions of a vessel/scaled model and on wave parameters the appropriate scaled values of the excitation frequency and amplitude can be calculated, following Equation C.1:

$$\omega_1 * \sqrt{\frac{l_1}{g}} = \omega_2 * \sqrt{\frac{l_2}{g}} \quad \text{and} \quad \frac{n_1}{l_1} = \frac{n_2}{l_2} \quad (\text{C.1})$$

ω_i and n_i stand for excitation frequency and amplitude and l_i for the width of the structure (subscript 1 corresponds to the real and 2 to the scaled structure).

Case study

Figure C.1 depicts, in a graphical way, the wave energy spectra of the ocean. It is shown that the three most common wave generation mechanisms (wind, earthquakes and planetary), result on waves with different frequency, although overlapping occurs. We are interested in wind generated waves of non-extreme conditions in such a frequency range that surface tension and the coriolis force do not affect the waves.

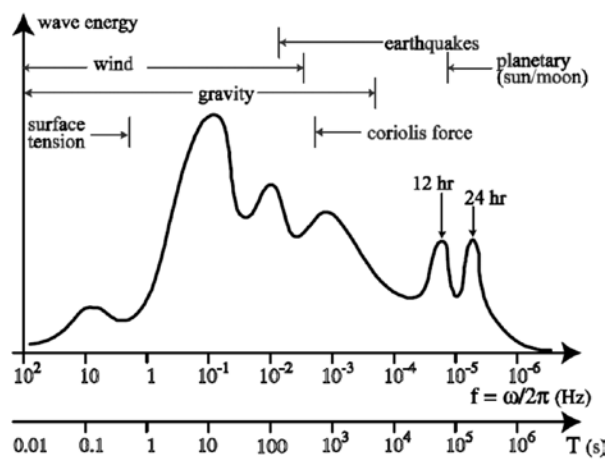


Figure C.1 Wave energy spectra with indication of generation mechanisms (source: Tchet 2005).

Furthermore, in order to understand the importance of radiation, diffraction and viscous drag forces on marine structures, depending on wave frequency, we refer to Figure C.2. Although this and similar drawings (e.g. Faltinsen 1993) are based on fixed cylinders with diameter D , it is assumed to be useful also for the case of our 2D rectangular floating structure. The incident waves are regular with height H and wavelength λ . As shown, depending on characteristic dimension of the body the importance of diffraction and viscous drag forces is varied.

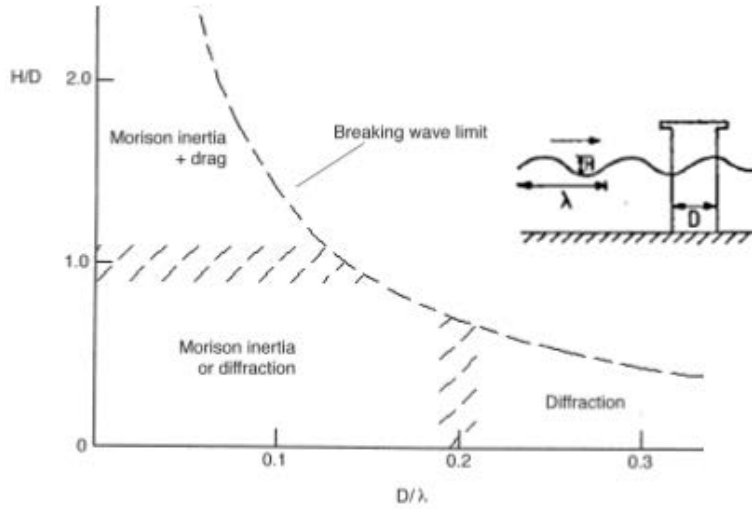


Figure C.2 Relative importance of potential (radiation and diffraction) or viscous (drag) flow effects on a fixed pile [source: Vassalos 2005 (body), Faltinsen 1993 (detail)].

In our case, the scaling process followed an inverse order. That is, we firstly selected the dimensions for our scaled model and then we derived its full scale analogue, based on specific frequency and amplitude excitation ranges. Reasoning for this order was our intention to perform:

- The tilting box test using the proposed by IMO (2012) scaled dimensions.
- Experimental validation of numerical results using laboratory equipment, that is restricted to specific tank dimensions and excitation ranges.

While various scaled models have been used throughout this work, below we perform calculations for the coupled ship-cargo model investigated in *Chapter 7*. Based on Equation B.1, the calculation of excitation's frequency and amplitude range of the full scale model (1:100 scale) is as follows:

Frequency ω_2 of incident waves for scaled model: 0.4 to 1 Hz	} \Rightarrow
Amplitude n_2 of incident waves for scaled model: 0 to 0.03 m	
Scaled Model's width (l_2): 0.34 m	
Full scale Vessel's width (l_1): 34 m	

Frequency range of sea waves for full scale structure: 0.04 to 0.1 Hz (Period range: 10 - 25 s)
 Amplitude range of sea waves on full scale structure: 0 to 3 m.

As indicated, the incident excitation values correspond to wind/gravity sea-waves when the full scale model is considered. Furthermore, the D/λ and H/D ratios are such that the diffraction forces and the forces due to viscous effects are less important. It is noted that, in most cases, a fixed value of wave amplitude is assumed and the response of the material inside the tank is investigated only under various values of the excitation frequency.

Appendix D:

Investigation of angle of repose using the shipboard test method

As discussed in *Chapter 2*, in IMSBC is described a second alternative to the “tilting box” method, identified as the “shipboard test method” for the prediction of the angle of repose (IMO 2012a). An important experimental investigation based on the shipboard method has been conducted by Train (1958). A lot of different studies, both experimental and numerical, have been presented since then (see for example the review by Poschel & Schwager 2005). In recent decades the DEM approach has been extensively used in order to investigate granular flows through a wedge-shaped or conical hopper (see for example Mollon & Zhao 2013). The most frequently observed phenomenon is the fluctuations in the velocity field, firstly reported by Baxter et al (1989). Since then, a lot of scholars confirmed the existence of decompression waves propagating upwards at a much higher speed than the flow itself. Furthermore, Vivanco et al. (2012) experimentally showed that the fluctuations tend to disappear for wider hopper opening.

Taking the above mentioned observations into account; and using our Molecular Dynamics algorithm, we conducted a series of numerical experiments based on the “shipboard test method”. Several tests were performed in order to investigate the dependence of the predicted angle on system configuration. Comparisons against results obtained by numerical implementation of the tilting box method are also included.

D.1 System description

A funnel with wall slope of 30 *deg* to the vertical axis was assumed, filled with 2500 spherical particles. As shown in Figure D.1, the particles were initially symmetrically distributed and let to settle inside the funnel. During this phase, both the top and the bottom opening of the hopper were closed in order to keep the particles inside the funnel. Once the system reached equilibrium, the two openings were removed and the material inside the funnel was free to flow.

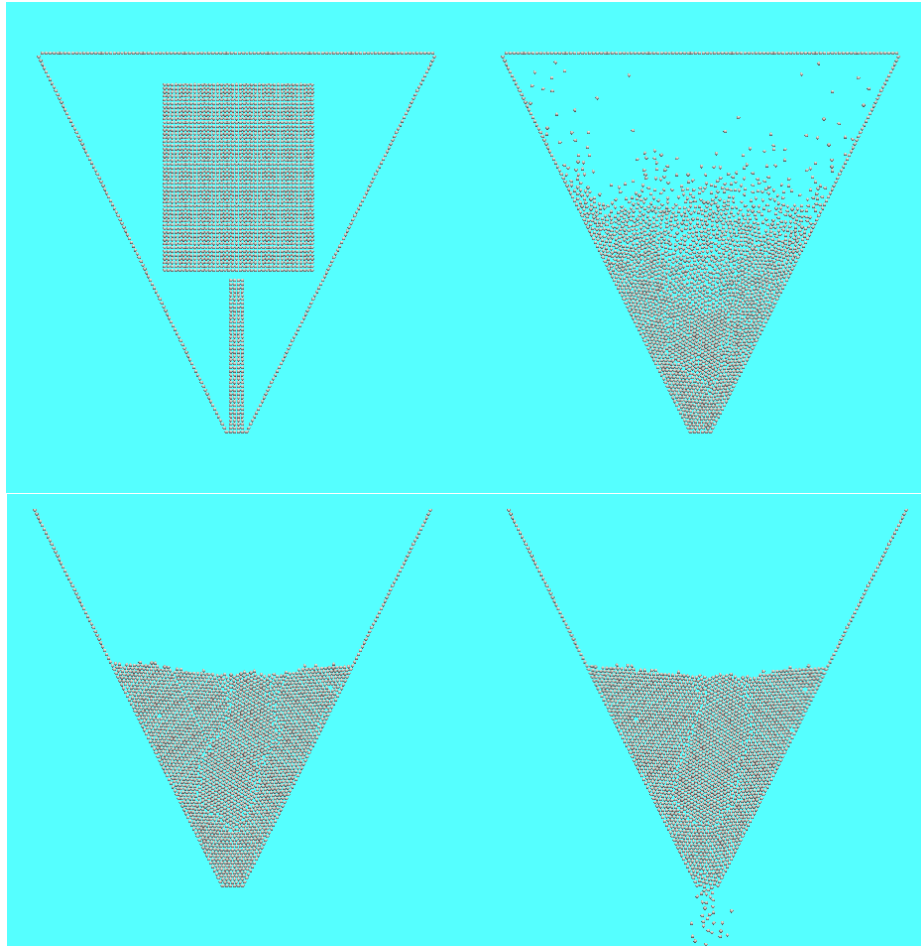


Figure D.1 Time instants for the initialization of the system : (0 s, 3.5 s, 10 s, 0.5 s after the tip opens, from top left to bottom right,, respectively).

D.1 Numerical experiments

Initially, the funnel was filled with glass spheres with diameter 0.5 cm and density 2.5 gr/cm^3 . The funnel opening had a fixed distance from the base (10 times the particle diameter) and the material was left to flow until a sand-pile was formed. It was found that, our simulation results are in good agreement with similar numerical experiments presented by Zhou et al ((2001)). Working in the same manner for several values of rolling friction, we calculated a standard deviation of about 4%. Convinced about the robustness of the MD method, we felt that we can proceed to the main numerical experiments planned for the current investigation, using spherical cellulose acetate particles with diameter 0.6 cm and density 1.38 gr/cm^3 .

Dependence of angle of repose on funnel tip width

Two different funnel tip openings have been selected in order to understand, in comparative manner, the behaviour of granular flow. In the first, the opening was equal to 6

particle diameters while in the second it was half this size. A smaller funnel opening (2 particle diameters) was proved to be inadequate for investigation since the particles showed difficulty to flow due to arching phenomena. Figure D.2 depicts time instants of particle flow from these two hoppers, 8 seconds after the flow started. As expected, the particles inside the first hopper (6 diameter opening), move more easily and thus their vertical velocity is higher. As a result, the pile for the funnel with the wider opening is constructed faster but it needs more particles. Despite that, we did not observe any variation in the predicted angle for the two cases.

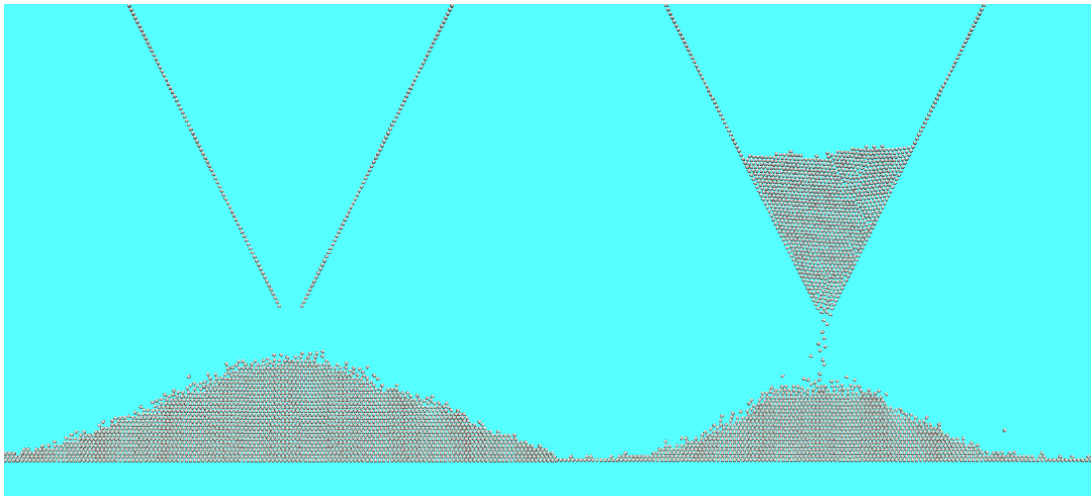


Figure D.2 Time instants (7.8 s) indicate the difference on pile formation between funnels with large (left) and small (right) funnel opening.

Dependence of angle of repose on funnel vertical velocity

Three different simulation results are produced per funnel configuration. Firstly, we tested the angle of repose when the funnel was allowed to move in the vertical plane; thus the funnel tip was all the time close to the top of the particles' cone. Furthermore, we measured the angle of repose when the funnel was fixed at a given height above the horizontal base. In both cases, the base was selected large enough (200 particle diameters) in order to follow IMOs directives. Time instants of particle flow when the funnel is free to move with velocity 2.5 and 5 *cm/s* are presented in Figure D.3 (top and middle respectively). In Figure D.3 (bottom) time instants for the second test series (fixed funnel height above the base) are presented. Each numerical experiment was repeated 12 times, for slightly different initial configurations. Each angle value appearing in Figure D.3 is the mean angle over the 12 experiments and the error is the mean square sample-to-sample fluctuation. As noticed, there is a dependence of the angle of repose on both funnel opening width (Figure D.4 left) and

vertical velocity of the funnel (Figure D.4 right), in the sense that the smaller the height/velocity, the larger the predicted value. These results are in good agreement with experimental observations made by Train (1958).

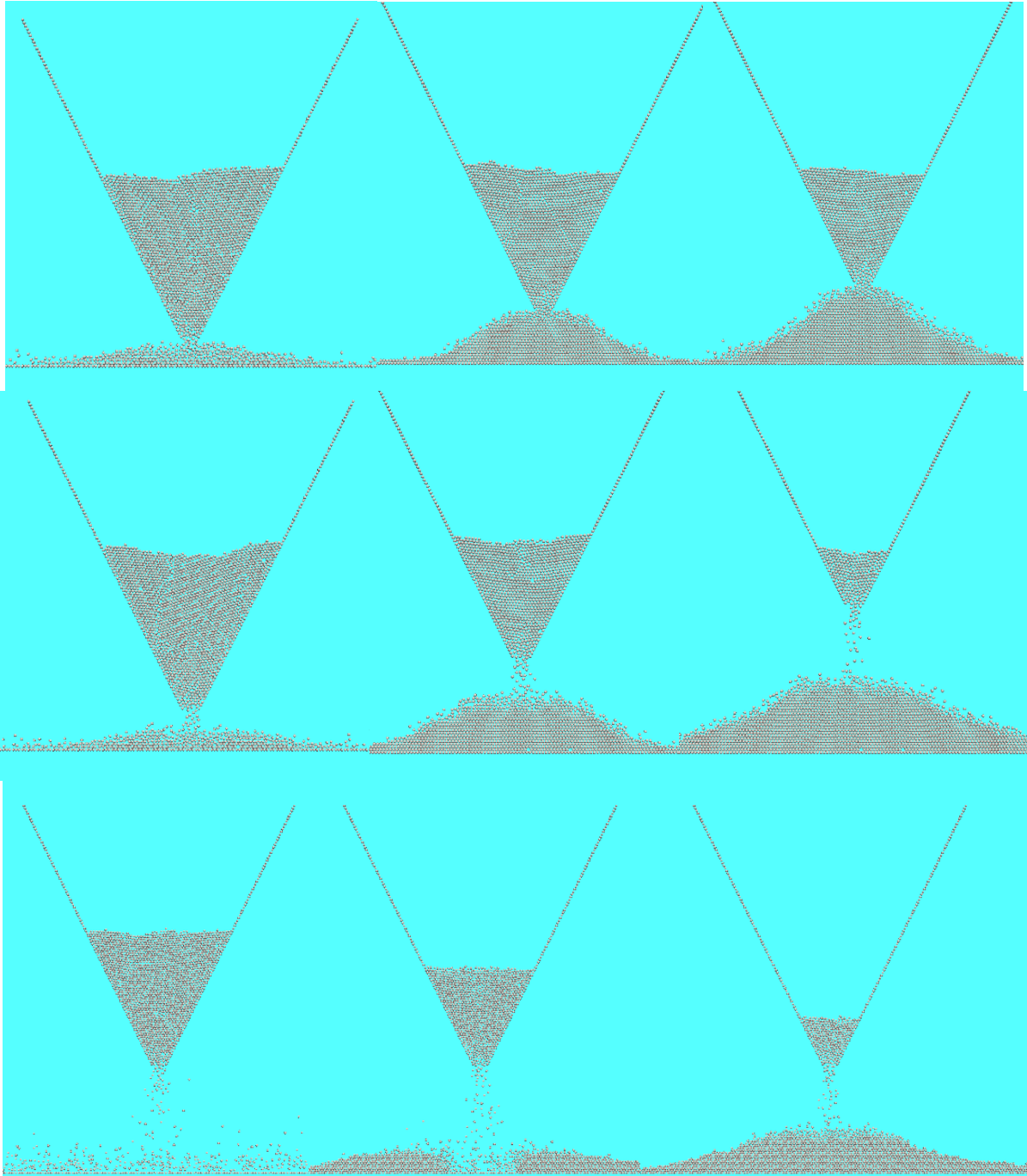


Figure D.3 Time instants of particle flow when the funnel is free to move with velocity 2.5 cm/s (top) and 5 cm/s (middle) or has a fixed height above the base (bottom).

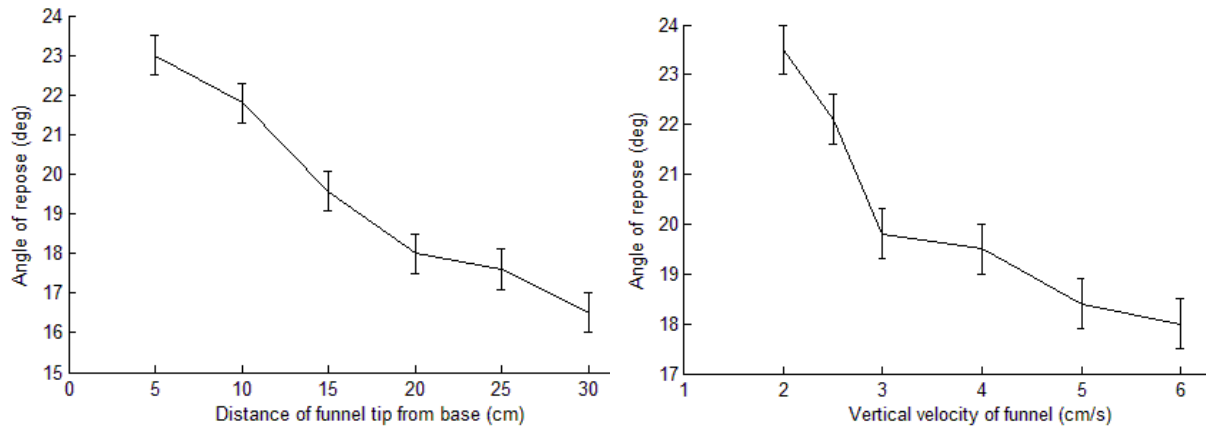


Figure D.4 Dependence of angle of repose on the funnel's distance from the base (left) and vertical velocity (right).

D.2 Comparison with tilting box test

Based on the previously discussed observations, we constructed 12 different initial configurations of the funnel with low vertical velocity (2.5 cm/s); thus the tip is all the times very close to the top of the formed pile (approx.. 2 cm). In Figure D.5 is summarized the outcome of these experiments in comparison with that predicted by the tilting box method. The values are presented in sequential order without taking any care for clustering these values. It is noticed that, the mean value of the predicted angle of repose (dotted line) is close to 21 deg (with standard deviation 0.5), almost 4 deg smaller than for tilting box test (solid line). This is however in very good agreement with IMO's (2012) predictions for difference close to 3 deg between the two methods (dashed-dotted line).

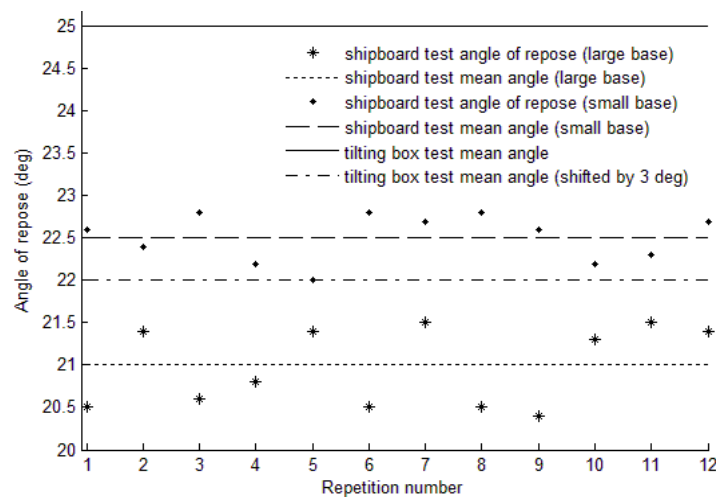


Figure D.5 Comparison between predicted angles for the shipboard test with large (dotted line) and small (dashed line) base and that predicted by the tilting box method.

In addition, Figure D.5 presents the predictions for the angle of repose for a case where the width of the base is of fixed size (ten times funnel tip width). As shown (dashed line), on that occasion the angle of repose has a larger value (mean value 22.5 deg) which is also smaller (close to 2.5 deg) than that predicted by tilting box tests. Figure D.6 presents time instants right after pile formation for the two cases.

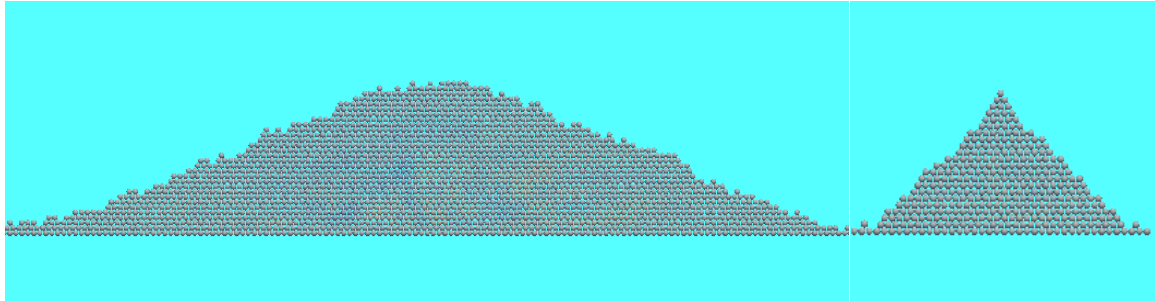


Figure D.6 Time instants right after pile formation for large (left) and small (right) base width.

D.3 Concluding remarks

A series of numerical experiments based on the “shipboard test method” were performed in order to investigate, at a preliminary level, the dependence of the predicted angle on system configuration. The investigation was based on simulations relying on “molecular dynamics” method. Cellulose acetate spheres with diameter 6 mm were considering. Comparison with angles predicted from tilting box method is also included.

Results showed a dependence of the predicted angles on system configuration. Specifically, it was shown that the angle of repose obtains smaller value when the funnel’s height or vertical velocity obtains larger values. The results are in good agreement with those of similar numerical or experimental studies presented in the literature. Comparisons with tilting box tests confirm, from a different perspective, the accuracy of the simulation results. At the same time, they corroborate by direct micro-scale simulation the empirical recommendation of IMO about the correspondence between the tilting box and the shipboard test method.

Appendix E:

Coupled ship-cargo 3 DOF equations of motion

In this Appendix is extracted a simplified set of motion equations for a freely floating body presenting symmetry around its longitudinal plane, meeting transversely harmonic waves (3-DOF approach). In reality, since the object of our investigation is the motion of this body when it is partly filled with granular material, the model possesses thousands of degrees of freedom due to the independent movement of the contained particles. Here however, we shall concentrate only on the ship model, relying basically on the one that has been proposed by Blagoveschensky (1962) developed for studying beam-sea stability. Following Newton's approach, the differential equations of motion of a vessel, free to move in sway, heave and roll (3 DOF), with reference to the inertial system discussed in Chapter 7, take the form:

$$\begin{aligned} m\ddot{y} &= \sum F_y \\ m\ddot{z} &= \sum F_z \\ I\ddot{\varphi} &= \sum M_x \end{aligned} \tag{E.1}$$

φ is the absolute roll angle, m and I are respectively the mass and roll moment of inertia F_y and F_z are the projections of the principal vector of the forces acting upon the vessel on the axes y , z respectively; and M_x is the corresponding moment of these forces about the x axis.

Our analysis is based on the assumption of inviscid, irrotational flow and linear wave induced motions in single sinusoidal (regular) excitation. We assume small wave amplitudes of first order and small wave slope, wave length much larger than the barge's width as well as *low forward speed of the barge such that any wave making due to forward motion is neglected*. Below, a brief description of the forces/moments that act on the barge due to water-vessel and cargo-vessel interaction is provided, leading to the description of the final system of differential equations for the motion of the system.

E.1 Water-vessel interaction

The forces that act on the body due to water-vessel interaction can be calculated by the integration of the pressure acting on the wetted surface of the vessel, described by Bernoulli's equation (e.g. Athanassoulis, 2008):

$$P = \rho \left(\frac{1}{2} (\nabla \Phi \nabla \Phi) + \frac{\partial \Phi}{\partial t} + gZ \right) \quad (\text{E.2})$$

$$Z = z - A \cos(ky - \omega t) \quad (\text{E.3})$$

A harmonic incident wave propagating in direction parallel to the y axis (with reference to the inertial system discussed in Chapter 7) has been assumed. Φ stands for the fluid velocity potential and $A \cos(ky - \omega t)$ for the sea surface elevation due to the wave. The first two terms at the right-hand-side of Eq. (E.2) represent the hydrodynamic contribution to the pressure while the last term the hydrostatic one. To first order, the velocity squared term can be neglected. Furthermore, due to the linear wave approach adopted in the current work we may write, as is almost standard practice, the velocity potential Φ as the sum of five independent components: the incident wave (Φ_I), the diffraction (Φ_D) and the three radiation potentials ($\Phi_R^2, \Phi_R^3, \Phi_R^4$) due to unit motion in each direction (sway, heave and roll, respectively).

$$\Phi = \Phi_I + \Phi_D + \Phi_R^{(2)} + \Phi_R^{(3)} + \Phi_R^{(4)} \quad (\text{E.4})$$

Hydrostatic forces:

The hydrostatic (restoring) forces/moments can be calculated by the integration of the last term of Eq. (E.2) over the wetted surface. In Blagoveshchensky (1962) is presented step-by-step this calculation, resulting in the following expressions for the heave restoring force and the roll restoring moment:

$$F_z^{HS} = -\rho g A_{WP} z + \rho g a_2 \cos(\omega t) \quad (\text{E.5})$$

$$M_x^{HS}(\varphi, \alpha) = -\rho g \nabla \overline{GM} \varphi + \rho g \overline{GM} A k \sin(\omega t) \quad (\text{E.6})$$

Here a_2 is given by $a_2 = \int_S \cos(ky) dS$ and for large wave-length-to-vessel-width ratio equals A_{WP} . Of course, there is no restoring term when the vessel is swayed.

Wave exciting forces:

The wave exciting force can, in principle, be calculated by the integration of the second term of Eq. (E.2) over the wetted surface, taking into account only the incident wave and diffraction component of the velocity potential (Φ_I, Φ_D). Φ_I is responsible for the hydrodynamic part of the Froude - Krylov force (also called Smith effect force) and corresponds to the integration of the pressure as if the ship was fully transparent for the incident waves. When the wavelength of the incoming waves are long compared with ship's breadth, Φ_I has been shown to be the dominating part (see for example Faltinsen 1993, see also Appendix C). In what follows, Φ_D is neglected. For regular waves the incident wave velocity potential is given by:

$$\Phi_I = \frac{Ag}{\omega} e^{kz} \sin(ky - \omega t) \quad (\text{E.7})$$

By combining Eq. (E.7) and (E.2), the following expressions for the wave exciting forces/moment are obtained (Blagoveshchensky 1962):

$$\begin{aligned} F_y^{HD} &= -\rho A_2 \omega^2 \sin(\omega t) \\ F_z^{HD} &= -\rho A_2 \omega^2 \cos(\omega t) \\ M_x^{HD} &= -IAk \omega^2 \sin(\omega t) \end{aligned} \quad (\text{E.8})$$

where $A_2 = \int_V e^{kz} \sin(ky) dV$. For large wave-length-to-vessel-width ratio it is equal to the barge's submerged volume at calm sea ∇_0 .

Radiation forces:

Integration of radiation potentials $\Phi_R^{(2)}, \Phi_R^{(3)}$ and $\Phi_R^{(4)}$ in Eq. (E.4) over the wetted surface leads to the calculation of radiation forces. These forces are a result of the radiation of waves away from the vessel due to its motion in calm water. In contrast though to wave exciting forces, there is no analytical description for radiation potentials. A common technique, to overcome this issue (see for example Faltinsen 1993 or Athanassoulis 2008) is to analyze these forces in two components, one in phase with vessel's acceleration and one with its velocity. Thus we may write the radiation terms in the form:

$$\mathbf{F}_i^R = \sum_{j=2}^4 (A_{ij} \ddot{n}_i + B_{ij} \dot{n}_i) \quad (\text{E.9})$$

where A_{ij} and B_{ij} are the frequency-dependent, due to the presence of the free surface, added mass and damping coefficients. For our case, where analysis of the steady state response of a symmetric body subjected to a regular incident wave is considered, Eq. (E.9) can accurately

describe the steady state ship response (Ogilvie 1964). However if irregular seas or transient response is of interest, memory effects become important and thus one should formulate the equations of motion in time-domain following Cummins' (1962) approach by incorporating the convolution integral of an impulse response function and body's velocity; or perhaps an approximating state-space formula based on a large number of ODE's (see for example Tigkas 2009).

The port/starboard (lateral) hull symmetry and linear theory imply that coupled equations of motions reduce to two sets of equations, one set of coupled equations for symmetric and another set for anti-symmetric motions (Abkowitz 1969). Thus, heave is, at first order, uncoupled from sway and roll. It is remarked however that, in our case, a different coupling arises due to the motion of the cargo particles, whose changing position, velocity and acceleration in heave affect ship sway and roll dynamics.

The following form of heave, sway and roll radiation excitations has been adopted:

$$\begin{aligned} F_y^R &= A_{22}\ddot{y} + B_{22}\dot{y} + A_{24}\ddot{\phi} + B_{24}\dot{\phi} \\ F_z^R &= A_{33}\ddot{z} + B_{33}\dot{z} \\ M_x^R &= A_{44}\ddot{\phi} + B_{44}\dot{\phi} + A_{42}\ddot{y} + B_{42}\dot{y} \end{aligned} \quad (E.10)$$

E.2 Cargo-vessel interaction

Taking into account the previous paragraph, the forces and moments in Eq (E.1) can, in general, be decomposed as follows:

$$\begin{aligned} \sum F_x &= F_x^{HS} + F_x^{HD} + F_x^D + F_x^R + F_x^{cargo} \\ \sum F_y &= F_y^{HS} + F_y^{HD} + F_y^D + F_y^R + F_y^{cargo} \\ \sum M_x &= M_x^{HS} + M_x^{HD} + M_x^D + M_x^R + M_x^{cargo} \end{aligned} \quad (E.11)$$

The first four terms of Eq. (E.11) are: the hydrostatic, the hydrodynamic part of Froude-Krylov, the diffraction and the radiation forces/moments due to water - vessel interaction.

F_x^{cargo} , F_y^{cargo} and M_x^{cargo} describe the impact force and moment generated by the particles' contact with nonzero relative velocity with hold's walls.

Furthermore, the coupling due to cargo's shift (weight displacement) is taken into account through the calculation of the hydrostatic forces. Specifically, Eq. (E.12) has been

used instead of its equivalent derived analytically (Eq. (E.6)) in order to accurately take into account the influence of cargo shift upon system's dynamic response.

$$M_x^{HS}(\varphi, \alpha) = M_x^B + M_x^S + M_x^C \quad (E.12)$$

$M_x^{HS}(\varphi, \alpha)$ stands for the restoring moment calculated as the sum of three moments ($M_x^B(\varphi, \alpha)$ due to buoyancy, $M_x^S(\varphi, \alpha)$ due to ship's weight and $M_x^C(\varphi, \alpha)$ due to cargo's weight) calculated numerically, taking account of the absolute roll angle (φ) and the slope (α) of the incident wave.

E.3 Final form of equations of motion

Substitution of all the above described forces into Eq. (E.1) results to the wave induced ship motion described by Eq. (E.13) which is solved in time, coupled with the nonlinear molecular dynamics model of the granular material:

$$\begin{aligned} (M + A_{22})\ddot{y} + B_{22}\dot{y} + A_{24}\ddot{\phi} + B_{24}\dot{\phi} &= -\rho\nabla_0 A\omega^2 \sin(\omega t) + F_y^{cargo} \\ (M + A_{33})\ddot{z} + B_{33}\dot{z} + \rho g A_{WP} z &= \rho g A_{WP} \cos(\omega t) - \rho\nabla_0 A\omega^2 \cos(\omega t) + F_z^{cargo} \\ (I + A_{44})\ddot{\phi} + B_{44}\dot{\phi} + A_{42}\ddot{y} + B_{42}\dot{y} + M_x^{HS}(\varphi, \alpha) &= -IAk\omega^2 \sin(\omega t) + M_x^{cargo} \end{aligned} \quad (E.13)$$

As said at the beginning, these equations are similar with the equations obtained by Blagoveshchensky (1962) for motions of a vessel with small width in comparison with the wave length (although in his case the radiation forces had not been included). It is noted also that, while damping effects due to viscosity should, in principle, be incorporated in the model, especially when motions in roll and sway are considered, in the simplified model of our approach we haven't included such damping terms. Last but not least, cases of break of symmetry due to cargo shift and hysteretic phenomena, and/or any substantial drifting effect, would require hydrodynamic reaction-type coupling between the sway, and roll motions which are also not considered here and they should be seen as future improvements of the model.

Appendix F: Initialisation of wave propagation

As already discussed in *Chapter 7*, for the purpose of our study we assumed zero initial conditions for barge's position and velocity; that is the barge starts its motion “from rest” when the harmonic excitation is introduced. While this assumption works well for sinusoidal terms of exciting forces, any cosine term inserts an unrealistic situation to our problem: at time 0 the exciting force has its highest value. Working with the coupled ship-cargo 3 DOF equations of motion (Eq. 7.6) in order to investigate possible effects of this “cold start” upon systems dynamic behaviour, we multiplied the exciting forces and moments with an appropriate transition function, allowing thus a “soft start” for the system:

$$D(\tau) = \begin{cases} 0, & \tau \leq 0 \\ e^{1-\frac{1}{1-(\tau-1)^2}}, & 0 < \tau < 1 \\ 1, & \tau > 1 \end{cases} \quad (\text{F.1})$$

where $\tau = \frac{t}{t_{ref}}$ is the ratio of simulation time (t) with some reference time value (t_{ref}).

As shown in Figure F.1 (left) the transition function has a value of 0 before the start of the motion and smoothly becomes 1 at some selected time. Figure F.1 (right) presents the normalized exciting force in heave both before and after the multiplication with the transition function (exciting wave frequency 4.7 rad/s and amplitude 2.5 cm).

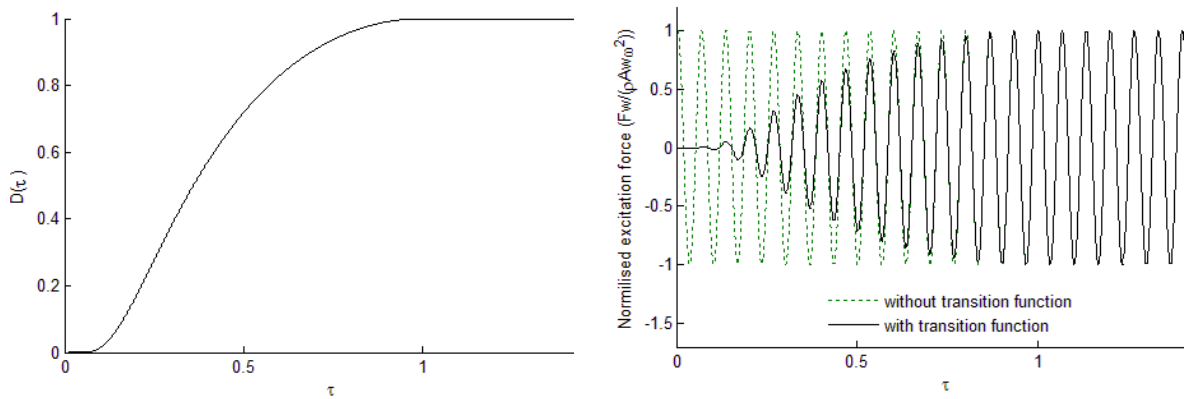


Figure F.1 Roll response of ship with (solid) and without (dotted) the use of transition function, for two characteristic values of excitation amplitude-frequency: left) 2.5 cm - 4.7 rad/s, right) 2.7 cm - 4.5 rad/s.

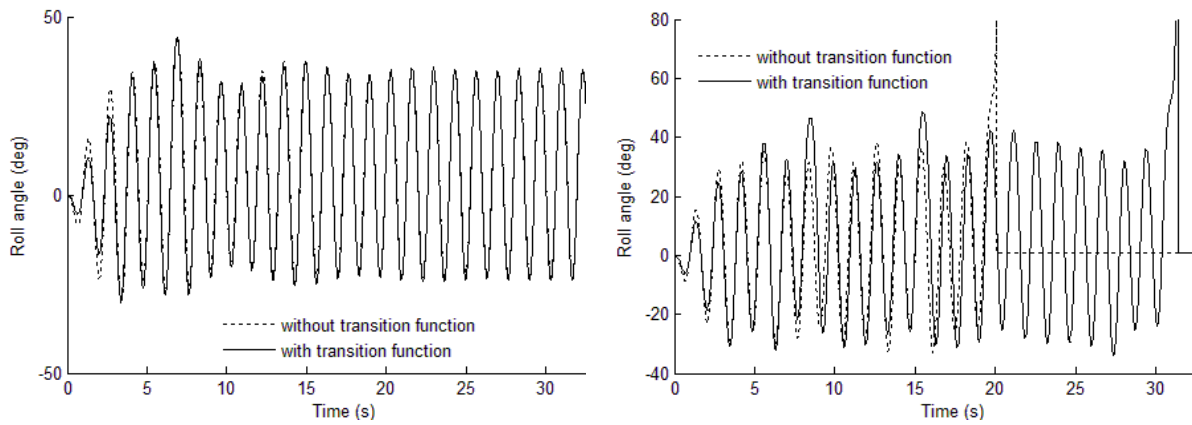


Figure F.2 Roll response of ship with (solid) and without (dotted) use of the transition function, for two characteristic values of excitation amplitude-frequency : left) 2.5 cm - 4.7 rad/s, right) 2.7 cm - 4.5 rad/s.

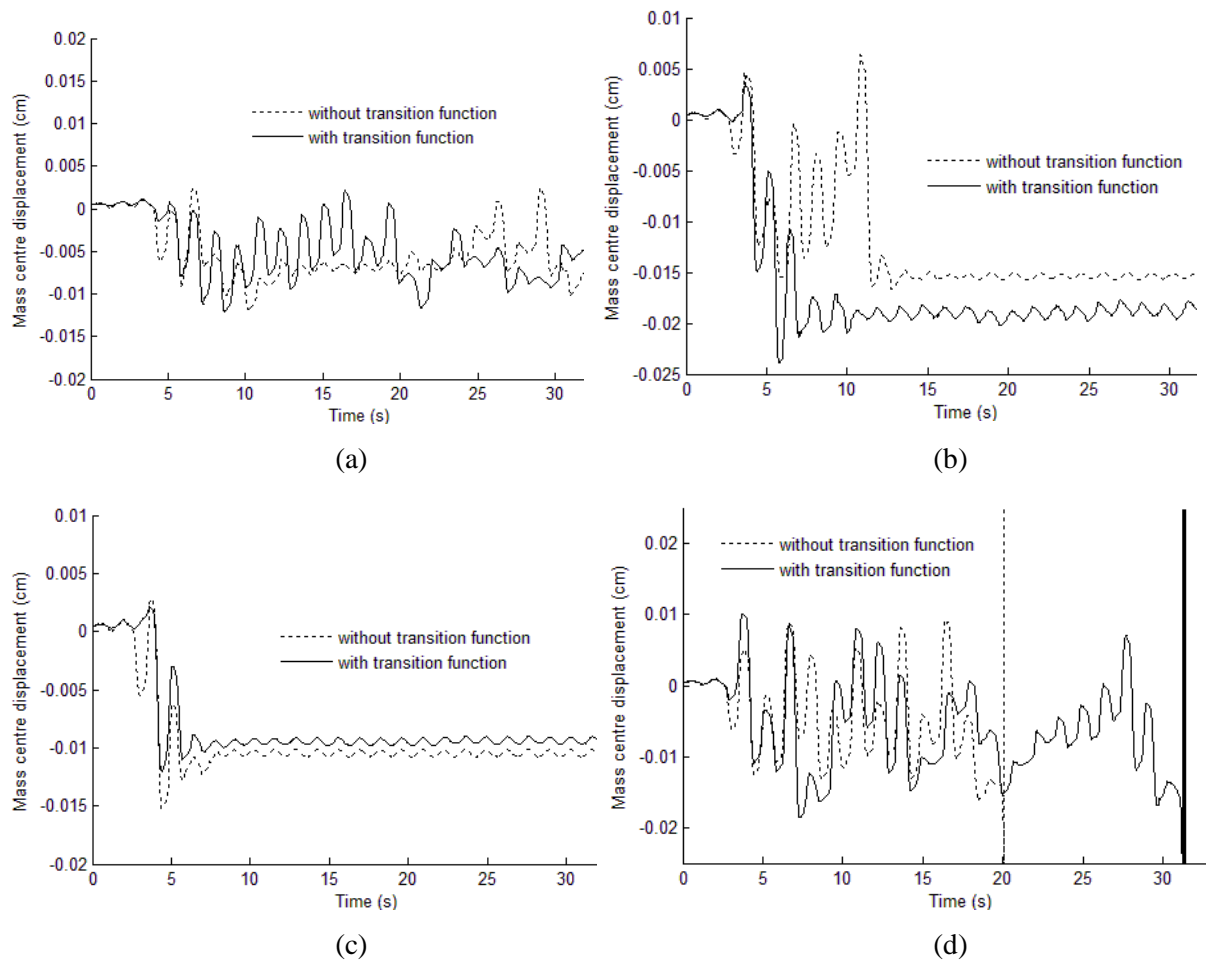


Figure F.3 Mass centre displacement of material inside the tank for equation of motion with (solid) and without (dotted) use of the transition function, for four characteristic values of excitation amplitude-frequency : a) 2 cm - 4.5 rad/s, b) 2.5 cm - 4.5 rad/s, c) 2.5 cm - 4.7 rad/s, d) 2.7 cm - 4.5 rad/s.

Following the same approach as in *Chapter 7*, we investigated the response of the barge under a wide range of excitation amplitudes/frequencies and different values of t_{ref} (from 1 to 20 times excitation's period). Comparison of these results against those extracted without the use of transition function indicated that, both the response of the barge and the motion of the material inside the tank are quite similar for the two systems (even though in one case capsize occurred a few seconds later for the system with the ramped excitation (Figure F.2 right). This is logical as it takes longer for the main effect from the involved excitation component to be felt. In Figure F.2 is presented a comparison of barge's response for two critical values of excitation amplitude - frequency and $t_{ref} = 5 * Excitation\ Period$. Furthermore, in Figure F.3 are compared the mass centre displacements, for four characteristic values of excitation amplitude - frequency and the same t_{ref} . One can conclude that, while differences are almost negligible in our case, the inclusion of the ramp function is advisable.